# Reduced models via machine learning to analyse the criticality of defects

Hugo Launay

PSL
UNIVERSITÉ PARIS

# THÈSE DE DOCTORAT
## DE L'UNIVERSITÉ PSL

Préparée à MINES ParisTech

# Reduced models via machine learning to analyse the criticality of defects
–
# Modèles réduits par apprentissage automatique pour l'étude de la nocivité de défauts


Soutenue par
**Hugo LAUNAY**
Le 03 décembre 2021


École doctorale n°621
**Ingénierie des Systèmes, Matériaux, Mécanique, Energétique**

Spécialité
**Mécanique**

Composition du jury :

| | |
|---|---|
| Isabelle BLOCH<br>Professeur, Télécom Paris | *Examinatrice (Présidente)* |
| David NERON<br>Professeur des Universités, ENS Paris Saclay | *Rapporteur* |
| Markus KAESTNER<br>Professeur des Universités, TU Dresden | *Rapporteur* |
| Laurent GALLIMARD<br>Professeur des Universités, Université Paris Nanterre | *Examinateur* |
| Jacques BESSON<br>Directeur de recherche CNRS, MINES ParisTech, UMR 7633 | *Examinateur* |
| David RYCKELYNCK<br>Professeur, MINES ParisTech | *Directeur de thèse* |
| Francois WILLOT<br>Directeur de recherche, MINES ParisTech | *Directeur de thèse* |

MINES ParisTech | PSL

# Remerciements

La première personne que je tiens à remercier est mon directeur de thèse, David RYCKELYNCK. Il m'a donné cette opportunité de travail et il m'a accompagné au plus près tout au long de ces trois années. Les nombreux échanges que nous avons pu avoir ont été tous plus intéressants les uns que les autres. Sa passion, sa motivation et son enthousiasme m'ont porté pendant toute la durée de mes recherches.

Mes remerciements vont ensuite à mon second directeur de thèse, François WILLOT. J'ai pu découvrir avec lui la méthode FFT et différents aspects de morphologie mathématique. Il a toujours su se rendre disponible pour moi et pour cela je l'en remercie très scincèrement. Sa rigueur scientifique m'a été d'une aide précieuse pour ma rédaction.

Je remercie mon troisième encadrant de thèse, Jacques BESSON. Sans lui l'implémentation de mes codes dans Zebulon aurait été bien plus compliquée... Il a contribué à porter un regard extérieur très enrichissant sur les méthodologies développées tout au long de ma thèse.

Je souhaite aussi remercier Laurent LACOURT qui n'a pas participé directement à l'encadrement de ma thèse mais qui pourtant a joué un rôle primordial dans son déroulement. Les nombreuses discussions que nous avons pu avoir et les codes que nous avons pu faire ensemble m'ont énormément aidé.

A Djamel MISSOUM-BENZIAN et à Farida AZZOUZ, merci pour leur encadrement lors de mon mastère DMS et pour m'avoir permis de mettre un permier pied dans le monde de la recherche.

Un merci tout particulier aux amis du Centre des Matériaux : Amar, Benjix, Gladouch, Lucky, Sergent Borrossi, Hugo ptit père, le démon Milani, féfé, Bastien, Chloé et la team DMS (Mélophile ou Thélanie, Robin mon hypercéphale préféré et chichi) !

A toutes les personnes que j'ai pu croiser au centre des matériaux et qui ont contribué de près ou de loin à mes recherches et rendre le quotidien du labo si agréable, je tiens à exprimer toute ma gratitude.

Je tiens ensuite à remercier les membres ma famille au sens large qui ont été présent au cours de ces trois ans de thèse et qui sont, de facon plus générale, toujours là pour moi. Un merci tout particulier à mes parents qui ont entendu parler de réduction de modèle, machine learning, de simulation numérique et autres termes parfois très obscurs mais toujours avec autant d'attention. Merci d'avoir relu "mes rapports pleins de hiéroglyphes" comme mon père les décrivait. Je remercie aussi sincèrement mes deux frères Tristan et Amaury pour leur soutien indéfectible, leur écoute et pour m'avoir aidé pour mes répétitions de soutenance entre autre.

Un merci tout particulier à mon cobureau préféré Dr. Rossen Tchakalov ! Il a été un véritable pilier pendant cette thèse. Des discussions toujours passionantes sur des sujets extrêmement variés et une écoute à l'autre extraordinaire.

Enfin je te remercie, Barbara, pour m'avoir accompagné tout au long de ces trois ans. Tu as vécu avec moi cette expérience unique que représente la thèse et tu as su m'épauler et me soutenir dans les bons et les mauvais moments, pour tout ca je te remercie.

# Contents

# Abbreviations

| Acronym | Definition |
|---|---|
| CNN | Convolutional Neuron Network |
| DEIM | Descrete Empirical Interpolation Method |
| DEM | Discrete Element Method |
| DOF | Degree Of Freedom |
| FEM | Finite Element Method |
| FFT | Fast Fourier Transform |
| FNN | Feedforward Neuron Network |
| FOM | Full Order Model |
| HLLE | Hessian-based Locally Linear Embedding |
| HROM | Hyper Reduced Order Model |
| LATIN | LArge Time INcrement |
| LLE | Locally-Linear Embedding |
| ML | Machine Learning |
| PCA | Principal Component Analysis |
| PGD | Proper Generalized Decomposition |
| POD | Proper Orthogonal Decomposition |
| RB | Reduced Basis |
| REV | Representative Elementary Volume |
| RID | Reduced Integration Domain |
| ROB | Reduced Order Basis |
| ROM | Reduced Order Model |
| SIF | Stress Intensity Factor |
| SVD | Singular Value Decomposition |
| $k$-NN | $k$ Nearest Neighbour |
| KPCA | Kernel Principal Component Analysis |
| TLV | Tight Local Volume |
| t-SNE | t-distributed Stochastic Neighbour Embedding |

# Chapter 1

# Context

**Contents**



**Résumé en français**


Au cours de leur vie, les structures finissent toujours par se dététériorer. Cela peut être dû à divers facteurs comme la corrosion, des impacts ou encore de la fatigue mécanique. De même le procédé de fabrication, comme le soudage, peut lui-même être à l'origine de défauts. L'impact des défauts sur la durée de vie des structures peut être très significatif car ces derniers jouent le rôle de concentrateur de contrainte. Ainsi, afin de ne pas rebuter toutes les pièces comprenant des défauts, des abaques et des critères bien précis sont utilisés afin de statuer sur la nocivité des défauts observés. Toutefois ces méthodes ont tendance à être trop conservatives et certaines piéces qui auraient pu être utilisées se trouvent mises au rebut.
Les méthodes de calculs numériques ont l'avantage d'évaluer plus précisement les quantités d'intérêts déterminantes et permettent donc de rebuter moins de pièces. Néanmoins cette démarche est coûteuse en temps et en puissance de calcul.
Des méthodes fondées sur l'apprentissage automatique permettent d'accélérer considérablement ces temps de calculs en tirant profit du grand nombre de données d'ores et déjà générées.
C'est dans ce cadre que s'inscrit ce travail de thèse.


## 1.1 Assessment of structures containing defects

### 1.1.1 Presence of defects in structures

In the course of their lifetime, structures always end being deteriorated. Many phenomena can be responsible for these deteriorations : corrosion, impacts, fatigue, scratches... Moreover the fabrication process, such as welding or stamping process for example, can also account for the creation of defects. This can explain the presence of defects such as cracks or pores within the structures. Once a crack appears it can propagate until the whole structure fails as Fig. 1.1a shows. Similarly the presence of pores dramatically lowers the structure mechanical properties as they play the role of stress concentrators. This type of defects is common in concrete structures (see Fig.1.1b) as well as in welded joints (see Fig.1.1c).

(a) (b) (c)

Figure 1.1: (a) Cracked pipeline (b) Pores within a concrete structure (c) tomography of pores within a welded joint [Lacourt, 2019].

Nevertheless it is not possible to reject all components that contain one or more defects, all the more so if this component is high-value added.
Hence it is necessary to set acceptance criteria in order to evaluate the criticality of the defects. In an industrial context, the evaluation time must be about the same as the control time so that

the production speed is not impacted.
Nowadays the tomography, radiography and ultrasounds methods enable a non destructive control of the components. One can visualize the defects located inside the bulk in three dimensions. The size of the observed defects can then be used as input data to assess the criticality of the defect.
In the framework of cracked structures assessment, the standard ISO 21153 is used in the fields of aero-spatial, nuclear and automotive among other things. This standard is based on the speed of propagation of cracks.
As regard defects like pores, other standards are used such as the standard ISO 15901 which evaluates the pore size distribution or else the standard AWS D17.1 that specifies the maximal sizes of defects and their minimal distance between each other.
Although these standards give a framework to dimension and assess the structures containing defects, they are usually made for specific geometries and loadings. On top of that, standards are usually conservative regarding the acceptance of structures and have a tendency to oversize them or to reject some of them that are sometime still functional.
As soon as one is outside the framework of these standards or if one needs to have finer results, the use of digital twins [E. H. and D. S., 2012] and numerical methods such as the Finite Element Method (FEM), the Discrete Element Method (DEM) or else the Fast Fourier Transformation (FFT) method turns out to be a very relevant choice. The FEM allows to treat non parametric configurations and to apply any type of loadings.
Besides segmentation methods have improved significantly over the last couple of years and allow to extract realistic images of defects contained in the structure. Hence representative defects obtained through out tomography can be inserted in FE meshes in such way that a digital twin of the component is obtained.
However the use of such methods tends to be extremely time consuming. It can be explained by the important size ratio between the defect and the whole structure. It results in very fine meshes containing a huge number of Degrees Of Freedom (DOFs). Therefore this computation times are not consistent with industrial expectations. These computation times are even larger when many configurations and loadings need to be tested for a same defect.

### 1.1.2 Evolution of numerical methods

Computation techniques are becoming more and more efficient and enable very accurate previsions. Besides, in the industry, the acceptance criteria are getting stricter and stricter and the assessment methods need to be more precise. Hence numerical computation times become even larger.
Numerical simulation techniques are now considered as a common assessment method and they have generated a huge amount of results over the past decades. Good use can be made of these numerical results : they can be taken as input data to learn faster models via machine learning and data driven approaches.
Moreover machine learning algorithms have recently been proposed to predict the mechanical behaviour of components made by additive manufacturing [Nasiri and Khosravani, 2021], for cracked propagation [Liu et al., 2020], for the lifetime fatigue prediction [Zhan et al., 2021] or else for the limit load prediction of pipings [Phan and Dhar, 2021].
Furthermore more complete models have been proposed where numerical simulation and machine learning have shown their complementarity [Martínez et al., 2021] [Wen et al., 2021]. The use of the data collected with all the numerical simulations that have been launched coupled with the richness of the computation techniques (FEM, FFT etc...) enables to obtain fast models which have the great advantage of being based on physics. This makes the interpretation of how they work much easier. This is called ”physics-informed machine learning”.
One of the major assets of machine learning techniques is that they prevent the parametric modeling of objects. This is particularly useful for the analysis of defects having random shapes and morphologies which can seen when image-based digital twins are used. This thesis is written according to this paradigm.

## 1.2 Objectives and thesis organization

Computer vision and machine learning have made great improvements during the past decades. Thanks to these techniques new dimensionality reduction methods have been created. In this work use will be made of computer vision and machine learning in order to assess structures containing defects, via fast image-based digital twins.
The objectives of the thesis are multiple. The quantities of interest for structure assessment are different depending on the considered case study. With regard to sane pipeline, the limit pressure has to be evaluated whereas the maximal stress must be computed when it comes to dealing with structures with pores undergoing cyclic loading. Concerning cracked components, the stress intensity factor is used for their assessment.
For these three quantities of interest, numerical computations that need to be launched often require very large computation times. In the framework of this thesis, new methodologies will be developed to compute these quantities of interest faster. More specifically, techniques based

on machine learning will be used. The problem solving methodology will essentially based on linear and non linear model order reduction coupled with machine learning techniques.
The present manuscript is articulated along 5 main chapters which will detailed the techniques to evaluate the quantities of interest cited before.
The notion of dimensionality reduction will be detailled in the second chapter and various methods will be investigated in order to enable a global understanding of what this general term covers.
Hyper reduction with reduced integration domain and the associated tools to obtain Reduced Order Model (ROM) will then be discussed. The Reduced Integration Domain (RID) can be seen as a submodel supplemented by a reduced basis approximation. A brief state of the art of the computer vision methods will be made and more specifically those that have been proposed for mechanical digital twins based on numerical images.
The third chapter will be addressed to the extension of the hyper reduction method to non elliptical problems for the determination of the limit loads. Problems such as beam buckling or elasto-plastic pipes collapse will be tackled.
The fourth chapter is devoted to the development of a new method based on mechanical and morphological clustering. This clustering will be used to select local reduced basis, designed for a morphological cluster, for hyper reduced computations. A study case of a welded joint containing a void will be covered. Finally the fifth chapter proposes an innovative method coupling computer vision and submodel resolution. Cracked specimens will be modelled and the crack geometry will enable the trained model to generate the adequate boundary conditions on a subdomain containing the crack. The sixth chapter concludes and offers various research perspectives.

# Chapter 2

# State of the art

**Contents**



**Résumé en français**


Dans ce chapitre la bibliographie des différents outils qui seront utilisés dans ce travail de thèse est présentée. Les approches de réduction dimensionnelle linéaire telles que la décomposition aux valeurs propres généralisée ou encore la décomposition orthogonale aux valeurs propres y sont détaillées. Les méthodes de réduction dimensionnelle non-linéaires sont ensuite abordées. Ces méthodes de réduction dimensionnelle permettent de mettre en place des modèles d'ordre réduit. Différents modèles d'ordre réduit sont présentés comme l'hyper-réduction ou la méthode "ROM-net".
Enfin, étant donné qu'une grande partie de ce travail de thèse est basé sur l'analyse d'image, des méthodes de visions par ordinateur sont présentées.


## 2.1 Dimensionality reduction

### 2.1.1 Linear approach to dimensionality reduction

The section, dedicated to dimensionality reduction, is inspired of [Fauque, 2018] where a state of the art of linear reduction methods is made. The linear dimensionality reduction is characterised by a tensor or vector representation of the latent space. This representation is obtained by a sum of product of functions.

#### Proper generalized decomposition

Proper Generalized Decomposition (PGD) is an *a priori* method, also called "on the fly" method, which enables to circumvent the difficulty related to the solution of multidimensional models.
For a solution $u$ depending on the variable $(x_1, ..., x_D) \in \Omega_1 \times ... \times \Omega_D$, $x_i$ designating spatial coordinates, time or any parameter of the problem, the approximation of rank $l$ of $u$ is represented with the equation 2.1 where $l$ and the $F_i^j(x_j)$, with $i \in [1, l]$ and $j \in [1, D]$, are already known.

$$u(x_1, .., x_D) \approx \sum_{i=1}^{l} F_i^1(x_1) \times \cdots \times F_i^D(x_D) \tag{2.1}$$

The number of terms $l$ needed to obtain a good reference solution approximation depends on how well it can be split. Functions $F_i^j(x_j)$ are found by an iterative enrichment. At the enrichment step $n+1$, the functions $F_i^j(x_j)$ from the previous steps $i \leq n$ are already known and the new product of the $D$ functions $F_i^j(x_j)$ has to be found. To do so, an approximation of rank $n+1$ of $u$ in the weak formulation of the problem is used. Hence a non-linear system is obtained and needs to be solved with an iterative algorithm such as a fixed point algorithm. The resolution of this system is similar to solving a one dimensional problem for each of the $D$ functions $F_i^j(x_j)$ defined in $\Omega_j$.

The curse of dimensionality that appears when considering the sampling of high dimensional space is circumvent by the PGD method by considering the solution space of partial differential equations [Ladevèze et al., 2018]. The number of dof of a PGD based model increases linearly with the dimension of the problem. This ability of the PGD to handle high dimensional problems can be found in a great number of articles, in particular [Ammar et al., 2006, Chinesta and Ladeveze, 2014, Chinesta et al., 2010] and the associated references.
PGD is actually a generalisation of the radial loading approximation used in the framework of the LATIN (LArge Time INcrement) method [Boucard and Ladeveze, 1999, Ladevèze et al., 2010]. The latter is a non-incremental in time resolution method and it has been developed for mechanical problems defined on a space-time domain $\Omega \times [0, t_f]$.
The LATIN method relies on three main principals. Firstly, a separation of the difficulties is made. The equations are separated in order to make a linear problem that can be global in space (equilibrium equation) and a local problem in space which can be non-linear (constitutive law, contact boundary conditions). The solution of the problem is then the intersection between the linear and local problems. Secondly, an iterative algorithm working in two steps that enables to find the solution in such a way that it verifies alternatively both problems (linear and local) until it converges.
Finally, the linear problem is solved with the use of a radial loading approximation of rank $l$ of the solution $u$ and is written as in eq.2.2.

$$u(x,t) \approx \sum_{i=1}^{l} X_i(x) \cdot T_i(t), \qquad (x,t) \in \Omega \times [0, t_f] \tag{2.2}$$

Since its introduction, the LATIN method has been applied to numerous problems in mechanics. The LATIN solver for PGD approximation has been recently extended to multiscale problems having large number of parameters in [Ladevèze et al., 2018] for simple mechanical problems.

### *A posteriori* method

The so-called *A posteriori* methods are data driven approaches to model order reduction. Simulation data are collected or generated prior training a reduced order model on these data. In this sense the *A posteriori* methods constitutes a machine learning methodology with a training phase to learn a subspace of approximation. Then, in the online phase, new data samples are treated and the equation are projected in the learnt subspace of approximation. The so collected data have usually been generated with Full Order Models (FOMs) that belong to the studied temporal and parametric space. These computations are commonly denoted as snapshots, using Sirovich terminology [Sirovich, 1987]. The Reduced Basis (RB) is either composed of snapshots or of vectors obtained by extracting the most important information present in those snapshots. This type of methods is similar to the Principal Component Analysis (PCA) frequently used in unsupervised machine learning. The ROM is obtained by a (Petrov-)Galerkin projection of the FOM on the RB.

### Projection on reduced basis methods

The strategy adopted by the reduced basis method (RBM) consists in projecting the FOM on a subspace generated by a basis of functions chosen to represent the FOM for a specific study case. First works on this thematic appeared in the late 70s and were developed for mechanical problems in linear and non-linear cases [Almroth et al., 1978, Nagy, 1979, Noor and Peters, 1980]. Later in the 2000s, a more mathematical framework was given to these methods [Prud'homme et al., 2002, Maday and Rønquist, 2002]. These works were crucial for the RBM since they led to an efficient criterion for the snapshot selection used to build the RB generating the approximation subspace. Use is made of greedy algorithm which will at the same time limit the number of FOM to compute and also limit the size of the RB used to reduce the model. A split into two main parts have also been introduced in these works :
→ An "offline" part, also called training/learning phase, during which the RB has also been constructed by launching FOMs simulations for various values in the parametric space.
→ An "online" part which consists in solving the reduced problem that depends on the parameters. The problem being projected on the approximation subspace, the complexity of the problem is much smaller than for the FOM.
Use of an error estimator is a must in order to guarantee the quality of the reduced problem solution.

### Singular value decomposition

The singular value decomposition [Eckart and Young, 1936, Golub and Van Loan, 1983, Stewart, 1993] (SVD) is detailed in the following section since it is greatly used in model order reduction. Indeed it offers a compressed RB by using some snapshots. SVD can decompose a rectangle matrix into three matrices with specific properties. This method can be seen as the generalization of the diagonalization to the rectangle matrices. Considering $\boldsymbol{S} \in \mathcal{R}^{\mathcal{N} \times N_s}$ a matrix of rank $d \leq \min(\mathcal{N}, N_s)$, by applying the SVD theory it exists a decomposition of $\boldsymbol{S}$ such that

$$\boldsymbol{S} = \boldsymbol{V}\ \boldsymbol{\Sigma}\ \boldsymbol{W}^T \tag{2.3}$$

Where $\boldsymbol{V} \in \mathcal{R}^{\mathcal{N}\times\mathcal{N}}$ and $\boldsymbol{W} \in \mathcal{R}^{N_s\times N_s}$ are orthogoanl matrices, $\boldsymbol{V}^T\boldsymbol{V} = \boldsymbol{V}\boldsymbol{V}^T = \boldsymbol{I}_{\mathcal{N}}$ and $\boldsymbol{W}^T\boldsymbol{W} = \boldsymbol{W}\boldsymbol{W}^T = \boldsymbol{I}_{N_s}$ and $\boldsymbol{\Sigma} \in \mathcal{R}^{\mathcal{N}\times N_s}$ is written as :

$$\boldsymbol{\Sigma} = \begin{pmatrix} \boldsymbol{D} & 0 \\ 0 & 0 \end{pmatrix} \in \mathcal{R}^{\mathcal{N}\times N} \text{ with } \boldsymbol{D} = \text{diag}(\sigma_1, \sigma_2, ..., \sigma_d) \text{ such that } \sigma_1 \geq \sigma_2 \geq ... \geq \sigma_d \geq 0.$$

The column vectors $\boldsymbol{V}[:, i]$ and $\boldsymbol{W}[:, i]$ are respectively called left singular vectors and right singular vectors of $\boldsymbol{S}$. The $\sigma_d$ are sorted in descending order and are called singular values. The left singular values of $\boldsymbol{S}$ correspond to the eigenvalues of $\boldsymbol{S}\boldsymbol{S}^T$, the right singular values of $\boldsymbol{S}$ correspond to the eigenvalues of $\boldsymbol{S}^T\boldsymbol{S}$ and the squared value of each singular value of $\boldsymbol{S}$ is equal to the corresponding eigenvalue of $\boldsymbol{S}\boldsymbol{S}^T$ and $\boldsymbol{S}^T\boldsymbol{S}$. This is directly obtained through the following relations :

$$\boldsymbol{S}\boldsymbol{S}^T = \boldsymbol{V}\boldsymbol{\Sigma}\boldsymbol{\Sigma}^T\boldsymbol{V}^T \tag{2.4}$$

$$\boldsymbol{S}^T\boldsymbol{S} = \boldsymbol{W}\boldsymbol{\Sigma}^T\boldsymbol{\Sigma}\boldsymbol{W}^T \tag{2.5}$$

More precisely the relation 2.3 can be simplified by removing the terms that gives a null result :

$$\boldsymbol{S} = \boldsymbol{V}[:, 1:d]\ \boldsymbol{\Sigma}\ \boldsymbol{W}^T[1:d, :] \tag{2.6}$$

The decomposition is unique (except for the sign of the right and left singular vectors). SVD enables to find the best approximation in Frobenius norm of a matrix $\boldsymbol{S}$ for a given number of vectors. Moreover the values of the singular values is directly link to the approximation error. The singular vectors which are associated to the largest singular values, are the ones that will approximate the best the matrix $\boldsymbol{S}$. The relation between the approximation error of a matrix $\boldsymbol{S}$ of rank $d$ by its truncated SVD $\tilde{\boldsymbol{S}}_l$ of rank $l \leq d$ and the singular values $\sigma_i$ of $\boldsymbol{S}$ can be written as :

$$||\boldsymbol{S} - \tilde{\boldsymbol{S}}_l||_F = \left( \sum_{k=l+1}^{d} \sigma_k 2 \right)^{\frac{1}{2}} \qquad \text{avec} \qquad \tilde{\boldsymbol{S}}_l = \boldsymbol{V}[:, 1:l]\ \boldsymbol{\Sigma}[1:l, 1:l]\ \boldsymbol{W}^T[1:l, 1:l] \tag{2.7}$$

A standard image that can be used for image processing is considered. The image has $779 \times 638$ pixels and is in black and white. It can be seen as a matrix of 779 lines and 638 columns. Each component of the matrix corresponds to a grey scale level between 0 and 255. It is then possible to visualize its representation of rank lower than 638 obtained by SVD on Fig.2.1. Only the most important singular vectors are taken into account. Fig.2.2 represents the relative error discrepancy with the squared Frobenius norm between the original and approximated images. The error evolves as a function of the rank of the approximated matrix by SVD.

Figure 2.1: Original image and the following SVD approximations of rank 5, 20, 63, 191 and 446.

The function decreases quickly for a high order of approximation. The evolution is quick between the images of rank 5, 20, and 63 as it can be seen on figure 2.1. Then the decrease is slower (see Fig.2.2) as it can be noticed for the approximated images of rank 191 and 446. Even if the decrease seems to be slow, the error becomes very low starting from rank 191 and is hard to see with naked eyes. This clearly shows the capacity of the SVD to approximate a matrix with another of a much lower rank. Besides the SVD is broadly used to compute the rank of a

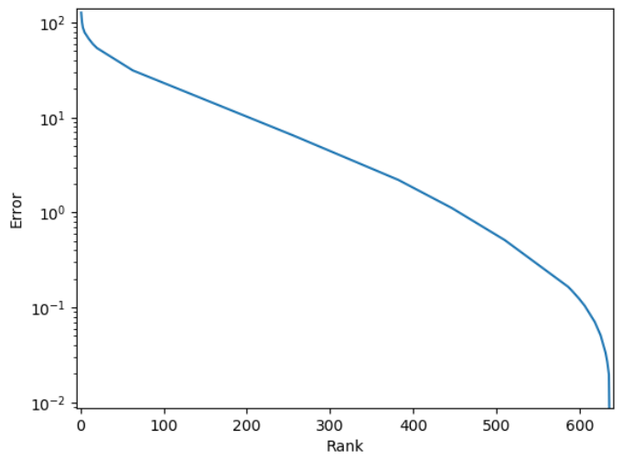


Figure 2.2: Decrease of the relative error in Frobenius norm between the original and the SVD approximated matrices.

matrix. Indeed the rank of the matrix $\boldsymbol{S}$ is directly given by the one of the matrix $\boldsymbol{D}$ which is diagonal.

$$\text{rank}(\boldsymbol{S}) = \text{rank}(\boldsymbol{D}) \tag{2.8}$$

In practice since the SVD of $\boldsymbol{S}$ is numerically evaluated, one needs to define a tolerance threshold $\varepsilon_{rank}$ from which a value is considered to equal to zero numerically. The rank of $\boldsymbol{S}$ is then :

$$d = \underset{i \in \mathbb{N}}{\text{argmin}}(\sigma_i > \varepsilon_{rang}) \tag{2.9}$$

SVD is still an active field of research. Due to its massive use for various applications, one of the main research areas is performance. As examples, one can cite the randomized algorithms [Mahoney, 2011] that enable to compute the truncated SVD for very large matrices. Another research focus is the generalization of the SVD to tensor with dimension strictly superior to two. One can cite as examples the High Order SVD [De Lathauwer et al., 2000] or else the hierarchical Tucker decomposition [Hackbusch and Kühn, 2009]. Techniques have been proposed [Brand, 2002, Ryckelynck et al., 2006] to approximate the SVD for matrices with a high number of columns with an incremental approach. The main idea of these methods is to update the approximations of the term found with the SVD by incorporating progressively the column of the matrix on which the SVD is applied. This technique is denoted as incremental SVD. These techniques can then be used to enrich the SVD of a matrix with new vectors obtained from new computations. A well-known extension of the SVD to self-supervized machine learning is autoencoders [Hinton and Salakhutdinov, 2006].

**Proper orthogonal decomposition**

The concept of Proper Orthogonal Decomposition (POD) has been introduced to extract coherent structures from a turbulent flow [Lumley, 1967]. Initially this method was developed for data analysis. Its goal was to extract a reduced number of variables containing the majority of the initial information. This global idea of data extraction was studied in many fields. The same idea is present in the SVD presented in 2.1.1, in the Principal Component Analysis [Pearson, 1901] (PCA) or else in the Karhunen-Loève development [Loève, 1955, Karhunen, 1946]. POD will be later reused in the snapshot method [Sirovich, 1987]. The main difference between the two POD is that Lumley's uses an average in time and a spatial correlation while Sirovich's does the opposite. Since with FOM there are generally much more dofs than temporal snapshots, the snapshot method will be more appropriate for this work.
The main idea behind POD is to search for vectors $(\boldsymbol{\psi}_i)_{i=1}^{l}$ two by two orthogonal. This enables to approximate as well as possible, in the mean square sense, the vector $(\boldsymbol{u}(\mu_j))_{j=1}^{N_s}$ which corresponds to the snapshots in model order reduction :

$$\min_{\boldsymbol{\psi}_1,\dots,\boldsymbol{\psi}_l} \sum_{j=1}^{N_s} ||\boldsymbol{u}(\mu_j) - \sum_{i=1}^{l} \langle \boldsymbol{u}(\mu_j), \boldsymbol{\psi}_i \rangle ||_X^2 \qquad \text{such that} \qquad \langle \boldsymbol{\psi}_i, \boldsymbol{\psi}_k \rangle_X = \delta_{ij} \qquad \forall i,k \in [1,l]^2 \tag{2.10}$$

If one looks at the minimization problem 2.10, using the canonical scalar product on $L^2$, it is possible to obtain a minimization problem discretised in space by writing the $\boldsymbol{u}(\mu_j)$ and the $\boldsymbol{\psi}_i$ onto the functions of the FOM $(\boldsymbol{\phi}_a)_{a=1}^{N}$. The scalar product $L^2$ and its norm is written as :

$$\langle \boldsymbol{u}, \boldsymbol{v} \rangle_{L^2} = \tilde{\boldsymbol{u}}^T \boldsymbol{M} \tilde{\boldsymbol{v}} \qquad \text{and} \qquad ||\boldsymbol{u}||_{L^2} = ||\boldsymbol{L}^T \tilde{\boldsymbol{u}}||_2 \tag{2.11}$$

with $\tilde{\boldsymbol{u}}, \tilde{\boldsymbol{v}}$ being the vectors containing the coefficients of $\boldsymbol{u}, \boldsymbol{v}$ written in the FOM basis. $\boldsymbol{M}$ is the mass matrix of the FOM defined as follows :

$$(\boldsymbol{M})_{ab} = \langle \boldsymbol{\phi}_a, \boldsymbol{\phi}_b \rangle_{L^2}, \qquad \forall a,b \in [1,N]^2 \tag{2.12}$$

with a Cholesky factorisation it follows :

$$\boldsymbol{M} = \boldsymbol{L}\boldsymbol{L}^T \tag{2.13}$$

Hence the minimisation problem becomes :

$$\boldsymbol{V} = \underset{\boldsymbol{Z}\in\mathcal{R}^{N\times 1}}{\operatorname{argmin}} ||\boldsymbol{A} - \boldsymbol{Z}\boldsymbol{Z}^T\boldsymbol{A}||_F^2 \qquad \text{such as :} \qquad \boldsymbol{Z}^T\boldsymbol{Z} = \boldsymbol{I} \tag{2.14}$$

with $\boldsymbol{A} = \boldsymbol{L}^T\boldsymbol{S}$ and $\boldsymbol{Z} = \boldsymbol{L}^T\boldsymbol{\Psi}$, where $\boldsymbol{S}$ and $\boldsymbol{\Psi}$ are respectively the column vectors containing the coefficient of $(\boldsymbol{u}(\mu_j))_{j=1}^{N_s}$ and $(\boldsymbol{\psi}_i)_{i=1}^{l}$ written in the FE basis. According to Eckart-Young theorem [Eckart and Young, 1936], the POD basis referred to as $\boldsymbol{V}$ and which is the solution of 2.14 and containing the $l$ column vectors is obtained by taking the $l$ first left singular vectors from the SVD of the matrix $\boldsymbol{A}$, $\boldsymbol{V} = \boldsymbol{V}[:, 1:l]$. It is then obtained $\boldsymbol{\Psi} = \boldsymbol{L}^T\boldsymbol{V}$.

Furthermore the SVD enables to obtain the number of vectors $l$ to be taken into account for the RB because it is possible to evaluate the error made for the matrix approximation (see equation 2.7). The information carried by the $k$ first singular vectors can be defined as follows :

$$\varepsilon(k) = \frac{\sum_{i=1}^{k}\sigma_i^2}{\sum_{i=1}^{d}\sigma_i^2} = 1 - \frac{\sum_{i=k+1}^{d}\sigma_i^2}{\sum_{i=1}^{d}\sigma_i^2} \tag{2.15}$$

$l$ is defined as the smallest number of vectors to be taken so that the information collected is superior to a specific threshold :

$$l = \underset{k\in\mathcal{R}^{N\times 1}}{\operatorname{argmin}}(\varepsilon(k) \geq 1 - \epsilon_{tol}) \tag{2.16}$$

Where $\epsilon_{tol}$ is the acceptable relative error of approximation.
In practice, due to the fact that the FE mass matrix is not easy to compute, instead of finding the POD basis that minimizes the continuous problem 2.10, the POD that minimize the error with the Frobenius norm is taken :

$$\boldsymbol{V} = \underset{\boldsymbol{Z}\in\mathcal{R}^{N\times 1}}{\operatorname{argmin}} ||\boldsymbol{S} - \boldsymbol{Z}\boldsymbol{Z}^T\boldsymbol{S}||_F^2 \qquad \text{such that :} \qquad \boldsymbol{Z}^T\boldsymbol{Z} = \boldsymbol{I} \tag{2.17}$$

To obtain $\boldsymbol{V}$ in such way that the minimization problem 2.17 is verified, the SVD must be applied on $\boldsymbol{S}$. Hence the approximation squared error with the Frobenius norm verifies :

$$\frac{||\boldsymbol{S} - \boldsymbol{V}\boldsymbol{V}^T\boldsymbol{S}||_F^2}{||\boldsymbol{S}||_F^2} \tag{2.18}$$

Where $\boldsymbol{V}\boldsymbol{V}^T\boldsymbol{S}$ is equivalent to $\boldsymbol{S}_l$ as defined in equation 2.7.
It is necessary to underline the fact that in the framework of model order reduction, the POD threshold used for the construction of the POD basis, which will be used to construct the ROM, does not enable to estimate the error generated by the ROM.

### 2.1.2 non-linear dimensionality reduction without mapping to the ambient space

#### Locally-linear embedding

Local non-linear methods focus on preserving neighborhood geometry when mapping points to lower dimensional subspaces, and these subspaces may be curved or otherwise non-Euclidean. On the whole, these approaches have been successful, and some have guarantees about global properties, as well. Locally-linear embedding (LLE) approaches the dimensionality reduction problem similarly to PCA but focuses on a neighbourhood mapping, rather than a global mapping including transformations, rotations, and rescaling dependent on geometrically-based weights [Roweis and Saul, 2000]. Coordinates are chosen such that :

$$\boldsymbol{Y} = \sum_i \left( Y_i - \sum_j W_{ij} Y_j \right)^2 \tag{2.19}$$

is minimized based on locally-linear errors based on the local weights on points $i$ and $j$. The algorithm typically involves 3 steps : 1) choosing a point's k neighbours, 2) reconstructing these points using local weights, and 3) mapping to a new subspace. By knitting together neighbourhoods, it is possible to infer some global geometric properties, and one advantage of this approach is its global optimization guarantees.
There are other local non-linear methods that exit such as the Laplacian Eigenmap (LE), the Hessian-based Locally Linear Embedding (HLLE) or else t-distributed Stochastic Neighbour Embedding (t-SNE).

**Kernel principal component analysis**

Global non-linear approaches aim to capture the full geometry of the data space in a mapping to lower- dimensional space, which may be non-Euclidean.
Kernel PCA (kPCA) extends the PCA algorithm to effectively capture non-linear features or bases within the PCA framework [Weinberger et al., 2004]. The basic algorithms start with a mapping of the data to another pre-specified space, which is usually non-linear. PCA is then performed on this new space (a kernel Hilbert space with well defined geometric properties), and the results are taken as the new set of bases. Common mapping functions include Gaussian kernels, sigmoid kernels, radial basis function kernels, and linear kernels. Results are competitive with other manifold learning methods, and many algorithms, such as support vector machines, are related to this approach.
Considering $N$ data points in $\mathcal{R}^d$. Generally the data cannot be linearly separated in $d < N$ dimensions and to the contrary they can almost always be in $d > N$ dimensions. An application $\boldsymbol{\Phi}(\boldsymbol{x}_i)$ is introduced such that :

$$\boldsymbol{\Phi} \ : \ \mathcal{R}^d \rightarrow \mathcal{R}^N \tag{2.20}$$

In this space it is easy to define a hyperplane to linearly separate the data. In this case the application $\boldsymbol{\Phi}$ creates linearly independent vectors for each data points therefore it is useless to perform any eigen decomposition as it would be done with standard PCA. Usually one avoids to work in the $\boldsymbol{\Phi}$-space (also called feature space). The covariance matrix in the feature space is defined as :

$$\bar{\boldsymbol{C}} = \frac{1}{N}\sum_{j=1}^{N} \boldsymbol{\Phi}(\boldsymbol{x}_j)\boldsymbol{\Phi}(\boldsymbol{x}_j)^T \tag{2.21}$$

The eigenvalues $\lambda$ and eigenvector $\boldsymbol{V}$ can be computed :

$$\lambda \boldsymbol{V} = \bar{\boldsymbol{C}}\boldsymbol{V} \tag{2.22}$$

The solutions $\boldsymbol{V}$ lie in the span of $\boldsymbol{\Phi}(\boldsymbol{x}_i)$ for $i = 1, ..., N$. Hence eq.2.23 can be written as :

$$\lambda(\boldsymbol{\Phi}(\boldsymbol{x}_i) \cdot \boldsymbol{V}) = (\boldsymbol{\Phi}(\boldsymbol{x}_i) \cdot \bar{\boldsymbol{C}}\boldsymbol{V}) \qquad \text{for all } i = 1, ..., N \tag{2.23}$$

Moreover since $\boldsymbol{V}$ lie in the span of $\boldsymbol{\Phi}(\boldsymbol{x}_i)$ for $i = 1, ..., N$, $\boldsymbol{V}$ can be written as a linear combination of these vectors. It follows :

$$\boldsymbol{V} = \sum_{i=1}^{N} \alpha_i \boldsymbol{\Phi}(\boldsymbol{x}_i) \tag{2.24}$$

Hence eq. 2.23 can be written differently :

$$\lambda \sum_{i=1}^{N} \alpha_i (\boldsymbol{\Phi}(\boldsymbol{x}_k) \cdot \boldsymbol{\Phi}(\boldsymbol{x}_i)) = \frac{1}{N}\sum_{i=1}^{N} \alpha_i (\boldsymbol{\Phi}(\boldsymbol{x}_k) \cdot \sum_{j=1}^{N} \boldsymbol{\Phi}(\boldsymbol{x}_j)) \cdot (\boldsymbol{\Phi}(\boldsymbol{x}_j) \cdot \boldsymbol{\Phi}(\boldsymbol{x}_i)) \tag{2.25a}$$

$$\text{for all } k = 1, \cdots, N \tag{2.25b}$$

The $N \times N$ kernel matrix is then introduced :

$$\boldsymbol{K}_{ij} = \boldsymbol{\Phi}(\boldsymbol{x}_i) \cdot \boldsymbol{\Phi}(\boldsymbol{x}_j) \tag{2.26}$$

which represents the inner product space of the otherwise intractable feature space. The dual form that arises in the creation of a kernel allows us to mathematically formulate a version of PCA in which we never actually solve the eigenvectors and eigenvalues of the covariance matrix in the $\boldsymbol{\Phi}$-space.The $N$-elements in each column of K represent the dot product of one point of the transformed data with respect to all the transformed points (N points).
So eq. 2.25b can then be written as :

$$N\lambda \boldsymbol{K}\boldsymbol{\alpha} = \boldsymbol{K}^2\boldsymbol{\alpha} \tag{2.27}$$

As K is symmetric, it has a set of Eigenvectors which spans the whole space, thus :

$$N\lambda \boldsymbol{\alpha} = \boldsymbol{K}\boldsymbol{\alpha} \tag{2.28}$$

Because we are never working directly in the feature space, the kernel formulation of PCA is restricted in that it does not compute the principal components themselves, but the projections of our data onto those components. More details on the kPCA are given in [Schölkopf et al., 1998]. An example of the use of the kPCA is given in [Pedregosa et al., 2011]. In this example kPCA makes it possible to find a projection of the data that makes them linearly separable.

The advantage of the non-linearity introduced by the kernel is clearly highlighted in this example compared to the classic PCA.

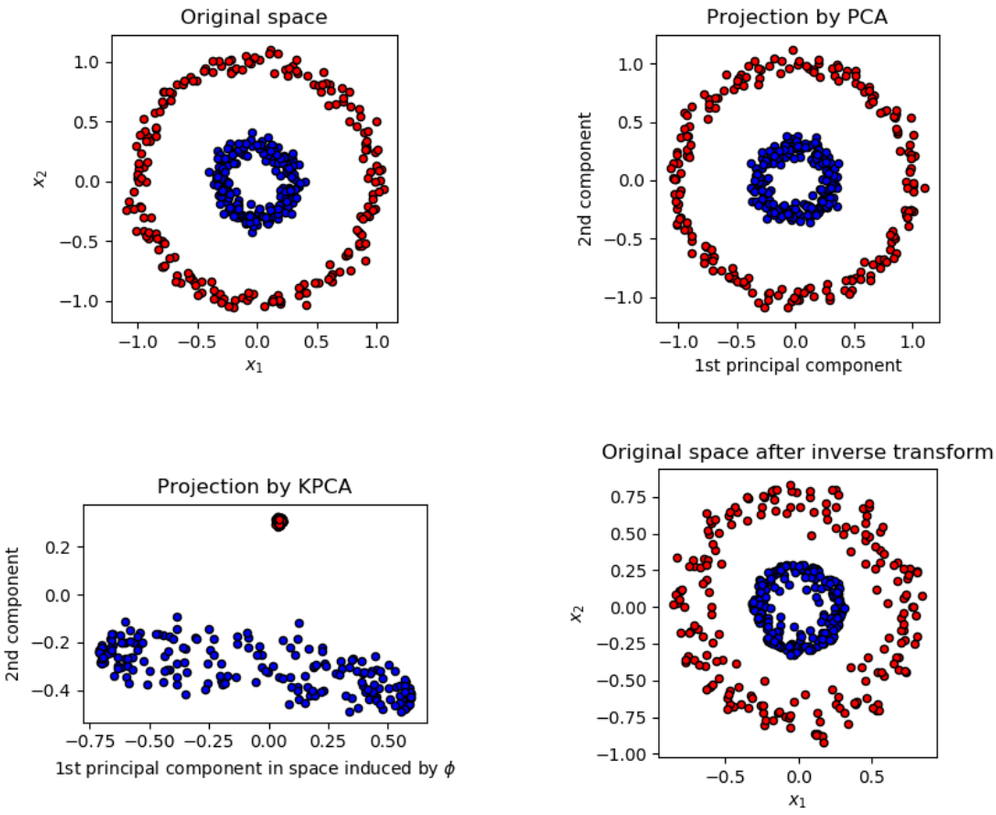


Figure 2.3: Kernel PCA taken from [Pedregosa et al., 2011].

### Multi dimensional scaling

Multi Dimensional Scaling (MDS) [I. Borg, 2005, Kruskal, 1964, Machado and Luchko, 2021] is also known as Principal Coordinates Analysis (PCoA). The method takes as input the dissimilarity matrix $D$ between the data and gives as output a coordinate matrix in the MDS space $\boldsymbol{X}$. This coordinate matrix minimizes a loss function also called strain. The strain is given by :

$$S = \left( \frac{\sum_{i,j} (\boldsymbol{B}_{ij} - \boldsymbol{X}_i^T \boldsymbol{X}_j)^2}{\sum_{i,j} \boldsymbol{B}_{ij}^2} \right)^{1/2} \tag{2.29}$$

$\boldsymbol{B}$ is obtained by double centering of the proximity matrix $\boldsymbol{P} = D_{ij}^2$ such as :

$$\boldsymbol{B} = -\frac{1}{2} \boldsymbol{C} \boldsymbol{P} \boldsymbol{C} \tag{2.30}$$

Where $\boldsymbol{C}$ is the centering matrix defined as :

$$\boldsymbol{C} = \boldsymbol{I}_n - \frac{1}{n} \boldsymbol{J}_n \tag{2.31}$$

Here $n$ is the number of samples, $\boldsymbol{I}_n$ is the $n \times n$ identity matrix and $\boldsymbol{J}_n$ is a $n \times n$ matrix containing only ones.
The eigenvalues $\boldsymbol{\Lambda}_{ii}$ and eigenvectors $\boldsymbol{E}_i$ are obtained by diagonalizing the $\boldsymbol{B}$ matrix. Finally the coordinate matrix in the MDS spacce $\boldsymbol{X}$ can be obtained such as :

$$\boldsymbol{X} = \boldsymbol{E}[:, : m] \boldsymbol{\Lambda}[:, : m]^{1/2} \tag{2.32}$$

Here $m$ indicates the number of dimensions wanted in MDS space. In the Euclidian case PCA and MDS are equivalent. One of the main interests of MDS is to obtain a euclidian distance representation based on a non Euclidian distance matrix.

### IsoMap

Linear methods reduce the dimensions based on Euclidean distances whereas ISOMAP [Yang et al., 2016](Isometric mapping) uses Geodesic distance approach among the multivariate data points. Let $\boldsymbol{X} = [\boldsymbol{x}_1, \boldsymbol{x}_2, ..., \boldsymbol{x}_N] \in \mathcal{R}^{M \times N}$ which denotes a set of $N$ points in the original input space with dimension $M$. The corresponding points in the lower dimensional space with dimension $m$, with $m \ll M$, are $\boldsymbol{Y} = [\boldsymbol{y}_1, \boldsymbol{y}_2, ..., \boldsymbol{y}_N] \in \mathcal{R}^{m \times N}$. The Euclidian distance between $\boldsymbol{x}_i$ and $\boldsymbol{x}_j$ is denoted as $d(\boldsymbol{x}_i, \boldsymbol{x}_j)$. Isomap is a global non-linear dimensionality reduction method. It aims at seeking an optimal subspace that best preserves the geodesic distances between every pair of points. The outline of Isomap [Tenenbaum et al., 2000] can be summarized as follows:
→ Determine the neighbourhood relationships. For every pair of data points, if $d(\boldsymbol{x}_i, \boldsymbol{x}_j)$ is smaller than a fixed radius $\varepsilon$ or $\boldsymbol{x}_j) \in k$-nearest neighbours ($k$-NN) of $\boldsymbol{x}_i$ then $\boldsymbol{x}_i$ and $\boldsymbol{x}_j$ are neighbours.
→ Compute geodesic distances. Construct a undirected graph $G(V, E)$, where node $\boldsymbol{v}_i \in V$

corresponds to point $\boldsymbol{x}_i$. If $\boldsymbol{x}_i$ and $\boldsymbol{x}_j$ are neighbours, the weight of edge $(\boldsymbol{x}_i, \boldsymbol{x}_j) \in E$ is set to $d(\boldsymbol{x}_i, \boldsymbol{x}_j)$, otherwise it is set to $+\infty$. Estimate geodesic distances between all pairs of data points by computing their shortest path distances $d_G(\boldsymbol{x}_i, \boldsymbol{x}_j)$ in $G$ using Dijkstra's [Sniedovich, 2010] or Floyd's [Hougardy, 2010] algorithm.
→ Construct low dimensional embedding. Define the optimization problem as follows:

$$\min_{\boldsymbol{Y}} \sum_{i,j} \Big( d(\boldsymbol{y}_i, \boldsymbol{y}_j) - d_G(\boldsymbol{x}_i, \boldsymbol{x}_j) \Big)^2 \tag{2.33}$$

Once the equation eq.2.33 is solved. The classic MDS method (detailed in paragraph 2.1.2) is then applied to obtain the lower dimensional representation $\boldsymbol{Y}$.

An example comparing PCA and IsoMap is given in Fig.2.4.

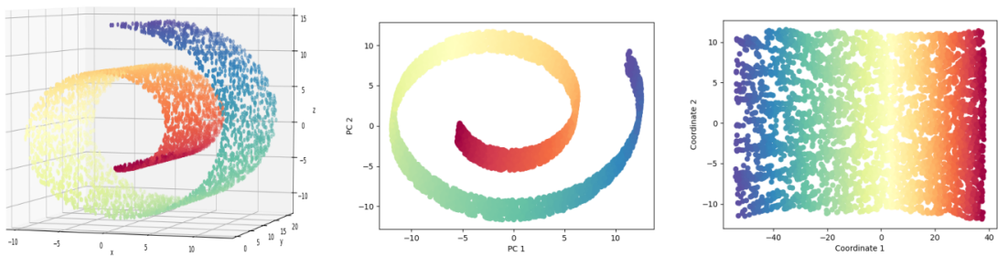


(a) (b) (c)

Figure 2.4: (a) 3D swiss roll data set, (b) PCA projection of the data set in 2D and (c) IsoMap projection in 2D.

It is clear that IsoMap tries to conserve the distance with the points in its neighbourhood contrary to PCA.

### 2.1.3 Autoencoder for dimensionality reduction

AutoEncoders (AE) are an unsupervised learning technique in which we leverage neural networks for the task of representation learning. More precisely this specific neural network architecture is made in a way that a bottleneck in the hidden layer of the neuronal network is imposed. The target output is the same as the input therefore the bottleneck forces a compressed representation of the original input.
An autoencoder is made of two main parts : a encoder which maps the input in a compressed latent space and a decoder which maps the compressed data from the latent space to the original space. Hence autoencoders enable a dimensionality reduction since the size of the latent sapce is smaller than the original space.
The encoder and decoder can be defined as transition functions $\Phi$ and $\Psi$. The purpose of the autoencoder is to minimize the difference between the input and the output. For this minimization problem if the $L^2$ norm is taken for the loss function it follows :

$$\begin{aligned} \Phi &: \mathcal{X} \to \mathcal{F}, \\ \Psi &: \mathcal{F} \to \mathcal{X}, \\ \Phi, \Psi &= \underset{\Phi,\Psi}{\operatorname{argmin}} ||X - (\Psi \circ \Phi)X||^2, \\ \dim(\mathcal{F}) &\ll \dim(\mathcal{X}). \end{aligned} \tag{2.34}$$

Here $\mathcal{X}$ and $\mathcal{F}$ denote the input space and the latent space respectively. For example, a very simple autoencoder is considered with one single hidden layer. The autoencoder takes as input $\boldsymbol{x} \in \mathcal{R}^d = \mathcal{X}$ and maps it into $\boldsymbol{h} \in \mathcal{R}^p = \mathcal{F}$.
In this case the hidden layer $\boldsymbol{h}$ is referred to as latent variables or latent representation. The input are weighted by coefficient $\boldsymbol{W}^{(1)} \in \mathcal{R}^{p \times d}$ and then an activation function $\sigma^{(1)}$ is applied :

$$\boldsymbol{h}_i = \sigma^{(1)}(\boldsymbol{W}^{(1)}_{ij} \boldsymbol{x}_j) \tag{2.35}$$

There are various activation functions that are commonly used such as the rectified linear function (ReLu) or else the sigmoid function. In this case it is assumed that the activation function is a sigmoid function :

$$\sigma^{(1)}(x) = \frac{1}{1 + e^{-x}} \tag{2.36}$$

After that, the decoder maps $\boldsymbol{h}$ to the reconstruction $\boldsymbol{x}'$ of the same shape as $\boldsymbol{x}$ :

$$\boldsymbol{x}'_j = \sigma^{(2)}(\boldsymbol{W}^{(2)}_{ji} \boldsymbol{h}_i) \tag{2.37}$$

Here $\sigma^{(2)}$ and $\boldsymbol{W}_{ji}^{(2)}$ are the activation function and the weights of the decoder and are not related to the ones of the encoder. For this example the the $L^2$ norm is taken for the loss function. So the loss $J$ to minimize can be written as :

$$J(\boldsymbol{W}) = ||\boldsymbol{x} - \boldsymbol{x}'||^2 = ||\boldsymbol{x} - \sigma^{(2)}\Big(\boldsymbol{W}^{(2)}\sigma^{(1)}(\boldsymbol{W}^{(1)}\boldsymbol{x})\Big)||^2 \tag{2.38}$$

As mentioned before, autoencoder training is performed through backpropagation of the error, just like other feedforward neural networks. Hence the quantities $\frac{\partial J(\boldsymbol{W})}{\partial \boldsymbol{W}_{ij}^l}$ are evaluated and used to update the weights thanks to a stochastic gradient descent for example (see eq.2.39):

$$\boldsymbol{W}_{ij}^l := \boldsymbol{W}_{ij}^l - \eta \frac{\partial J(\boldsymbol{W})}{\partial \boldsymbol{W}_{ij}^l} \tag{2.39}$$

It is important to keep in mind that many other activation functions, cost functions and optimization methods can be used to train a neurone network. The ones that have been chosen are just to illustrate the global methodology. Moreover only one hidden layer is used in the example but usually many layers are used. Once the AE is trained, it has learned a compressed representation of the input space and contrary to PCA or SVD the relation can be highly non-linear as Fig.2.5 illustrates.

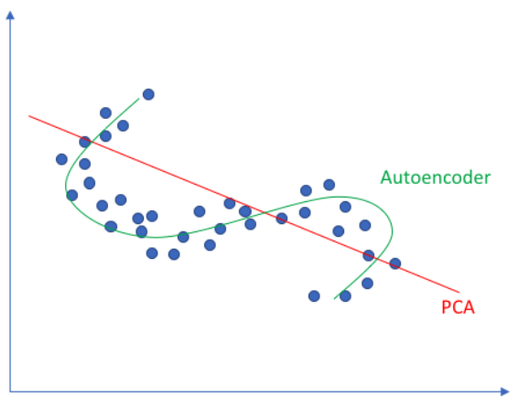


Figure 2.5: Autoencoder versus PCA.

The previous figure illustrates that autoencoders manage to represent curved manifold contrary to PCA. This comparison is underlined in [Hinton and Salakhutdinov, 2006] where faces are reconstructed either with PCA or with a trained autoencoder Fig.2.6

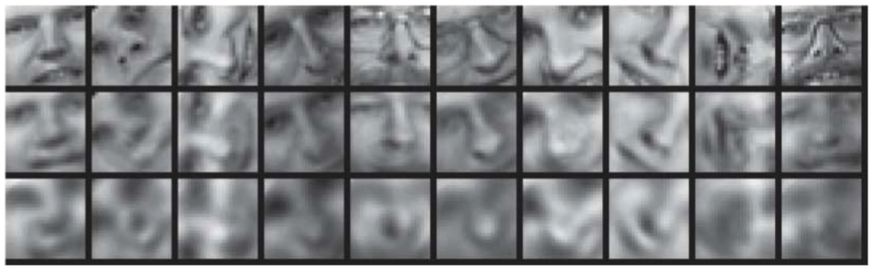

Figure 2.6: Top to bottom: A random test image from each class; reconstructions by the 30-dimensional autoencoder; reconstructions by 30-dimensional standard PCA. (taken from [Hinton and Salakhutdinov, 2006]).

Fig.2.6 shows that the autoender gives better results to reconstruct the faces. The average squared errors are 126 for the AE and 135 with the PCA. This is due to the fact that autoencoders can catch the non-linearity of a curved manifold contrary to PCA.
In [Lee and Carlberg, 2020], another deep learning strategy for model order reduction is proposed for parametrized partial differential equations. The governing equations are mapped onto a non-linear manifold thanks to a deep convolutional autoencoder. Contrary to projection-based model order reduction methods using linear dimensionality reduction techniques such as the POD or the snapshot POD, this methodology performs a non-linear dimensionality reduction. The reduced (or generalized) coordinates in the latent space defined by the autoencoder's bottleneck layer are combined by the decoder in a non-linear fashion to get the high-dimensional state approximation. Use is made of autoencoders in other works to find the solution of the partial differential equation in the latent space [Mojgani and Balajewicz, 2020, Fu et al., 2021, Geneva

and Zabaras, 2020]. Nevertheless the minimization problem to solve the PDE is much more non-linear, resulting in complex computations when the input space is large.
When the decoder is linear, this methodology is equivalent to classical projection-based model order reduction.

## 2.2 Hyper reduction

### 2.2.1 HROM

#### Problem formulation

Many reduced order model techniques exist, all having their pros and cons. A comparison is made between some of them in [Fritzen et al., 2016].
Hyper reduction (HR), which will be greatly used in this work, uses the reduced basis projection method but is slightly different in the sense that solely a little number of Degrees Of Freedom (DOFs) can be determined during the resolution. This is due to the fact that the resolution is made on a reduced mesh also called Reduced Integration Domain (RID). The RID can be seen as a submodel supplemented by boundary conditions similar to Dirichlet boundary conditions but using a reduced basis approximation as explained in [Ryckelynck et al., 2016].
This specificity makes it possible to dramatically reduce the computation time since the projection is done on a RB restricted to the RID. The speed up in time is particularly large for non-linear problem solved with a Newton algorithm because for each iteration a projection of the jacobian matrix is required. Although HR have been introduced to deal with material having non-linear constitutive law and contact problems, the following equations are detailed for an elastic material in order to make it easier to understand the global methodology.
Since the HROM rely on the FOM, a detailed way to create a FOM with the FEM is explained. Considering domain $\Omega \in \mathcal{R}^D$ representing a structure of dimension $D$ in its reference configuration. The balance equation between the stress tensor $\underset{\sim}{\sigma}$ and the volumetric density of forces $\boldsymbol{f}$ is given by :

$$\mathrm{div}\underset{\sim}{\sigma} + \boldsymbol{f} = 0 \qquad \text{in} \qquad \Omega \tag{2.40}$$

The material is supposed to be purely elastic. With the small strain hypothesis, the behaviour can be written as follow :

$$\underset{\sim}{\sigma} = \underset{\approx}{C} : \underset{\sim}{\varepsilon} \qquad \text{in} \qquad \Omega \tag{2.41}$$

Where $\underset{\sim}{\sigma}$ is the second order stress tensor and $\underset{\approx}{C}$ is the fourth order elasticity tensor. The strain tensor $\underset{\sim}{\varepsilon}$ is obtained with the displacement field $\boldsymbol{u}$ :

$$\underset{\sim}{\varepsilon} = \frac{1}{2}(\mathrm{grad}\boldsymbol{u} + (\mathrm{grad}\boldsymbol{u})^T) \qquad \text{in} \qquad \Omega \tag{2.42}$$

The structure undergoes some surface loadings $\boldsymbol{g}$ on $\Gamma^N$ (Neumann boundary conditions) and a displacement field $\boldsymbol{u}_0$ is imposed on $\Gamma^D$ (Dirichlet boundary conditions):

$$\boldsymbol{u} = \boldsymbol{u}_0 \qquad \text{on} \qquad \Gamma^D \tag{2.43}$$

$$\underset{\sim}{\sigma}\boldsymbol{n} = \boldsymbol{g} \qquad \text{on} \qquad \Gamma^N \tag{2.44}$$

The strong formulation of the elastic problem with the small strain hypothesis can be written as follows :

$$\begin{cases} -\mathrm{div}(\underset{\sim}{\sigma}) = \boldsymbol{f} & \text{in} \quad \Omega & (2.45a) \\ \underset{\sim}{\sigma} = \underset{\approx}{C} : \underset{\sim}{\varepsilon} & \text{in} \quad \Omega & (2.45b) \\ \underset{\sim}{\varepsilon} = \frac{1}{2}(\mathrm{grad}\boldsymbol{u} + (\mathrm{grad}\boldsymbol{u})^T) & \text{in} \quad \Omega & (2.45c) \\ \boldsymbol{u} = \boldsymbol{u}_0 & \text{on} \quad \Gamma^D & (2.45d) \\ \underset{\sim}{\sigma}\boldsymbol{n} = \boldsymbol{g} & \text{on} \quad \Gamma^N & (2.45e) \end{cases}$$

The weak formulation of the problem can then be defined. The virtual displacement $\boldsymbol{v}$ is introduced. The primal integral formulation, which is equivalent to eq.2.40, is obtained with the scalar product $L^2(\Omega)$ with the virtual displacement $\boldsymbol{v}$ :

$$-\int_\Omega \mathrm{div}(\underset{\sim}{\sigma})^T \cdot \boldsymbol{v} \; \mathrm{d}\Omega = \int_\Omega \boldsymbol{f}^T \cdot \boldsymbol{v} \; \mathrm{d}\Omega \tag{2.46}$$

The term of under the first integral can be replaced by :

$$\mathrm{div}(\underset{\sim}{\sigma}^T \cdot \boldsymbol{v}) = \mathrm{div}(\underset{\sim}{\sigma})^T \cdot \boldsymbol{v} + \underset{\sim}{\sigma} : \mathrm{grad}(\boldsymbol{v}) \tag{2.47}$$

By injecting 2.47 in 2.46 it follows :

$$-\int_\Omega \mathrm{div}(\underset{\sim}{\sigma}^T \cdot \boldsymbol{v}) \; \mathrm{d}\Omega + \int_\Omega \underset{\sim}{\sigma} : \mathrm{grad}(\boldsymbol{v}) \; \mathrm{d}\Omega = \int_\Omega \boldsymbol{f}^T \cdot \boldsymbol{v} \tag{2.48}$$

Since $\underset{\sim}{\sigma}$ is symmetric the term under the first integral can be written differently :

$$(\underset{\sim}{\sigma} \cdot \boldsymbol{v})^T \cdot \boldsymbol{n} = (\underset{\sim}{\sigma} \cdot \boldsymbol{n})^T \boldsymbol{v} \tag{2.49}$$

The symmetric property of $\underset{\sim}{\sigma}$ also enables to simplify the second term of eq.2.48 because the double contracted product between $\underset{\sim}{\sigma}$ and the antisymetric part of grad($\boldsymbol{v}$) is null. The decomposition of grad($\boldsymbol{v}$) as the sum of a symmetric and antisymmetric tensor is written as :

$$\text{grad}(\boldsymbol{v}) = \underset{\sim}{\varepsilon}(\boldsymbol{v}) + \frac{1}{2}(\text{grad}(\boldsymbol{v}) - \text{grad}(\boldsymbol{v})^T) \tag{2.50}$$

With these two modifications the following classic weak form is obtained :

$$\int_\Omega \underset{\sim}{\sigma}) : \underset{\sim}{\varepsilon}(\boldsymbol{v}) \ \mathrm{d}\Omega = \int_\Omega \boldsymbol{f}^T \cdot \boldsymbol{v} \ \mathrm{d}\Omega + \int_{\partial\Omega} (\underset{\sim}{\sigma}\boldsymbol{n})^T \cdot \boldsymbol{v} \ \mathrm{d}\Gamma \tag{2.51}$$

**Finite element method in elastic case**

The global domain $\Omega$ is discretized with the use of many elements $K_i$ such as $\bigcup_i \bar{K}_i = \bar{\Omega}$. This spatial discretization is called mesh.
It is convenient to introduce the functions $\boldsymbol{\phi}_i = \phi_j \mathbf{e}_k$ where $i = (j-1)\times d+k$, $i = 1, ..., \mathcal{N}$, $j = 1, ..., n$, $k = 1, ..., d$, $d$ is the dimension of the problem and $\mathbf{e}_k$ refers to the canonical vectors of a Cartesian coordinates system. The approximation of the displacement with the shape functions $(\boldsymbol{\phi}_i)_{i=1}^{\mathcal{N}}$ reads:

$$\boldsymbol{v}(\mathbf{x}) = \boldsymbol{v}_0(\mathbf{x}) + \sum_{i=1}^{\mathcal{N}} \boldsymbol{\phi}_i(\mathbf{x}) u_i, \qquad \forall \mathbf{x} \in \Omega, \tag{2.52}$$

where $\mathcal{N} = n \times d$ is the number of DOFs of the structure, $\boldsymbol{v}_0$ is a given displacement field that fulfills the Dirichlet boundary conditions, $\boldsymbol{v}$ is the approximate finite element solution and $\mathbf{u} = (u_i)_{i=1}^{\mathcal{N}}$ the vector of the related DOFs.
With the classical finite element method if follows :

(2.53)

$$\begin{cases} \text{find } \boldsymbol{u} \in \mathcal{R}^{\mathcal{N}} \text{such that} & \text{(2.54a)} \\ \boldsymbol{K}\boldsymbol{u} = \boldsymbol{f}_{ext} & \text{(2.54b)} \end{cases}$$

Where $\boldsymbol{K}$ and $\boldsymbol{f}_{ext}$ are respectively the stiffness matrix and the global external forces defined as :

$$\boldsymbol{K}_{ij} = \int_\Omega \underset{\sim}{\varepsilon}(\phi_j) : \underset{\approx}{C} : \underset{\sim}{\varepsilon}(\phi_i) \ \mathrm{d}\Omega \tag{2.55}$$

$$\boldsymbol{f}_{ext\ i} = \int_\Omega \boldsymbol{f}^T \cdot \phi_i \ \mathrm{d}\Omega + \int_{\partial\Omega} (\underset{\sim}{\sigma}\boldsymbol{n})^T \cdot \phi_i \ \mathrm{d}\Gamma \tag{2.56}$$

**Reduced basis construction**

With the reduced order methods the main idea is to find the solution of the problem in a reduced space of approximation that does not depend on the mesh any more.
The displacement field is written as follows :

$$\boldsymbol{u}(\boldsymbol{x}) = \sum_{k=1}^{N} \boldsymbol{\psi}_k(\boldsymbol{x}) \cdot \boldsymbol{\gamma}, \qquad \forall \boldsymbol{x} \in \Omega \tag{2.57}$$

With $N \ll \mathcal{N}$. The goal is to find a small number of functions $(\boldsymbol{\psi}_k)_{k=1}^{l}$ that enables to have an accurate approximation of $\boldsymbol{u}$. To do so, methods using snapshots allow a good approximation of the studied solution space (see section 2.1). Usually, in order to obtain the smallest RB, the POD method is applied. Each function $\boldsymbol{\psi}_k$ of the RB can be expressed with the FE shape functions $(\boldsymbol{\phi}_i)_{i=1}^{\mathcal{N}}$. With $\boldsymbol{V}$ the discretized RB :

$$\boldsymbol{\psi}_k(\boldsymbol{x}) = \sum_{i=1}^{\mathcal{N}} \boldsymbol{\phi}_i(\boldsymbol{x})(\boldsymbol{V})_{ik}, \qquad \forall \boldsymbol{x} \in \Omega \tag{2.58}$$

The displacement field $\boldsymbol{u}(\boldsymbol{x})$ can then be expressed as a function of the modes contained in the RB $\boldsymbol{V}$.

$$\boldsymbol{u}(\boldsymbol{x}) = \sum_{i=1}^{\mathcal{N}} \boldsymbol{\phi}(\boldsymbol{x})(\sum_{k=1}^{N} (\boldsymbol{V})_{ik} \boldsymbol{\gamma}_k) \tag{2.59}$$

Finally, using the FE formulation, the displacement field can be expressed as :

$$\boldsymbol{u} = \boldsymbol{V}\boldsymbol{\gamma}_k \tag{2.60}$$

$\boldsymbol{\gamma}$ is the vector that contains the DOFs associated to the RB. The ROM is then obtained by replacing $\boldsymbol{u}$ by its projection in the reduced space. By projecting also the global external forces the following reduced FE problem is obtained :

$$\begin{cases} \text{find } \boldsymbol{\gamma} \in \mathcal{R}^N \text{such that} & \text{(2.61a)} \\ \quad \boldsymbol{V}^T \boldsymbol{K} \boldsymbol{V} \boldsymbol{\gamma} = \boldsymbol{V}^T \boldsymbol{f}_{ext} & \text{(2.61b)} \end{cases}$$

**HROM resolution**

The specificity of the HROM is the notion of RID. In this work the DEIM is used to select the important zone constitutive of the RID [Chaturantabut and Sorensen, 2009, Barrault and Al., 2004]. This algorithm takes as input the RB $\boldsymbol{V}$ and return a set of interpolation indexes $\mathcal{F}$. The Discrete Empirical Interpolation Method (DEIM) can be applied to more than one reduced basis in order to catch more information [Ryckelynck et al., 2016]. Additional layers can be added to the RID to improve the accuracy of the HROM. The RID is defined by 2.62 where supp($\phi$) denotes the support of the FE shape functions $\phi_i$.

$$\Omega_A = \bigcup_{i \in \mathcal{F}} \text{supp}(\boldsymbol{\phi}) \tag{2.62}$$

The subdomain $\Omega_B$ which is the complementary of $\Omega_A$ and verifies $\Omega = \Omega_A \cup \Omega_B$ and :

$$\Gamma^I = \Omega_A \cap \Omega_B \tag{2.63}$$

Where $\Gamma^I$ is the interface between the two subdomains. $\mathcal{I}$ is then introduced as :

$$\mathcal{I} = \{ i \in [1, \mathcal{N}] \quad | \quad \int_{\Gamma^I} \boldsymbol{\phi}_i^T \boldsymbol{\phi}_i \, \mathrm{d}\Gamma \neq 0 \} \tag{2.64}$$

And $\mathcal{F}$ the set of DOFs not connected to $\Omega_B$ :

$$\mathcal{F} = \{ i \in [1, \mathcal{N}] \quad | \quad \int_{\Omega_B} \boldsymbol{\phi}_i^T \boldsymbol{\phi}_i \, \mathrm{d}\Omega = 0 \} \tag{2.65}$$

An example of RID where these domains can be visualized is given on Fig.2.7. The RID is in red in the figure. The nodes that are strictly inside the RID, whose DOFs are the set $\mathcal{F}$, are in black. The nodes that are at the interface between the RID and the whole domain whose DOFs are denoted $\mathcal{I}$ are in green.

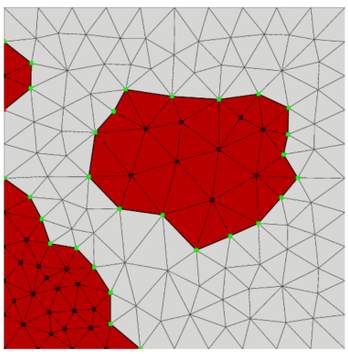

Figure 2.7: Example of RID in red with the interface DOFs in green and the DOFs strictly inside the RID in black.

It has been remarked that just the DOFs $\mathcal{F} \cup \mathcal{I}$ are connected to $\mathcal{F}$. Hence the hyper reduced problem is obtained :

$$\begin{cases} \text{find } \boldsymbol{\gamma} \in \mathcal{R}^N \text{such that} & \text{(2.66a)} \\ \boldsymbol{V}[\mathcal{F}, :]^T \boldsymbol{K}[\mathcal{F}, \mathcal{F} \cup \mathcal{I}] \boldsymbol{V}[\mathcal{F} \cup \mathcal{I}, :] \boldsymbol{\gamma} = \boldsymbol{V}[\mathcal{F}, :]^T \boldsymbol{f}_{ext}[\mathcal{F}] & \text{(2.66b)} \end{cases}$$

The system to solve is of size $N \times N$ and the domain where the constitutive has to be integrate is much smaller than the whole domain. This results in great speed ups of the HROM.
An improvement of the HROM has been made recently [Fauque et al., 2018, Fauque, 2018], consisting in making a finite element correction, this method is called hybrid hyper reduction (H2R). The correction is made by applying the solution of the HR problem on the frontiers of the RID via a penalisation approach. This solution is then used as Dirichlet boundary conditions for the finite element correction.

### 2.2.2 Two scales HROM

Hyper reduced methods have proven themselves in low dimensional context (lower than 10). As soon as the number of parameters increases the cost of the offline phase skyrockets. This phenomenon, known as the "curse of the dimensionality", has been the topic of some researches on high number of parameters in multiscale problems [Ladevèze et al., 2018]. The size of the parametric space $D^{\mu}$ has to be defined prior to the training phase. This is not a problem in general but when considering non parametric problem, for data coming for imaging techniques for image-based digital twins, it is difficult to pave the parametric space appropriately. Indeed the parametric space depends on the number of defects taken into account. For instance if a simple spherical defect is considered, it is defined by 4 parameters (3 for its position and 1 for its size). Hence for a population of $n$ defects, the size of the parametric space is at least $4n$. Multi holes plates under specific loading have been computed with a PGD approach [Ghnatios et al., 2019]. In this case the material is supposed to be purely elastic and many configurations of cylindrical defects are computed. In this case the dimension of the parametric space is still low since only simple problems are tackled. When non parametric cases are treated this approach is impossible even more so when plasticity is added.

A two-scales approach have been developed in order to circumvent this problem. The idea is to create a ROB with two contributions. The contribution of the global structure without defect is locally enriched with the contribution of the defects. The training phase is made by assuming the scale separation hypothesis. A linear enrichment approach has been studied to introduce the effect of notch in panels undergoing a dynamic loading [Wang et al., 2018] and a non-linear approach have been developed in [Lacourt, 2019, Lacourt et al., 2020]. The latter will be used in the present work therefore it is more detailed.

The first computed contribution is global and does not take the defects into account. It describes the mechanical behaviour of the observed component by using assumed effective material properties. In practice the effective properties of the sane material are often considered. It has a specific number of parameters (material coefficient or loading parameters) present in $\boldsymbol{\mu}^G \in \mathcal{D}^G$. It is possible to obtain a reduced basis specific to the sane structure denoted $\boldsymbol{V}^G$ that contains the $N^G$ global modes. These modes are defined on the domain of the sane structure $\Omega^G$.
A fluctuation reduced basis is created for each specific defect. The domain $\Omega^d$ is cubic and centered in $\boldsymbol{x}_0$. The defect is then introduced in the domain in a way that the center of gravity is in $\boldsymbol{x}_0$. The domain $\Omega^d$ is large enough to satisfy the dilution assumption :

$$\forall \boldsymbol{x} \in \partial\Omega^d, \Delta\boldsymbol{u} = \boldsymbol{0} \tag{2.67}$$

With this method, in order to adapt as much as possible the fluctuation modes to the problem to treat, the mean strain tensor $\underset{\sim}{E}(t)$ applied to the domain $\Omega^d$ must be close to the loading that the defect in the component undergoes. To do so $\underset{\sim}{E}(t)$ is computed with the simulation of the component without defect. The loading seen by the closest Gauss point to gravity center of the defect to introduce is used as boundary conditions for the simulation to compute the fluctuation modes. The simulation on the domain $\Omega^d$ with the defect enables to create a snapshot matrix used to compute the $N^f$ fluctuation modes $\boldsymbol{\psi}_k^f$ and are stored in the matrix $\boldsymbol{V}^f$.
The first step with the whole methodology is to compute the fluctuation modes associated to the defect and the global modes associated to the sane structure $\boldsymbol{V}^G$ as described in the previous paragraph. Once $\boldsymbol{V}^f$ and $\boldsymbol{V}^G$ are computed a HR simulation can be launched. The global modes are defined on $\Omega^G$ and the fluctuation modes on $\Omega^d$.
A real mesh of the component containing the defect needs to be created, which defines the target domain $\Omega^\star$. The global and local modes are then projected on the target mesh. A RID $\Omega_R^\star$ can then be created. Firstly the global RID $\Omega_R^G$ by applying the DEIM on $\boldsymbol{V}^G$ and then a RID $\Omega_R^f$ associated to the fluctuation modes contained in $\boldsymbol{V}^f$ is created. The final RID is the union of these two domains : $\Omega_R^\star = \Omega_R^G \cup \Omega_R^f$. Once the reduced domain $\Omega_R^\star$ is created, global and fluctuation modes can be projected on it.

The matrix notation of global and fluctuation modes restricted to the RID $\Omega_R^\star$ are respectively denoted $\boldsymbol{V}_R^G$ and $\boldsymbol{V}_R^f$. The computation is then made with the approximated matrix : $\boldsymbol{V}_R^{app} = \left[\boldsymbol{V}_R^G | \boldsymbol{V}_R^G\right]$
The reduced basis $\boldsymbol{V}_R^{app}$ represents the reduced basis specific to the component containing the defect and introduces a scale coupling between the defect and the structure.
This methodology makes the offline phase less time consuming. Very large speedups, between 100 and 1000, have been obtained in [Lacourt, 2019, Lacourt et al., 2020] when fluctuation modes are precomputed. Precomputing fluctuation modes for non parametric defects is an important issue addressed in this thesis.

### 2.2.3 ROM-net

In projection based model order reduction method use is made of a reduced basis and the solution manifold is suppose to be a vector subspace. But the use of a single reduced basis to find the solution belonging to manifolds that are not involved in a small vector subspace can lead to important approximation errors. To circumvent this problem, piecewise-linear approach to

model order reduction have been proposed in [Rewienski and White, 2003], where a partition of the time interval has to be setup. A sketch of the piecewise-linear approach using local reduced order models is shown in Fig.2.8.

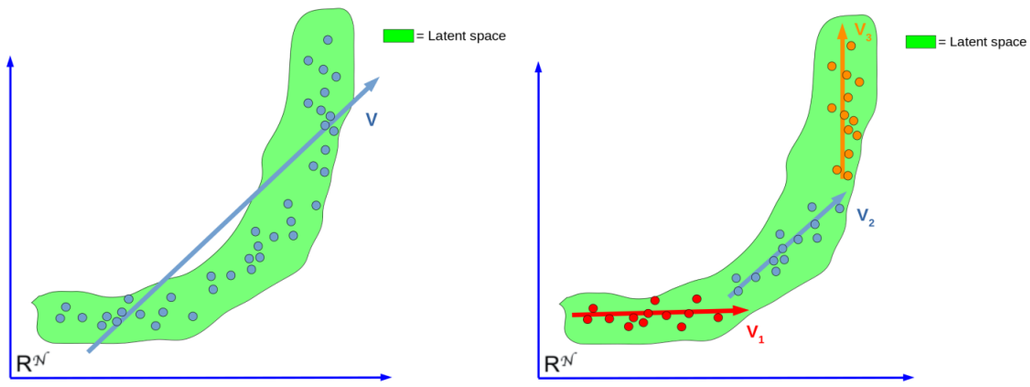


Figure 2.8: Linear (left) versus piecewise-linear (right) dimensional reduction.

The partition of the time interval usually follows an adaptive strategy as in [Dihlmann et al., 2011]. This non-linear approach to model order reduction have been extended to parametric partial differential equations by using local reduced order models in [Haasdonk et al., 2011], for a clustering of data in the parameter space. A clustering of data in the state space (or solution space) has been proposed in [Amsallem et al., 2012, Washabaugh et al., 2012, Wieland, 2015]. This last clustering approach, in the state space, has been designed for model order reduction. The extension of hyper-reduction shemes to local reduced order models is straightforward. This has been developed in [Amsallem et al., 2015] and in [Redeker and Haasdonk, 2014] for the empirical interpolation method and for the discrete empirical interpolation method in [Peherstorfer et al., 2014]. In the local model order reduction context, many approaches are based on a notion of distance in order to (1) partition solutions and construct local subspaces offline and (2) determine online subspace which is currently used to define the reduced order model (ROM) solution. Methods consisting in selecting the ROM of the closest cluster in the sense of the Euclidean distance have been developed in [Amsallem et al., 2012, Washabaugh et al., 2012, Grimberg et al., 2020].
The notion of ROM-net has been defined for local reduced order models, in [Daniel et al., 2020, Daniel et al., 2021a], when partial differential equations have a huge parameter space when considering fields as input parameters or images as input parameters [Nguyen et al., 2018]. The dimension of the parameter space, for tensors of data or images, is so huge that we refer to this kind of problem as a non-parametric modelling of the input variability in partial differential equations. For such problems, both distance evaluations to construct local subspaces and online selection of a local reduced order model, are very complex tasks. The global workflow, online, of a ROM-net is illustrated in Fig.2.9.

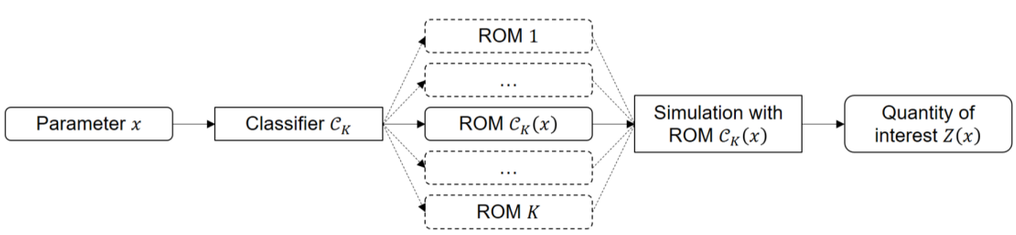


Figure 2.9: Exploitation phase of a dictionary-based ROM-net. $K$ local ROMs are combined with a classifier $\mathcal{C}_K$ for an automatic recommendation, used to predict the quantity of interest $Z(x)$ (taken from [Daniel et al., 2021a]).

In a ROM-net the online selection of a local reduced order model is performed by an artificial neural network. This allows to take advantage of recent advances in computer vision using convolutional neural networks for image classification or, more generally, tensor classification [LeCun et al., 2015]. Moreover, distances related to projection error on local reduced bases are more accurate than Euclidian distance, to cluster simulation data, as shown in [Amsallem and Haasdonk, 2016]. When considering relative errors, distances measuring principal angles between local reduced bases have been introduced for ROM-net in [Daniel et al., 2021b]. Thanks to a clustering approach, a dictionary of local ROMs is created. It works as follow :

→ For each input of the training set, a simplified problem is solved. This simplified physical problem is less time consuming than the real target problem (it can be solved on a coarse mesh for example).
→ These simplified problem enable to create simplified ROMs containing the global physical information.
→ Based on a chosen measure of dissimilarity, the clustering algorithm creates clusters with these simplified ROMs.
→ With the clustering results, a few relevant training examples are selected to created high fidelity ROMs.
→ These high fidelity ROMs are then used as labels for the classification task.

### 2.2.4 Simulation data via Fast Fourier Transform (FFT) computation method

In the previous section, hyper reduction techniques have been presented in the framework of finite element method. Reduced basis can also be learned from simulation data obtained with different computation methods such as the Fast Fourier Transform (FFT). In this work FFT methods will be used for the computation of image-based digital twins, therefore an brief explanation of its methodology is given. This section is highly inspired of [Brisard and Dormieux, 2010]. For the sake of simplicity the explanation is made in a two dimensional case.

Let consider a domain $\Omega \subset \mathcal{R}^2$ which is the rectangular unit-cell of an heterogeneous, periodic medium, with local stiffness $\underset{\approx}{\mathbb{C}}(\boldsymbol{x})$. The dimensions of this unit-cell will be denoted $W \times H$, while the basis vectors, parallel to its sides, will be denoted $\boldsymbol{e}_x$ and $\boldsymbol{e}_y$. This material is submitted to the macroscopic strain $\boldsymbol{E}$, and the resulting displacements locally fluctuate about their macroscopic counterpart $\boldsymbol{E} \cdot \boldsymbol{x}$. In periodic homogenization, the microstructure as well as the fluctuations of the displacement are periodic. Asymptotic expansion techniques then show that the solution of the following elementary problem.

$$
\begin{aligned}
\operatorname{div}(\underset{\approx}{\mathbb{C}}(\boldsymbol{x})) : \underset{\sim}{\varepsilon}(\boldsymbol{x}) &= 0 \qquad (\boldsymbol{x} \in \Omega) && \text{(2.68a)}\\
\underset{\sim}{\varepsilon}_{ij}(\boldsymbol{x}) &= \frac{1}{2}\left(\partial_i \boldsymbol{u}_j(\boldsymbol{x}) + \partial_j \boldsymbol{u}_i(\boldsymbol{x})\right) \qquad (\boldsymbol{x} \in \Omega) && \text{(2.68b)}\\
\boldsymbol{u}(\boldsymbol{x} + mW\boldsymbol{e}_x) &= \boldsymbol{u}(\boldsymbol{x}) + mW\boldsymbol{E} \cdot \boldsymbol{e}_x \qquad (\boldsymbol{x} \in \mathcal{R}^2, m \in \mathbb{Z}) && \text{(2.68c)}\\
\boldsymbol{u}(\boldsymbol{x} + nH\boldsymbol{e}_y) &= \boldsymbol{u}(\boldsymbol{x}) + nH\boldsymbol{E} \cdot \boldsymbol{e}_x \qquad (\boldsymbol{x} \in \mathcal{R}^2, n \in \mathbb{Z}) && \text{(2.68d)}
\end{aligned}
$$

In these equations, $\underset{\sim}{\varepsilon}(\boldsymbol{x})$ denotes the microscopic strain deriving from the displacement $\boldsymbol{u}(\boldsymbol{x})$. Equations (2.68c) and (2.68d) express the periodicity of the displacements.
Similarly to non-periodic materials, the introduction of a so-called reference material of homogeneous stiffness $\underset{\approx}{\mathbb{C}}_0$ can dramatically ease the solution of the problem (2.68a)-(2.68d). Indeed, the local constitutive law may be transformed as follows

$$
\underset{\sim}{\sigma}(\boldsymbol{x}) = \underset{\approx}{\mathbb{C}}_0 : \underset{\sim}{\varepsilon}(\boldsymbol{x}) + [\underset{\approx}{\mathbb{C}}(\boldsymbol{x}) - \underset{\approx}{\mathbb{C}}_0] : \underset{\sim}{\varepsilon}(\boldsymbol{x}) = \underset{\approx}{\mathbb{C}}_0 : \underset{\sim}{\varepsilon}(\boldsymbol{x}) + \underset{\sim}{\tau}(\boldsymbol{x}) \tag{2.69}
$$

where the polarization $\underset{\sim}{\tau}(\boldsymbol{x}) = [\underset{\approx}{\mathbb{C}}(\boldsymbol{x}) - \underset{\approx}{\mathbb{C}}_0] : \underset{\sim}{\varepsilon}(\boldsymbol{x})$ has been introduced. Assuming for the time being that $\underset{\sim}{\tau}(\boldsymbol{x})$ is known, it is readily seen that the problem (2.68a)-(2.68d) reduces to a simple elasticity problem formulated on a prestressed, homogeneous medium, the solution of which reads

$$
\underset{\sim}{\varepsilon}(\boldsymbol{x}) = \boldsymbol{E} - (\underset{\approx}{\boldsymbol{\Gamma}}_0 \circledast \underset{\sim}{\tau})(\boldsymbol{x}) \tag{2.70}
$$

where $\circledast$ represents the convolution product. $\underset{\approx}{\boldsymbol{\Gamma}}_0$ is the Green operator for strain which is a fourth order tensor. This tensor is related to the reference material $\underset{\approx}{\mathbb{C}}_0$. Since the polarization field is not known an implicit equation on the strain field is obtained :

$$
\underset{\sim}{\varepsilon}(\boldsymbol{x}) + \left(\underset{\approx}{\boldsymbol{\Gamma}}_0 \circledast [\underset{\approx}{\mathbb{C}}(\boldsymbol{x}) - \underset{\approx}{\mathbb{C}}_0] : \underset{\sim}{\varepsilon}(\boldsymbol{x})\right) = \boldsymbol{E} \tag{2.71}
$$

The so obtained equation (eq.2.71) is the Lippmann-Schwinger equation. The convolution product in eq.2.71 is easily computed in the Fourier space.

$$
\hat{\underset{\sim}{\varepsilon}}(\boldsymbol{k}) = -\hat{\underset{\approx}{\boldsymbol{\Gamma}}}_0(\boldsymbol{k}) : \hat{\underset{\sim}{\tau}}(\boldsymbol{k}) \tag{2.72}
$$

where the wave-vector denoted $\boldsymbol{k}$ is defined as follows :

$$
\boldsymbol{k} = \boldsymbol{k}_{ab} = \frac{2\pi a}{W}\boldsymbol{e}_x + \frac{2\pi b}{3H}\boldsymbol{e}_y \qquad (a, b \in \mathbb{Z}) \tag{2.73}
$$

When isotropic material is considered with a shear modulus $\mu_0$ and a Poisson ration $\nu_0$, the Fourier coefficients of the fourth rank Green operator can be evaluated :

$$
\hat{\underset{\approx}{\boldsymbol{\Gamma}}}_{0,ijhl}(\boldsymbol{k}) = \frac{1}{4\mu_0}(\delta_{ih}n_j n_l + \delta_{il}n_j n_h + \delta_{jh}n_i n_l + \delta_{jl}n_i n_h) - \frac{1}{2 * \mu_0(1-\nu_0)} n_i n_j n_h n_l \tag{2.74}
$$

with $\boldsymbol{n} = \boldsymbol{k}/k$ and $k = |\boldsymbol{k}| \quad (\boldsymbol{k} \neq \boldsymbol{0})$.
The basic scheme solves iteratively the Lippmann-Schwinger (eq.2.71), using Neumann series. The iterations read, in the real space :

$$\underset{\sim}{\boldsymbol{\varepsilon}}^0(\boldsymbol{x}) = \boldsymbol{E} \tag{2.75a}$$

$$\underset{\sim}{\boldsymbol{\varepsilon}}^{n+1}(\boldsymbol{x}) = \boldsymbol{E} - \left(\underset{\approx}{\boldsymbol{\Gamma}}_0 \circledast [(\underset{\approx}{\mathbb{C}} - \underset{\approx}{\mathbb{C}}_0) : \underset{\sim}{\boldsymbol{\varepsilon}}^n]\right)(\boldsymbol{x}) \tag{2.75b}$$

The FFT is very efficient thanks to the fact that the direct product $(\underset{\approx}{\mathbb{C}} - \underset{\approx}{\mathbb{C}}_0) : \underset{\sim}{\boldsymbol{\varepsilon}}^n$ is evaluated in the real space while the convolution is made in the Fourier space. The iterations of this scheme consist in four main steps :

→ 1 - application of the constitutive law in the real space : $\underset{\sim}{\boldsymbol{\tau}}^n(\boldsymbol{x}) = [\underset{\approx}{\mathbb{C}}(\boldsymbol{x}) - \underset{\approx}{\mathbb{C}}_0] : \underset{\sim}{\boldsymbol{\varepsilon}}^n(\boldsymbol{x})$
→ 2 - computation of the Fourier coefficients $\hat{\underset{\sim}{\boldsymbol{\tau}}}(\boldsymbol{k}_{ab})$
→ 3 - computation of the convolution product in the Fourier space
→ 4 - computation of $\underset{\sim}{\boldsymbol{\varepsilon}}(\boldsymbol{x})$ from its Fourier coefficients $\hat{\underset{\sim}{\boldsymbol{\varepsilon}}}(\boldsymbol{k}_{ab})$ by means of a Fourier series.

The results of the FFT computation depends on the discretisation of the unit cell. At each iteration the field $\underset{\sim}{\boldsymbol{\varepsilon}}(\boldsymbol{x})$ is approximated by a piecewise-constant field (each pixel contains a constant field). The steps 2 and 4 of the previous scheme are replaced by discrete Fourier transforms, which in turn can be evaluated very efficiently by the fast Fourier transform (FFT). A limitation of this method is that the convergence is very slow [Michel et al., 2001].It has been proved that the basic scheme was not convergent in the case of infinite contrast between the phases, which led them to devise the augmented Lagrangian scheme. Nevertheless other improved schemes have been developed such as the work of [Willot et al., 2013, Michel et al., 2001, Vinogradov and Milton, 2008] in which fast convergence is achieved thanks to the use of modified Green operator.

## 2.3 Computer vision techniques and mechanics

### 2.3.1 Gappy POD

Hyper reduction will be greatly used in this thesis. Once the hyper reduced problem is solved the results are obtained on a RID which is much smaller than the complete domain. Hence there is missing information to be recovered. This problematic of missing information has been tackled in [Everson and Sirovich, 1995] in which pictures with missing pixels are fully recovered. In this work a set of empirical eigenfunctions is taken and is used to recover the modal coefficients for each gappy snapshot by a least-squares procedure. Once these coefficients are obtained, they permit gaps to be filled in a reasonable manner and to recover the whole picture.
Considering a set of $N$ eigenfaces of $\mathcal{P}$ pixels vectorized. The eigenfaces are concatenated and orthogonalized in a basis $\boldsymbol{V}$. A mask is applied on a face $\boldsymbol{p}$ leave only a set of $\mathcal{F}$ pixels. The face with the mask is denoted as $\boldsymbol{p}[\mathcal{F}]$. The best linear approximation to recover the face $\boldsymbol{p}$ knowing only $\boldsymbol{p}[\mathcal{F}]$ is the solution of following minimization problem :

$$\boldsymbol{\gamma}^\star = \underset{\gamma^\star}{\operatorname{argmin}} ||\boldsymbol{p}[\mathcal{F}] - \boldsymbol{V}[\mathcal{F},:]\boldsymbol{\gamma}^\star||^2 \tag{2.76}$$

The solution is given by :

$$\boldsymbol{\gamma}^\star = (\boldsymbol{V}[\mathcal{F},:]^T\boldsymbol{V}[\mathcal{F},:])^{-1}\boldsymbol{V}[\mathcal{F},:]^T\boldsymbol{p}[\mathcal{F}] \tag{2.77}$$

Hence the reconstructed face $\tilde{\boldsymbol{p}}$ using the only the pixels of $\boldsymbol{p}[\mathcal{F}]$ is given by :

$$\tilde{\boldsymbol{p}} = \boldsymbol{V}(\boldsymbol{V}[\mathcal{F},:]^T\boldsymbol{V}[\mathcal{F},:])^{-1}\boldsymbol{V}[\mathcal{F},:]^T\boldsymbol{p}[\mathcal{F}] \tag{2.78}$$

An example of this method is given in Fig.2.10. Here the initial dataset is composed of 42 empirical modes (eigenfaces) are taken to construct a basis $\boldsymbol{V}$. The initial face that is to be reconstructed is not part of the original dataset. A 11% mask is applied on the initial face.

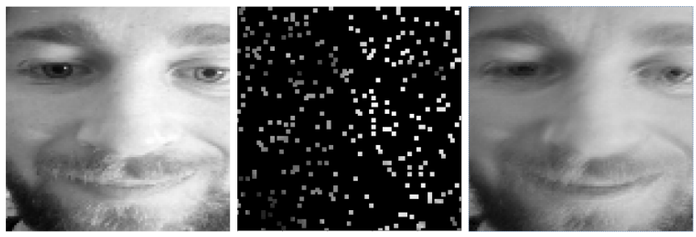


Figure 2.10: Reconstruction of a face from a 11% mask. The reconstructed face c was determined with 42 empirical modes of the reduced basis $\boldsymbol{V}$ and only the white pixels shown in b. The original face, which was not a member of the original ensemble, is shown in (a).

This method is based on a linear approximation techniques. This is a direct method but just like PCA or SVD it cannot represent curved manifold.
In the case of hyper reduction, once the hyper reduced computation is done, the results are obtained on the RID solely. The same principle of gappy POD can then be applied in order to recover the whole field from an incomplete set of data computed by hyper-reduction. Considering a reduced basis $\boldsymbol{V}^{\sigma}$ containing some von Mises stresses modes. The Gappy POD procedure can be applied to recover the whole von Mises stress field (see eq.2.79) :

$$\boldsymbol{\sigma}^{HR}_{gappy} = \boldsymbol{V}^{\sigma}(\boldsymbol{V}^{\sigma}[\mathcal{F},:]^{T}\boldsymbol{V}^{\sigma}[\mathcal{F},:])^{-1}\boldsymbol{V}^{\sigma}[\mathcal{F},:]^{T}\boldsymbol{\sigma}^{HR}[\mathcal{F}] \tag{2.79}$$

Fig.2.3.1 illustrates an example of the recovering process of the von Mises stress field in the case of a bending beam.

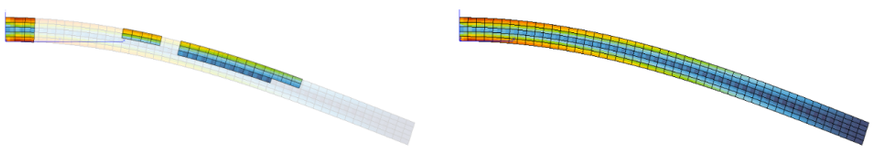

(a) (b)

Figure 2.11: (a)RID with $\sigma^{VM}$ field and full field in shadow (b) recovery of the full field with the gappy POD process.

It makes it possible to take advantage of a RID for fast integration of the constitutive law without losing the global information on the whole mesh.

### 2.3.2 Morphological feature extraction

In the framework of the analysis of image-based digital twins, it is important to consider morphological feature extraction. It can be really useful to classify images or shapes. Linear and non-linear dimensional reduction, as presented in section 2.1.1 and 2.1.2, respectively can be used to project the image in a lower dimensional space and use this reduced coordinates as features. Besides many techniques have been developed in the field of image processing. A survey of these techniques is made in [Yang et al., 2008].

#### Principal axes

Eccentricity is the measure of aspect ratio. It is the ratio of the length of major axis to the length of minor axis. It can be calculated by principal axes method.
Principal axes of a given shape can be uniquely denoted as the two segments of lines that cross each other orthogonally in the centroid of the shape and represent the directions with zero cross-correlation. This way, a contour is seen as an instance from a statistical distribution. Let us consider the covariance matrix $\boldsymbol{C}$ of a contour:

$$\boldsymbol{C} = \frac{1}{N}\sum_{i=0}^{N-1}\begin{pmatrix} x_i - g_x \\ y_i - g_y \end{pmatrix}\begin{pmatrix} x_i - g_x \\ y_i - g_y \end{pmatrix}^{T} = \begin{pmatrix} c_{xx} & c_{xy} \\ c_{yx} & c_{yy} \end{pmatrix} \tag{2.80}$$

With :

$$\begin{array}{rcl} c_{xx} & = & \frac{1}{N}\sum_{i=0}^{N-1}(x_i - g_x)^2 \\ c_{xy} & = & \frac{1}{N}\sum_{i=0}^{N-1}(x_i - g_x)(y_i - g_y) \\ c_{yx} & = & \frac{1}{N}\sum_{i=0}^{N-1}(y_i - g_y)(x_i - g_x) \\ c_{xx} & = & \frac{1}{N}\sum_{i=0}^{N-1}(y_i - g_y)^2 \end{array} \tag{2.81}$$

Where $G(g_x, g_y)$ is the centroid of the shape and here $c_{xy} = c_{yx}$. The length of the two principal axes is equal to the eigenvalues $\lambda_1$ and $\lambda_2$ of the covariance matrix $\boldsymbol{C}$.
The eccentricity $E$ of a shape is defined as :

$$E = \frac{\lambda_2}{\lambda_1} \tag{2.82}$$

Fig. 2.12 illustrates the principal axis on a structure :

The eccentricity is a scalar that can be used to make an easy classification of shape for example.

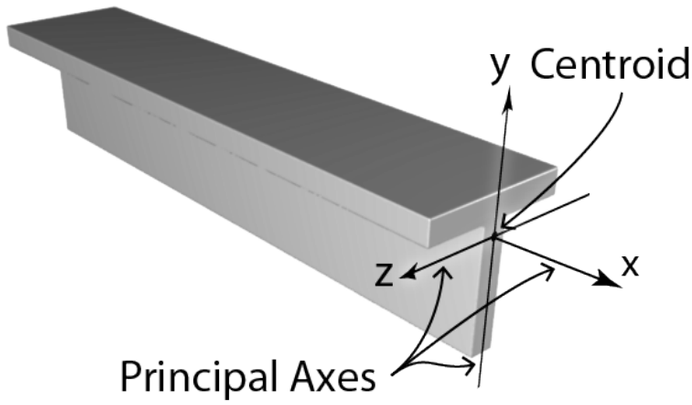


Figure 2.12: Principal axes on a beam structure.

**Shape matrix**

Shape matrix descriptor is an $M \times N$ matrix to present a region shape. Square model of shape matrix, also called grid descriptor, is constructed by the following : for the shape $S$, construct a square centered on the center of gravity $G$ of $S$;the size of each side is equal to $2L$ where $L$ is the maximum Euclidian distance from $G$ to a point $M$ on the boundary of the shape. Point $M$ lies in the center of one side and $GM$ is perpendicular to this side. The square is divided into $N \times N$ subsquares and denotes $S_{kj},\ k, j = 1, \cdots, N$, the subsquares of the constructed grid. The shape matrix is denoted as $\boldsymbol{B}_{kj}$, with :

$$\boldsymbol{B}_{kj} = \begin{cases} 1, & \text{if } \mu(S_{kj} \cap S) \geq \mu(S_{kj})/2, \\ 0, & \text{otherwise.} \end{cases} \tag{2.83}$$

Where $\mu(F)$ is the area of the planar region $F$.
Fig. 2.13 gives an example of how shape matrix method works :

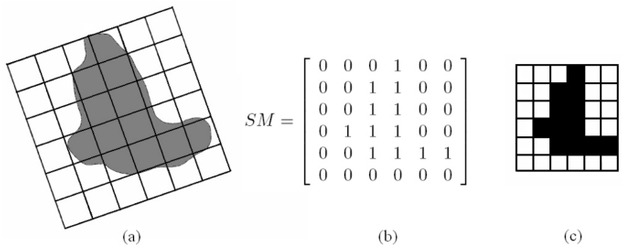


Figure 2.13: (a) Original region; (b) shape matrix; (c) reconstruction of the shape.

These shape matrices can then be taken as input to classify various shapes.

**Region based Fourier descriptors**

Region-based Fourier Descriptor (FD) is referred to as Generic FD (GFD), which can be used for general applications. Basically, GFD is derived by applying a Modified Polar Fourier Transform (MPFT) on shape image [Yadav et al., 2007, Zhang and Lu, 2002]. In order to apply MPFT, the polar shape image is treated as a normal rectangular image. The steps are :
-The approximated normalized image is rotated counter clockwise by an angular step sufficiently small.
-The pixel values along positive x-direction starting from the image center are copied and pasted into a new matrix as row elements.
-Steps 1 and 2 are repeated until the image is rotated by 360°.
The result of these steps is that an image in polar space plots into Cartesian space.
The Fourier transform is acquired by applying a discrete 2D Fourier transform on this shape image.

$$pf(\rho, \phi) = \sum_r \sum_i f(r, \theta_i) exp[j2\pi(\frac{r}{R}\rho + \frac{2\pi i}{T}\phi)] \tag{2.84}$$

Where $0 \leq r = \sqrt{(x - g_x)^2 + (y - g_y)^2} < R$ and $\theta = i(2\pi/T)$; $0 \leq \rho < R$, $0 \leq \phi < T$. Here $(g_x, g_y)$ is the center of mass of the shape, R and T are respectively the radial and angular resolutions. Fig.2.14 shows a simple 2D image, its reconstruction with 50 FD, the normalized Fourier transform and the normalized FD.

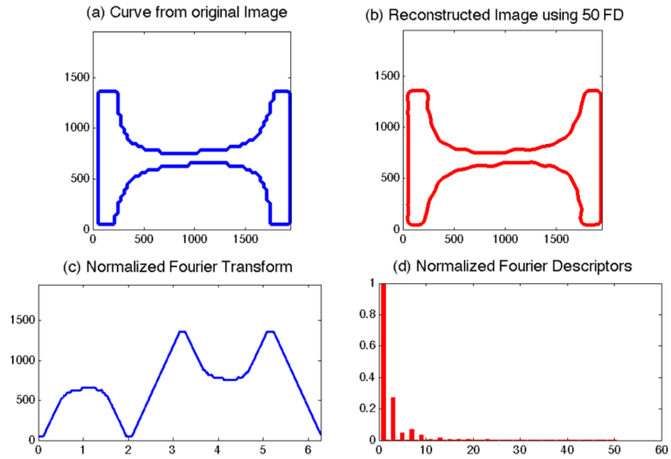


Figure 2.14: (a) Curve from original image; (b) reconstructed image with 50 FD; (c) normalized Fourier transform; (d) normalized Fourier descriptors.

Here again the Fourier coefficient that describes the shape can be used as input information in order to classify them or to make a clustering for example. In [Bhonsle et al., 2009] the Fourier descriptor are used on cancer cell images in order to perform clustering.
A global graph of different shape feature extraction techniques is given in Fig.2.15 which is taken from [Yang et al., 2008]

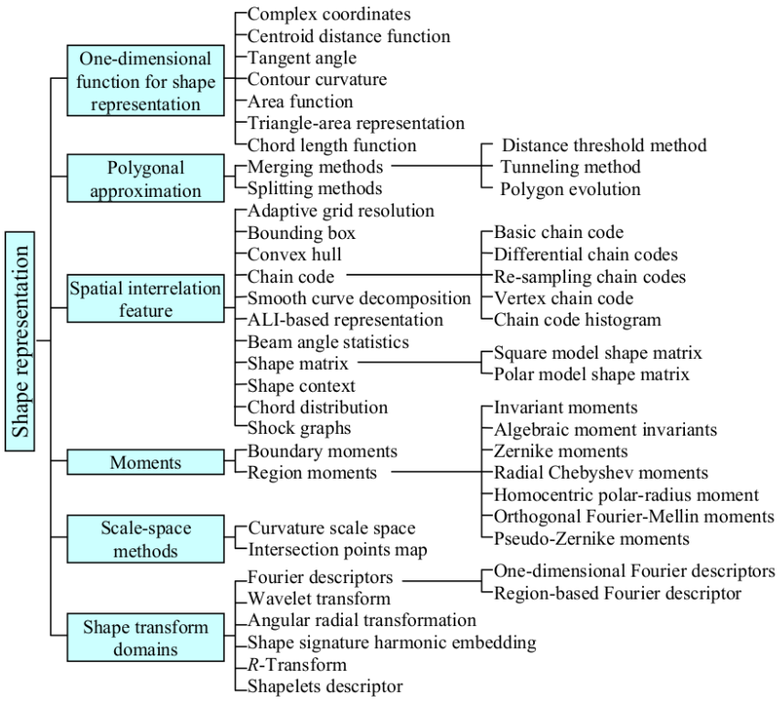


Figure 2.15: An overview of shape description techniques (taken from [Yang et al., 2008])

Since these features can be expressed as vectors they can be used for any classification algorithm (random forest, neuron networks,...) to classify different images. Even interpolation and extrapolation of these vectors can be considered to generate new data. These criteria can also be used for statistical analysis of the data set.
In the field of mechanics these methods are also used to classify or to get a statistical inight of defects which are present in structure. For example in [Lacourt, 2019] a statistical analysis is made. It takes as morphological input the principal axes and their associated eigenvalue in order to highlight the morphological repartition of defects. In this case the defects were pores in welded joints.
In [Yang and Su, 2009] segmented images of pipes with defects are analysed. The major axis and eccentricity of defect are computed and used to assess the structure. Another example of morphological feature extraction is made in [Pidaparti et al., 2010]. In this case an image analysis based on wavelet transforms and fractals is used to study the corrosion morphology of nickel aluminum bronze metal under varying corrosion conditions and applied stresses. Image feature parameters are extracted thanks to wavelet transforms and analysed to classify the pits/cracks in the metal samples.

### 2.3.3 Convolutional neuron network

Over the last decades computer vision and machine learning have achieved incredible results and this is partly due to the rise of Convolutional Neuron Networks (CNNs). The way CNNs work is comparable to standard neuron networks apart from the fact that they apply the convolutional product. One of the reasons why CNNs are hugely popular is because of their architecture. More precisely there is no need for feature extraction. The system learns to do feature extraction and the core concept of CNN is the following, it uses convolution of image and filters to generate invariant features which are passed on to the next layer
Many details are given on the way CNNs works in [Ñanculef et al., 2020]. Given an unknown function $f_0 : \mathcal{X} \to \mathcal{Y}$ that one needs to learn from data, neural networks implement a hypothesis $f_0 : \mathcal{X} \to \mathcal{Y}$ that decomposes as the composition $f = f_1 \circ f_2 \circ \cdots \circ f_M$ of more simple functions $f_m$ referred to as layers. In classic feed-forward networks (FFNs), layers receive as input a vector $\boldsymbol{a}^{(m-1)}$ of size $l_{m-1}$ and compute as output a vector $\boldsymbol{a}^{(m)}$ of size $l_m$, implementing a map of the form $\boldsymbol{a}^{(m)} = g_m(\boldsymbol{W}^{(m)}\boldsymbol{a}^{(m-1)} + \boldsymbol{b}^{(m)})$, where $\boldsymbol{W}^{(m)}$ is matrix of shape $l_m \times l_{m-1}$, $\boldsymbol{b} \in \mathcal{R}^{\boldsymbol{I}_m}$ and $g_m(.)$ is a non-linear function applied component-wise. Compared to FFNs, the early layers of a CNN allow two additional types of computation : convolution and pooling.
Convolutional layers receive as input an image $\boldsymbol{A}^{(m-1)}$ (with $K_m$ channels) and compute as output a new image $\boldsymbol{A}^{(m)}$ (composed of $O_m$ channels). The output at each channel is known as a feature map, and is computed as :

$$\boldsymbol{A}_o^{(m)} = g_m\Big(\sum_k \boldsymbol{W}_{ok}^{(m)} \circledast \boldsymbol{A}_k^{(m-1)} + \boldsymbol{b}_o^{(m)}\Big) \tag{2.85}$$

where $\circledast$ denotes the (2D) convolution operation.

$$\boldsymbol{W}_{ok} \circledast \boldsymbol{A}_k[s,t] = \sum_{p,q} \boldsymbol{A}_k[s+p, t+q]\boldsymbol{W}_{ok}[P-1-p, Q-1-q] \tag{2.86}$$

Where $\boldsymbol{W}_{ok}$ is a matrix of shape $P_m \times Q_m$ and $b_0^m \in \mathcal{R}$. The matrix $\boldsymbol{W}_{ok}$ parameterizes a spatial filter that the layer can use to detect or enhance some feature in the incoming image. The specific action of this filter is automatically learnt from data in the training process of the network. Pooling layers of a CNN implement a spatial dimensionality reduction operation designed to reduce the number of trainable parameters for the next layers and allow them to focus on larger areas of the input pattern. Given an image $\boldsymbol{A}(m-1)$ a typical pooling layer with pool sizes $P_m, Q_m \in \mathcal{N}$, and strides $\alpha_m, \beta_m \in \mathcal{N}$ implements a channel-wise operation of the form :

$$\boldsymbol{A}_o^{(m)}[s,t] = \kappa \cdot \sum_{p,q} \Big(\boldsymbol{A}_o^{(m-1)}[\alpha_m s + p, \beta_m t + q]\Big)^{\rho 1/\rho} \tag{2.87}$$

where $\kappa, \rho \in \mathcal{N}$ are fixed parameters. Note that using $P_m = Q_m = \alpha_m = \beta_m$ corresponds to divide each channel of the input image into nonoverlapping $P_m \times Q_m$ patches and substitute the values in that region by a single value determined by $\rho$ and $\kappa$. In max pooling layers ($\rho = +\infty, \kappa = 1$), this value is the maximum of the values found in the patch. In average pooling layers ($\rho = 1, \kappa = 1/PQ$), one takes the average of the values in the corresponding patch. The right choice of this function can make the model more robust to distortions in the input pattern.
Fig.2.16 illustrates how CNNs work.

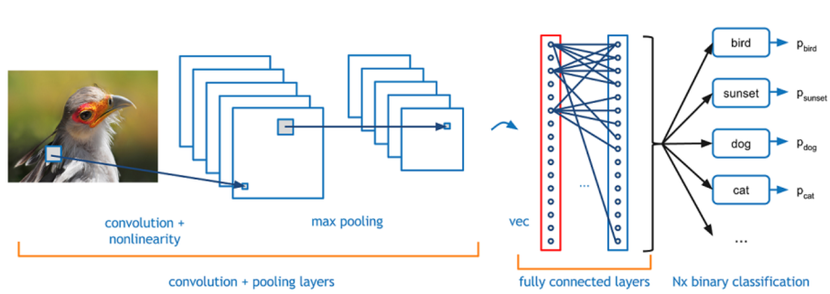


Figure 2.16: Example of a CNN architecture.

CNN and more precisely LeNet-5, a pioneering 7-level convolutional network by [Lecun et al., 1998], that classifies digits has achieved great results. It represents a turning point in the history of neuron networks and image recognition.

CNNs are also more and more used in the field of mechanics. In [Nguyen et al., 2018], CNNs enables to recommend a reduced order model for fast stress prediction according to various possible loading environments. This approach is applied on a macroscopic part by using a digital image of a mechanical test. The selected reduced basis is then used for a fast hyper reduced computation.

In [Daniel et al., 2020] a general framework for projection-based model order reduction assisted by deep neural networks is proposed. The proposed methodology consists in using CNNs to recommend a reduced-order model given an input tensor describing the temperature field in the structure. The temperature field strongly influences the quantities of interest of the mechanical problem.
Even the stress intensity factor, which is a key quantity to be determined in fracture mechanics, has been evaluated with CNNs in [Long et al., 2021]. A CNN for predicting the stress intensity factor (SIF) at the crack tip is designed. Based on the proposed CNN, the SIF can be automatically predicted through computational vision.

# Chapter 3

# Hyper-reduction for limit pressure evaluation

**Contents**



**Résumé en français**


Dans ce chapitre, un schéma "hyper-réduit" de l'algorithme de Crisfield est présenté et est appliqué aux simulations de flambage et aux instabilités plastiques. Les deux systèmes linéaires et l'équation d'ellipse entrant dans l'algorithme sont projetés sur un espace réduit et résolus dans un domaine d'intégration réduit, résultant en un système d'équations "hyper-réduites". La Gappy POD est utilisée pour récupérer les contraintes en dehors du domaine d'intégration réduit.
Diverses méthodes sont proposées pour construire différentes bases réduites. Pour ce faire, les données de simulation obtenues avec la méthode des éléments finis sont utilisées. Un critère d'erreur basé sur les contraintes pour les calculs hyper réduits est proposé.
Un algorithme "glouton" couplé à ce critère d'erreur est utilisé pour générer intelligemment des simulations par éléments finis complètes. Ces dernières permettent ainsi d'enrichir la base réduite et mettent en avant l'adéquation du critère d'erreur choisi.
Enfin, les résultats numériques relatifs aux structures élastoplastiques subissant des déformations importantes (transformations finies) sont présentés en mettant l'accent sur les prédictions de flambement et de charge limite.
Une étude paramétrique sur la géométrie de la structure est réalisée afin de déterminer le domaine de validité du modèle hyper-réduite proposée.


## 3.1 Introduction

Oil and gas transmission pipelines are subjected to high internal pressures. An accurate assessment of the burst pressure is essential for the design and integrity management of the pipelines [Lam and Zhou, 2016]. Pipe elbows are an import part of a transmission pipeline system. Due to the existence of the bend curvature, the mechanical behavior of pipe elbows is different from that of straight pipes. Under the internal pressure, the stress distribution of a thin-walled straight pipe is uniform along both the axial and circumferential directions. However, for an elbow, the hoop stress in the intrados is markedly higher than those in the extrados and attached straight pipes. Hence, in a pipeline system, pipe elbows are more critical compared with straight pipes [Khalaj Khalajestani et al., 2015]. In 1978, Goodall proposed a formula to calculate the lower bound of the burst pressure of defect-free pipe elbows [Goodall, 1978]. In [Miller, 1988], Miller pointed out that the Goodall model should be used with caution because it had not been validated by experiments. The published experimental studies on the burst pressure of thin-walled defect-free elbows are limited. In [Kim et al., 2013] the author carried out 8 burst tests of thick-walled elbows with local wall thinning under combined internal pressure and in-plane bending moment. In [Li et al., 2001, Duan and Shen, 2006], a series of burst pressure models were proposed for defected elbows subjected to internal pressure only by combining the Goodall model with the well-known burst pressure models for corroded straight pipes. However, those burst pressure models were shown to be overly conservative compared with FEA results. As discussed in [Lee et al., 2015, Zhang et al., 2015] , the burst pressures predicted by the Goodall model are overly conservative compared with the finite element analysis (FEA) results. Despite this, the Goodall model is widely used in the pipeline industry due mainly to its simplicity. However, overly conservative predictions lead to unnecessary repair and retrofit actions, which translate to significant cost penalties to pipeline operators.
FEA is time consuming though more accurate. The computation of the limit pressure in pipes is not possible if a classical Newton scheme is used. Usually a Riks algorithm is adopted since

it can overcome the instability of the limit load very well.
In this chapter an adaptation of the standard HROM method is developed for the Riks algorithm and coupled with a greedy algorithm in order to generate the right amount of data to create an appropriate RB. The so developed model can then pave the parametric space to determine the limit load for various configurations of pipes. It is a first step for fast global simulations on sane structures, prior considering the influence of defects on burst pressure.
The rest of this chapter is taken from the article [Launay et al., 2021] published in "Intenrational Journal of Solids and Structures". The online version can be found with the following doi : https://doi.org/10.1016/j.ijsolstr.2020.10.014

## 3.2 Hyper-reduced arc-length algorithm for stability analysis in elastoplasticity

# Hyper-reduced arc-length algorithm for stability analysis in elastoplasticity

H. Launay[a], J. Besson[a], D. Ryckelynck[a,*], F. Willot[a,b]

[a] *MINES ParisTech, PSL research university, Centre des Matériaux, CNRS UMR 7633, 91003 Evry, France*

[b] *Centre de Morphologie Mathématiques, 77300 Fontainebleau, France*

**Abstract**

In this article an "hyper-reduced" scheme for the Crisfield's algorithm (Crisfield, 1981) applied to buckling simulations and plastic instabilities is presented. The two linear systems and the ellipse equation entering the algorithm are projected on a reduced space and solved in a reduced integration domain, resulting in a system of "hyper-reduced" equations. Use is made of the Gappy proper orthogonal decomposition to recover stresses outside the reduced integration domain. Various methods are proposed to construct a reduced bases, making use of simulation data obtained with standard finite element method and a stress-based error criterion for the hyper reduced calculations is proposed. A "greedy" algorithm coupled with this error criterion is used to generate intelligently full standard finite element simulations and enrich the reduced base, demonstrating the adequacy of the error criterion. Finally, numerical results pertaining to elastoplastic structures undergoing finite strains, with emphasis on buckling and limit load predictions are presented. A parametric study on the geometry of the structure is carried out in order to determine the domain of validity of the proposed hyper-reduced modeling approach.

*Keywords:* Model order reduction; Hyper-reduction; Reduced integration domain; Crisfield algorithm; POD; Plastic instability; Buckling; Limit load

## 1. Introduction

Micromechanical computations are often coupled with parametric studies to probe the mechanical behavior of structures undergoing plastic instabilities, and determine the effect of shape and geometry, material laws and mechanical loadings. The prediction of the limit load of structures [1] is an important aim of many of these methods. However efficient the approaches might be, the scope of a parametric study, its extent in the space of parameters, is constrained by the numerical method it employs – and ultimately by how fast numerical computations can be carried out. Parametric studies become especially challenging when dealing with unstable elasto-plastic problems, modeled as sets of partial differential equations, each of which must be solved numerically. The computational complexity of the resulting method is driven by the size of the approximation space used to represent the solution of the problem. As an example, the size of the "full-order model" (FOM), used in the finite element method, is proportional to the number of discrete unknowns, and is generally quite high. To overcome this limitation, methods employing reduced bases have been developed since the 1970s [2] and have seen wide applications in a variety of mechanical problems [3, 4]. As a principle, the reduced base defines the approximation space on which solutions are sought for. The corresponding reduced-order model (ROM) is obtained by projecting the full-order model on the reduced base. Techniques for deriving a model-order reduction method based on projections have been developed for a long time [5]. Nevertheless, recent publications show interesting hybrid approaches combining deep-learning and reduced-modeling for partial differential equations (PDEs). In [6], for instance, a solution of PDEs obtained by neural networks is proposed. In the context of non-parametric modeling, other authors [7, 8] make use of convolutional neural networks to tailor hyper-reduced order models, which are useful when the number of parameters is large, typically more than 100.

Hyper-reduction methods [9], which, commonly, make use of the Newton-Raphson scheme, offer computational speed-up for stable elastoplastic simulations [10, 11]. The Newton-Raphson algorithm is, however, not robust enough when dealing with unstable elastoplastic problems, where critical loads or buckling must be accounted for. The Newton Raphson algorithm may diverge, for instance, due to snap-through or a snap-back equilibrium states [12]. The "asymptotic numerical method" [13] or the "arc-length

*Corresponding author

*URL:* david.ryckelynck@mines-paristech.fr (D. Ryckelynck)

method" [14, 15, 16] have been developed to treat these problems. The arc-length method is a general technique for structural analysis originally developed by Riks [17]. Later, other authors [18, 19] have developed refined schemes. Arc-length algorithms are especially useful to treat highly-nonlinear problems such as delamination or fracture [20, 21].

The present work is devoted to the estimation of the critical load of ductile pipelines undergoing rupture [22, 23]. The critical loads of structures may be estimated using charts at virtually no cost [24]. This approach provides results instantaneously. Yet, it is valid for specific geometries only, and overestimate the effect of geometry in many cases. To predict accurately the critical load of pipelines, the size and shape of the structures should be taken into account. In the present article, a hyper-reduction method based on Crisfield's algorithm is proposed as a way to limit the computational cost of solving an implicit nonlinear balanced equations, while offering accurate mechanical predictions.

Many reduced-order models have been developed to deal with such nonlinear problems. In interpolation methods, the nonlinear terms of interest are estimated by interpolation at a few spatial locations [25]. In particular, in the discrete empirical interpolation method (DEIM) [26], the set of interpolation points is obtained using a proper orthogonal decomposition (POD) base. In cubature methods [27, 28, 29, 30], spatial integrals involved in the weak formulation are estimated using a few unassembled elemental contributions. The elements of interest and weight coefficients are determined using an optimization process. The third types of methods are boundary value problems restricted to a reduced integration domain (RID) [31]. The RID usually involve elements connected to interpolation points computed by the DEIM algorithm, and can be obtained by considering several POD reduced bases. This last approach has been successfully applied to elasto-plastic [32] and contact problems [11] and is followed here. For simplicity, the boundary value problem restricted to a reduced integration domain is denoted "HR" hereafter.

In the present work, the hyper-reduction method is extended to the Crisfield's algorithm consists in coupling the usual hyper-reduced residual to a reduced ellipse equation. With Crisfield's method two linear systems are solved resulting in two solutions. The global solution is a linear combination of these two vectors, under a constraint prescribed by an ellipse. In this paper, various reduced order bases (ROB) constructions are considered by taking into account the contributions to the global solution. In order to choose relevant snapshots, a greedy sampling algorithm coupled with an error indicator is proposed. This strategy ensures the robustness of the reduced order model with respect to variations of the model parameters. In order to undertake fast parametric studies, a reduced model is developed by projecting the mechanical equations on a reduced order base (ROB) with a hyper-reduced method.

Section 2 presents the notation that will be used. The Crisfield algorithm is described in section 3 whereas section 4 is dedicated to the classical hyper-reduced method. Section 5 details the hyper-reduced arc-length algorithm. Section 6 shows various results with this method. Finally in section 7 the speed up of this method is discussed.

## 2. Notations

In this article, scalar values are denoted by lowercase roman letters, vectors by bold lowercases, and matrices by uppercase, bold letters, e.g. $a$, $\mathbf{a}$ and $\mathbf{A}$ respectively. The notation $\mathbf{A}[L_1, L_2]$ designates the submatrix of $\mathbf{A}$ formed by the subset $L_1$ of the rows of $\mathbf{A}$ and the subset $L_2$ of the columns of $\mathbf{A}$. We use the Python-notation $\mathbf{A}[L_1, :]$ for the submatrix formed by a subset $L_1$ of the rows of $\mathbf{A}$. Second-order tensors are denoted by underlined capitals (e.g. $\underset{\sim}{A}$) whereas fourth-order tensors are underlined twice ($\underset{\approx}{C}$). Double-dots (:) designate a double contraction over the last two and first two indices of the left and right tensors, respectively. As such $\underset{\sim}{A} : \underset{\sim}{B}$ is the scalar $\sum_{ij} \underset{\sim}{A}_{ij} \underset{\sim}{B}_{ij}$ whereas $\underset{\approx}{C} : \underset{\sim}{B}$ is the second-order tensor $\sum_{kl} \underset{\approx}{C}_{ijkl} \underset{\sim}{B}_{kl}$.

The Euclidian norm (or 2-norm) is denoted by the symbols $||.||_2$. It is defined by $||\mathbf{u}||_2 = (\mathbf{u}^T \cdot \mathbf{u})^{1/2} = \left(\sum_i u_i^2\right)^{1/2}$ where the superscript $^T$ designates a matrix transpose. The 2-norm of matrices is given by the spectral norm $||\mathbf{A}||_2 = \sigma_{max}(\mathbf{A})$, where $\sigma_{max}(\mathbf{A})$ denotes the largest singular value of $\mathbf{A}$.

## 3. Crisfield's algorithm for unstable finite element problems

The present section is devoted to Crisfield's algorithm. This algorithm, developed to achieve convergence in unstable problems, is described hereafter. In the context of the finite element (FE) model [33], the shape functions of the FE base are denoted by $(\phi_j)_{j=1}^n$ with $n$ the number of discretization nodes. It is convenient to introduce the functions $\boldsymbol{\phi}_i = \phi_j \mathbf{e}_k$ where $i = (j-1) \times d + k$, $i = 1, ..., \mathcal{N}$, $j = 1, ..., n$, $k = 1, ..., d$, $d$ is the

dimension of the problem and $\mathbf{e}_k$ refer to the canonical vectors of a Cartesian coordinates system. The approximation of the displacement with the shape functions $(\boldsymbol{\phi}_i)_{i=1}^{\mathcal{N}}$ reads:

$$\boldsymbol{v}(\mathbf{x}) = \boldsymbol{v}_0(\mathbf{x}) + \sum_{i=1}^{\mathcal{N}} \boldsymbol{\phi}_i(\mathbf{x}) u_i, \qquad \forall \mathbf{x} \in \Omega, \tag{1}$$

where $\mathcal{N} = n \times d$ is the number of degrees of freedom (DOF) of the structure, $\boldsymbol{v}_0$ is a given displacement field that fulfills the Dirichlet boundary conditions, $\boldsymbol{v}$ is the approximate finite element solution and $\mathbf{u} = (u_i)_{i=1}^{\mathcal{N}}$ the vector of the related degrees of freedom. The Cauchy stress that fulfills the constitutive equations is denoted by $\underset{\sim}{\sigma}(\mathbf{u})$. Denote $\mathbf{f}^{int} \in \mathbb{R}^{\mathcal{N}}$ a vector of generalized internal forces which depends on $\mathbf{u}$ such that:

$$f_i^{int}(\mathbf{u}) = \int_\Omega \frac{1}{2} \left( \underset{\sim}{\nabla} \boldsymbol{\phi}_i + \underset{\sim}{\nabla}^T \boldsymbol{\phi}_i \right) : \underset{\sim}{\sigma}(\mathbf{u}) \, d\Omega, \qquad i = 1, \dots \mathcal{N}, \tag{2}$$

where $\Omega$ is the current configuration. The focus of the present work is now limited to implicit solutions of finite element balance equations, where use is made of an arc-length algorithm [34]. Because of instabilities or plasticity, the target loading may be out of reach. Accordingly, the magnitude of the loading, denoted $\lambda \in \mathbb{R}$, should be determined as well as the displacement field. The residual of the FE balance equation reads:

$$\mathbf{r}(\mathbf{u}, \lambda) = \mathbf{f}^{int}(\mathbf{u}) - \lambda \, \mathbf{f}^{ext}, \tag{3}$$

where $\mathbf{f}^{ext} \in \mathbb{R}^{\mathcal{N}}$ denotes the vector of general external loading. The residual is assumed to be null in the initial configuration:

$$\mathbf{f}^{int}(\mathbf{u}_0) - \lambda_0 \, \mathbf{f}^{ext} = 0. \tag{4}$$

The couple of variables $(\Delta\mathbf{u},\ \Delta\lambda)$ is determined so as to satisfy a null residual in the current configuration:

$$\mathbf{r}(\mathbf{u}_0 + \Delta\mathbf{u}, \lambda_0 + \Delta\lambda) = 0. \tag{5}$$

As a consequence of the above (5), point $(\mathbf{u}_0 + \Delta\mathbf{u},\ \lambda_0 + \Delta\lambda)$ belongs to the equilibrium path. Assume that the residual is not zero at point $(\mathbf{u}_0 + \Delta\mathbf{u},\ \lambda_0 + \Delta\lambda)$, i.e. $\mathbf{r}(\mathbf{u}_0 + \Delta\mathbf{u}, \lambda_0 + \Delta\lambda) \neq 0$. A solution at a nearby point $(\mathbf{u}_0 + \Delta\mathbf{u} + \delta\mathbf{u},\ \lambda_0 + \Delta\lambda + \delta\lambda)$ is sought for. A Taylor expansion provides the expression:

$$\mathbf{r}(\mathbf{u}_0 + \Delta\mathbf{u} + \delta\mathbf{u}, \lambda_0 + \Delta\lambda + \delta\lambda) \approx \mathbf{r}(\mathbf{u}_0 + \Delta\mathbf{u}, \lambda_0 + \Delta\lambda) + \mathbf{K} \cdot \delta\mathbf{u} - \delta\lambda \, \mathbf{f}^{ext} \tag{6}$$

where $\mathbf{K} = \partial \mathbf{f}^{int} / \partial \mathbf{u}|_{\mathbf{u}=\mathbf{u}_0+\Delta\mathbf{u}}$. The linearized balance equation accordingly reads:

$$\mathbf{K} \cdot \delta\mathbf{u} - \delta\lambda \, \mathbf{f}^{ext} = -\mathbf{r}(\mathbf{u}_0 + \Delta\mathbf{u}, \lambda_0 + \Delta\lambda) \tag{7}$$

The variables $\delta\mathbf{u}$ and $\delta\lambda$ being the unknowns, equation (7) does not yield a unique solution. Indeed the problem is constrained by $\mathcal{N}$ scalar equations depending on $\mathcal{N} + 1$ unknowns – including $\delta\lambda$. The problem ought to be supplemented by an additional "arc-length equation" [15] which describes an ellipse in the space of displacement and loading parameters. The latter reads:

$$(\Delta\mathbf{u} + \delta\mathbf{u})^T \cdot (\Delta\mathbf{u} + \delta\mathbf{u}) + \beta^2 (\Delta\lambda + \delta\lambda)^2 (\mathbf{f}^{ext\ T} \cdot \mathbf{f}^{ext}) = \Delta\ell^2, \tag{8}$$

$\Delta\ell$ represents the radius of the circle on which the solution $(\delta\mathbf{u}, \delta\lambda)$ must be found. This is a user defined parameter relative to the size of the increment. In the above, $\beta$ is also a user defined parameter which monitors the shape of the ellipse. As an example $\beta$=1 leads to a circle hence the name "arc-length method". Figure1 depicts the arc-length algorithm with the choice $\beta = 1$.

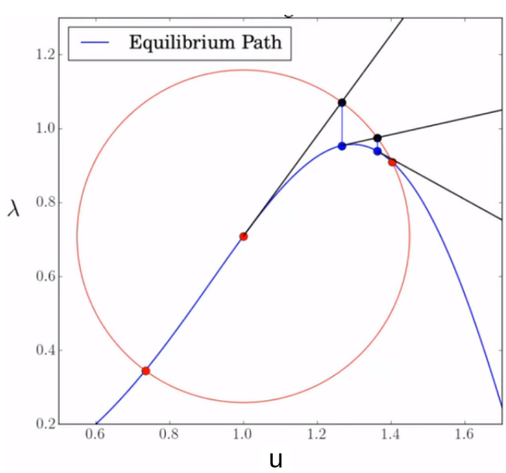


Figure 1: Arc-length method.

Each blue point represents the solution of an iteration until it converges at the red dot on the right. Following [18], equation (7) can be written:

$$\mathbf{K} \cdot \delta\mathbf{u} = \delta\lambda\, \mathbf{f}^{ext} - \mathbf{r}(\mathbf{u}_0 + \Delta\mathbf{u}, \lambda_0 + \Delta\lambda). \tag{9}$$

which is solved in terms of two solutions $\delta\mathbf{u}_b$ and $\delta\mathbf{u}_t$ for the linearised balance equation:

$$\begin{cases} \mathbf{K}.\delta\mathbf{u}_t = \mathbf{f}^{ext} \\ \mathbf{K}.\delta\mathbf{u}_b = -\mathbf{r}(\mathbf{u}_0 + \Delta\mathbf{u}, \lambda_0 + \Delta\lambda) \\ \delta\mathbf{u} = \delta\mathbf{u}_b + \delta\lambda\, \delta\mathbf{u}_t. \end{cases} \tag{10}$$

As shown by the above, the Crisfield algorithm involves two balance equations of the finite element model. Equation (10a) relates to the target loading whereas equation (10b), similar to the linear step involved in the Newton-Raphson algorithm, relates to the residual stresses in the structure. The projection-based model-order reduction aimes to reduce the computational complexity of these two balance equation related to the two primal variables $\delta\mathbf{u}_b$ and $\delta\mathbf{u}_t$. According to (10c), equation (8) may be rewritten as:

$$\begin{aligned} &(\Delta\mathbf{u} + \delta\mathbf{u})^T \cdot (\Delta\mathbf{u} + \delta\mathbf{u}) + \beta^2(\Delta\lambda + \delta\lambda)^2(\mathbf{f}^{ext\ T} \cdot \mathbf{f}^{ext}) = \Delta\ell^2 \\ &\Longleftrightarrow \\ &\alpha_1\delta\lambda^2 + \alpha_2\delta\lambda + \alpha_3 = 0, \end{aligned} \tag{11}$$

where:

$$\begin{aligned} \alpha_1 &= \delta\mathbf{u}_t^T \cdot \delta\mathbf{u}_t + \beta^2\mathbf{f}^{ext\ T} \cdot \mathbf{f}^{ext} \\ \alpha_2 &= 2(\Delta\mathbf{u} + \delta\mathbf{u}_b)^T \cdot \delta\mathbf{u}_t + \beta^2\Delta\lambda\mathbf{f}^{ext\ T} \cdot \mathbf{f}^{ext} \\ \alpha_3 &= (\Delta\mathbf{u} + \delta\mathbf{u}_b)^T \cdot (\Delta\mathbf{u} + \delta\mathbf{u}_b) + \beta^2\Delta\lambda\mathbf{f}^{ext\ T} \cdot \mathbf{f}^{ext} - \Delta\ell^2 \end{aligned} \tag{12}$$

As expected for ellipses, equation (11) admits two solutions, denoted $\delta\lambda_1$ and $\delta\lambda_2$ Following on the "dot-product rule" introduced in [35], the solution in the equilibrium path maximizes the quantity:

$$D^{(i)} = (\Delta\mathbf{u} + \delta\mathbf{u}^{(i)})^T \cdot \Delta\mathbf{u} + \beta^2\Delta\lambda(\Delta\lambda + \delta\lambda^{(i)})\ \left(\mathbf{f}^{ext}\right)^T \cdot \mathbf{f}^{ext}, \qquad i = 1, 2, \tag{13}$$

which ensures that the selected solution is the closest to previously-computed solutions. This rule allows one to deform the structure while preventing elastic unloading in most of the cases. Once $\delta\mathbf{u}$ and $\delta\lambda$ is obtained, the incremental displacement $\Delta\mathbf{u}$ and incremental loading parameter $\Delta\lambda$ are updated until the norm of the residual is smaller than a specified threshold. Furthermore, when convergence is found to be slow, a novel incremental solution is sought for the same problem with a lower $\Delta\ell$ parameter.

It is emphasized that equation (8) mixes displacement and force, and therefore the variables $\alpha_i$ have no clear physical meaning. To overcome this problem, the parameter $\beta$ may be set to zero, in which case $\Delta\ell$ denotes the distance between the two possible values of $\Delta\mathbf{u}$. In the rest of the study, the value of $\beta$ is assumed to be zero.

## 4. Hyper-reduction method

This section is devoted to the usual hyper-reduced method using the Newton-Raphson algorithm, in this case the balance equation takes the form of equation (9), with $\delta\lambda = 0$ and $\Delta\lambda$ being the loading increment which is a constant in this case. Therefore only the iterative displacement vector $\delta\mathbf{u}$ is unknown.The following equation is obtained :

$$\mathbf{K} \cdot \delta\mathbf{u} = -\mathbf{r}(\mathbf{u}_0 + \Delta\mathbf{u}, \lambda_0 + \Delta\lambda). \tag{14}$$

As previously stated, this approach belongs to projection-based reduction methods, and aims to reduce the number of DOFs by projecting the balance equation on a smaller approximation space. Here, hyper-reduction is applied in the framework of a posteriori model reduction methods and unsupervised machine learning methods. In these methods, the computational task is divided in two phases, namely an "offline" and "online phase". In the offline phase, simulation data are generated by the solution of the high-fidelity equations, possibly for various parameter values in a training set $\mathcal{D}_{train}$. These simulation data are called training data and are required to train reduced bases and a reduced integration domain (RID). In the online phase, the HR model is used to predict the displacements and other quantities of interest resulting from parameters values which do not belong to the training set. Offline phases are time-consuming as they require solutions of the FOM for different sampling points in the parameter space. Nevertheless, they allow for low-cost online simulations afterwards, provided the hyper-reduced order model (HROM) can be used. Projection-based model order reduction methods may be combined

with robust machine-learning methods. Hybrid approaches [7, 8] have been proposed which make use of physical equations and data science techniques. These methods are particularly efficient ways to take advantage of simulation data. In this context, and in the context of model-order reduction, it is useful to save these data in memory storage systems.

The HR method [10] uses a projection on a reduced base to reduce the number of DOFs, but it also uses the fact that solving the equations on a RID is sufficient to find the reduced DOFs with less computational complexity than using the full domain. This particularity improves the computational time savings, especially for nonlinearities that cannot be precomputed offline. Indeed, the RID, built during the offline part, reduces the cost of the projections to get the reduced non-constant stiffness matrix from the Jacobian matrix. The reduced base for displacement approximation is obtained via the singular value decomposition (SVD). The reader is referred to [2] for a discussion of the connections between proper orthogonal decomposition methods (POD) and SVD. The SVD is a common numerical tool in machine learning and especially useful when computing principal components. According to the Young Eckart theorem [36], it provides, in particular, the optimal low-rank approximation of the simulation data generated during the offline phase. In the following details on the methodology of the hyper-reduction method are given.

Let us denote $\mathcal{N}_\mathcal{S}$ the number of displacement fields available at the end of the offline phase. The nodal value of these finite element fields are stored in a snapshot matrix $\mathbf{Q} \in \mathbb{R}^{\mathcal{N}\times\mathcal{N}_\mathcal{S}}$. For each parameter in the training set $\mathcal{D}_{train}$, and at each time increment the approximation of the balance equation is satisfied and the displacement $\mathbf{u}$ computed by the parametric finite element model is saved as a column of $\mathbf{Q}$, such that $\exists j \in \{1,\dots,\mathcal{N}_\mathcal{S}\}$ with $\mathbf{Q}[:,j] = \mathbf{u}$. Then, a truncated singular value decomposition is applied in order to extract the reduced base $\mathbf{V}$ according to the following optimal low-rank approximation:

$$\mathbf{Q} = \mathbf{V}\cdot\mathbf{\Sigma}\cdot\mathbf{W}^T + \mathbf{R}, \quad \mathbf{V}^T\cdot\mathbf{V} = \mathbf{I}_N, \quad \mathbf{W}^T\cdot\mathbf{W} = \mathbf{I}_N, \quad \mathbf{V}^T\cdot\mathbf{R} = 0, \quad \frac{\|\mathbf{R}\|_2^2}{\|\mathbf{Q}\|_2^2} < \epsilon_{tol}, \tag{15}$$

where $\mathbf{I}_N$ is the identity matrix and belongs to $\mathbb{R}^{N\times N}$, $\mathbf{R}$ belongs to $\mathbb{R}^{\mathcal{N}\times\mathcal{N}_\mathcal{S}}$ and $\epsilon_{tol}$ is an error-criterion. The matrices $\mathbf{V} \in \mathbb{R}^{\mathcal{N}\times N}$ and $\mathbf{W} \in \mathbb{R}^{\mathcal{N}_\mathcal{S}\times N}$ are orthogonal matrices and $\mathbf{\Sigma} \in \mathbb{R}^{N\times N}$ is a diagonal matrix which contains the highest singular values $\sigma_j$ in descending order (i.e. $\sigma_j \geq \sigma_{j+1}$). In the present case, simulation data are related to a finite element model so that each column of $\mathbf{V}$ is the nodal values of an empirical mode $\boldsymbol{\psi}_k$ where:

$$\boldsymbol{\psi}_k(\mathbf{x}) = \sum_{i=1}^{\mathcal{N}} \boldsymbol{\phi}_i(\mathbf{x})\, V_{ik}, \qquad k = 1,\dots N, \qquad \mathbf{x} \in \Omega. \tag{16}$$

The importance of an empirical mode is quantified by the corresponding value $\sigma_j$. The truncation of the SVD, and the number of empirical modes stored in $\mathbf{V}$, is monitored by the error-criterion $\epsilon_{tol}$. Ideally, the reduced base $\mathbf{V}$ contains a few vectors and allows one to approximate the space spanned by the snapshots.

The above reduced-base construction may be applied to any finite element variables, either defined at the nodes of the mesh, or at the Gauss points inside elements. A reduced-base is most often generated for both displacement variables and stresses separately (details about the stress field involved in the computation of $\mathbf{f}_{int}$ will be given in Section 6.1). In the present work, the stress-related reduced base is denoted by $\mathbf{V}^\sigma$.

Following on the Gappy POD [37], any vector $\mathbf{u}$ which belongs to the column space *colspan*$(\mathbf{V})$ of $\mathbf{V}$ may be recovered by using few entries $\mathbf{u}[\mathcal{F}]$ of $\mathbf{u}$, if $\mathbf{V}[\mathcal{F},:]$ is a full column rank matrix. Such recovery procedure takes the form:

$$\mathbf{u} \in \mathit{colspan}(\mathbf{V}), \qquad \mathbf{u} = \mathbf{V}\cdot\left(\mathbf{V}[\mathcal{F},:]^T\cdot\mathbf{V}[\mathcal{F},:]\right)^{-1}\cdot\mathbf{V}[\mathcal{F},:]^T\cdot\mathbf{u}[\mathcal{F}]. \tag{17}$$

In the case $\mathcal{F} = \mathcal{P}$, where $\mathcal{P}$ denotes the set of interpolation points for columns of $\mathbf{V}$ obtained by the discrete empirical interpolation method (DEIM) [26], the matrix $\mathbf{V}[\mathcal{P},:]$ is square invertible and the recovery procedure simplifies as:

$$\mathbf{u} \in \mathit{colspan}(\mathbf{V}) \quad \mathbf{u} = \mathbf{V}\cdot\mathbf{V}[\mathcal{P},:]^{-1}\cdot\mathbf{u}[\mathcal{P}]. \tag{18}$$

Moreover, if $\mathcal{P} \subset \mathcal{F}$, then $\mathbf{V}[\mathcal{F},:]$ is full-column rank.

A heuristic rule is followed to construct the RID: the extent of the RID must enable the recovery of the finite element displacement fields and the finite element stresses when they both belong to *colspan*$(\mathbf{V})$ and *colspan*$(\mathbf{V}^\sigma)$ respectively. Notice that the recovery of the stress enables the estimation of $\mathbf{f}_{int}$ and of the residual, without using an interpolation scheme for $\mathbf{f}_{int}$. The set of interpolation points related to $\mathbf{V}^\sigma$ is denoted by $\mathcal{P}^\sigma$. Hence, $\mathcal{F}$ is generated such that $\mathcal{P}\cup\mathcal{P}^\sigma \subset \mathcal{F}$ which allows one to recover the stress and the

displacement, making use of the Gappy POD. In many practical situations, $\mathcal{F}$ also includes the degrees of freedom of a zone of interest.

The RID, denoted by $\Omega_A \subset \Omega$, is assumed to be the support of the finite element shape functions $\boldsymbol{\phi}_i$ ($i \in \mathcal{F}$):

$$\Omega_A = \cup_{i\in\mathcal{F}} \text{sup}(\boldsymbol{\phi}_i). \tag{19}$$

Denote $\Omega_B = \Omega \backslash \Omega_A$ the complementary set of $\Omega_A$ and $\Gamma^I = \overline{\Omega_A} \cap \overline{\Omega_B}$ the interface common to $\Omega_A$ and $\Omega_B$. The following property holds:

$$\mathcal{F} = \left\{ i \in \{1, ..., \mathcal{N}\} \mid \int_{\Omega_B} \boldsymbol{\phi}_i^T \,.\, \boldsymbol{\phi}_i \; d\Omega = 0 \right\} \tag{20}$$

Let us now introduce $\mathcal{I}$, the set of degrees of freedom indices related to the interface $\Gamma^I$:

$$\mathcal{I} = \left\{ i \in \{1, ..., \mathcal{N}\} \mid \int_{\Gamma^I} \boldsymbol{\phi}_i^T \,.\, \boldsymbol{\phi}_i \; d\Gamma \neq 0 \right\} \tag{21}$$

The matrix $\mathbf{K}$ entering equation is sparse. The assumption is made that non zero-entries in $\mathbf{K}[\mathcal{F}, :]$ are only in the submatrix $\mathbf{K}[\mathcal{F}, \mathcal{F} \cup \mathcal{I}]$ and these entries can be computed by using solely the reduced mesh that covers $\Omega_A$. This assumption is too strong in case of contact problems as shown in [11]. For the sake of simplicity, the focus of this article is, hereafter limited to contactless problems. The reader is refered to [11] for more details on hyper-reduction methods associated to contact problems.

The HR method is based on the equation (17) in the case that the variable $\mathbf{u}$ must be computed via a balance equation. In the following the balance equation (14) is considered. The hyper-reduced coordinates vector $\delta\boldsymbol{\gamma}$ is introduced such that $\delta\mathbf{u} = \mathbf{V} \cdot \delta\boldsymbol{\gamma}$. The values contained in this vector are weights for the modes of the reduced-base vector $\mathbf{V}$. The obtained hyper-reduced solution is a linear combination of the modes of the reduced base. The hyper-reduced problem consists in finding $\delta\boldsymbol{\gamma} \in \mathbb{R}^N$ such that $\delta\mathbf{u} = \mathbf{V}\, \delta\boldsymbol{\gamma}$ and:

$$\mathbf{V}[\mathcal{F}, :]^T \cdot \mathbf{K}[\mathcal{F}, \mathcal{F} \cup \mathcal{I}] \cdot \mathbf{V}[\mathcal{F} \cup \mathcal{I}, :] \cdot \delta\boldsymbol{\gamma} = -\mathbf{V}[\mathcal{F}, :]^T \cdot \mathbf{r}(\mathbf{u} + \Delta\mathbf{u}, \lambda_0)[\mathcal{F}]. \tag{22}$$

The hyper-reduced matrix and the hyper-reduced residual are given by:

$$\mathbf{K}^{HR} = \mathbf{V}[\mathcal{F}, :]^T \cdot \mathbf{K}[\mathcal{F}, \mathcal{F} \cup \mathcal{I}] \cdot \mathbf{V}[\mathcal{F} \cup \mathcal{I}, :], \tag{23a}$$

$$\mathbf{r}^{HR}(\mathbf{u}_0 + \Delta\mathbf{u}, \lambda) = \mathbf{V}[\mathcal{F}, :]^T \cdot \mathbf{r}(\mathbf{u}_0 + \Delta\mathbf{u}, \lambda)[\mathcal{F}]. \tag{23b}$$

Let us emphasize the following remarks:

- Formally, if $\mathbf{r} = -\delta\mathbf{u}$ and $\mathbf{K}$ is the identity matrix, then $\mathcal{I} = \emptyset$ and the HR balance equation is equivalent to the recovery equation of the Gappy POD.
- The matrix $\mathbf{V}[\mathcal{F}, :]^T$ in Equation (22) is related to the test functions $\boldsymbol{\psi}_k^Z = \sum_{i\in\mathcal{F}} \boldsymbol{\phi}_i V_{ik}$ for $k = 1, \dots N$. When introduced as a weak form of the hyper-reduced balance equations, it is emphasized that the test functions have a similar form that obtained for Dirichlet boundary conditions on the interface $\Gamma^I$. The reader is referred to [31] for more details about the boundary conditions used for hyper-reduced problems.

## 5. Hyper-reduced arc-length algorithm

The extension of the HR method to the Crisfield's algorithm is straightforward when choosing the same reduced base and the same RID for the two balance equations involved in the system of equations (10). This reduced base must be accurate enough for the approximation of both $\delta\mathbf{u}_t$ and $\delta\mathbf{u}_b$. Consider now the hyper-reduced external forces vector:

$$\mathbf{f}_{HR}^{ext} = \mathbf{V}[\mathcal{F}, :]^T \cdot \mathbf{f}^{ext}[\mathcal{F}]. \tag{24}$$

In the hyper-reduced arc-length problem, $\delta\boldsymbol{\gamma}_t \in \mathbb{R}^N$, $\delta\boldsymbol{\gamma}_b \in \mathbb{R}^N$ and $\delta\lambda$ are sought for such that $\delta\mathbf{u}_t = \mathbf{V} \cdot \delta\boldsymbol{\gamma}_t$, $\delta\mathbf{u}_b = \mathbf{V} \cdot \delta\boldsymbol{\gamma}_b$ and:

$$\begin{cases} \mathbf{K}^{HR} \cdot \delta\boldsymbol{\gamma}_t = \mathbf{f}_{HR}^{ext} \\ \mathbf{K}^{HR} \cdot \delta\boldsymbol{\gamma}_b = -\mathbf{r}^{HR}(\mathbf{u}_0 + \mathbf{V}\Delta\boldsymbol{\gamma}, \lambda_0 + \Delta\lambda) \\ \delta\boldsymbol{\gamma} = \delta\boldsymbol{\gamma}_b + \delta\lambda\, \delta\boldsymbol{\gamma}_t \\ (\Delta\boldsymbol{\gamma} + \delta\boldsymbol{\gamma})^T \cdot (\Delta\boldsymbol{\gamma} + \delta\boldsymbol{\gamma}) + \beta^2(\Delta\lambda + \delta\lambda)^2(\mathbf{f}^{ext\ T} \cdot \mathbf{f}^{ext}) = \Delta\ell^2, \end{cases} \tag{25}$$

where $\Delta\boldsymbol{\gamma}$ has been updated to $\Delta\boldsymbol{\gamma} + \delta\boldsymbol{\gamma}$, assuming the norm of $\mathbf{r}^{HR}(\mathbf{u}_0 + \mathbf{V} \cdot \Delta\boldsymbol{\gamma}, \lambda_0 + \Delta\lambda)$ is lower than a given tolerance. Here equation (25d) defines a reduced form of equation (8)

**Property:** If $\Delta\mathbf{u} = \mathbf{V}\cdot\Delta\gamma$, $\delta\mathbf{u} = \mathbf{V}\cdot\delta\gamma$ and $\mathbf{V}^T\cdot\mathbf{V} = \mathbf{I}$, then the solutions of equation (25d) and that of (8) are identical.

The above is a consequence of (8), which entails:

$$(\Delta\boldsymbol{\gamma} + \delta\boldsymbol{\gamma})^T \cdot \mathbf{V}^T \cdot \mathbf{V} \cdot (\Delta\boldsymbol{\gamma} + \delta\boldsymbol{\gamma}) + \beta^2(\Delta\lambda + \delta\lambda)^2(\mathbf{f}^{ext\ T} \cdot \mathbf{f}^{ext}) = \Delta\ell^2.$$

and reduce to the equation (25d) after replacing $\mathbf{V}^T \cdot \mathbf{V}$ by $\mathbf{I}$.

**Property:** If $\delta\mathbf{u}_t = \mathbf{V} \cdot \delta\gamma_t$, $\delta\mathbf{u}_b = \mathbf{V} \cdot \delta\gamma_b$, $\lambda$ are the exact solutions of equations (10) and (8), then $\gamma_t$, $\gamma_b$ and $\lambda$ are the solutions of the hyper-reduced arc-length equations (25).

Proof: If $\delta\mathbf{u}_t = \mathbf{V} \cdot \delta\gamma_t$, $\delta\mathbf{u}_b = \mathbf{V} \cdot \delta\gamma_b$ and $\lambda$ are the exact solutions of the original equations, then:

$$\begin{aligned}
\exists\Delta\gamma: \quad \Delta\mathbf{u} &= \mathbf{V}.\Delta\gamma, && \text{(26a)}\\
\mathbf{K}[\mathcal{F}, \mathcal{F}\cup\mathcal{I}].\mathbf{V}[\mathcal{F}\cup\mathcal{I}, :]\delta\gamma_t &= \mathbf{f}^{ext}[\mathcal{F}], && \text{(26b)}\\
\mathbf{K}[\mathcal{F}, \mathcal{F}\cup\mathcal{I}]\mathbf{V}[\mathcal{F}\cup\mathcal{I}, :]\delta\gamma_b &= -\mathbf{r}(\mathbf{u} + \Delta\mathbf{u}, \lambda_0 + \Delta\lambda)[\mathcal{F}], && \text{(26c)}\\
\delta\boldsymbol{\gamma} &= \delta\gamma_b + \delta\lambda\,\delta\gamma_t, && \text{(26d)}\\
(\Delta\boldsymbol{\gamma} + \delta\boldsymbol{\gamma})^T \cdot (\Delta\boldsymbol{\gamma} + \delta\boldsymbol{\gamma}) &= \Delta\ell^2 - \beta^2(\Delta\lambda + \delta\lambda)^2(\mathbf{f}^{ext\ T} \cdot \mathbf{f}^{ext}). && \text{(26e)}
\end{aligned}$$

According to the above, the hyper-reduced arc-length equations (25) are fulfilled by $\delta\gamma_t$, $\delta\gamma_b$ and $\delta\lambda$.

Let us now investigate the computational complexity of the proposed method. The later does not scale proportionally to $\mathcal{N}$, as a finite element model would do. Instead, $\mathbf{K}^{HR}$ being a full matrix, the solution of hyper-reduced linear systems has a computational complexity proportional to $N^3$. So in order to achieve a good speed up of the method it is necessary to have $N^3 \ll \mathcal{N}$. Moreover, for a given residual $\mathbf{r}$, the computation of $\mathbf{r}^{HR}$ has a complexity proportional to $N$ card$(\mathcal{F})$, where card$(\mathcal{F})$ is the number of elements of $\mathcal{F}$ whereas, for a given Jacobian matrix $\mathbf{K}$, that of $\mathbf{K}^{HR}$ is proportional to $N^2$ card$(\mathcal{F})$ + $N$ card$(\mathcal{F})$ [card$(\mathcal{F})$ + card$(\mathcal{I})$]. Eventually, the residual $\mathbf{r}[\mathcal{F}]$ and the Jacobian matrix $\mathbf{K}[\mathcal{F}, \mathcal{F}\cup\mathcal{I}]$ are computed over the RID. The lower the value of $N$ and card$(\mathcal{F})$, the lower the computational complexity of the hyper-reduced arc-length equations.

Section 6 investigates the constructions of the reduced bases in the following cases:

- (i): Vector $\mathbf{Q}$ contains the simulation data related to $\mathbf{u}$ solely;
- (ii): in $\mathbf{V}$ two reduced bases, generated for $\mathbf{u}_t$ and $\mathbf{u}_b$ separately, are merged;
- (iii): in $\mathbf{Q}$ the simulation data related to $\mathbf{u}_t$ and $\mathbf{u}_b$ are merged, before computing $\mathbf{V}$.

## 6. Numerical results and discussion

### *6.1. Hyper-elastic buckling*

In the sequel the finite element simulation of structures subjected to post-buckling is considered (see [38, 39] for details about post-buckling). This section demonstrates the robustness of the hyper-reduced arc-length method through a simple example in the framework of finite elastic strains. Focus is made on reduced-matrices $\mathbf{K}^{HR}$ when it is ill-conditioned.

Let us consider the highly-nonlinear buckling beam problem subjected to plain strain loading. The beam is parameterized by its slenderness, i.e. the ratio of length over height. The length is kept constant ($L = 200$ mm) and the slenderness is monitored by the height $\mu \in [8, 14]$. A morphing is applied to a reference mesh so as to generate a geometry corresponding to a given slenderness. The position vector $\mathbf{x}$ reads, accordingly:

$$\mathbf{x} = \left\{ \begin{array}{c} x_1 \\ \mu x_2 \end{array} \right\}, \tag{27}$$

where $x_1 \in [0, L]$(mm) and $x_2 \in [0, 1]$(mm) are coordinates in the reference mesh. The mesh is made of 295 linear elements (720 DOFs). The beam is fully clamped on one of its extremity while a pressure is applied on the opposite side, as shown in Figure 2.

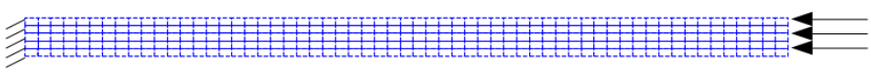

Figure 2: Meshed beam and boundary conditions.

The Young modulus for this simulation is $E = 210000$ MPa and the Poisson coefficient $\nu = 0.3$. The material follows the hyper-elastic Saint-Venant-Kirchhoff model:

$$\begin{cases} \text{Deformation gradient tensor:} & \underset{\sim}{F} = \underset{\sim}{I} + \underset{\sim}{\nabla} \boldsymbol{v} \\ \text{Green-Lagrange strain tensor:} & \underset{\sim}{E} = \frac{1}{2}(\underset{\sim}{F}^T \cdot \underset{\sim}{F} - \underset{\sim}{I}) \\ \text{Constitutive law:} & \underset{\sim}{S} = \underset{\sim\sim}{\mathbb{C}} : \underset{\sim}{E} \\ \text{Cauchy stress:} & \underset{\sim}{\sigma} = \det^{-1}(\underset{\sim}{F})\ \underset{\sim}{F} \cdot \underset{\sim}{S} \cdot \underset{\sim}{F}^T \\ \text{Internal forces:} & f_i^{int} = \int_\Omega \frac{1}{2}(\underset{\sim}{\nabla} \boldsymbol{\phi}_i + \underset{\sim}{\nabla}^T \boldsymbol{\phi}_i) : \underset{\sim}{\sigma}\, d\Omega, \qquad i = 1, \dots \mathcal{N}, \end{cases} \tag{28}$$

where $\Omega$ denotes the current configuration. Simulation data for the training phase are generated for four sampling points in the parameter space: $\mu = 8$, 9, 10, 11. In the HR method it is common to make one single SVD on one global snapshot matrix that contains all the simulation results. Use is made of four simulations to apply separately a singular value decomposition on each of them hence four reduced bases are created. The resulting bases are then concatenated with each other without orthogonalization to create the reduced base:

$$\mathbf{V} = [\mathbf{V}^{(1)}, \mathbf{V}^{(2)}, \mathbf{V}^{(3)}, \mathbf{V}^{(4)}]. \tag{29}$$

Since the bases $\mathbf{V}^{(i)}$ are not orthogonal to each other, $\mathbf{V}$ is not orthogonal. Moreover $\mathbf{V}$ contains modes that are very similar to each other since the geometrical parameters are not too far from each others, and therefore the hyper-reduced tangent matrix $\mathbf{K}^{HR}$ is nearly singular. Nevertheless, the ill-conditioned system is kept as it is, to underline the robustness of the approach. If a linear system is ill-conditioned its response will vary a lot with respect to a small perturbation in the data. Let us consider a linear system with a positive-definite square matrix $\mathbf{A}$, a vector $\mathbf{b}$ and the unknown vector $\mathbf{u}$. If $\mathbf{A} \cdot \mathbf{u} = \mathbf{b}$ and $\mathbf{A} \cdot \mathbf{u}' = \mathbf{b}'$ one obtains, with $\Delta\mathbf{u} = \mathbf{u}' - \mathbf{u}$ and $\Delta\mathbf{b} = \mathbf{b}' - \mathbf{b}$:

$$\frac{||\Delta\mathbf{u}||_2}{||\mathbf{u}||_2} \leq \kappa(\mathbf{A}) \frac{||\Delta\mathbf{b}||_2}{||\mathbf{b}||_2}, \tag{30}$$

where the condition number $\kappa(\mathbf{A})$ is defined by:

$$\kappa(\mathbf{A}) = ||\mathbf{A}||_2 \times ||\mathbf{A}^{-1}||_2 = \frac{\sigma^A_{max}}{\sigma^A_{min}}, \tag{31}$$

and $\sigma^A_{max}$, $\sigma^A_{min}$ are the highest (respectively, the lowest) eigenvalue of $\mathbf{A}$. The bigger the condition number, the less precise the solution ($\mathbf{u}$ in this case) will be.

Herefater, the DEIM is applied on the global reduced base $\mathbf{V}$ in order to select the nodes of the RID, enforcing $\mathcal{F} = \mathcal{P}$. In the following example no stress base was created. In the online test, the height takes on the value $\mu = 13.2$ mm. The reduced buckling beam at the end (red) and in initial position (blue) are shown in Figure (3).

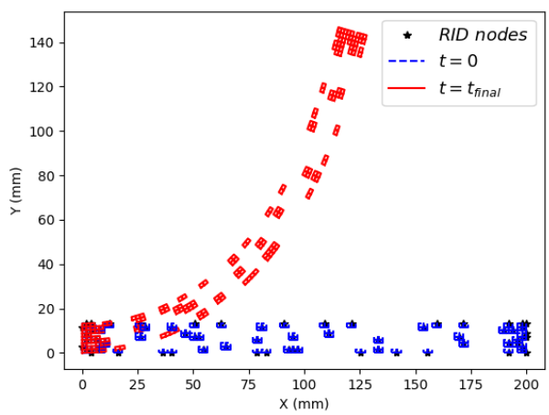


Figure 3: Hyper-reduced model at $t = 0$ (blue) and at t=$t_{final}$ in red, for height $\mu = 13.2$ mm.

Here, the RID corresponds exactly to the elements attached to the selected node by the DEIM ($\mathcal{F} = \mathcal{P}$). The vertical displacement of the node at the bottom right, denoted M is plotted in Figure 4 as a function of the applied load. The nonlinear response due to buckling appears for a limit load equal to 1250 N and 1200 N when the FOM and the HROM are used, respectively. To check the accuracy of the proposed hyper-reduced arc-length algorithm, a FOM is run with the same parameter. The FOM and HROM

responses are shown in Figure (4a). The exact error on the total displacement field is calculated by the quantity :

$$\eta = \frac{||\mathbf{u}_{HROM} - \mathbf{u}_{FOM}||_2}{||\mathbf{u}_{FOM}||_2}. \tag{32}$$

The later is represented in Fig. (4b).

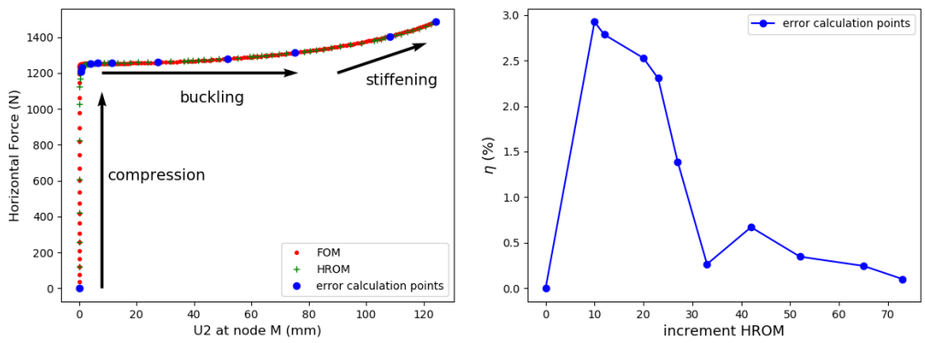


(a) (b)

Figure 4: (a) Load [N], as a function of the vertical displacement [mm] at point M, with $\mu = 13.2$. (b) Error estimate (%) as a function of the increments of the HROM simulation.

It has been observed that the condition number of $\mathbf{K}^{HR}$ evolves during the simulation, but remains very large (around $10^{16}$), and, accordingly, $\mathbf{K}^{HR}$ is nearly singular. The robustness of the algorithm is warranted by the additional ellipse equation (25d) which prevents the divergence of the response since the latter must be contained within in the circle. Furthermore, for every loading increment the error stays between 0.1% and 2.9%. The largest error is observed when buckling occurs. Even in such strongly-nonlinear problem with ill-conditioned tangent matrix, convergence is obtained after a few iterations at each loading increment. These numerical results emphasize the robustness of the proposed hyper-reduced arc-length algorithm.

### *6.2. Limit load prediction for a simple elasto-plastic problem*

To illustrate the assets of hyper-reduced arc-length algorithm one proposes a nonlinear problem that involves finite strains and plasticity. Let's consider a 3D thick wall pipe under internal pressure with a pure plastic behaviour. The material constitutive equations are given below:

$$\left\{\begin{array}{rl}
\text{Strain gradient decomposition:} & \underset{\sim}{F} = \underset{\sim}{R}.\underset{\sim}{U} \\
\text{Deformation rate:} & \underset{\sim}{L} = \dot{\underset{\sim}{F}}.\underset{\sim}{F}^{-1} \\
\text{Stretch rate:} & \underset{\sim}{D} = \frac{1}{2}(\underset{\sim}{L} + \underset{\sim}{L}^{-T}) \\
\text{Local strain rate:} & \dot{\underset{\sim}{e}} = \underset{\sim}{R}^{T}.\underset{\sim}{D}.\underset{\sim}{R} \\
\text{The elastic/plastic partition is supposed:} & \underset{\sim}{e} = \underset{\sim}{e}^{e} + \underset{\sim}{e}^{p} \\
\text{Constitutive law:} & \underset{\sim}{S} = \underset{\approx}{\mathbb{C}} : \underset{\sim}{e}^{e} \\
\text{Relation with global Cauchy stress:} & \underset{\sim}{\sigma} = \det^{-1}(\underset{\sim}{F})\ \underset{\sim}{R}.\underset{\sim}{S}.\underset{\sim}{R}^{T} \\
\text{Second invariant of the stress tensor :} & J_2(\underset{\sim}{\sigma}) = \sqrt{\frac{3}{2}\ dev(\underset{\sim}{\sigma}) : dev(\underset{\sim}{\sigma})} \\
\text{Yield stress:} & R_0 \\
\text{Yield function:} & f(\underset{\sim}{\sigma}, R) = J_2(\underset{\sim}{\sigma}) - R_0 \\
\text{Internal forces:} & f_{int\,i} = \int_\Omega \frac{1}{2}(\underset{\sim}{\nabla}\boldsymbol{\phi}_i + \underset{\sim}{\nabla}^{T}\boldsymbol{\phi}_i) : \underset{\sim}{\sigma}\, d\Omega,\ i = 1, \dots \mathcal{N}
\end{array}\right. \tag{33}$$

The Young modulus used for this simulation is $E = 200000$ MPa, the Poisson coefficient is $\nu = 0.3$ and the elasticity limit is $R_0 = 400$ MPa. As it can be seen in the material constitutive equations give before there is no hardening in this example. The considered pipe is fully clamped on each side and undergo internal pressure.

In the present work, a parametric study is conducted by varying the geometric parameters and determining the pipe's critical pressure. The pipe length is fixed hereafter to $L = 300$mm whereas the thickness and external radius vary. The full-order model is made up of $9,180$ linear hexahedra ($\mathcal{N} = 37,536$ DOF, see Fig. 5) and an updated Lagrangian formulation is used.

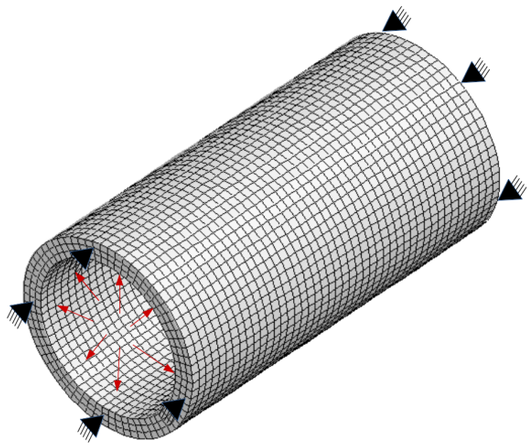

Figure 5: Meshed pipe with boundary conditions.

As announced in section (5), two linear systems are solved for a given linearized residual. Many choices for the reduced base are possible. The snapshot matrices $\mathbf{Q}$, $\mathbf{Q}_t$ and $\mathbf{Q}_b$ contain, respectively, the solution $\mathbf{u}$, $\mathbf{u}_t$ and $\mathbf{u}_b$ for each point in $\mathcal{D}_{train}$, and at any time the equilibrium path is reached. Hereafter, results obtained for three different reduced bases $\mathbf{V}_A$, $\mathbf{V}_B$ and $\mathbf{V}_C$ are compared. The later are constructed as follow:

$$\text{reduced base } \mathbf{V}_A: \quad \left\{ \mathbf{Q} = \mathbf{V}_A.\mathbf{\Sigma}_A.\mathbf{W}_A^T + \mathbf{R}_A, \quad \|\mathbf{R}_A\|_2^2/\|\mathbf{Q}\|_2^2 < \epsilon_{tol}, \right. \tag{34a}$$

$$\text{reduced base } \mathbf{V}_B: \quad \left\{ \begin{array}{rcll} \mathbf{Q}_t & = & \mathbf{V}_t.\mathbf{\Sigma}_t.\mathbf{W}_t^T + \mathbf{R}_t, & \|\mathbf{R}_t\|_2^2/\|\mathbf{Q}_t\|_2^2 < \epsilon_{tol}, \\ \mathbf{Q}_b & = & \mathbf{V}_b.\mathbf{\Sigma}_b.\mathbf{W}_b^T + \mathbf{R}_b, & \|\mathbf{R}_b\|_2^2/\|\mathbf{Q}_b\|_2^2 < \epsilon_{tol}, \\ \mathbf{V}_B & = & [\mathbf{V}_t,\ \mathbf{V}_b], & \end{array} \right. \tag{34b}$$

$$\text{reduced base } \mathbf{V}_C: \quad \left\{ \begin{array}{rcll} \mathbf{Q}_{tb} & = & [\mathbf{Q}_t,\ \mathbf{Q}_b], & \\ \mathbf{Q}_{tb} & = & \mathbf{V}_C.\mathbf{\Sigma}_C.\mathbf{W}_C^T + \mathbf{R}_C, & \|\mathbf{R}_C\|_2^2/\|\mathbf{Q}_{tb}\|_2^2 < \epsilon_{tol}. \end{array} \right. \tag{34c}$$

Four offline classical finite element simulations are carried out with different values of thickness and external radius. An online target simulation is defined with another couple (thickness, external radius). This online simulation is performed three times with the three different reduced bases $\mathbf{V}_A$, $\mathbf{V}_B$ and $\mathbf{V}_C$. Table (1) gives the parameter values used in the simulations. The later follow the thickest pipes for deep offshore. It is emphasized that the online simulation lies beyond the parametric-training region.

| | External radius (mm) | Thickness(mm) |
|---|---|---|
| Offline | 75 | 15 |
| Offline | 80 | 20 |
| Offline | 80 | 15 |
| Offline | 75 | 20 |
| *Online* | *70* | *10* |

Table 1: Parameters for offline ($\mathcal{D}_{train}$) and online simulations

A criterion is now introduced in order to stop the numerical simulations and to estimate the critical pressure. As a rule, the computation of the equilibrium path is stopped whenever the pressure has decreased by more than 4% from its maximum value. Figure (6) shows the local pressure as a function of the norm of the displacement along an arbitrary node in the middle of the plane.

The red and blue arrows spot the values of the critical pressure and the corresponding displacement for a point on the external skin of the pipe in the mid-plane. The values are respectively for the FOM simulation : (0.9 mm ; 115,4 MPa) and HROM simulation : (1,3 mm ; 114,94 MPa). The error is estimated after the simulation has been completed. In order to have the exact error, a FOM simulation with the same parameters as used in the HROM simulation is carried out. Maps of the displacement component $U_1$ is shown in Figure 7 as computed in the RID and along the full mesh. The small part of the reduced mesh on the left of the image contains the point used to plot the loading curve in Figure 6. Details about the construction of the RID are given in appendix 9. It is emphasized that the construction of the RID is empirical and depends on the considered problem.

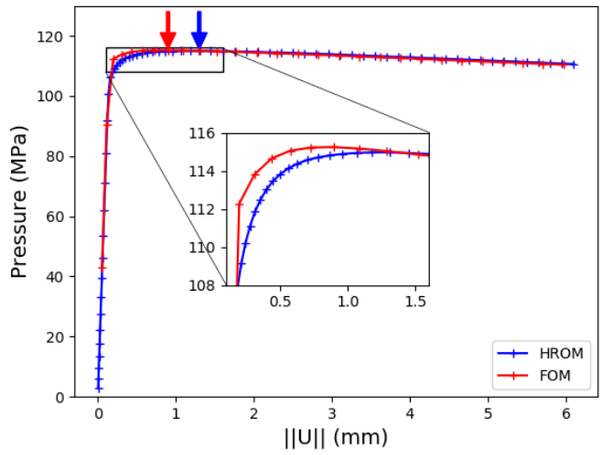


Figure 6: Internal pressure (MPa) as a function of the norm of the displacement (mm) of a node in the middle plane (offline in blue and online in red). Computation carried out using the reduced base matrix $\mathbf{V}_B$. The limit load is indicated by the arrow.

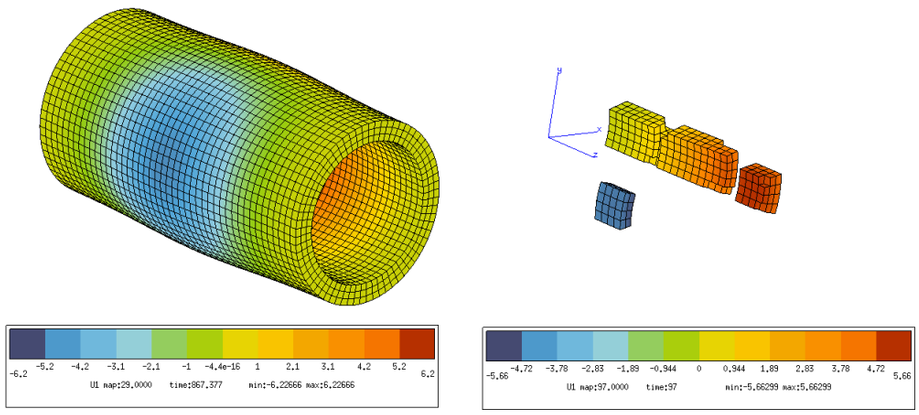

(a) (b)

Figure 7: Displacement component $U_1$ (mm) computed on the full mesh (a) and on the RID (b) using the reduced base matrix $\mathbf{V}_B$.

In the following, the absolute error relative to the displacement $U_1$ is defined by:

$$\varepsilon^{U_1} = \max\left\{\frac{|\mathbf{U_1}^{HROM} - \mathbf{U_1}^{FOM}|}{\max|\mathbf{U_1}^{FOM}|}\right\}, \tag{35}$$

where the max operator in the denominator has been introduced to take into account the fact that $U_1$ might be zero. Similar error criteria are considered for the other displacement and stress components. Table 2 reports the errors for the 3 displacement components and the six stress components, for each of the three reduced bases, i.e. $\mathbf{V}_A$, $\mathbf{V}_B$ and $\mathbf{V}_C$. The values in bold, corresponding to the most accurate computations, indicate that base $\mathbf{V}_A$ gives the best results as compared to the two other bases, while also using standard simulation outputs. Therefore, the construction method for this base is used in the rest of this work.

| | $\mathbf{V}_A$ | $\mathbf{V}_B$ | $\mathbf{V}_C$ |
|---|---|---|---|
| $N$ | **8** | 11 | 9 |
| $\text{card}(\mathcal{F})$ | **1 830** | 2 985 | 3 009 |
| $\varepsilon^{U1} = \varepsilon^{U2}$ | 3.80% | 1.91% | **0.45**% |
| $\varepsilon^{U3}$ | **3.84**% | 4.17% | 4.81% |
| $\varepsilon^{\sigma^{11}} = \varepsilon^{\sigma^{22}}$ | **3.46**% | 7.63% | 10.64% |
| $\varepsilon^{\sigma^{33}}$ | **2.75**% | 6.61% | 6.69% |
| $\varepsilon^{\sigma^{31}} = \varepsilon^{\sigma^{32}}$ | **5.63**% | 9.94% | 9.97% |
| $\varepsilon^{\sigma^{12}}$ | **5.63**% | 16.44% | 19.05% |

Table 2: Error relative to the displacement and stress components, for different constructions of the reduced base.

*6.3. Greedy sampling and validity domain for a realistic problem*

In this subsection, a parametric study is carried out on an elbowed pipe. Many studies have been carried out on elbow pipes [22, 23, 40]. The geometric parameters are chosen according to the work of [22]. This study focuses on determining the critical internal pressure this structure can sustain. Compare to the previous problem, the geometry as well as the mesh and boundary conditions are modified. Four geometric parameters are considered: the thickness $e$, the external radius $R_{ext}$, the curvature radius $r_{curv}$ and the angle of elbow $\alpha$. As in the previous section a morphing method is used to modify the mesh. A sensitivity-analysis of each parameter is carried out by varying each value of $\pm 5\%$ (see Table 3). The mesh used in this study has $16,000$ linear 8-nodes elements resulting in $24,633$ nodes and $\mathcal{N} = 73,899$ DOFs. Both symmetries of the problem have been taken into account hence only one quarter of the pipe is considered. The mesh is represented in Figure 8. Additionally, an error indicator developped in the context of small strain [41] is coupled with a greedy algorithm in order to reduce the amount of training data. In small strain setting, the equilibrium equation is a linear equation and is fulfilled, in its weak form, by the stress computed during the offline phase. It turns out that the related reduced bases $\mathbf{V}^\sigma$ is a convenient subspace for stresses. For problems in the more general context of finite strain, the equilibrium equation strongly depends on the displacement in the domain $\Omega$ and is a nonlinear equation. Nevertheless, it is assumed in the following that the training set $\mathcal{D}_{train}$ is large enough, and is able to represent accurately both the displacement fields and the stress field via their respective reduced bases $\mathbf{V}$ and $\mathbf{V}^\sigma$.

| $R_{ext}$ (mm) | $r_{curv}$ (mm) | $e$ (mm) | $\alpha$ (°) |
|---|---|---|---|
| 39.9 | 114 | 4.75 | 42.75 |
| 44.1 | 126 | 5.25 | 47.25 |

Table 3: Range of geometrical parameters, for the training set of simulation data.

In the following, consistency criteria are introduced and used as error indicator for the sampling of the parameter space by a greedy algorithm. Each time a hyper-reduced arc length simulation predicts a displacement by using $\mathbf{V}$, the projection on $\mathbf{V}^\sigma$ of the related stresses is expected to yield an accurate solution. The error indicator is accordingly defined by:

$$\varepsilon^* = \min_{\boldsymbol{\gamma}^*} \frac{||\sigma^{HR} - \mathbf{V}^\sigma[\mathcal{F},:] \cdot \boldsymbol{\gamma}^*||_2}{||\sigma^{HR}||_2}, \tag{36}$$

$$\text{achieved with:} \quad \boldsymbol{\gamma}^* = \left(\mathbf{V}^\sigma[\mathcal{F},:]^T \cdot \mathbf{V}^\sigma[\mathcal{F},:]\right)^{-1} \cdot \mathbf{V}^\sigma[\mathcal{F},:]^T \cdot \sigma^{HR}, \tag{37}$$

where $\boldsymbol{\gamma}^*$ is the reduced coordinate vector related to the Gappy POD applied to the stress. This vector minimizes the gap between the stress field obtained with the hyper-reduced arc length simulation, $\sigma^{HR}$, and the its projection on $\mathbf{V}^\sigma$ over the RID. The product $\mathbf{V}^\sigma \cdot \boldsymbol{\gamma}^*$ is the recovered stress over $\Omega$ related to the Gappy POD. Because of the finite strains involved in the equilibrium path, we have not established a formal relationship between the error indicator and the true error on the displacements. But this relationship exists for standard materials undergoing small deformations [41]. A greedy algorithm is accordingly applied to construct the global reduced base (see [11]):

(i) the sampling point in the parameter space for which the error is maximal is first obtained, according to the error estimator based on the HR simulation;

(ii) second, the FOM simulation data relative to this point is included in the training set for the global reduced base, and the reduced base is computed again;

(iii) hyper-reduced predictions and error predictions are then performed for all sampling points.

Note that the first sampling point in the parameter space is the center of the hyper-cube.

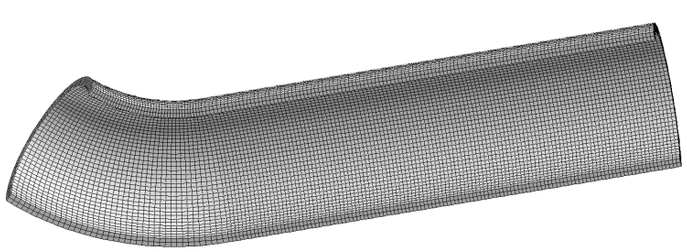

Figure 8: Elbowed pipes meshed.

The parametric space is regularly sampled on a $m \times m \times m \times m$ grid where $m$ is the number of values each parameter can take. In the present case, $m = 2$ generating 16 simulations to which is added the first sampling point at the center of the hyper-cube resulting in 17 simulations. After applying five times the greedy algorithm, five FOM simulations are added to the training set. The 12 other hyper-reduced simulations where thus required to certify the model. The 12 related simulation data are denoted validation data in the following. Figure (9) shows the evolution of the error indicator during the iterations of the greedy algorithm. The training set that is selected with this method is indicated by the black numbers.

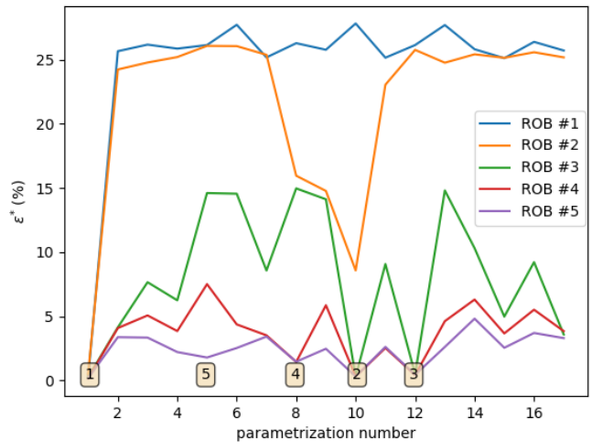


Figure 9: Error indicator for the different hyper-reduced arc length simulations over the sampling point of the parameter space, where the ROB number $i + 1$ is obtained after the $i^{th}$ iteration of the greedy algorithm. The brown squares with numbers inside indicate the sampling point inserted in the training set $\mathcal{D}_{train}$ and their iteration index.

.

The greedy algorithm is found to be very efficient. No more than five iterations of the algorithm are needed in the present study, resulting in a global error of less than 5%. The resulting RID is composed of $8,511$ nodes. The last reduced base $\mathbf{V}$ contains $N = 27$ empirical modes, with $\epsilon_{tol} = 1e^{-8}$ and $N^3 < \mathcal{N}$. The reduced base $\mathbf{V}^\sigma$ contains 50 empirical modes. The RID construction, shown in Figure 10, follows the procedure in Appendix 9. The resulting HROM is denoted HROM5-27-50 in the the following. As expected, plasticity localizes at the curvature where stress concentration occurs. Note that the obtained RID is rather large compared to the one that is usually seen with standard hyper-reduction methods. This should be explained by the loss of ellipticity in the equations, encountered in limit load problems.

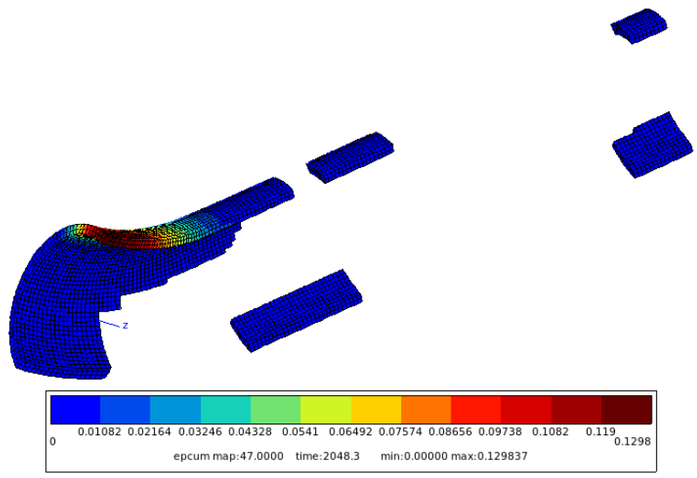


Figure 10: Cumulated plasticity on the RID of the elbowed pipe.

The error indicator is now compared with one based on the full-order model prediction, in order to investigate its reliability. This time, the simulation of the loading path stops when a decrease of 1% of the pressure is observed, compared its maximal value. Note however that a small error on the limit load estimate may induce a much larger error on the displacement. Therefore, displacement fields are compared according to their angle

with the solution obtained with the FOM. The later reads:

$$\Theta = \cos^{-1}\left\{\frac{\left(\mathbf{u}^{HR}[\mathcal{F}]\right)^T \cdot \mathbf{u}^{FOM}[\mathcal{F}]}{||\mathbf{u}^{HR}[\mathcal{F}]||_2||\mathbf{u}^{FOM}[\mathcal{F}]||_2}\right\} \in [0, \frac{\Pi}{2}]. \tag{38}$$

The angle $\Theta$ is computed for each of the 17 simulations as it is necessary to evaluate the error estimator. The correlation between $\Theta$ and $\varepsilon^*$, show a linear relation between $\Theta$ and $\varepsilon^*$, except for two points are far from the zone of interest delimited by an error of 25% (see Figure 11). The computation of the error angle $\Theta$ requires all FOM simulations, contrary to the error estimator $\varepsilon^*$. For the later, a reduced base on the stress field is sufficient. Therefore, this error estimator will be used in the rest of this work. Using HROM5-27-50, one may now carry out HROM calculations on a finer grid of the parameter space. The parametric space is re-sampled along a $3\times3\times3\times3$ grid, resulting in 81 HROM simulations and to the error map represented in Figure (12).

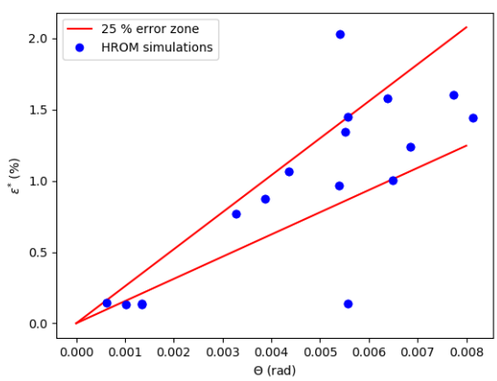


Figure 11: Error indicator $\Theta$ (rad) versus error estimator $\varepsilon^*(\%)$ on the 17 HROM simulations.

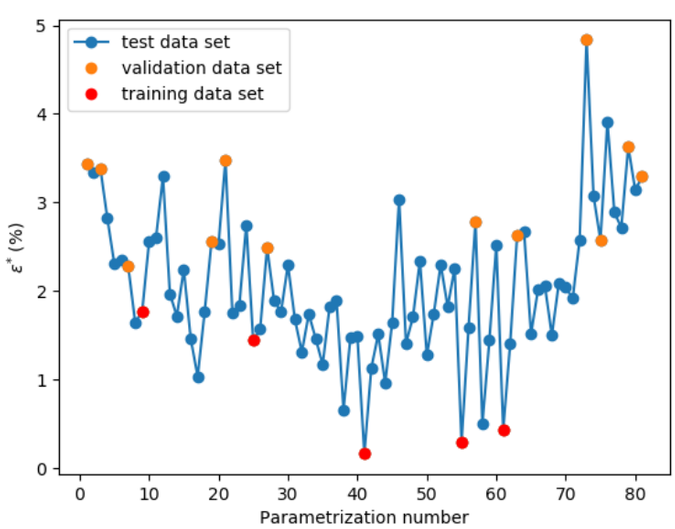


Figure 12: Error estimate $\varepsilon^*$ for the 81 HROM simulations. The red dots represent the training data set used to created the reduced base, the orange dots are the validation data set used to certify our model and the blue dots are the test data set.

The global minimum of the error estimate is a simulation from the training set and the global maximum is a simulation from the validation data set. The values of the parameters for the test data set lie between the minimum and maximum values of the parameters in the validation data set. The error indicator is inferior to 5%, highlighting how accurate is the hyper-reduced model for the interpolation. Then one can continue the stability analysis with the so developped hyper reduced model (HROM5-27-50). The most sensitive parameter is determined using the parallel coordinate plot method [42]. A parallel coordinate plot is introduced (Figure 13). The four first coordinates are relative to the parameters (thickness, external radius etc.) whereas the last one is the simulation output of interest (i.e. the critical pressure). The red lines in Figure (13a) are related to sampling points in the parameter space which lead to a high critical pressure, in the present case $P_c^{max}$ $+0\%$ $-2.5\%$. If all red lines intersect at the same parameter value,

for a specific set of parameters, that parameter is strongly sensitive with respect to the simulation output. According to graph (13a), the external radius as well as the thickness are the parameters most sensitive to the highest critical pressure. Obviously, a small external radius and a big thickness. results in a high critical pressure, as shown by the red lines in Fig. (13a)). To estimate how robust the proposed model is, a coordinate plot is represented, again, in Fig. (13b) to determine which parameter influence the error indicator the most. The map is defined by relative variations of $+0\% - 25\%$ on the outputs. The external radius, the thickness and the radius of curvature influence most the error indicator. The external radius and the radius of curvature are not independent in the chosen parametrization. Indeed the curvature radius is defined according to the middle line of the pipe. Therefore the larger the external radius, the smaller the radius of curvature of the upper skin of the pipe.

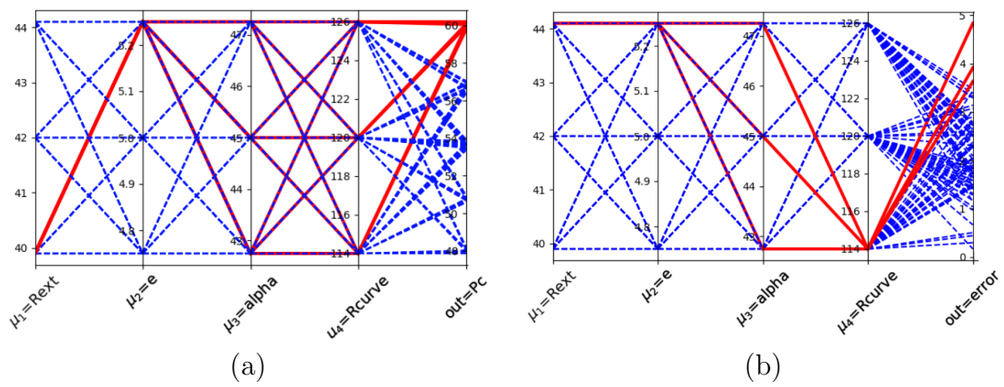


(a) (b)

Figure 13: Parallel coordinates plots. Each axis represents a parameter except for the output, indicated last one on the right along the $x$-axis. (a) Critical pressure. (b) Error estimate.

The training set is made of five FOM simulations. Denoting $CPU_{FOM} = 5672$s the computational time of the FOM simulations, and $CPU_{HR} = 1035$s that of the HROM simulations, the speed-up, defined by:

$$\text{speed-up} = \frac{CPU_{FOM} \times 81}{CPU_{HR} \times 81 + CPU_{FOM} \times 5}, \tag{39}$$

is about 4.1, slightly lower than the direct speed up : $CPU_{FOM}/CPU_{HROM} = 5.48$.

By varying the thickness and the radius of curvature and fixing the others parameters to $Rext = 42mm$ and $\alpha = 45$ °, a domain of validity is defined, where the error indicator is inferior to 10%. In that case, the hyper-reduced model HROM5-27-50 does not only interpolate but also extrapolate training data. A variation of $\pm 25\%$ of the thickness and of the curvature radius is applied and the parametric space is divided in a grid of $10 \times 10$ points, resulting in 100 HROM simulations. Figure (14) shows that the HROM model has a quite a large validity domain in spite of its construction, which uses only 5 high fidelity simulations.

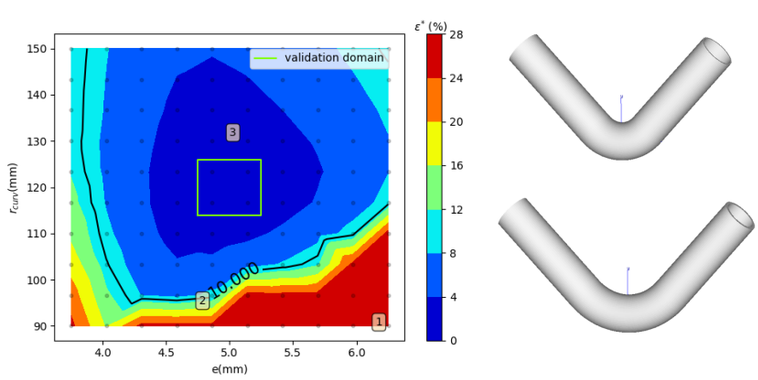


(a) (b)

Figure 14: Map of the error estimate for the hyper-reduced model with isocontour equal to 10%, for varying curvature radius and thickness. Each black point in the background represents a HROM simulation and the green square represents the domain of the validation dataset (on the left). Representation of the pipe with minimum and maximum values of both parameters simultaneously (on the right).

The parameters for three test points in the parameter space, indicated on Figure 14.a, are given in table 4. The error on the von Mises stress corresponding to the three test points indicated by the black numbers in Figure 14.a may be calculated on each Gauss

| Number | $r_{curv}$ (mm) | $e$ mm) |
|---|---|---|
| 1 | 90 | 6.25 |
| 2 | 96.66 | 4.86 |
| 3 | 130 | 5.13 |

Table 4: Set of parameters of the three simulations indicated in Figure 14

point of the RID and of the full mesh, once the gappy POD has been applied to stresses. A reference computation has been carried out with the FOM for these three configurations. The correlation curves for stress predictions are shown in Figure (15).

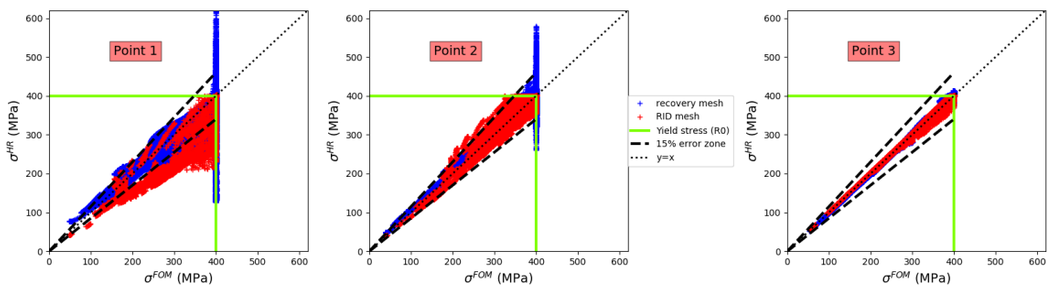


Figure 15: Error for the von Mises stress, for test points 1, 2, 3 in the parameter space (table 4). Each marker represents a gauss point, the $x$-axis is the reference value and the $y$-axis the value computed with the hyper-reduced method. Red points are related to the prediction in the RID. Blue points are related to the gappy POD for the stress recovery over $\Omega$.

As shown in Figure (15), the prediction of the equivalent stress on the RID is more accurate than on the full mesh. Outside the RID, the gappy POD gives stresses that violate the limit $R_0$ enforced by perfect plasticity. In the RID, the stresses are obtained by integrating the constitutive relations. Therefore they are plastically admissible. These results confirm that the proposed error indicator is relevant in this example. In order to show the robustness of the HROM5-27-50 model, variations of the two other parameters (external radius and angle) have also been considered. Constant values have been given to the curvature radius (120mm) and the thickness (5mm). As previsously, the parameters vary within $\pm 25\%$ and the parametric space is divided in a grid of $10 \times 10$ points. The assumed validity domain given by an error indicator less than 10% is once again quite large, which shows the robustness of the hyper-reduced arc length method (Fig. 16).

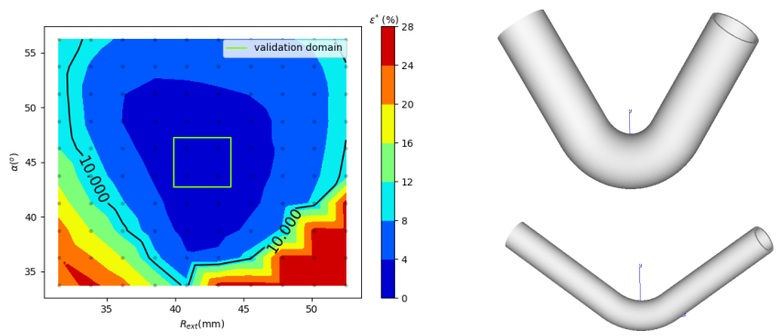


(a) (b)

Figure 16: Map of the error estimate for the hyper-reduced model with isocontour equal to 10% for varying external radii and angles (a). Each black point in the background represents a HROM simulation and the green square represents the domain of the validation dataset. (b) Representation of the pipe with minimum and maximum values of both parameters simultaneously.

## 7. Speed-up

The previous simulations have been carried out on 24 processors. In the HR simulations, most of the CPU time is spent for the integration of the material constitutive law and the computation of the internal reactions. The later represents 77% of the computational time while the construction of the hyper-reduced matrix represents 2% and the solving time of the linear system represents 3%. The rest of the time is used for other tasks. Accordingly, the size of the RID plays an important role on the speed-up. This shows the robustness of the method despite the moderate speed-up, equal to 5.5.

In order to increase the speed-up less modes in the HR model have been used, as well as less RID elements. In the present section, a hyper-reduced model, denoted HROM5-9-73 created with the 5 FOM simulations and made of 9 displacement modes, 73 stress modes modes and a RID of 8,694 DOFs is considered. This model is used to simulate the problem represented by point 2 in Figure (14). Figure (17) shows the RID now used, to be compared with that of HROM5-27-50 (Figure 10). The much-reduced RID contains $2,898$ nodes instead of $8,511$ nodes as in HROM5-27-50. Numerical investigations show that the speed-up now equals 14.5. Enhancing the speed-up, however, leads to a larger error. With model HROM5-9-73 is around 30% instead 15% for model HROM5-27-50. Although the error of the stress field is twice larger, the error on the estimate for the limit load (about 47.1MPa with the FOM model) is less than 1%.

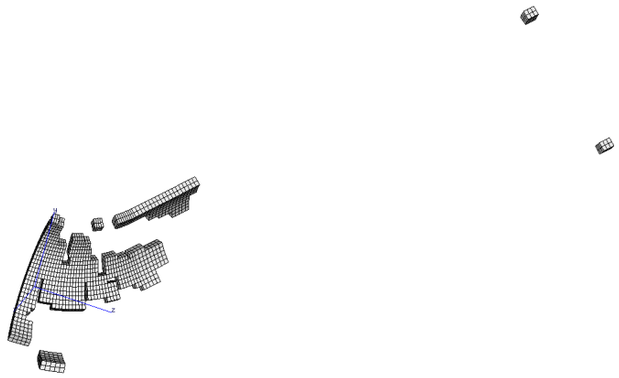

Figure 17: RID of HROM5-9-73.

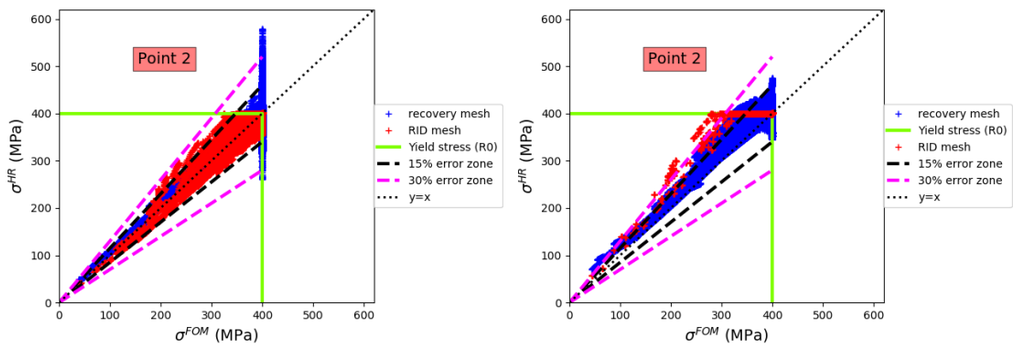


Figure 18: Error on the von Mises stress, for test points 2 in the parameter space. Each marker of the following graph represents a gauss point, the $x$-axis represents the reference value and the $y$-axis the value computed with the proposed method. Red point are related to the prediction in the RID. Blue points are related to the gappy POD for the stress recovery over $\Omega$. (a) HROM5-27-50. (b) HROM5-9-73.

## 8. Conclusion

An extension to the hyper-reduced method based on a reduced integration domain has been introduced. It should be emphasized that "snap-back" phenomena [34], which go beyond the scope of this paper, are not addressed in the present work. It accurately predicts buckling and yields accurate limit-loads, in the context of finite strain and elasto-plastic behaviour. The method has been tested on an academic problem, that of a 2D hyper elastic buckling beam. In spite of a ill-conditioned tangent matrix, the algorithm shows good convergence properties, making use of the hyper reduced arc-length algorithm. Various constructions of the reduced base have been considered through the example of a straight pipe under internal pressure. The different contributions of each linear system to be solved have been taken into account to determined the best construction method of the reduced base. It has been found that the best ones uses standard simulation outputs to train reduced bases. Moreover, an error indicator based on the stress field has been proposed, and coupled with a greedy algorithm in order to choose snapshots that are simulated via finite element model. Using this estimator the domain of validity of the model has been determined for an elbowed pipe in a four dimensions-parametric space. The hyper-reduced model shows excellent results not only when interpolating data but also, for extrapolating (at least in a limited range beyond the training set). Our results show the efficiency and robusteness of the proposed strategy in terms of accuracy of the

solution and of stability of the hyper-reduced algorithm. A promising result as well is the speed-up, between 4 and 14 in the examples studied.

## 9. Appendix: RID construction

To detail the construction of the RID, it is convenient to introduce two mathematical operators. The first one collects the degrees of freedom over a sub-domain $\Omega_\alpha$ and is defined by:

$$\mathcal{C}(\Omega_\alpha) = \{i \in \{1, \ldots \mathcal{N}\}, \int_{\Omega_\alpha} \boldsymbol{\phi}_i^2 \, d\Omega > 0\}$$

The second one aggregates the support of the FE shape functions having their index in a set $\mathcal{L}$:

$$\mathcal{V}(\mathcal{L}) = \cup_{i \in \mathcal{L}} \text{supp}(\boldsymbol{\phi}_i), \quad \mathcal{V}(\mathcal{L}) \subset \Omega$$

The extension of this subdomain by adding $n$ layers of connected elements reads:

$$(\mathcal{V} \circ \mathcal{C})^n \circ \mathcal{V}(\mathcal{L}).$$

The operator $\mathcal{V}$ is adapted to displacement fields, which are approximated by FE shape functions. A similar operator may be introduced for stresses. When collecting simulation data related to stresses, in the matrix $\mathbf{Q}^\sigma$, all stress components at all Gauss points are stored for all elements. Each row of $\mathbf{Q}^\sigma$ is related to one component of the stress tensor, at a Gauss point in an element. Then, the DEIM algorithm applied to $\mathbf{V}^\sigma$ gives a set of indices of components of the stress tensor, at some Gauss points, in some elements. Denoted this set $\mathcal{P}^\sigma$ and denote $\mathcal{V}^\sigma(\mathcal{P}^\sigma)$ the support of the elements related to set $\mathcal{P}^\sigma$. Then, $\mathcal{V}^\sigma(\mathcal{P}^\sigma)$ is a subdomain of $\Omega$.

In the second example, the RID construction is:

$$\Omega_A = (\mathcal{V} \circ \mathcal{C})^2 \circ (\mathcal{V}(\mathcal{P}) \cup \mathcal{V}^\sigma(\mathcal{P}^\sigma)) \cup \mathcal{V} \circ \mathcal{C} \circ \mathcal{V}(\{i_o\})$$

where $i_o$ is the degree of freedom used to plot the load-displacement curve in Figure 7.

## 10. References


[1] S. Acharyya, s. Dhar, A complete gtn model for prediction of ductile failure of pipe, Journal of Materials Science 43 (2008) 1897–1909. doi:10.1007/s10853-007-2369-0.

[2] S. Volkwein, Proper orthogonal decomposition:theory and reduced-order modelling, Lecture notes, University of Konstanz, Department of Mathematics and Statistics.

[3] G. Kerschen, J.-C. Golinval, A. VAKAKIS, L. BERGMAN, The method of proper orthogonal decomposition for dynamical characterization and order reduction of mechanical systems: An overview, Nonlinear Dynamics 41 (2005) 147–169. doi:10.1007/s11071-005-2803-2.

[4] N. Aubry, P. Holmes, J. Lumley, E. Stone, The dynamics of coherent structures in the wall region of a turbulent boundary layer, Journal of Fluid Mechanics 192 (1988) 115 – 173. doi:10.1017/S0022112088001818.

[5] B. Almroth, F. Brogan, P. Stern, Automatic choice of global shape functions in structural analysis, AIAA Journal 16 (1978) 525–528. doi:10.2514/3.7539.

[6] M. Raissi, P. Perdikaris, G. Karniadakis, Physics-informed neural networks: A deep learning framework for solving forward and inverse problems involving nonlinear partial differential equations, Journal of Computational Physics 378. doi:10.1016/j.jcp.2018.10.045.

[7] F. Nguyen, S. Barhli, D. Muñoz, D. Ryckelynck, Computer vision with error estimation for reduced order modeling of macroscopic mechanical tests, Complexity 2018 (2018) 1–10. doi:10.1155/2018/3791543.

[8] T. Daniel, F. Casenave, N. Akkari, D. Ryckelynck, Model order reduction assisted by deep neural networks (rom-net), Advanced Modeling and Simulation in Engineering Sciences 7. doi:10.1186/s40323-020-00153-6.

[9] D. Ryckelynck, A priori hyperreduction method: An adaptive approach, Journal of Computational Physics 202 (2005) 346–366. doi:10.1016/j.jcp.2004.07.015.

[10] D. Ryckelynck, F. Vincent, S. Cantournet, Multidimensional a priori hyper-reduction of mechanical models involving internal variables, Multidimensional a priori hyper-reduction of mechanical models involving internal variables 225 (2012) 28–43. doi:10.1016/j.cma.2012.03.005.

[11] J. Fauque, I. Ramière, D. Ryckelynck, Hybrid hyper-reduced modeling for contact mechanics problems, International Journal for Numerical Methods in Engineering 115. doi:10.1002/nme.5798.

[12] G.-L. She, Y.-R. Ren, K.-M. Yan, On snap-buckling of porous fg curved nanobeams, Acta Astronautica 161 (2019) 475–484. doi:10.1016/j.actaastro.2019.04.010.

[13] A. Hamdaoui, B. Braikat, N. Tounsi, N. Damil, On the use of pade approximant in the asymptotic numerical method anm to compute the post-buckling of shells, Finite Elements in Analysis and Design 137 (2017) 1–10. doi:10.1016/j.finel.2017.08.004.

[14] C. Tsai, A. Palazotto, A modified riks approach to composite shell snapping using a high-order shear deformation theory, Computers and Structures 35 (1990) 221–226. doi:10.1016/0045-7949(90)90341-X.

[15] C. Tsai, A. Palazotto, Nonlinear and multiple snapping responses of cylindrical panels comparing displacement control and riks method, Computers and Structures - COMPUT STRUCT 41 (1991) 605–610. doi:10.1016/0045-7949(91)90172-I.

[16] W. Zhao, M. Chen, H. Chen, A novel trajectory interpolation algorithm for wedm - unit generalized arc length increment method, Procedia CIRP 6 (2013) 256–261. doi:10.1016/j.procir.2013.03.074.

[17] E. Riks, An incremental approach to the solution of snapping and buckling problems, Int. J. Solids Struct. 7 (1971) 1581–1599.

[18] M. Crisfield, A fast incremental/iterative solution procedure that handles "snap-through", Computers and Structures 13 (1981) 55–62. doi:10.1016/0045-7949(81)90108-5.

[19] E. de Souza Neto, Y. Feng, On the determination of the path direction for arc-length methods in the presence of bifurcations and 'snap-backs', Computer Methods in Applied Mechanics and Engineering - COMPUT METHOD APPL MECH ENG 179 (1999) 81–89. doi:10.1016/S0045-7825(99)00042-0.

[20] A. Akbari R., P. Kerfriden, S. Bordas, Scale selection in nonlinear fracture mechanics of heterogeneous materials, Philosophical Magazine 95 (2015) 3328–3347. doi:10.1080/14786435.2015.1061716.

[21] O. Allix, P. Kerfriden, P. Gosselet, On the control of the load increments for a proper description of multiple delamination in a domain decomposition framework, International Journal for Numerical Methods in Engineering 83 (2010) 1518 – 1540. doi:10.1002/nme.2884.

[22] Q. Wang, W. Zhou, Burst pressure models for thin-walled pipe elbows, International Journal of Mechanical Sciences 159. doi:10.1016/j.ijmecsci.2019.05.027.

[23] M. Khalaj Khalajestani, M. Bahaari, A. Salehi, S. Shahbazi, Predicting the limit pressure capacity of pipe elbows containing single defects, Applied Ocean Research 53 (2015) 15–22. doi:10.1016/j.apor.2015.07.002.

[24] U. Zerbst, Al, Chapter 5 - the model parameters.

[25] K. Carlberg, J. Cortial, D. Amsallem, M. Zahr, C. Farhat, The gnat nonlinear model reduction method and its application to fluid dynamics problems, 6th AIAA Theoretical Fluid Mechanics Conferencedoi:10.2514/6.2011-3112.

[26] S. Chaturantabut, D. Sorensen, Discrete empirical interpolation for nonlinear model reduction, Proceedings of the IEEE Conference on Decision and Control 32 (2010) 4316 – 4321. doi:10.1109/CDC.2009.5400045.

[27] S. An, T. Kim, D. James, Optimizing cubature for efficient integration of subspace deformations, ACM transactions on graphics 27 (2009) 165. doi:10.1145/1409060.1409118.

[28] C. Farhat, P. Avery, T. Chapman, J. Cortial, Dimensional reduction of nonlinear finite element dynamic models with finite rotations and energy-based mesh sampling and weighting for computational efficiency, International Journal for Numerical Methods in Engineering 98. doi:10.1002/nme.4668.

[29] J. Hernández, M. Caicedo-Silva, A. Ferrer Ferre, Dimensional hyper-reduction of nonlinear finite element models via empirical cubature, Computer Methods in Applied Mechanics and Engineering 313. doi:10.1016/j.cma.2016.10.022.

[30] F. Casenave, N. Akkari, F. Bordeu, C. Rey, D. Ryckelynck, A nonintrusive distributed reduced order modeling framework for nonlinear structural mechanics – application to elastoviscoplastic computations, International Journal for Numerical Methods in Engineering 121. doi:10.1002/nme.6187.

[31] D. Ryckelynck, K. Lampoh, S. Quilicy, Hyper-reduced predictions for lifetime assessment of elasto-plastic structures, Meccanica 51. doi:10.1007/s11012-015-0244-7.

[32] D. Ryckelynck, Hyper-reduction of mechanical models involving internal variables, International Journal for Numerical Methods in Engineering 77 (2009) 75 – 89. doi:10.1002/nme.2406.

[33] P. Ciarlet, The finite element method for elliptic problems, Mathematics of Computation 36 (2002) xxviii+530. doi:10.2307/2007669.

[34] A. Carpinteri, F. Accornero, Multiple snap-back instabilities in progressive microcracking coalescence, Engineering Fracture Mechanics 187. doi:10.1016/j.engfracmech.2017.11.034.

[35] N. Vasios, Nonlinear analysis of structures : The arc length method: Formulation, implementation and applications.

[36] C. Eckart, G. Young, The approximation of one matrix by another of lower rank, Psychometrika 1 (1936) 211–218. doi:10.1007/BF02288367.

[37] R. Everson, L. Sirovich, Karhunen–loève procedure for gappy data, JOSA A 12. doi:10.1364/JOSAA.12.001657.

[38] L. Barriere, J.-C. Passieux, B. Castanié, S. Marguet, P. Cresta, An adaptive model reduction strategy for post-buckling analysis of stiffened structures, Thin-Walled Structures 73 (2013) 81–93. doi:10.1016/j.tws.2013.07.009.

[39] F. Pichi, G. Rozza, Reduced basis approaches for parametrized bifurcation problems held by non-linear von kármán equations, Journal of Scientific Computingdoi:10.1007/s10915-019-01003-3.

[40] S. H. Zhang, D. Zhao, C. Gao, Limit analysis of defect-free pipe elbow under internal pressure with mean yield criterion, Applied Mechanics and Materials 127. doi:10.4028/www.scientific.net/AMM.127.79.

[41] D. Ryckelynck, G. Laurent, S. Jules, Estimation of the validity domain of hyper-reduction approximations in generalized standard elastoviscoplasticity, Advanced Modeling and Simulation in Engineering Sciences 2. doi:10.1186/s40323-015-0027-7.

[42] M. d'Ocagne, Coordonnées parallèles et axiales, Gauthier-Villars.

# Chapter 4

# Determination of voids criticity in welded joints via image-based modeling

**Contents**



**Résumé en français**


Une méthodologie est développée afin de classer les défauts en fonction de leur morphologie et de la réponse mécanique induite par une sollicitation.
L'approche proposée est assez générale et s'appuie sur les opérateurs morphologiques et la décomposition harmonique sphérique comme moyen de caractériser la géométrie des pores. Pour caractériser l'impact mécanique de ces pores la distance de Grassman est évaluée à partir de calculs FFT.
Cette approche est implémentée et détaillée sur un ensemble de pores de gaz piégés. Ces derniers sont observés à l'aide de tomographie à rayons X effectuée sur des joints soudés. Ces pores altèrent significativement la fiabilité mécanique de ces structures.
L'espace des réponses morphologiques et mécaniques est d'abord partitionné en clusters en utilisant un clustering de type "k-medoids" et les fonctions de distance associées.
La seconde étape consiste à utiliser des réseaux neuronaux denses pour associer la représentation morphologique d'un défaut à sa réponse mécanique.
Il apparait que la méthode fournit des prédictions mécaniques précises si les données d'apprentissage contiennent un nombre suffisant de défauts représentant chaque classe mécanique. Pour ce faire, l'ensemble original de défauts est complété par des techniques d'augmentation des données. Les formes de pores générées artificiellement sont obtenues à l'aide de la décomposition harmonique sphérique et d'une décomposition en valeur singulière de la fonction de distance signée des pores.
Une discussion est menée sur les applications possibles de la présente méthode et sur la façon dont les médoïdes ainsi que leur réponse mécanique peuvent être utilisés. Ces médoïdes peuvent servir de base réduite pour les techniques d'hyper-réduction, dans lesquelles les effets mécaniques des défauts et des structures sont décorrélés. Une étude statistique est ensuite menée sur la base de données de pores. Les calculs hyper-réduits sont réalisés avec le médoïde trouvé en utilisant le réseau de neurones. Ce dernier prend en entrée les caractéristiques morphologiques d'un défaut et lui associe la base réduite la plus adéquate.


## 4.1 Introduction

In this chapter welded structures undergoing cyclic loadings are considered. Defects such as gas pores can be formed and trapped in the fusion zone during laser welding. These defects can significantly affect the mechanical reliability of the welded joint. More precisely the number of loading cycles (even with low amplitude) can dramatically decrease when pores are present since they play the role of stress concentrators [MAD, 2002, Fomin and Kashaev, 2017]. The structure's lifetime decrease is even bigger as the pores are close to the surface or to another defect [Fan et al., 2003]. Similarly the size of the observed defect as a direct impact on the lifetime

of the structure [Murakami, 2002]. Indeed below a threshold size, the impact of the defect on the fatigue lifetime is null and then the bigger the defect the shorter the lifetime. Moreover the shape of defects has also a direct impact on the local mechanical response of the structure and so on the lifetime [Fan et al., 2003, Qian et al., 2016]. Current nondestructive inspection technologies are able to detect micro-voids in a mass production context. Finite element analysis can therefore be used to assess the lifetime of an observed component via image-based modeling of digital twins. Unfortunately, running a simulation per component entails a huge and generally unaffordable computational cost. In addition, voids do not admit a parametric modeling. In this chapter, a numerical method is proposed to study the impact of defects on the mechanical response of a welded joint. It is based on machine learning for the classification of pores coupled with model order reduction techniques in the framework of ROM-net methodology [Daniel et al., 2020]. The latter decrease the computational cost of each simulation related to an image-based modeling. To tackle the reduction of nonparametric defects, a multiscale construction proposed in [Lacourt, 2019, Lacourt et al., 2020] of the reduced basis is used, although no scale separation is assumed when computing the mechanical response of the structure. Some empirical modes are representing the structure behaviour and other empirical modes are related to the defect-induced local fluctuations. They are then assembled to simulate a defective joint. This methodology has proved its worth. The improvement that is proposed in this section is to avoid computing the local RB and to use machine learning techniques to selected the most appropriate existing one which is present in a database. The computation of the local RB represents an important part of the multiscale HROM method in terms of computation time hence even larger speed up would be obtained by avoiding the computation of the local RB.
The following section is a study submitted to Journal of Mathematics in Industry (JMI) with the following DOI : https://doi.org/10.1186/s13362-021-00114-7. Compared to the submitted version, one paragraph (page 7 of the article) has been added as well as an appendix (page 13 of the article), in order to give more details on the training of the neural network (text highlighted in blue). Results are unchanged.

## 4.2 Mechanical assessment of defects in welded joints : morphological classification and data augmentation

(will be inserted by the editor)

# Mechanical assessment of defects in welded joints: morphological classification and data augmentation

**H. Launay · F. Willot · D. Ryckelynck · J. Besson**

Received: date / Accepted: date

**Abstract** We develop a methodology for classifying defects based on their morphology and induced mechanical response. The proposed approach is fairly general and relies on morphological operators (Angulo & Meyer, 2009) and spherical harmonic decomposition as a way to characterize the geometry of the pores, and on the Grassman distance evaluated on FFT-based computations (Willot, 2015), for the predicted elastic response. We implement and detail our approach on a set of trapped gas pores observed in X-ray tomography of welded joints, that significantly alter the mechanical reliability of these materials (Lacourt et al, 2020). The space of morphological and mechanical responses is first partitioned into clusters using the "k-medoids" criterion and associated distance functions. Second, we use multiple-layer perceptron neuronal networks to associate a defect and corresponding morphological representation to its mechanical response. It is found that the method provides accurate mechanical predictions if the training data contains a sufficient number of defects representing each mechanical class. To do so, we supplement the original set of defects by data augmentation techniques. Artificially-generated pore shapes are obtained using the spherical harmonic decomposition and a singular value decomposition performed on the pores signed distance transform. We discuss possible applications of the present method, and how medoids and their associated mechanical response may be used to provide a natural basis for reduced-order models and hyper-reduction techniques, in which the mechanical effects of defects and structures are decorrelated (Ryckelynck et al, 2020).

**Keywords** Model-Order Reduction · FFT Method · Data Augmentation · Clustering · Defects · Shape space

**PACS** 62.20.-x · 02.50.-r · 02.30.Zz

**Mathematics Subject Classification (2020)** 74B05 · 74S25 · 68T99

## 1 Introduction

Our ability to design and produce materials with desired properties has dramatically improved, and commonly integrates sensors, control, simulation data and computerized predictions (see reviews in [1,2,3]). These techniques combine material imaging [4] and digital-twins frameworks [5] for manufacturing and evaluating material properties. In mechanics, numerous applications concern control, defects and anomaly detection [6] or fatigue-design of materials [7,8]. Machine learning algorithms, notably, have been proposed in the aeronautical field [9], fabrication process [10] or pipelines applications [11], and have been combined with numerical computations to study defects in ball bearings [12]. Simulation-driven machine learning methods based on existing mechanical models are especially attractive as they avoid the explicit parametrization of defects being modeled. Assessing and certifying the mechanical properties of structures containing defects nevertheless requires advanced micro-mechanical models, as well as non-destructive imaging techniques such as X-ray tomography [13] or ultrasonic measurements [14].

This is due to the recognition that composites (or, for that matter, porous) microstructures, often exhibit widely-varying effective responses, as demonstrated by homogenization theories [15,16] and in optimal-design problems [17]. A broad range of mechanical properties may be achieved by tailoring the inner geometrical arrangement of microstructures, as surveyed in e.g. [18,19,20]. Aside for a few rigorous results obtained for particular geometries, e.g. the Eshelby [21] or Vigdergauz [22] inclusions, the effect of the shapes of pores on the overall mechanical response is difficult to quantify even for linearly-elastic media, and usually involves sophisticated mathematical tools. In plane strain, the presence of corners [23], up to the limiting case of a crack tip [24], bottlenecks [25,26], and high-aspect ratios are known to be mechanically-determining factors, as highlighted by studies based on conformal mappings [27] or radon transforms techniques [28].

Although these rigorous and (semi-)analytical results are useful as guides, they are restricted to linear media under plane strain or stress, with notable exceptions [29,30]. They do not allow one to explore the links between morphology and mechanical response, important in industrial problems. The latter often involve inverse-design problems within a given class of microstructures or morphologies, that results from manufacturing constraints [31,32]. In energetic granular materials, for instance, particles shape and size depend on crystallography and may be controlled by surface treatment, to some extent [33]. Furthermore, the overall material response alone, characterized by an effective stiffness tensor, is insufficient for determining the full mechanical response. The local response, sensitive to the internal microstructure arrangement of a given material system, must be accounted for. Damage localization, which leads to brittle or ductile fracture in composite materials, is driven by the local stress state in the microstructure, which is itself a complex result of the load distribution within the material.

H. Launay, D. Ryckelynck, J. Besson
Mines Paris, PSL Research University, Centre des Matériaux, CNRS UMR 7633
63-65 rue Henri-Auguste Desbruères, BP 87, 91003 Évry, France
Tel.: +33 1 60 76 30 00
E-mail: {firstname.familyname}@mines-paristech.fr

F. Willot
Mines Paris, PSL Research University, Centre de Morphologie Mathématique
35 rue S$^{t}$ Honoré, 77300 Fontainebleau, France
Tel.: +33 1 64 69 48 07
E-mail: francois.willot@mines-paristech.fr

Lately, shape statistics based on morphological operators have been devised [34,35] and so-called shape spaces [36] have gained attraction as a versatile method for quantifying shapes, seen as points in a high-dimensional metric space representing Fourier-based expansions. On a sphere, the Laplace-Beltrami eigenfunctions have an explicit form in terms of spherical harmonics [37,38], which can then be used to represent continuous shapes [39], seen as deformation of the sphere, or as mapping between a sphere and an arbitrary shape. This decomposition is especially useful for modeling data on a regular grid (i.e. on images), in computer graphics [40], medical image analysis [41] or material science [42]. In the context of mechanics, sophisticated image analysis approaches based on machine-learning methods have already been employed to detect, and more generally classify, "critical" defects as exemplified in several industrial problems [11,10]. Other approaches have sought to infer the mechanical response of materials using temperature fields [43]. These methods can be supplemented by transfer learning [44] and shape explorations techniques to determine mechanically-relevant criteria for assessing the effect or criticality of defects.

The purpose of the present work is twofold. First, a methology is developed to explore and classify defects based on shapes and mechanical response, using morphological transforms, spherical harmonics, and the Grassmann distance. To illustrate our approach, a set of defects previously observed in tomography images of welded joins is analyzed to serve as a model problem. Second, use is made of machine learning methods to compare and correlate the resulting classifications. The adequacy of the method for detecting critical defects, and other possible applications, are discussed, as well as future works, such as those exploring the dependency of our results on the choosen metrics.

The present article is organized as follows. Sec. (2) presents the set of defects used as the basis for the present study, whereas Sec. (3) deals with the various distances used for clustering, including full-field mechanical computations. Our main results, which concern the mechanicaly-based clustering of shapes, are given in Sec. (4). These results are compared to those obtained after data augmentation of the initial set of defect in Sec. (5). We conclude in Sec. (6).

## 2 Data set of defects and goal of the present work

The present work is based on a data set of defects obtained in L. Lacourt's PhD thesis [45]. These defects have been extracted from a segmented X-ray tomography image of welded joints, see [46]. The data set consists in 1288 defects in total, each containing between 500 and 100,000 voxels. Smaller defects present in the original image have been discarded in the present study. Slightly more than half of the defects are close to spheres, whereas the rest of them display various convex and non-convex shapes (Fig. 1), see [47].

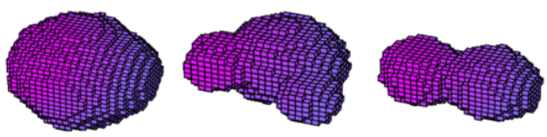

**Fig. 1** Views in three dimensions of three non-spherical defects, segmented from the tomography image of welded joints.

After segmentation, each defect is embedded in a bounding box in 3D, with edges aligned with the axis ($e_1$, $e_2$, $e_3$) of a Cartesian coordinates system. The shape has been rotated so that its first ans second principal axis are aligned with $e_1$ and $e_2$. A reflection with respect to the plane ($e_1$, $e_2$) is carried out so that the highest absolute coordinate along $e_3$ is positive. Finally, a homothety is performed so that the dimension of the shape along axis $e_1$ is 1/4 that of the embedding box. For all shapes, the embedding box is a cube containing $L^3 = 80^3$ voxels. Accordingly, the shapes have varying volume fractions, but the same diameter with respect to their bounding box, . This is so that cracks or pores with very high aspect ratios can be discretized with similar resolution.

The effects of such defects on the mechanical response of a structure can be efficiently estimated using the two-scales hyper-reduction method proposed in [46] for fatigue. In this method, schematized in Fig. (2), the effect of the overall structure and of defects are dissociated, whereas interactions between the two are taken into account by the far-field [48,49].

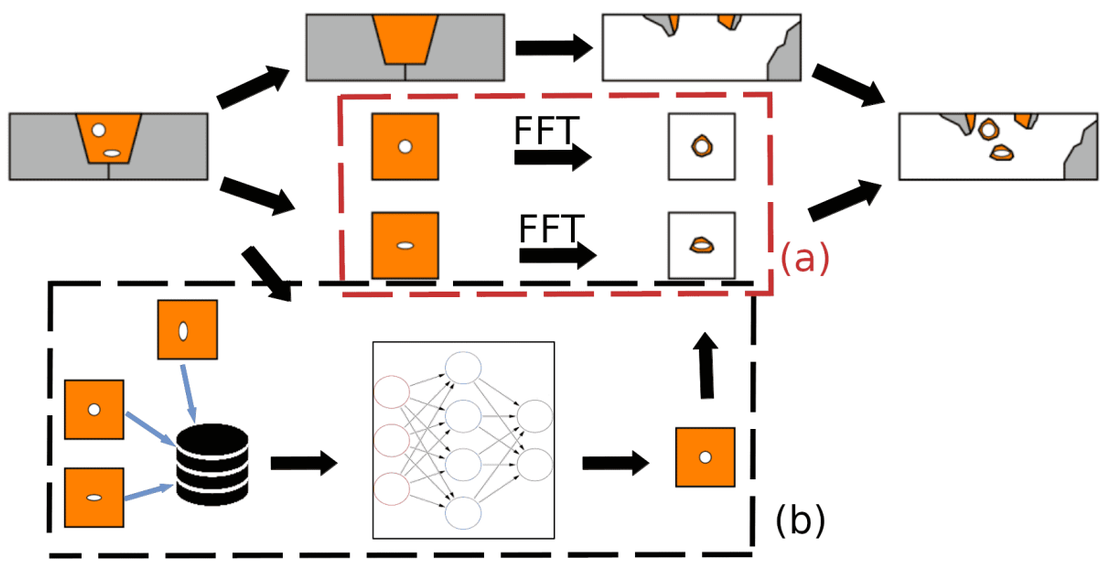


**Fig. 2** Schematic view of the hyper-reduction method. The structure and defects are treated separately. Orange: fusion zone; grey: base metal. Areas in white are not meshed. In the classical method [46], numerical computations are performed for each new defect (rectangle a). In the proposed approach, the pre-computed mechanical response of a nearest defect is used (rectangle b).

In practice, a reduced basis is computed for the structure without defect and another one for the defect. A "global reduced basis" is then computed by transferring both reduced basis on the real mesh containing the defect and concatenating them. Using this reduced basis, a "hyper-reduced" simulation is performed on a reduced domain of integration (Fig. 2, orange and grey regions). As such, numerical computations are carried out on a sane structure without pores, and on isolated defects, rather than on the entire structure containing defects. Generally speaking, the method is most efficient when dealing with complex and time-consuming constitutive-laws. Speed-up as high as $10^2$ and $10^3$ have been obtained in fatigue in mechanics, for elastoplastic behavior, and about 10 in linear-elastic cases [50].

While the hyper-reduced method improves on standard finite element techniques, computing the reduced basis of defects can be time-consuming. This point needs to be addressed in industrial applications where the effect of defects must be quantified in near real-time. Often, the pores shape is random, but follows a certain probability distribution that needs to be estimated. The mechanical responses of shapes close to one another need not be computed twice, in general. However, as noted in Sec. (1), while different shapes may yield similar mechanical response, small difference such as the presence of corners, could induce different mechanical responses. The goal of this work is to investigate whether one may pick an appropriate reduced basis for a defect by learning the mechanical responses of a set of other defects, and how they relate to their shapes. To do this, the mechanical computations for the fields around a defect (rectangle a, Fig. 2) are replaced by statistical learning, making use of pre-computed mechanical fields used as training data (rectangle b, Fig. 2). The full scheme in Fig. (2) will not be implemented in the present work. Instead we focus on the task in rectangle (b) of the same graph, and consider linear elasticity as a proof of concept for our approach.

## 3 Mechanical and morphological distances

In the following, we make use of a Fourier-based scheme with rotated discrete Green operator [51] to carry out mechanical computations. The method uses periodic boundary conditions, relevant for quasi-isolated defects and has been found to be efficient when compared to finite element, both in terms of memory computations, accuracy and CPU time [52]. For each defect, six FFT computations with prescribed overall strain $\boldsymbol{\varepsilon}$ are carried out, corresponding to the six independent strain loadings, in our case $E_i = \langle \varepsilon_i \rangle$, ($i = xx$, $xy$, $xz$, $yy$, $yz$, $zz$) with $E_j = 0$ ($j \neq i$). Accordingly, the data consists in a fourth-order tensorial field, denoted localization tensor in homogenization theories, which has both minor and major symmetry. Figure (3) shows as an example two strain components obtained under uniaxial extension. The fluctuation of the strain field inside the pore depends on the choice of the Green operator and has no physical meaning, except for the mean of the strain in the pore. Accordingly, the strain field inside the pore is replaced by its mean in all mechanical computations.

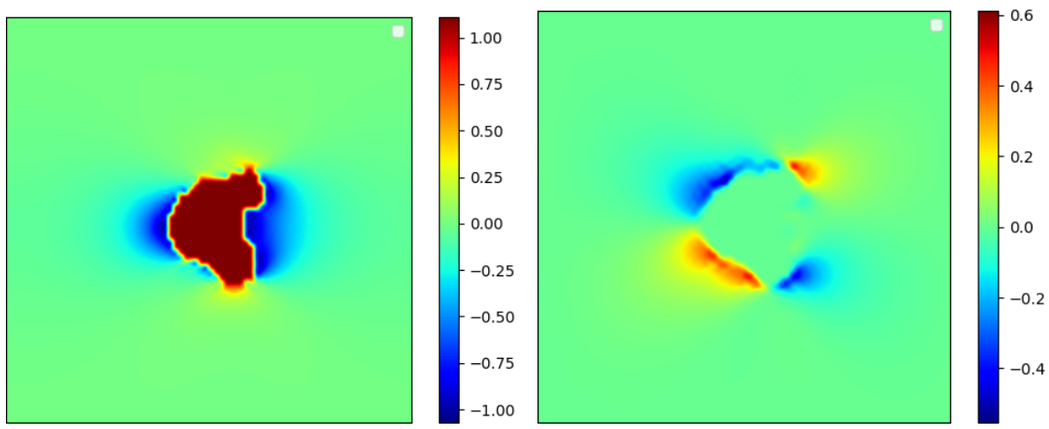


**Fig. 3** 2D cut of two longitudinal and shear strain components $\varepsilon_{yy}$ (a) and $\varepsilon_{yz}$ (b) for the middle defect in Fig. (1), with axis $e_y$ and $e_z$ vertical and normal to the figure. Macroscopic strain loading: $E_{yy} = \langle \varepsilon_{yy} \rangle = 1\%$ (color scale in percent).

In the rest of this study, use is made of the Grassman distance [53,54] schematized in Fig. (4), for evaluating the dissimilarity between mechanical responses.

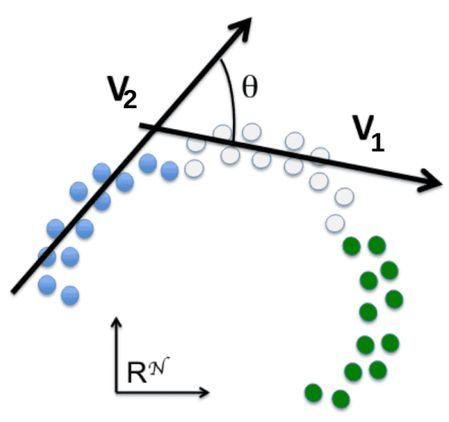


**Fig. 4** Schematic representation of the Grassmann distance for the mechanical clustering.

Consider two matrices $V_1$, $V_2 \in \mathbb{R}^{\mathcal{N}} \times \mathbb{R}^N$ representing the full-field mechanical response of two defects, where $N = 6$ is the number of applied macroscopic loadings and $\mathcal{N} = 6L^3$ are the number of strain components in all voxels for a given loading. The Grassman distance between $V_1$ and $V_2$ is given by:

$$d^g(V_1, V_2) = \|\Theta\|_{\mathcal{F}} = \sqrt{\sum_i \theta_i^2}, \tag{1}$$

where $\|\cdot\|_{\mathcal{F}}$ is the Frobenius distance and $\Theta$ is a diagonal matrix with eigenvalues $\theta_i$ obtained from the singular value decomposition:

$$V_1^t \cdot V_2 = W_1 \cdot \cos(\Theta) \cdot W_2^t, \qquad W_1^t \cdot W_1 = W_2^t \cdot W_2 = I, \tag{2}$$

and $I$ is the identity, and $W_1$, $W_2 \in \mathbb{R}^N \times \mathbb{R}^N$ are orthogonal matrices. Distance (1) measures the dissimilarity between two defects by considering the subspaces (Grassman manifolds) generated by the set of strain responses for each loading to the two defects [55]. The distance is appropriate for mechanical responses with the same number of applied loadings. In the more general case of time-varying loadings, with different number of time steps for each defect, the Schubert distance [56] may be used instead.

The Grassmann distance involves a singular value decomposition performed on matrix $V_1^t \cdot V_2$ (see Eq. 2) of size $N \times N$. These computations become time-consuming when a large number of objects (more than $1,200$ here) must be compared to one another. To improve on the computation of the Grassmann distances, we define a subdomain $\Omega$ of size $(L/2)^3$, included in the bounding box, and containing all defects. We define two alternative pseudo-Grassmann distances, computed as in (1) with the data for $V_1$ and $V_2$ restricted to either $\Omega$ or its boundary $\partial\Omega$. A representation of these two subdomains is given in appendix 7.1. The computations of the pseudo-Grassmann distances in $\Omega$ and $\partial\Omega$ is much more efficient as the bounding box $\Omega$ has a volume eight times smaller compared to the entire domain. Histograms for the (pseudo-)Grassmannn distances between 400 defects are represented in Fig. (5a). The distribution of distances for the pseudo-Grassmann distance computed using $\partial\Omega$ is strongly different from that of the Grassmann distance, indicating that the former can not be substituted to the latter. However, this is not so for the pseudo-Grassmann distance computed on the entire subdomain $\Omega$ which is close to the results obtained for the Grassmann distance, see Fig. (5b). Accordingly, in the rest of this study, the Grassman distance is evalued on the subdomain $\Omega$ only.

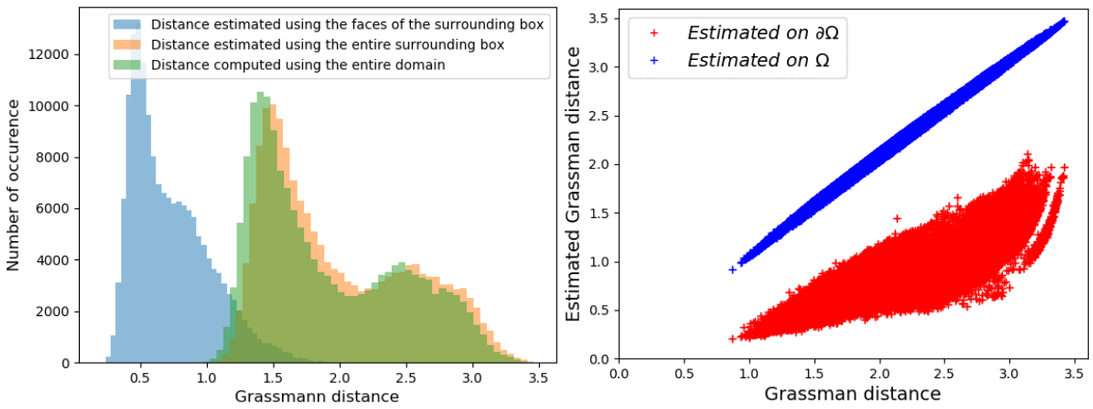


(a) (b)

**Fig. 5** Histograms of the Grassmann distances for defects $1-400$ (a) and corresponding point-cloud representation (b). The distance is estimated using the volume of the surrounding box $\Omega$, the faces $\partial\Omega$ of the surrounding box or computed using the entire domain.

The shape of defects is quantified by two means, a morphological and spectral decomposition. Consider first the morphological transform based on the signed distance function:

$$f(x) = \begin{cases} d(x, \partial\mathcal{P}) & \text{if } x \in \mathcal{P}^c, \\ -d(x, \partial\mathcal{P}) & \text{if } x \in \mathcal{P}, \end{cases} \tag{3}$$

for a pore $\mathcal{P}$, with boundary $\partial P$. This distance is obtained by propagating a distance function with quasi-Euclidean metric, and leads to spherical iso-lines far from the defect. Figure 6 shows the distance field of defect 9 in midplane $z = 2l$.

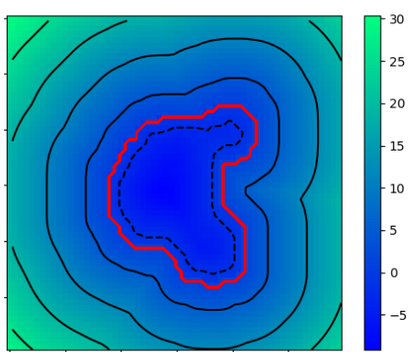

**Fig. 6** Distance field for defect 9 in midplane $z = l/2$.

The signed distance fields for two defects $\mathcal{P}_1$, $\mathcal{P}_2$ is vectorized into two arrays denoted $F_1$ and $F_2 \in \mathbb{R}^{L^3}$ and we denote "morphological distance" the distance:

$$d^m(\mathcal{P}_1, \mathcal{P}_2) = \|F_1 - F_2\|_2, \tag{4}$$

where $\|\cdot\|_2$ is the Euclidean distance.

We also define a distance based on the spectral decomposition for the Laplace-Baltrami expansion [42,57]. This expansion can be conveniently written in terms of spherical harmonics in the case of the sphere [58]. The latter form a basis for square-integrable functions on the unit sphere and this decomposition can accordingly be used to characterize star-shaped defects. We briefly recall how this spectral decomposition is estimated on digital images (the reader is refered to [58] for a detailed discussion). The decomposition reads, in spherical coordinates ($\theta$, $\phi$):

$$x_k(\theta,\phi) = \sum_{0\leq \ell,\, |m|\leq \ell} c_{k\ell}^m Y_\ell^m(\theta,\phi), \quad Y_\ell^m(\theta,\phi) = \sqrt{\frac{2\ell+(\ell-m)!}{4\pi(\ell-m)!}} P_\ell^m cos(\theta) \mathrm{e}^{im\phi}, \tag{5}$$

where $P$ are Legendre polynomials and $x_k$ are the coordinates ($k = 1, 2, 3$) of points along the surface of the defect. In practice, a set of $25 \times 25$ pixels are picked along the surface of the object, distributed uniformly along all directions from the center, providing values for the $x_k(\theta,\phi)$. The center is the minimial of the signed distance function. The double sum in (5) is truncated to $|m| \leq \ell \leq \ell_{\max} = 10$ and a least-square optimization procedure is used to determine the coefficients $c_{k\ell}^m$. The latter are used to define the distance:

$$d^{sh}(\mathcal{P}_1, \mathcal{P}_2) = \sqrt{\sum_{k\ell,m} \|c_{k,\ell}^m(\mathcal{P}_1) - c_{k,\ell}^m(\mathcal{P}_2)\|^2}. \tag{6}$$

Conversely, Eq. (5) can be used to reconstruct a shape, for a given set of values $c_\ell^m$. Two shapes and their associated reconstitution are shown in Fig. (7).

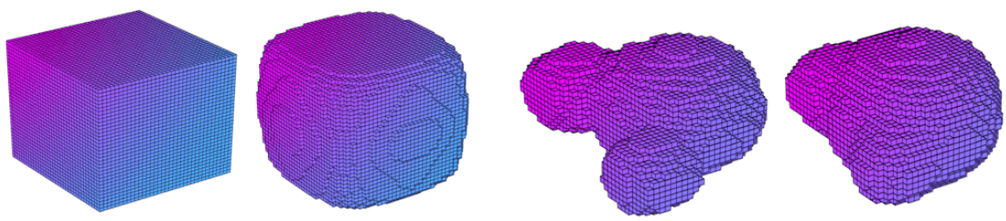

(a) (b)

**Fig. 7** Two shapes and their reconstruction with spherical harmonics (right). a) A cube. b) The middle defect in Fig. (1).

The difference between the two are a consequence of the truncation of the spectral decomposition, and of the way interpolation points on the surface are chosen, i.e. uniformly distributed along all directions on the sphere rather than uniformly-distributed on the surface of the object. This reconstruction is imperfect and only captures some of the features of each shape.

## 4 Clustering analysis

In this section, we consider the $k$-medoids clustering algorithm, which provides us with a set of classes as well as a most-central point (the "medoid") in each class, that is present in the data set. The classification algorithm, which minimizes distances to the medoids, is based on the matrix of distances between points, and does not require the coordinates of each point [59]. Additionaly, since the medoid is present in the data set, its pre-computed reduced basis can be used in hyper-reduced methods for taking into account defects that belong to a known mechanical class.

We split the data set into two groups, a training set of 936 defects and a testing set containing 508 defects. The training set corresponds to the data collected on two-third of the welded joint and has been obtained on two tomography images. The test data corresponds to the rest of the welded joint, and has been obtained by a third tomography. Accordingly, the data in the two sets are not randomly drawn from a collection of defects, but instead are obtained from different sources, as would be expected in industrial applications. Our results are shown in Fig. (8) for the Grassman distance as well as the two shape distances. The points cloud representation in three dimensions is obtained by multidimensional scaling [60].

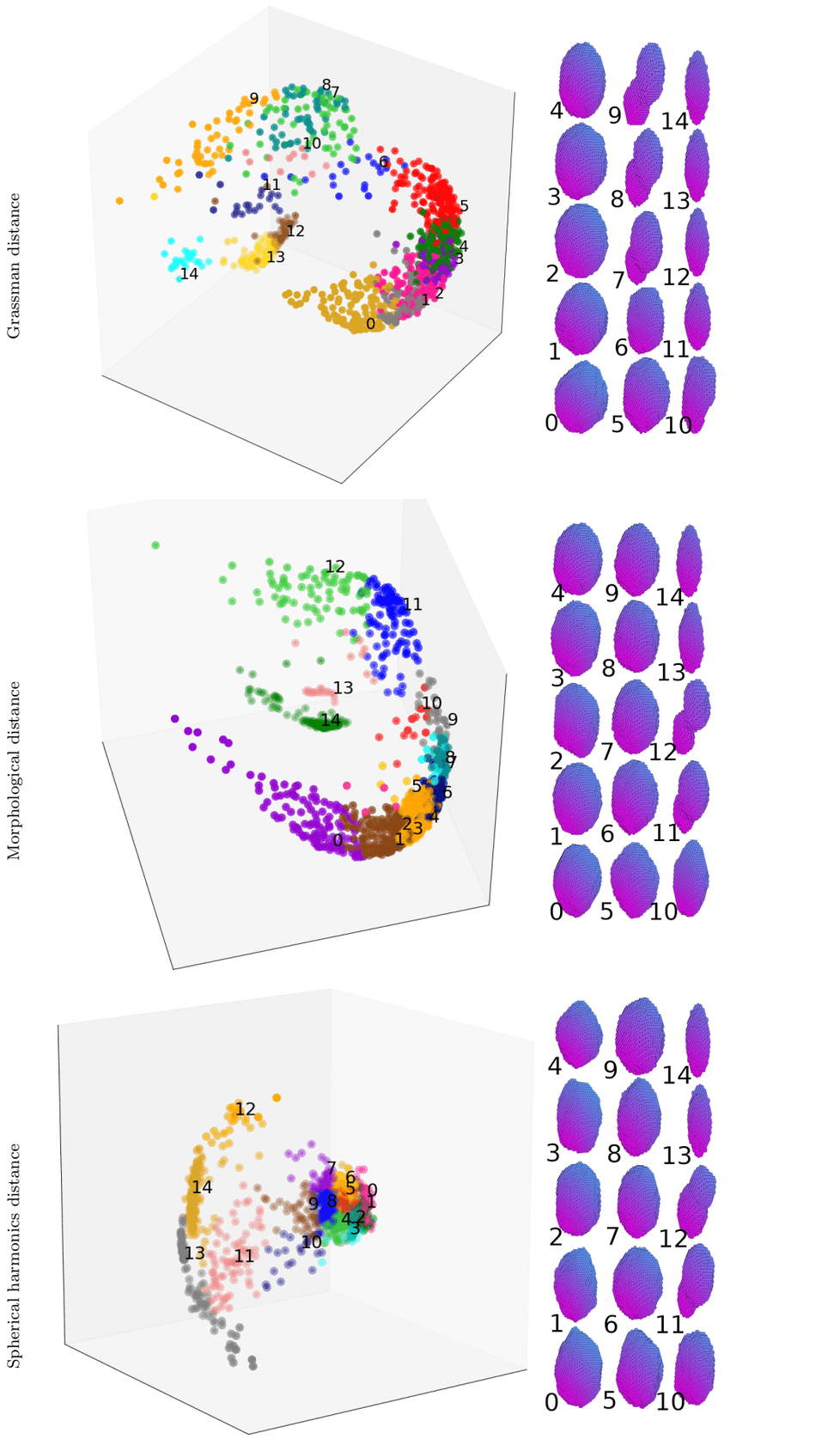


**Fig. 8** Clustering provided by the $k$-medoids algorithm using the Grassmann, morphological and spherical harmonics distances. Medoids on right.

Partly-overlapping clusters on this representation may actually be separated when additional dimensions are considered. In this view with reduced dimension, the data form a continuous cloud of points. The medoids (right) exhibit spherical, oblate and non-convex shapes. The amount of information contained in the multidimensional scaling is plotted as a function of the dimension in Fig. (9a) in the case of the Grassman distance, showing a strong decrease of the amount of unknown information up to $d \approx 8$ and a slower decrease after that. The effect of the number of clusters is shown in Fig. (9b), which represents the intra-clusters distance, i.e. the sum of the distances of each shape to its medoid. This distance decreases with the number of clusters. The "typical" number of clusters corresponding to this decrease is about 5, at which point the curve displays an elbow.

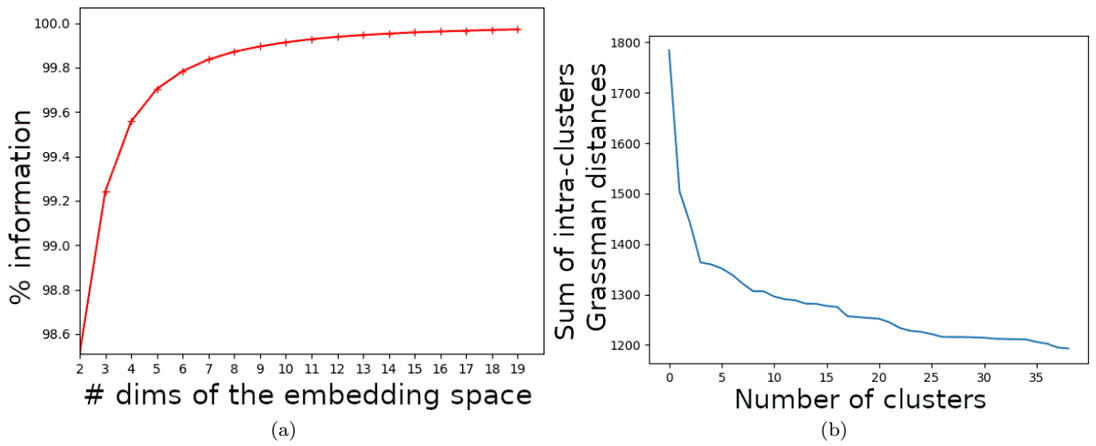


(a) (b)

**Fig. 9** a) Amount of information recovered by the multi-dimensional scaling vs. number of dimensions, for the Grassman-based distance (see Fig. 8). b) Intra-clusters distance vs. number of clusters.

Shape clustering as determined by the $k$-mdeoids analysis can not be used directly to assign a defect to its mechanical cluster, as shown in Fig. (10). This figure represents the confusion matrix that summarizes the number of shapes that belong to a given mechanical cluster and to a cluster based on either the morphological of spherical harmonics distance.

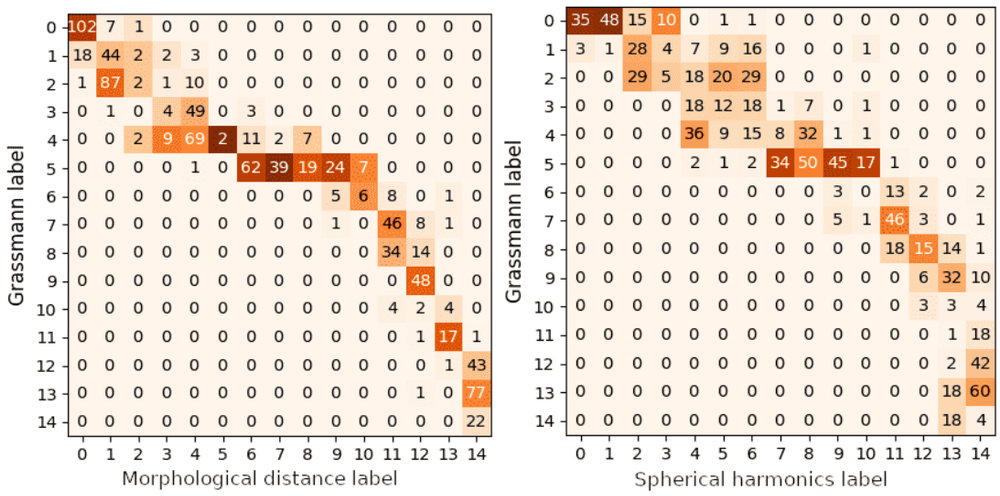


**Fig. 10** Confusion matrix showing the number of shapes in Grassmann-based clusters with respect to clusters based on the morphological distance (left) and the spherical harmonics distance (right)

Cluster labels are the same as in Fig. (8). The color scale indicates a concentration of shapes from a geometrical cluster into a specific mechanical cluster.

Assigning a mechanical cluster to a shape based on its morphological or spherical-harmonics cluster would result in 74% and 87% erroneous labeling, respectively. Instead, we consider a classifier based on a dense neural networks (Fig. 11). The input to the network are the distances to the medoids based on the morphological distance. The network is trained to predict the label of the cluster corresponding to the Grassmann distance.

| | Morphological distance to medoid | | |
|---|---|---|---|
| | Medoid 1 | ... | Medoid k |
| Shape 1 | 1.5 | ... | 2.2 |
| Shape 2 | 1.2 | ... | 1.1 |
| ... | ... | ... | ... |
| Shape N | 3.6 | ... | 2.7 |

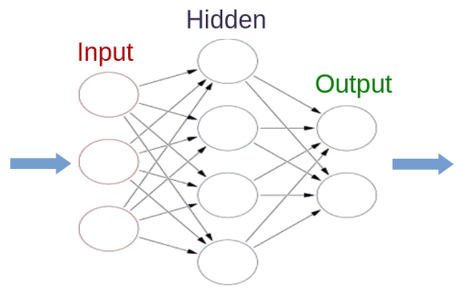


| | Grassmann labelling |
|---|---|
| Shape 1 | 1 |
| Shape 2 | 10 |
| ... | ... |
| Shape N | 5 |

**Fig. 11** Classifier methodology.

The trained neuron network has 3 hidden layer of 15 neurones each. The model optimizes the log-loss function given in eq.7).

$$\mathcal{L}_{logLoss} = -\sum_{c=1}^{M} y_{o,c}.log(p_{o,c}) \tag{7}$$

Where $M$ is the number of classes, $y$ is a binary indicator and $p$ the predicted probability of the observation $o$ being of class $c$. The activation function that have been chosen for each layer is a rectified linear function. The training set is split into two different sets : a standard training set to fit the parameter representing 90%

of the initial training set and a validation set to assess that the model also fit data which haven't been see which represents 10% of the initial training set. The validation set is also used to impose an early stopping criterion. The loss curves of the training phase are given in appendix 7.2. Fig. (12) shows the confusion matrix representing the predicted and true labels, that summarizes the assignement by the network of a mechanical cluster for the various shapes, either in the training or test sets. The percentage of misclassified shapes by cluster is given on the right column.

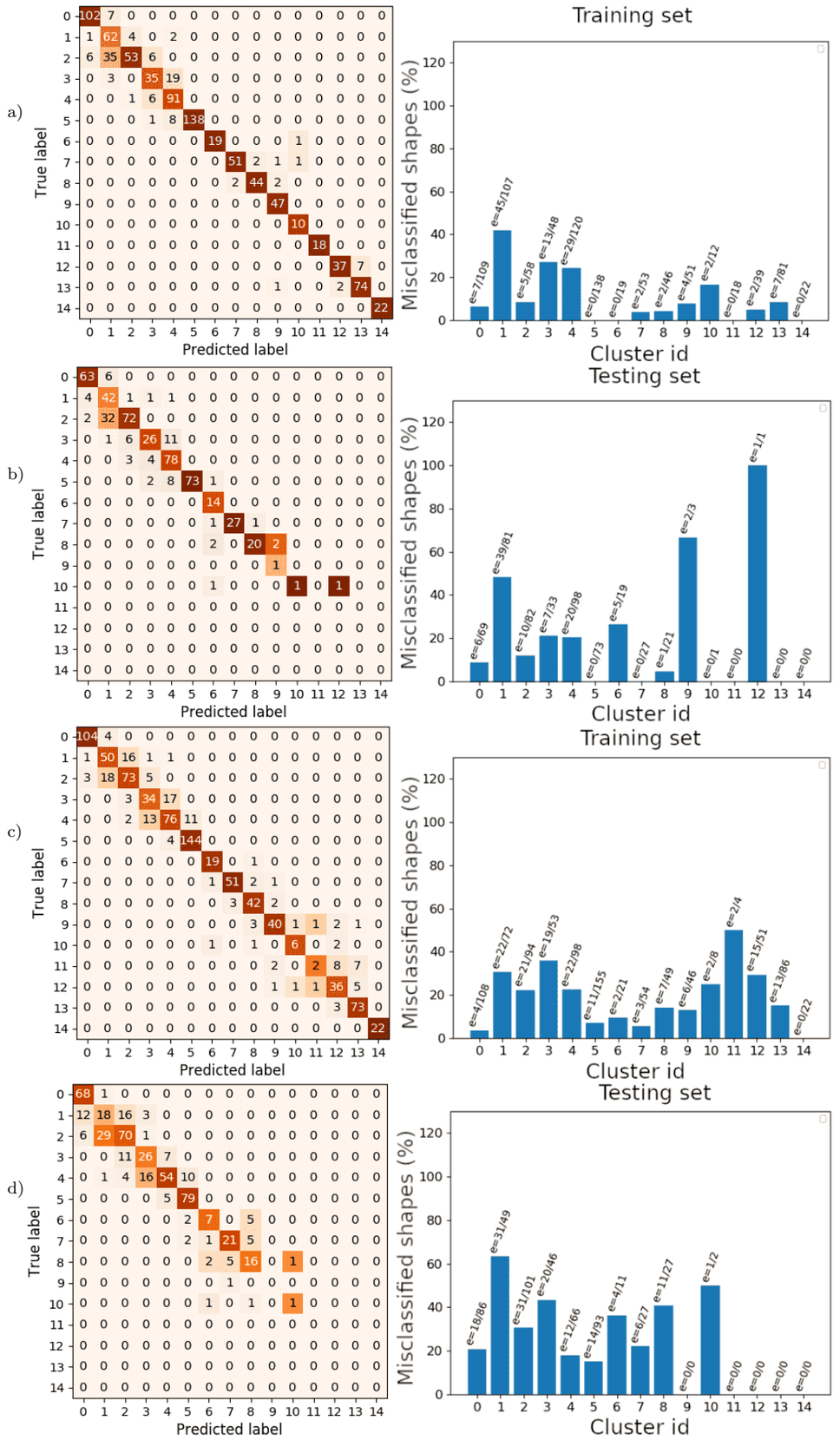


**Fig. 12** Left column: confusion matrices for the training (rows a, c) and testing sets (rows b, d) between Grassmann clustering (true label) and the label predicted by the dense neural network using the signed (rows a, b) and spherical harmonics distances (rows c, d). Right: percentage of misclassified shapes in each cluster.

To quantify these results, we define an error on the training set $e_{\mathrm{tr}} = M_{\mathrm{tr}}/N_{\mathrm{tr}}$ as the ratio of correct label predictions $M_{\mathrm{tr}}$ divided by the total number of predictions $N_{\mathrm{tr}}$ in the training set. We consider likewise a similarly-defined error $e_{\mathrm{te}}$ for the testing set. We also introduce a second error criterion $e'_{\mathrm{tr}}$, equal to the mean of the proportion of misclassified shapes in each (non-empty) mechanical cluster for the training data, and likewise $e'_{\mathrm{te}}$ for the testing set. These various errors highlight sub-optimal performances of $e_{\mathrm{tr}} = 12.8\%$, $e'_{\mathrm{tr}} = 10.3\%$ for the training data, as well as $e_{\mathrm{te}} = 17.9\%$ and $e'_{\mathrm{te}} = 25.7\%$ for the testing set. Higher errors $e_{\mathrm{tr}} = 16.2\%$, $e'_{\mathrm{tr}} = 18.9\%$, $e_{\mathrm{te}} = 29.1\%$ and $e'_{\mathrm{te}} = 34.1\%$ are observed when using spherical harmonics instead of the morphological distance (Fig. 12, rows 3 and 4). These results may be attributed to the small number of defects in some classes, as will be investigated in the next section.

## 5 Data augmentation

To improve on the results presented in Sec. (5), we focus on data augmentation. Both the morphological and spherical harmonics distances are defined as Euclidean distances of vectors in multi-dimensional spaces. As explored in [34], these types of representations can be used for data interpolation as well. Let us consider the linear interpolations ($0 \leq s \leq 1$):

$$F(s) = sF(\mathcal{P}_1) + (1-s)F(\mathcal{P}_2), \quad c^m_{k\ell}(s) = s\, c^m_{k\ell}(\mathcal{P}_1) + (1-s)c^m_{k\ell}(\mathcal{P}_2), \tag{8}$$

with respect to two shapes $\mathcal{P}_1$ and $\mathcal{P}_2$, where $F$ and $c^m_{k\ell}$ are defined in Eqs. (3), (4) (6) and (5). The vectors $F(s)$ and $c^m_{k\ell}(s)$ provide continuous interpolations between the two shapes, as illustrated in Fig. (13).

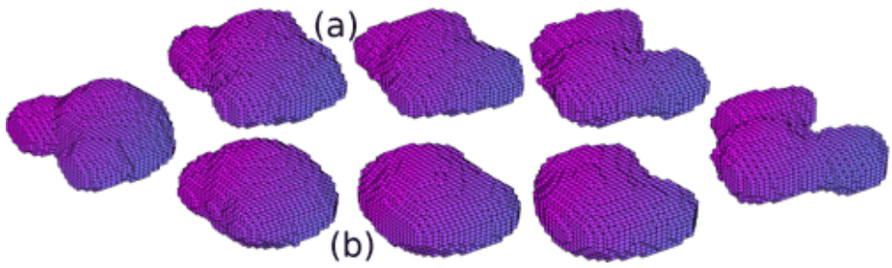


**Fig. 13** Interpolation between two shapes. a) Morphological distance. b) Spherical harmonics distance.

An alternative approach consists in using a singular value decomposition on the matrix containing as columns the spherical harmonics decomposition $c^m_{k\ell}(\mathcal{P}_i)$ for all defects $\mathcal{P}_i$. Considering as an example the first three singular values, a new shape may be represented as a point in a three-dimensional space. By paving this space with a set of points, one generates new defects that interpolate between the shapes corresponding to the three singular values. The set of points representing shapes in the coordinates system corresponding to the first three singular values is represented in Fig. (14a). Fig. (14b) shows random shapes generated in this space.

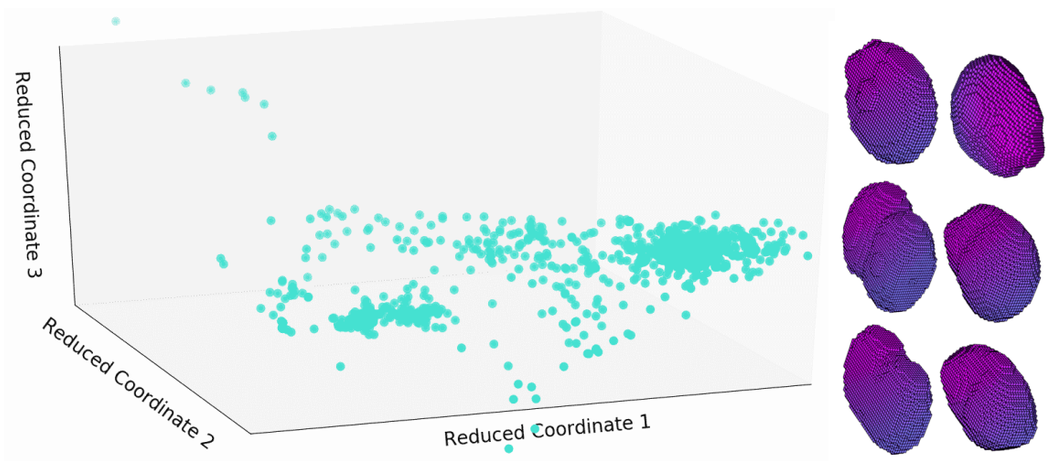


**Fig. 14** a) Shapes in the three first singular components space. b) Examples of shapes in the three first singular components space.

We now generate 3,128 artificial shapes with the above data augmentation techniques. The linear interpolation method in Eq. (8) is used preferentially on set of shapes that belong to mechanical clusters with few shapes. We then classify the shapes according to the $k$-medoids method, as described in Sec. (4). Results corresponding to the mechanical, morphological and spherical harmonics clustering are shown in Fig. (15).

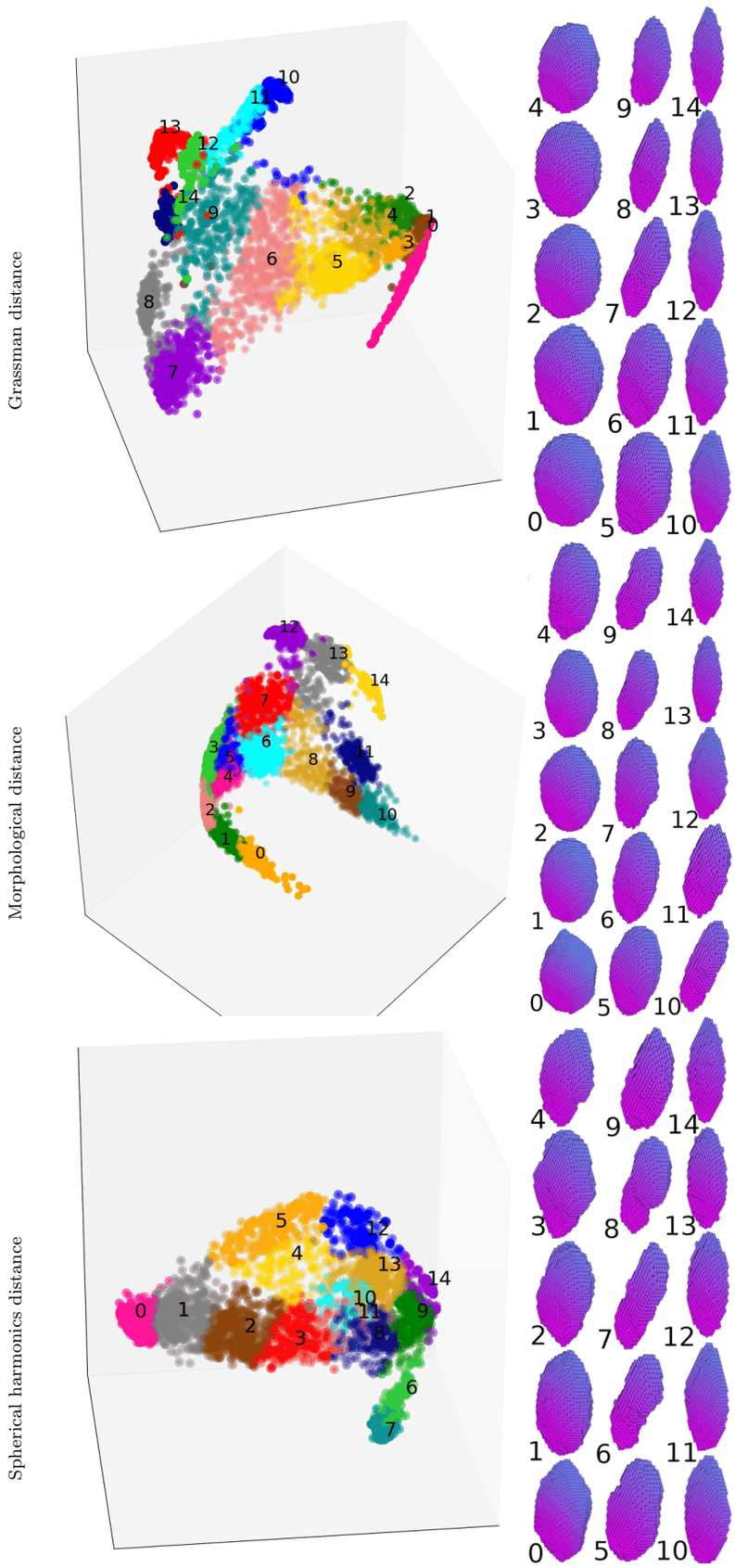


**Fig. 15** Clustering provided by the $k$-medoids algorithm using the Grassmann, morphological and spherical harmonics distances, after data augmentation. Medoids on right.

The points cloud are much more dense and homoegneous as compared to the same results obtained without data augmentation (Fig. 8) and suggest the latent space is better represented. Despite this, mechanical clusters can not be predicted using either the morphological or spherical harmonics clustering (Fig. 16): their respective errors read $e_{\text{te}} = 77\%$ and $e_{\text{te}} = 67\%$.

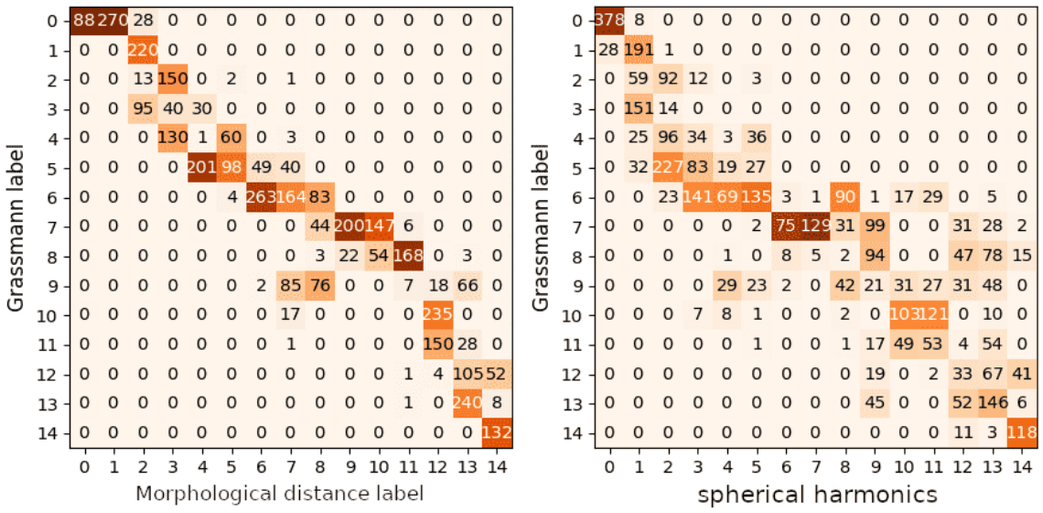


(a) (b)

**Fig. 16** Confusion matrices showing the number of shapes in the clustering based on the Grassmann distance and that based on either the morphological (a) and spherical harmonics (b) distance, after data augmentation.

Again, use is made of a classifier based on a dense neural network that is trained to predict the mechanical cluster using distances to the medoids. Fig. (17) shows the confusion matrix obtained for the training and testing sets, when either the morphological or spherical harmonics distances are considered. The proportion of misclassified shapes by cluster is shown on the right.

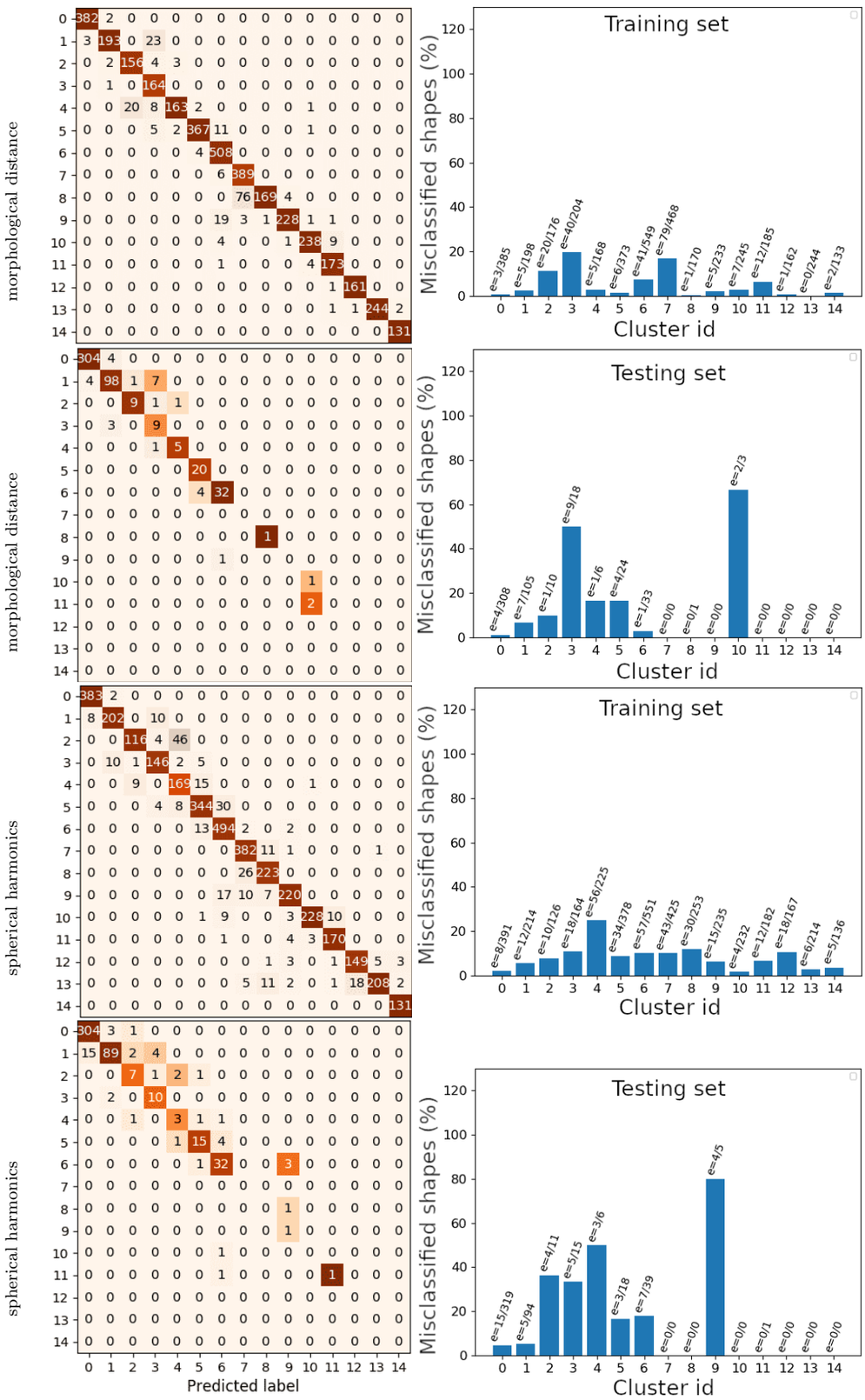


**Fig. 17** Left column: confusion matrices for the training (rows 1, 3) and testing sets (rows 2, 4) showing the true Grassmann clustering label vs. the label predicted by the neural network using the morphological (rows 1, 2) and spherical-harmonics distance (rows 3, 4). Right: percentage of misclassified shapes in each cluster after data augmentation.

In the case of the morphological distance, the errors for the training set read $e_{\mathrm{tr}} = 5.7\%$, $e'_{\mathrm{tr}} = 5.3\%$ and $e_{\mathrm{te}} = 5.8\%$, $e'_{\mathrm{te}} = 18.9\%$ for the testing set, When spherical harmonics are considered, errors are slighly higher. They read $e_{\mathrm{tr}} = 8.4\%$, $e'_{\mathrm{tr}} = 8.3\%$ for the training data and $e_{\mathrm{te}} = 9.1\%$, $e'_{\mathrm{te}} = 27.1\%$ for the testing set (see Tab. 1 for a summary of the various errors.)

| | No data augmentation | | Data augmentation | |
|---|---|---|---|---|
| | $e(\%)$ | $e'(\%)$ | $e(\%)$ | $e'(\%)$ |
| Morphological distance (train) | 12.8 | 10.1 | 5.7 | 5.3 |
| Morphological distance (test) | 17.9 | 25.7 | 5.8 | 18.9 |
| Spherical harmonics (train) | 16.2 | 18.9 | 8.4 | 8.3 |
| Spherical harmonics (test) | 29.1 | 34.1 | 9.1 | 27.1 |

**Table 1** Percentage of wrongly-assigned labels, averaged over all shapes, or over mechanical clusters, for the training data, with either the morphological or spherical harmonics distances, using data augmentation.

In any case, these errors are significantly lower than that obtained without data augmentation (Fig. 12), highlighting the benefits of data augmentation. Furthermore, the errors of the neural network consist most often in predicting a label which is a neighbor of the correct mechanical cluster, with similar mechanical response. This materializes into a band-diagonal structure for the confusion matrices.

## 6 Concluding remarks

In the present work, data-analysis and clustering methods have been proposed for classifying the mechanical properties of porous defects. Although the approach is restricted to linear elasticity, it is fairly general and can be adapted to nonlinear or time-dependant mechanical responses. While we use conventional clustering and data analysis tools, the methods rely on distances defined in the space of the defects mechanical responses (i.e. a 3D tensorial field) and on geometrical distances based on a morphological transform and a spectral decomposition. Such distances allow us to explore a wide space of defects, and perform data augmentation, without the need for explicit parametrization of shapes. Our methodology is detailed on a set of defects observed in welded joints. It is found that reliable results on clustering require a large number of shapes in each mechanical class. Furthermore, a simple neural network was able to link mechanical and geometrical clusters with a satisfying accuracy, within the space of defects close to that observed in welded joints. Nevertheless, the method applies to arbitrary shape, and may be extended to other types of defects. These results should be useful in particular for a refined two-scale hyper reduction method, as outlined in the introduction, where mechanical properties of defects may be selected on the fly, without solving balance equations.

Possible improvements and future works include hierarchical clustering, extension of the spherical harmonics decomposition to non-star shaped defects, and data augmentation with shape extrapolation, instead of interpolation. In particular, the spherical harmonics decomposition provides a natural basis for data augmentation as well as mechanical clustering.

*Availability of data and materials* The data for the present work has presently not been made available.

*Competing interests* The authors declare no competing interests.

*Authors' contributions* F.W., D.R. and J.B. suggested the idea of research and formulated the model problem. The numerical computations and data analysis were carried out by H.L. The manuscript was drafted by H.L. and subsequently extended and edited by F.W. All authors gave their final approval for publication.

*Acknowledgements* The authors wish to thank L. Lacourt for providing the images of defects used in the present study, and to F. N'Guyen for segmenting the numerical images. F. Willot and H. Launay are grateful to J. Angulo for fruitful discussions.

## 7 Appendix

### 7.1 Subdomain definition

To speed up the Grassmann distance between defect a subdomain $\Omega$ of size $(L/2)^3$ has been defined. The Grassmann distance have been evaluated on $\Omega$ and $\partial\Omega$. Figure 18 illustrates the position of $\partial\Omega$ around a spherical defect in cut view.

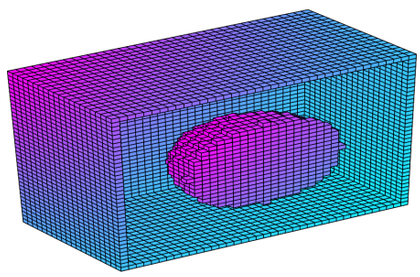

**Fig. 18** Cut view of the subdomain $\partial\Omega$ around a spherical defect.

### 7.2 Neuron network training

A sum up of the loss and accuracy curves are given in Fig.19. The loss function that have been used is the log loss function described in eq.7.

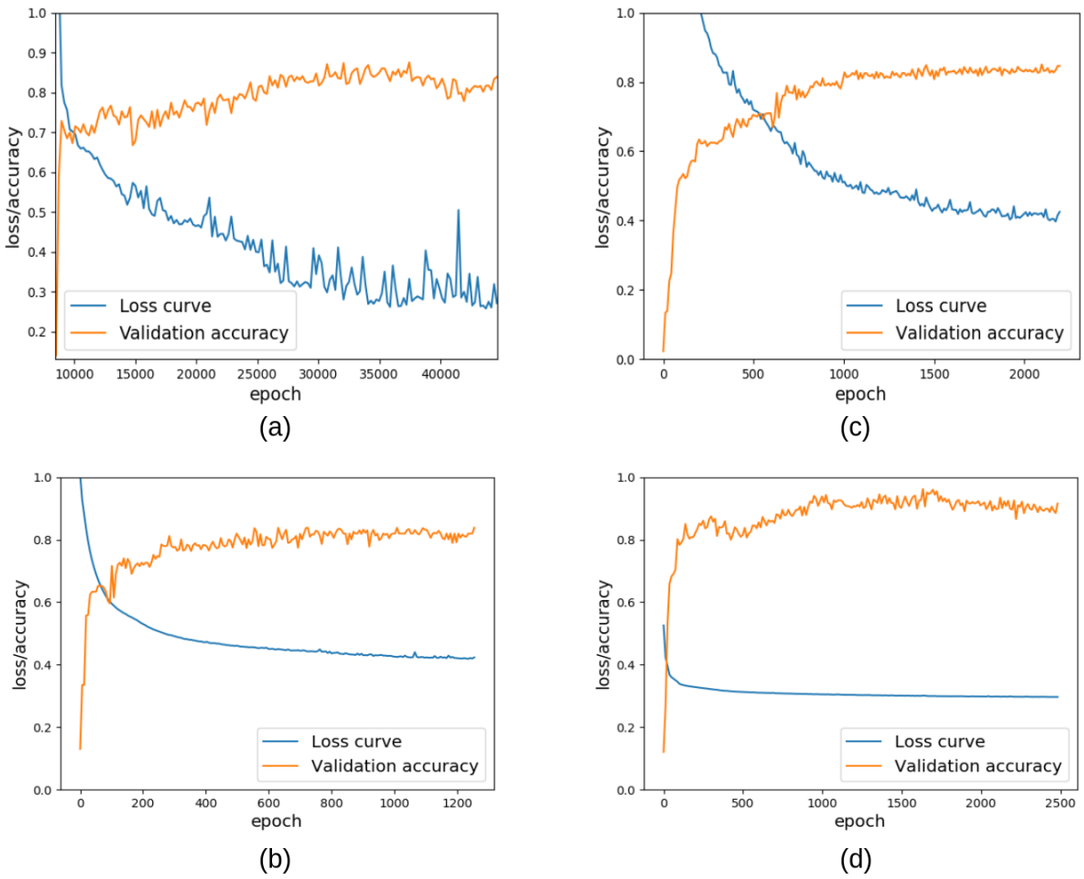


**Fig. 19** Loss and validation for morphological distance ((a) without data augmentation, (c) with data augmentation) and spherical harmonics distance ((b) without data augmentation, (d) without data augmentation).

## References


1. P. Osterrieder, L. Budde, and T. Friedli, "The smart factory as a key construct of industry 4.0: A systematic literature review," *International Journal of Production Economics*, vol. 221, p. 107476, 2020.
2. A. Kusiak, "Smart manufacturing," *International Journal of Production Research*, vol. 56, no. 1-2, pp. 508–517, 2018.
3. J. Rüb and H. Bahemia, "A review of the literature on smart factory implementation," in *2019 IEEE International Conference on Engineering, Technology and Innovation (ICE/ITMC)*, pp. 1–9, 2019.
4. B. Wang, S. Zhong, T.-L. Lee, K. S. Fancey, and J. Mi, "Non-destructive testing and evaluation of composite materials/structures: A state-of-the-art review," *Advances in mechanical engineering*, vol. 12, no. 4, p. 1687814020913761, 2020.
5. J. Wang, L. Ye, R. Gao, C. Li, and L. Zhang, "Digital twin for rotating machinery fault diagnosis in smart manufacturing," *International Journal of Production Research*, vol. 57, no. 12, pp. 3920–3934, 2019.
6. D. Gunasegaram, A. Murphy, M. Matthews, and T. DebRoy, "The case for digital twins in metal additive manufacturing," *Journal of Physics: Materials*, vol. 4, no. 4, p. 040401, 2021.
7. Y. Murakami, "Material defects as the basis of fatigue design," *International Journal of Fatigue*, vol. 41, pp. 2–10, 2012.
8. Y. Murakami and M. Endo, "Effects of defects, inclusions and inhomogeneities on fatigue strength," *International journal of fatigue*, vol. 16, no. 3, pp. 163–182, 1994.
9. M. San Biagio, C. Beltran-Gonzalez, S. Giunta, A. Del Bue, and V. Murino, "Automatic inspection of aeronautic components," *Machine Vision and Applications*, vol. 28, pp. 1–15, 2017.
10. C. Escobar and R. Morales Menendez, "Machine learning techniques for quality control in high conformance manufacturing environment," *Advances in Mechanical Engineering*, vol. 10, p. 168781401875551, 2018.
11. M. Layouni, M. Hamdi, and S. Tahar, "Detection and sizing of metal loss defects in oil and gas pipelines using pattern-adapted wavelets and machine learning," *Applied Soft Computing*, vol. 52, pp. 247–261, 2017.
12. C. Sobie, C. Freitas, and M. Nicolai, "Simulation driven machine learning: Bearing fault classification," *Mechanical Systems and Signal Processing*, vol. 99, pp. 403–419, 2018.
13. S. Dinda, J. Warnett, M. Williams, G. Roy, and P. Srirangam, "3D imaging and quantification of porosity in electron beam welded dissimilar steel to Fe-Al alloy joints by X-ray tomography," *Materials and Design*, vol. 96, pp. 224–231, 2016.
14. S. Lin, S. Shams, H. Choi, and H. Azari, "Ultrasonic imaging of multi-layer concrete structures," *NDT & E International*, vol. 98, pp. 101–109, 2018.
15. G. W. Milton, *The Theory of Composites*. Cambridge: Cambridge Univ. Press, 2003.
16. G. W. Milton, "Some open problems in the theory of composites," *Philosophical Transactions of the Royal Society A*, vol. 379, no. 2201, p. 20200115, 2021.
17. G. Allaire, E. Bonnetier, G. Francfort, and F. Jouve, "Shape optimization by the homogenization method," *Numerische Mathematik*, vol. 76, no. 1, pp. 27–68, 1997.
18. V. V. Jikov, S. M. Kozlov, and O. A. Oleinik, *Homogenization of differential operators and integral functionals*. Springer Science & Business Media, 2012.
19. S. Torquato, *Random heterogeneous materials: microstructure and macroscopic properties*, vol. 16. New-York, USA: Springer Science & Business Media, 2013.
20. L. Tartar, *The general theory of homogenization: a personalized introduction*, vol. 7. Springer Science & Business Media, 2009.
21. L. Liu, "Solutions to the Eshelby conjectures," *Proceedings of the Royal Society A: Mathematical, Physical and Engineering Sciences*, vol. 464, no. 2091, pp. 573–594, 2008.
22. Y. Grabovsky and R. V. Kohn, "Microstructures minimizing the energy of a two phase elastic composite in two space dimensions. II: the Vigdergauz microstructure," *Journal of the Mechanics and Physics of Solids*, vol. 43, no. 6, pp. 949–972, 1995.
23. V. Mantič, A. Barroso, and F. París, "Singular elastic solutions in anisotropic multimaterial corners: applications to composites," in *Mathematical methods and models in composites* (V. Mantič, ed.), pp. 425–495, London: Imperial College Press, 2014.
24. M. L. Williams, "On the stress distribution at the base of a stationary crack," *Journal of Applied Mechanics*, vol. 24, pp. 109–114, 1957.
25. Z. Moschovidis and T. Mura, "Two-ellipsoidal inhomogeneities by the equivalent inclusion method," *Journal of Applied Mechanics*, vol. Trans. ACME, no. 42, pp. 847–852, 1975.
26. C. Fond, A. Riccardi, R. Schirrer, and F. Montheillet, "Mechanical interaction between spherical inhomogeneities: an assessment of a method based on the equivalent inclusion," *European Journal of Mechanics-A/Solids*, vol. 20, no. 1, pp. 59–75, 2001.

27. J. Besson, "Effect of inclusion shape and volume fraction on the densification of particulate composites," *Mechanics of materials*, vol. 19, no. 2-3, pp. 103–117, 1995.
28. P. Franciosi, S. Barboura, and Y. Charles, "Analytical mean green operators/eshelby tensors for patterns of coaxial finite long or flat cylinders in isotropic matrices," *International Journal of Solids and Structures*, vol. 66, pp. 1–19, 2015.
29. J. Rice, "A path independent integral and the approximate analysis of strain concentration by notches and cracks," *Journal of Applied Mechanics*, vol. 35, no. 2, pp. 379–386, 1968.
30. A. Nádai, *Theory of Flow and Fracture of Solids; Volume 2*. New York, NY, McGraw-Hill Book Company Incorporated, 1963.
31. H. Wang, A. Pietrasanta, D. Jeulin, F. Willot, M. Faessel, S. L., and M. Moreaud, "Modeling of mesoporous alumina microstructure by 3D random models of platelets," *Journal of Microscopy*, vol. 260, no. 3, pp. 287–301, 2015.
32. B. Abdallah, F. Willot, and D. Jeulin, "Morphological modeling of three-phase microstructures of anode layers using sem images," *Journal of Microscopy*, vol. 263, no. 1, pp. 51–63, 2016.
33. E. Kaeshammer, L. Borne, F. Willot, P. Dokládal, and S. Belon, "Morphological characterization and elastic response of a granular material," *Computational Material Science*, vol. 190, p. 110247, 2021.
34. J. Angulo and F. Meyer, "Morphological exploration of shape spaces," in *9*$^{\text{th}}$ *International Symposium on Mathematical Morphology and Its Applications to Signal and Image Processing*, vol. 5720 of *Lecture Notes in Computer Science*, (Groningen, Netherlands), pp. 226–237, Springer, 2009.
35. S. Velasco-Forero and J. Angulo, "Statistical shape modeling using morphological representations," in *20*$^{\text{th}}$ *International Conference on Pattern Recognition*, pp. 3537–3540, IEEE, 2010.
36. M. Kilian, N. J. Mitra, and H. Pottmann, "Geometric modeling in shape space," in *ACM Transactions on Graphics (TOG)*, vol. 26, p. 64, 2007.
37. B. Lévy, "Laplace-beltrami eigenfunctions towards an algorithm that" understands" geometry," in *IEEE International Conference on Shape Modeling and Applications 2006 (SMI'06)*, pp. 13–13, 2006.
38. D. Jakobson, N. Nadirashvili, and J. Toth, "Geometric properties of eigenfunctions," *Russian Mathematical Surveys*, vol. 56, no. 6, p. 1085, 2001.
39. L. Shen, H. Farid, and M. McPeek, "Modeling three-dimensional morphological structures using spherical harmonics," *Evolution: international journal of organic evolution*, vol. 63, no. 4, pp. 1003–1016, 2009.
40. K. Zhou, H. Bao, and J. Shi, "3d surface filtering using spherical harmonics," *Computer-Aided Design*, vol. 36, no. 4, pp. 363–375, 2004.
41. G. Gerig, M. Styner, M. Shenton, and J. Lieberman, "Shape versus size: Improved understanding of the morphology of brain structures," in *International Conference on Medical Image Computing and Computer-Assisted Intervention*, pp. 24–32, 2001.
42. J. Feinauer, A. Spettl, I. Manke, S. Strege, A. Kwade, A. Pott, and V. Schmidt, "Structural characterization of particle systems using spherical harmonics," *Materials Characterization*, vol. 106, pp. 123–133, 2015.
43. T. Daniel, F. Casenave, N. Akkari, and D. Ryckelynck, "Model order reduction assisted by deep neural networks (ROM-net)," *Advanced Modeling and Simulation in Engineering Sciences*, vol. 7, no. 1, pp. 1–27, 2020.
44. S. Pan and Q. Yang, "A survey on transfer learning," *IEEE Transactions on Knowledge and Data Engineering*, vol. 22, no. 10, pp. 1345–1359, 2010.
45. L. Lacourt, *Étude numérique de la nocivité des défauts dans les soudures*. PhD thesis, Mines ParisTech – Université PSL, 2019.
46. L. Lacourt, D. Ryckelynck, S. Forest, V. de Rancourt, and S. Flouriot, "Hyper-reduced direct numerical simulation of voids in welded joints via image-based modeling," *International Journal for Numerical Methods in Engineering*, vol. 121, no. 11, pp. 2581–2599, 2020.
47. L. Lacourt, S. Forest, D. Ryckelynck, F. Willot, S. Flouriot, and V. de Rancourt, "étude numérique de la nocivité des défauts dans les soudures," (Presqu'île de Giens), Computational Structural Mechanics Association, 2019. Colloque National en Calcul des Structures, Giens, France, May 13-17, 2019. Online at https://hal.archives-ouvertes.fr/hal-02412756.
48. H. Launay, J. Besson, D. Ryckelynck, and F. Willot, "Hyper-reduced arc-length algorithm for stability analysis in elastoplasticity," *International Journal of Solids and Structures*, vol. 208–209, pp. 167–180, 2020.
49. J. Fauque, I. Ramiere, and D. Ryckelynck, "Hybrid hyper-reduced modeling for contact mechanics problems," *International Journal for Numerical Methods in Engineering*, vol. 115, no. 1, pp. 117–139, 2018.
50. D. Ryckelynck, T. Goessel, and F. Nguyen, "Mechanical dissimilarity of defects in welded joints via grassmann manifold and machine learning," *Comptes Rendus. Mécanique*, vol. 348, no. 10-11, pp. 911–935, 2020.
51. F. Willot, B. Abdallah, and Y.-P. Pellegrini, "Fourier-based schemes with modified green operator for computing the electrical response of heterogeneous media with accurate local fields," *International Journal for Numerical Methods in Engineering*, vol. 98, no. 7, pp. 518–533, 2014.
52. J. Gasnier, F. Willot, H. Trumel, D. Jeulin, and J. Besson, "Thermoelastic properties of microcracked polycrystals. Part I: Adequacy of Fourier-based methods for cracked elastic bodies," *International Journal of Solids and Structures*, vol. 155, pp. 248–256, 2018.
53. D. Amsallem and C. Farhat, "Interpolation method for adapting reduced-order models and application to aeroelasticity," *AIAA Journal*, vol. 46, no. 7, pp. 1803–1813, 2008.
54. R. Mosquera, A. Hamdouni, A. El Hamidi, and C. Allery, "POD basis interpolation via inverse distance weighting on grassmann manifolds," *Discrete and Continuous Dynamical Systems – S*, vol. 12, no. 6, pp. 1743–1759, 2018.
55. R. Shigenaka, B. Raytchev, T. Tamaki, and K. Kaneda, "Face sequence recognition using grassmann distances and grassmann kernels," in *The 2012 International Joint Conference on Neural Networks (IJCNN)*, pp. 1–7, IEEE, 2012.
56. K. Ye and L.-H. Lim, "Schubert varieties and distances between subspaces of different dimensions," *SIAM Journal on Matrix Analysis and Applications*, vol. 37, no. 3, pp. 1176–1197, 2016.
57. E. Garboczi, "Three-dimensional mathematical analysis of particle shape using X-ray tomography and spherical harmonics: Application to aggregates used in concrete," *Cement and Concrete Research*, vol. 32, no. 10, pp. 1621–1638, 2002.
58. L. Shen, H. Farid, and M. McPeek, "Modeling three-dimensional morphological structures using spherical harmonics," *Evolution*, vol. 63, no. 4, pp. 1003–1016, 2009.
59. H. Park and C. Jun, "A simple and fast algorithm for K-medoids clustering," *Expert Systems with Applications*, vol. 36, no. 2, Part 2, pp. 3336–3341, 2009.
60. I. Borg and P. Groenen, *Modern multidimensional scaling: Theory and applications*. Springer Science & Business Media, 2005.

## 4.3 Application to a simple welded structure

### 4.3.1 Goals

The aim of this section is to put into practice the reduced basis selection method that has been detailed in the previous section 4.2. Based on the morphological shape of the defect, a neuronal network is recommending the most appropriate reduced basis. This selected reduced basis is then used for a hyper reduced computation. Such recommending system is termed ROM-net [Daniel et al., 2020].Here the idea is not to measure the performance of the classier but rather to evaluate the results of the hyper reduced predictions.

### 4.3.2 Structure and mechanical problem

The structure that is used for this example is a welded joint. It is represented with two steel plates linked by a weld (represented in red in Fig.4.1b). This structure is obtained with the sofware zDefects. The welded zone is randomly defined, it is not perfectly centered and is not perfectly symmetric either. Its curves are obtained with Bézier functions. The dimensions of the struture are $2.5mm$ heigh, $20mm$ length and a $5mm$ extrusion is then done (see Fig.4.1a). A defect is inserted at the center of the welded zone. The element used for the mesh are linear tetrahedrons and the number of degree of freedom $\mathcal{N}$ varies with the shape of defect that is considered. It is around $\mathcal{N} = 160\ 000$ (Fig. 4.1b).

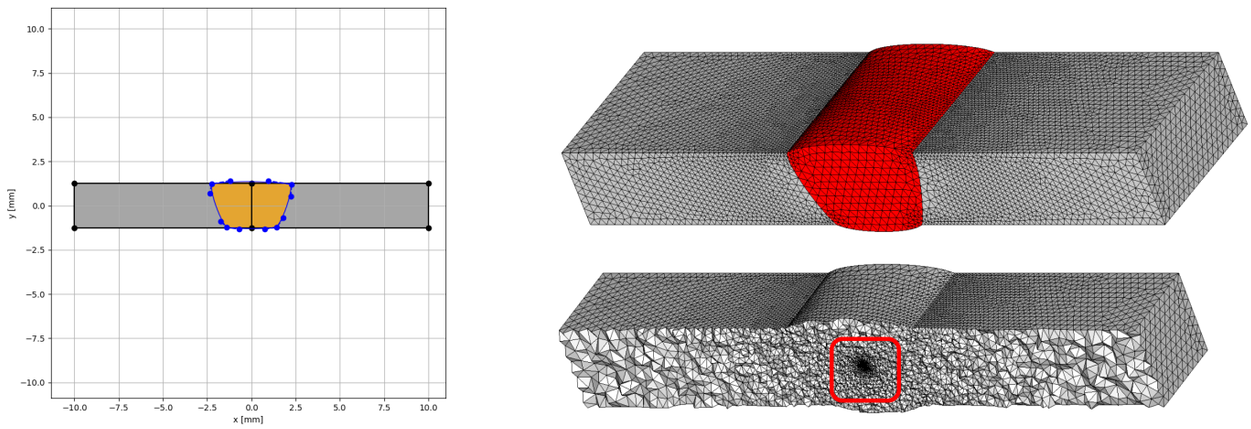


(a) (b)

Figure 4.1: (a) Sketch of the two plates and the welded joint (b) 3D mesh of the welded structure and a cut view with the localisation of the defect (red square).

The two plates are elastic as well as the welded zone. In this part of the study the small strain hypothesis is admited.

$$\begin{cases} \text{Strain :} & \underset{\sim}{\varepsilon} = \frac{1}{2}(\underset{\sim}{\nabla} u + \underset{\sim}{\nabla} u^T) \\ \text{Constitutive law :} & \underset{\sim}{\sigma} = \underset{\approx}{\mathbb{C}} : \underset{\sim}{\varepsilon} \\ \text{Second invariant of the stress tensor :} & J_2(\underset{\sim}{\sigma}) = \sqrt{\frac{3}{2}\ dev(\underset{\sim}{\sigma}) : dev(\underset{\sim}{\sigma})} \\ \text{Equilibrium :} & \text{div}(\underset{\sim}{\sigma}) = 0 \end{cases} \tag{4.1}$$

The Young modulus of the welded zone is $E = 190GPa$ and for the two plates is equal to $E = 210GPa$. In both cases the Poisson coefficient is equal to $\nu = 0.3$. Concerning the boundary conditions, the left side of the structure is fully clamped while a horizontal displacement of $2mm$ is imposed on the right side.

### 4.3.3 Methodology

The global methodology has been defined in the section 4.2. In this section, for the sake of simplicity, the computation of the reduced basis and the computation of the whole structure have been done with the finite element method. The complete computation chain is illustrated in Fig.4.2.

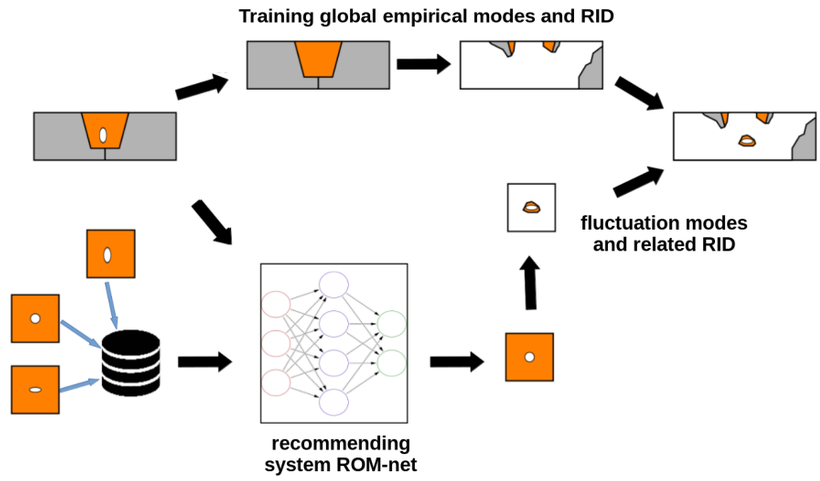


Figure 4.2: Online scheme.

For this application the defect number 2790 (which has a rather complex shape) is considered. Its medoid is the defect number 67 The selection of its medoid has been done with the methodology detailed in section 4.2 (see Fig.4.3).

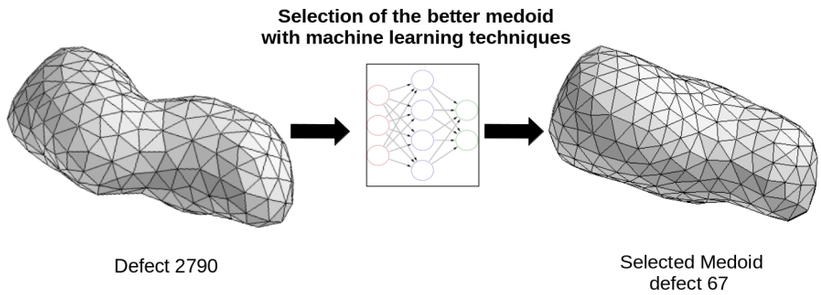


Figure 4.3: Selection of the associated medoid for defect 2790 with machine learning techniques.

The global modes can be computed in advance and once for all since the global structure is always the same. Here, local defects do not change effective material properties. Similarly the local modes will not have to computed since it is the ones of the selected medoid (already computed) that will used (Fig.4.4a, Fig.4.4b).

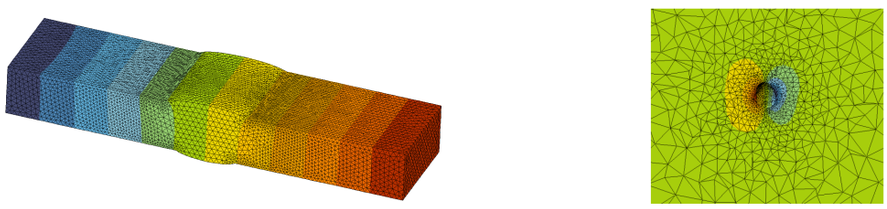

(a) (b)

Figure 4.4: (a) Visualisation of one of the global modes, (b) visualisation of one of the local modes.

The local reduced basis of the defect $V^d$ is introduced. The reduced basis has been computed thanks to a computation on a representative elementary volume (REV) and has been transferred on the true complete mesh (containing the true defect) afterwards. Identically the reduced basis of the structure without defect $V^s$ has been transferred on the real mesh with defect afterward. The reduced basis used for the hyper reduced computation of the structure with defect is the concatenation of these two reduced basis $V^{tot} = [V^s, V^d]$ as proposed in [Lacourt, 2019, Lacourt et al., 2020].
In order to improve the results during the hyper reduced computation, a finite element correction is applied. It consists in applying the displacement, solution of the hyper reduced computation, on the frontier of the reduced integration domain and used this displacement as Dirichlet boundary conditions for a small classical finite element problem. The correction phase is rather fast since the finite element problem is made on a reduced integration domain. This correction enables to minimize the error due to the fact that a different reduced basis from the one of the considered defect is used. At the frontier of the RID the field of the real reduced basis and the one of the medoid are quite similar.

### 4.3.4 Elastic behaviour

Firstly a single defect is considered : defect number 2790. An elastic computation is launched on the latter. The von Mises stress fields seem identical with the hyper reduced order model (HROM) and with the full order model (FOM) (Fig.4.5).

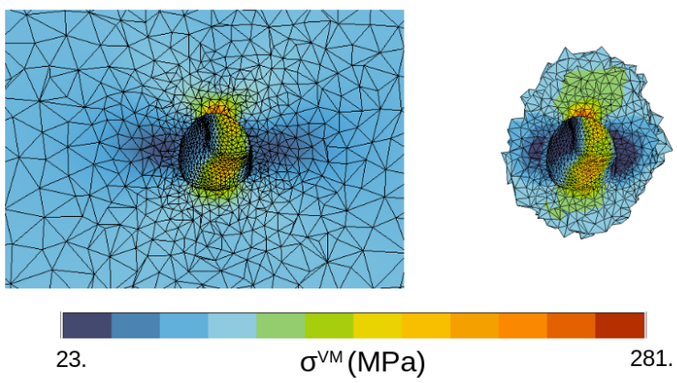


Figure 4.5: Von Mises stress field of defect 2790 with the FOM (left) and with the HROM (right).

A graphic comparing the von Mises stress at each Gauss point for the two different simulations is made in order to evaluate the error between the two models (Fig. 4.6).

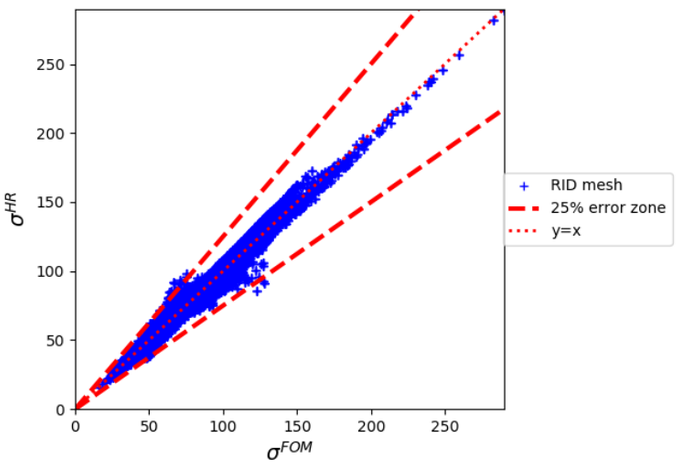


Figure 4.6: Comparison of the von Mises stress between the FOM and the HROM.

Fig. 4.6 shows that the error is inferior to 25% and illustrates that the method works well in this case for the defect 2790.
A statistical study is then made in order to have a more global view of the method. The error is defined in equation 4.2.

$$\eta^{\sigma} = \frac{\int_{\Omega} |\Delta\sigma^{VM}|}{\int_{\Omega} \sigma^{VM}_{FOM}}, \qquad \text{where } \Delta\sigma^{VM} = \sigma^{VM}_{FOM} - \sigma^{VM}_{HR}, \tag{4.2}$$

The so developed method enables to associate a reduced basis to a new defect based on morphological criterion. With the purpose of seeing the assets of this method, three groups of defects are defined. Defects for which the right medoid has been found, defects for which a wrong medoid has been selected and a group of defects for which always the same medoid (randomly picked) has been taken. The last group is very important since it does not use the classifier. To the contrary for the group of defect that has been badly classified, it has been shown in section 4.2 that the wrong medoid is usually a neighbour of the right medoid. Similar results have been obtained in [Daniel et al., 2020] when considering random temperature fields as input images for hyper-reduction modelling. Therefore the mechanical response for this group is probably not as bad as if a random medoid was taken. It is the third group that will enable to see whether this hypothesis is right or not. Fig. 4.7a shows the probability density function on the error $\eta^{\sigma}$ whereas Fig. 4.7b represents the cumulated probability of the error $\eta^{\sigma}$.

Fig. 4.7a shows that the use of such a classifier enables to have errors in average equal to 2.1% when the right medoid is selected, 4.47% when the classifier gives a wrong medoid and 12.38% when a random medoid is used. One can notice that the larger the RID around the defect the

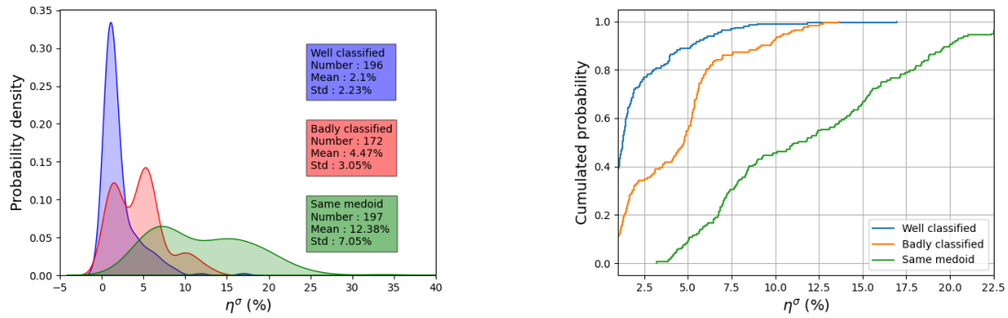


(a) (b)

Figure 4.7: (a) Probability density function for the error $\eta^\sigma$ (b) Cumulated probability for the error $\eta^\sigma$.

lower the variability of boundary conditions when computing a finite element correction around the defect, because displacement fluctuations are decreasing functions of the distance to the defect. With the cumulated probability show in Fig. 4.7b it is possible to evaluate the 95% quantiles. The following values are obtained 6.70%, 10.79% and 22.51% respectively for the well classified defects, badly classified defects and when always the same random medoid is taken. These graphs clearly show that the error is much lower when a wrong medoid is given by the classifier than when a random medoid is used. As supposed before this is due to the fact that when the classifier gives a wrong medoid, it is a neighbour medoid that is selected.
One tries to know whether a relation between the morphological distance between a defect and its medoid and the error between the FOM and the HROM exists. Therefore a graphic is drawn with the morphological distance of the defects to their medoid in x axis and the error $\eta^\sigma$ in y axis (Fig. 4.8). The defects that have been selected to draw this graph are the defects that have been well classified. The following notation is introduced $d^m(\mathcal{P}_i^k, m^k)$ where $d^m$ corresponds to the morphological distance (detailed in section 4.2), $\mathcal{P}_i^k$ is the defect $i$ associated to the medoid of the cluster $k$ and $m^k$ is the medoid of the cluster $k$.

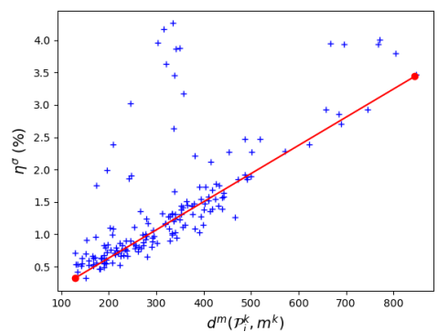


Figure 4.8: Error $\eta^\sigma$ as a function of the morphological distance.

An imperfect relation seems to exists betweeen the morphological distance to the medoid and the error made during the HR computation. By applying the least mean square method to obtain the better linear relation (shown in red on Fig. 4.8), the mean relative error between the linear relation and the data and is equal to 28.0%. The $R^2$ score whose formula is given in eq.4.3 and is equal to 0.51.

$$R^2 = 1 - \frac{RSS}{TSS} \tag{4.3}$$

$$RSS = \sum_i (\eta_i^\sigma - f_i)^2 \tag{4.4}$$

$$TSS = \sum_i (\eta_i^\sigma - \bar{\eta^\sigma})^2 \tag{4.5}$$

Where $R^2$ is the coefficient of determination, $TSS$ is the total sum of squares and $RSS$ is sum of squares of residuals. $f_i$ is the value of the error estimation with the linear fit and $\bar{\eta^\sigma}$ is the average error estimation of all data. The relation being not perfect, this method can not be seen as an error estimator. Nevertheless an interesting indication is given with this graph. The found relation seems to be close to a lower bound which is less conservative for the error estimation.
When HROMs are used, large speed ups are obtained if $N^3 \ll \mathcal{N}$. Where $N$ represents the number of modes contained in the reduced basis (here $N = 7$) and $\mathcal{N}$ the number of dof of the FOM. As explained in 4.3.3 a finite element correction is applied in order to improve the results. Hence to have large speed ups the following condition is required : $(N^3 + \mathcal{F}) \ll \mathcal{N}$. With $\mathcal{F}$ the

number of dof of the RID which is around 8 500. In the studied case the following inequality is obtained :

$$\frac{\mathcal{N}}{(N^3+\mathcal{F})} \approx 18 \tag{4.6}$$

This ratio is not so hight therefore it is not possible to achieve large speed ups as it can be seen on Tab. 4.9.

| | CPU time | Speed up |
|---|---|---|
| FOM | 2445 | |
| Local RB computation | 368.9 | |
| HROM | 462.57 | 5.28 |
| HROM Medoid | 93.67 | 26.10 |

Figure 4.9: Table of speed ups

### 4.3.5 Plastic behaviour

In this section the welded joint is supposed to have an elasto plastic behaviour (without hardening). Both plates stays with an elastic behaviour. The modifications due to plasticity are not taken into account for the construction of the reduced basis of the defects. The reduced basis of the defect only contains the elastic modes. It is supposed that the plasticity is very local and that the finite element correction is sufficient to correct the local modifications due to the adding of the plasticity. The plastic behaviour of the welded joint is described by eq.4.7.

$$\begin{cases} \text{Strain :} & \underset{\sim}{\varepsilon} = \frac{1}{2}(\underset{\sim}{\nabla} u + \underset{\sim}{\nabla} u^T) \\ \text{The elastic/plastic partition is supposed :} & \underset{\sim}{\varepsilon} = \underset{\sim}{\varepsilon}^e + \underset{\sim}{\varepsilon}^p \\ \text{Constitutive law :} & \underset{\sim}{\sigma} = \underset{\approx}{\mathbb{C}} : \underset{\sim}{\varepsilon}^e \\ \text{Second invariant of the stress tensor :} & J_2(\underset{\sim}{\sigma}) = \sqrt{\frac{3}{2}\, dev(\underset{\sim}{\sigma}) : dev(\underset{\sim}{\sigma})} \\ \text{Yield stress :} & R_0 \\ \text{Yield function :} & f(\underset{\sim}{\sigma}, R) = J_2(\underset{\sim}{\sigma}) - R_0 \\ \text{Equilibrium :} & \text{div}(\underset{\sim}{\sigma}) = 0 \end{cases} \tag{4.7}$$

The yield stress of the welded zone is equal to $R_0 = 200MPa$.
Fig. 4.10 shows the cumulated plasticity field for the FOM and the HROM.

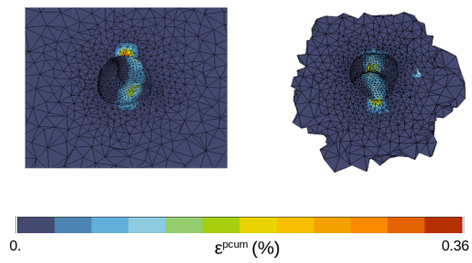


Figure 4.10: Cumulated plasticity field of defect 2790 with FOM (left) and HROM (right).

The value of the cumulated plasticity is rather small but it corresponds to the classical elasticity limit of 0.2%.
A graph comparing the von Mises stress and the cumulated plasticity for both simulations (FOM and HROM) is made in order to evaluate discrepancies between the two models (Fig. 4.11a and Fig. 4.11b)

The error is less than 25% and shows that the so developed methodology works well for defect 2790 and that it can be extended to plastic case as long as the plastic field is very local. A statistical study is then carried out with the purpose of having a more global view of the method. The error on the plasticity is defined in equation 4.8.

$$\eta^{\varepsilon} = \frac{\int_\Omega |\Delta\varepsilon^{pcum}|}{\int_\Omega \varepsilon^{pcum}_{FOM}}, \qquad \text{where } \Delta\varepsilon^{pcum} = \varepsilon^{pcum}_{FOM} - \varepsilon^{pcum}_{HR}, \tag{4.8}$$

The probability density as well as the cumulated probability are shown on Fig. 4.12a and Fig. 4.12b.

It can be seen on Fig. 4.12a that the use of such a classifier enables to have average errors of 23.37% when the right is selected, 32.76% when the classifier makes is wrong and 45.0% when the same random medoid is always taken. The 95% quantile shown in Fig. 4.12b give the following results 42.00%, 52.79% and 66.30% respectively for the well classified, badly classified and when the same medoid is used. Once again, as for the elastic case, it can be seen that when the classifier gives a wrong medoid the error is smaller than when a random medoid is taken.

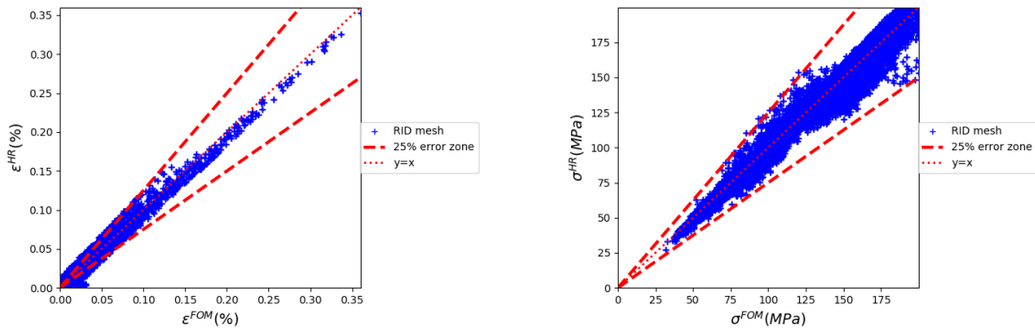


(a) (b)

Figure 4.11: (a) Comparison of the cumulated plasticity and (b) of the von Mises stress between the FOM and the HROM.

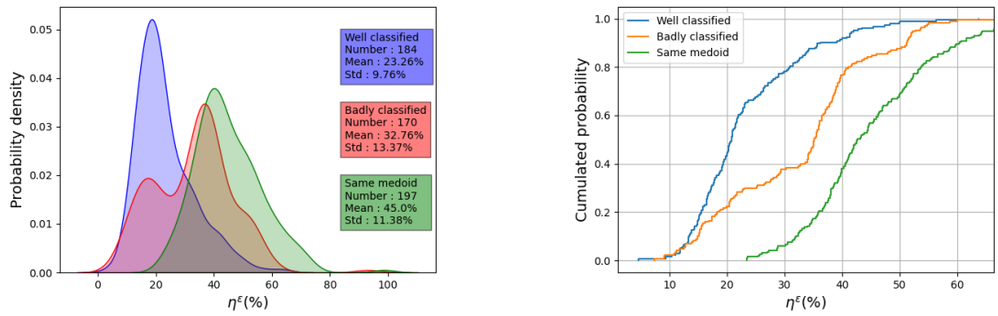


(a) (b)

Figure 4.12: (a) Probability density function for the error $\eta^{\varepsilon}$ (b) Cumulated probability for the error $\eta^{\varepsilon}$.

The errors obtained in the plastic case are much larger than in the plastic case.
Similarly to what have been done in the elastic case, the hypothesis of a relation between the error $\eta^{\varepsilon}$ obtained during the HROM simulation and the morphological distance to the medoid is investigated (Fig. 4.13).

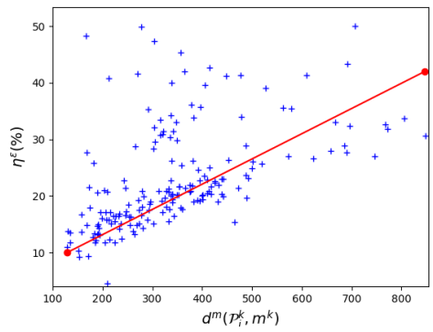


Figure 4.13: Error $\eta^{\varepsilon}$ as a function of the morphological distance.

As for the elastic case, an imperfect relation seems to exist between the error $\eta^{\varepsilon}$ and the morphological distance. Once again the least mean square method is applied to obtain a linear relation. The mean relative error between this relation and the data is equal to 27.9% and the $R^2$ scare is equal to 0.22.

| | CPU time | Speed up |
|---|---|---|
| FOM | 6927 | |
| Local RB computation | 368.9 | |
| HROM | 523.8 | 13.2 |
| HROM Medoid | 154.9 | 44.8 |

Figure 4.14: Tableau des speed ups dans le cas plastique

Speed ups are larger when plasticity is taken into account. Since the ratio between the modes, the dof of the full mesh and the dof of the RID is still the same, it is not possible to

achieve large speed ups.

Since the effect of plasticity is directly linked with the loading history, it is interesting to apply a non monotonous loading to the structure. The point C is spotted on Fig. 4.15a, it corresponds to the location where the plasticity is the most important. One cycle of traction, compression and return to the initial position is applied on the structure as indicated on Fig. 4.15b.

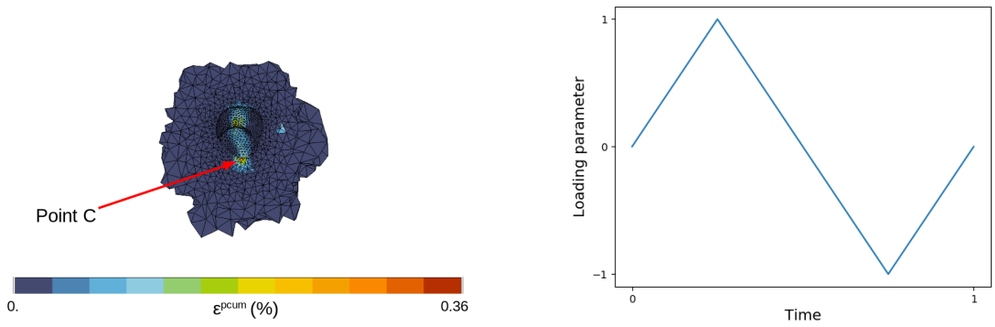


(a) (b)

Figure 4.15: (a) Position of point C where the plasticity is the most important (b) loading cycle function.

Since the point C belongs to the RID, it is possible to draw all the components of the stress and strain tensors during the computation for this point (Fig. 4.16).

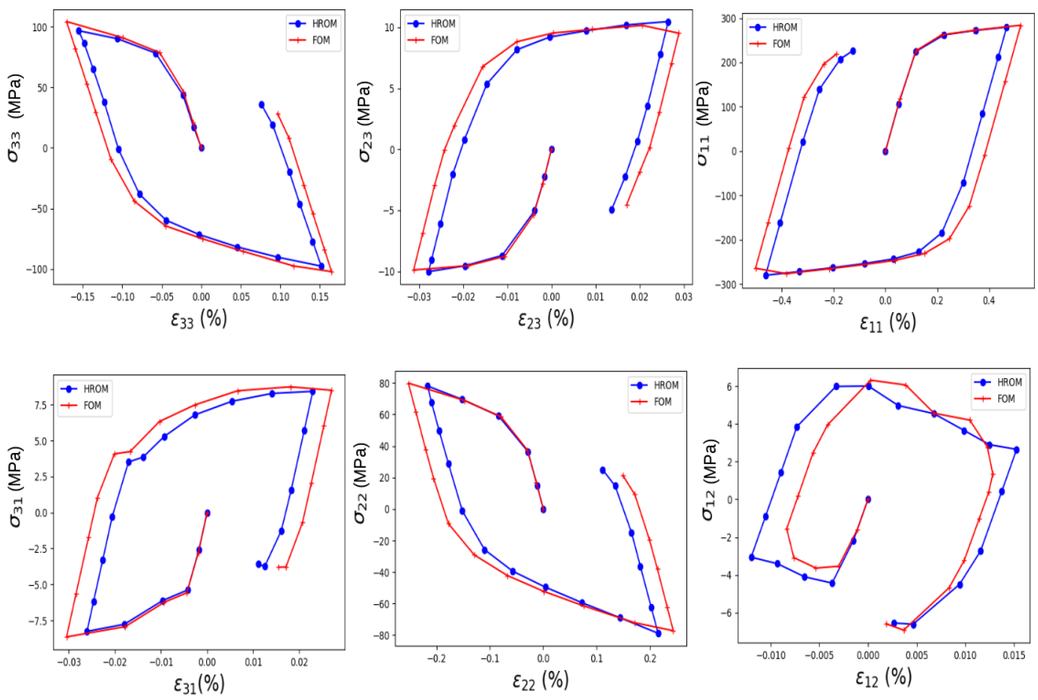


Figure 4.16: Cycle de chargement mesuré au point C.

For this study case of defect 2790, the loading curves for every components are very similar between the FOM and the HROM.
Speed ups obtained for the non monotonous load are detailed in Tab 4.17.

| | CPU time | Speed up |
|---|---|---|
| FOM | 70370 | |
| Local RB computation | 368.9 | |
| HROM | 1706 | 41.2 |
| HROM Medoid | 1338 | 52.6 |

Figure 4.17: Tableau des speed ups dans le cas plastique

Speed ups are very similar to the one obtained with the monotonic loading for the HROM with medoid selection approach. The speed up of the standard HROM method is large since training of the local reduced basis is preformed on the first elastic step which represent a small fraction of the cyclic loading.
Larger speed ups can be obtained by reducing the RID. Nevertheless this method is directly link to the size of the RID. The smaller the RID the closer to the defect the frontier of the RID

is. Since the BC that are applied are relative to these of the medoid and not to the considered defect if the frontier of the RID are to close of the defect, bad results will be obtained. A trade of between speed and accuracy has to be made.
When the RID is very large the impact of the global modes of the defect is not useful since the finite element correction is sufficient to capture precisely the fluctuation around the defect. But in this case barely no speed up will be obtained since most of the dof are located around the defect. To the contrary if the RID is small enough it is necessary to use the modes contained in the reduced basis of the selected medoid. This has been highlighted with the naive model.

### 4.3.6 Conclusion and outlooks

Results obtained for the elastic case are satisfying. The mean error and the 95% quantile when the classifier gives the right answer are respectively of 2.23% and 6.67%. The error when the classifier is wrong are still inferior to these of obtained when always the same random medoid is used. This is due to the fact that a neighbour of the right medoid is taken.
Error in the plastic case are larger.The mean error and the 95% quantile when the classifier gives the right answer are respectively of 23.37% and 42.0%. It is very likely that increasing the number of cluster would give much better results for the HROM computation. As the tendency shows, for both elastic and plastic cases, the higher the distance to the medoid the larger the error. The use of divisive hierarchical clustering might be also a good approach to avoid the problematic due to the high number of spherical defect. This would increase the variety of the medoids. The morphological and mecanical diversity of the cluster so formed should improve the HROM computation predictions.
Another interesting approach would be to apply to the medoid not the six elastic loading but rather the loading that the gauss point located where the defect should be in the sane structure sees. This is the methodology that is used in [Lacourt, 2019, Lacourt et al., 2020]. The so constructed reduced basis should be more appropriate for the HROM computation.
It is important to keep in mind that this section played the role of proof of concept.

# Chapter 5

# Machine learning for the assessment of non parametric cracks in structures

**Contents**




**Résumé en français**

En mécanique des milieux continus, la prédiction de la nocivité des défauts nécessite de résoudre approximativement des équations différentielles partielles avec des conditions aux limites données. Dans ce chapitre, les conditions aux limites sont apprises pour de petits volumes locaux dénotés "Tight Little Volumes" (TLV) qui entourent les fissures dans des volumes 3D. Une approche non-paramétrique basée sur les données est utilisée pour définir l'espace des défauts, en considérant des défauts observés par tomographie à rayons X. La dimension de l'espace ambiant pour les images observées des défauts est énorme. Un schéma non-linéaire de réduction dimensionnelle est proposé afin de former un espace latent réduit pour la morphologie des défauts et leurs effets mécaniques locaux dans le TLV. Les autoencodeurs multimodaux permettent de mélanger des données morphologiques et mécaniques. Il contient un seul espace latent qui est ici appelé espace latent mécanique. Mais cet espace latent est alimenté par deux encodeurs. L'un est lié aux images des défauts et l'autre aux champs mécaniques dans le TLV. Les variables latentes sont des variables d'entrée pour un décodeur géométrique et pour un décodeur mécanique. Dans ce travail, les variables mécaniques sont des champs de déplacement. L'autoencodeur sur les variables mécaniques permet de réduire la taille du modèle par projection.
La principale nouveauté de ce document est une approche de sous-modélisation assistée par l'intelligence artificielle. Ici, pour les images de fissure de l'ensemble de test, les conditions limites de Dirichlet sont appliquées au TLV. Ces conditions limites sont prévues par le décodeur mécanique avec un vecteur latent prévu par l'encodeur morphologique. C'est dans ce but qu'un "mapping" est effectué par réseau de neurones pour convertir les variables latentes morphologiques en variables latentes mécaniques. Ce "mapping" est dénoté "direct mapping". Un "inverse mapping" est également formé pour l'estimation de l'erreur par rapport aux prédictions morphologiques.
Les erreurs sur les prédictions mécaniques sont proches de 5% avec des accélérations de calcul allant jusqu'à 120 fois plus vite. Les variables latentes prédites par les images des défauts sont propices à une meilleure compréhension des prédictions.


## 5.1 Introduction

First models to predict failure of cracked structures have been designed more than 50 years ago. Firstly, they were proposed in the framework of linear fracture mechanics and then extended to plasticity and viscoplasticity through nonlinear fracture mechanics about 30 years ago. The Stress Intensity Factor (SIF) helps describing the state of the stress as well as the level of stress singularity around the crack tip [Irwin, 1957]. The SIF plays a major role when linear elastic fracture is considered. It is also widely used for the prediction of fatigue life of structural components. The importance of SIF is such that numerous analytical, experimental and numerical methods are available for its determination. Many analytical and semi-analytical solutions are available [Tada et al., 2000, Henshell and Shaw, 1975]. Nevertheless these solutions are valid for simple cracked configurations only. The computation of the SIF can also be done thanks to numerical methods such as the FEM.
The inverse square root singularity which exists at the crack tip, makes it difficult to evaluate the SIF. Various numerical techniques exist to compute the SIF, one can cite displacement extrapolation technique (DET) [Barsoum, 1977], interior collocation technique [Jogdand and Murthy, 2010], interaction integral (I-integral) [Shih et al., 1986] and J-integral [Rice, 1968].

The J-integral method is widely used nowadays. The SIF computation is particularly usefull when fatigue crack propagation is studied. Though these previous methods make it possible to estimate the criticality of a crack, their executive processes are usually complex and difficult. Indeed a large number of DOFs is needed around the crack front and leads to large meshes and important computation times. Moreover the SIF directly depends on the input conditions including the applied loadings, geometrical boundaries, as well as crack sizes and shapes among other things. In order to avoid these large computations, one could make surrogate models to evaluate the SIF but the large number of inputs needed (such as applied loadings, geometrical boundaries, as well as crack sizes and shapes) makes it difficult to parametrize the response.
Machine learning approaches can be a way to overcome this problem. More precisely deep learning methods using image processing techniques have been used to study cracks [Jang et al., 2019, Bae et al., 2021]. Various models are used for deep learning applications and one of the most popular is the Convolutional Neural Networks (CNNs). Their major advantage is that they need less computation than standard neuronal networks since their neurones are sparsely connected. Moreover some processes, such as "pooling", reduce the number of parameters to fit [LeCun et al., 2015]. CNNs have proven themselves in the field of image recognition and have been extended to the field of defect detection. For example a deep CNN have been used in [Cha et al., 2017] to spot cracks in concrete structures.
Other CNNs have been trained to detect crack under water in the framework of nuclear inspection videos [Chen and Jahanshahi, 2018]. In the cited work the CNNs detects whether a crack exists or not, but the model does not estimate its criticality. The precise evaluation of the degree of damage of the structure is necessary in order to rule on the safety of the structure. Here, the proposed approach couples CNN to finite element predictions, via image-based estimation of boundary conditions. It paves the way for a new transfer learning of knowledge from mechanics of material to computer vision for defect harmfulness assessment.
The rest of this chapter is taken from a manuscript submitted to International Journal for Numerical Methods in Engineering with the following DOI : https://doi.org/10.1002/nme.6905.

## 5.2 Deep Multimodal autoencoder for crack criticality assessment

# Deep Multimodal autoencoder for crack criticality assessment

H. Launay[a], D. Ryckelynck[a,*], L. Lacourt[a], J. Besson[a], A. Mondon[a], F. Willot[a,b]

[a]*Mines Paris, PSL research university, Centre des Matériaux, CNRS UMR 7633, 91003 Évry, France*
[b]*Mines Paris, PSL research university, Centre de Morphologie Mathématique, 77300 Fontainebleau, France*

Published in International Journal of Numerical Engineering. DOI : https://doi.org/10.1002/nme.6905

**Abstract**

In continuum mechanics, the prediction of defect harmfulness requires to solve approximately partial differential equations with given boundary conditions. In this contribution boundary conditions are learnt for tight local volumes (TLV) surrounding cracks in 3D volumes. A non-parametric data-driven approach is used to define the space of defects, by considering defects observed via X-Ray computed tomography [1, 2]. The dimension of the ambient space for the observed images of defects is huge. A nonlinear dimensionality reduction scheme is proposed in order to train a reduced latent space for both the morphology of defects and their local mechanical effects in the TLV. A multimodal autoencoder [3] enables to mix morphological and mechanical data. It contains a single latent space, termed mechanical latent space. But this latent space is fed by two encoders. One is related to the images of defects and the other to mechanical fields in the TLV. The latent variables are input variables for a geometrical decoder and for a mechanical decoder. In this work, mechanical variables are displacement fields. The autoencoder on mechanical variables enables projection-based model order reduction as proposed in [4]. The main novelty of this paper is a submodeling approach assisted by artificial intelligence. Here, for defect images in the test set, Dirichlet boundary conditions are applied to TLV. These boundary conditions are forecasted by the mechanical decoder with a latent vector predicted by the morphological encoder. For that purpose, a mapping is trained to convert morphological latent variables into mechanical latent variables, denoted "direct mapping". An "inverse mapping" is also trained for error estimation with respect to morphological predictions. Errors on mechanical predictions are close to 5% with simulation speed-up ranging for 3 to 120. We show that latent variables forecasted by the images of defects are prone to a better understanding of the predictions.

*Keywords:* Multimodal autoencoder; CNN; Transfer Learning; Finite Element Method; Digital Twin

## 1. Introduction

The assessment of cracked structures is still an active field of research in mechanical engineering [5]. Charts [6] can be used to estimate some quantities of interest on cracked structures but they are not accurate enough and are focused on specific cases. Finite element methods can be used to improve results and to deal with arbitrary crack configurations. Chart-based and other equivalent methods give a criterion for deciding if a component is safe or unsafe. Although this is sufficient in practice for deciding if a component must be

*Corresponding author
*URL:* david.ryckelynck@mines-paristech.fr (D. Ryckelynck)

rejected, these approaches are less robust than methods making use of full-field numerical computations, that provide more information as well as an understanding of the mechanical phenomena involved. Nevertheless such an approach leads to prohibitive computation times due to the fact that the crack needs to be meshed very finely. In this work focus is made on planar cracks in 3D volumes.

Moreover mechanical data are expected to fulfill partial differential equations (PDE) and neural networks have been proposed to solve partial differential equations in [7]. Machine learning algorithms have recently been proposed to analyse the criticality of defects for pipelines [8], in the aeronautical field [9] and for fabrication process [10]. Besides machine learning and numerical simulation have proven their complementarity for example for the study of defect in ball bearings [11]. The Simulation-driven machine learning approach is very attractive when we have mechanical models at our disposal. The use of machine learning techniques enables us to get rid of the parametrization of the object to model. This is crucial when considering defects observed by imaging techniques.

Besides the efficiency of multimodal autoencoder (MMAE) have recently been shown [12, 13]. The aim of this method is to use different inputs such as sound, text or images for example and reconstruct them after having compressed them in a common smaller latent space [3]. In the online phase a single input channel can be used to reconstruct all the output channels, this is denoted the cross-modal reconstruction.

In the present work, we show that morphological data and mechanical data related to defects are sharing a common latent space designed using MMAEs. In this paper a digital twin of a specimen containing non parametric cracks is considered. A multimodal autoencoder is trained with two different channels being the 2D crack image and its associated 3D displacement field. In the online phase the 2D image is used as input to reconstruct the 2 channels. The reconstructed displacement field is then transferred on the external surface of a tight local volume (TLV) and used as boundary condition of a small finite element problem. Since the boundary conditions are learnt, a full-field numerical computations on the entire system is not required. This results in better speed-up compared to a submodelling approach where additional simulations at the global scale have to predict these boundary conditions. Moreover, the bounding box in a submodel approach must be rather large so that the crack-induced fluctuations on the boundary can be neglected. An accurate prediction of the boundary conditions, including for small subdomains, is among the main goals of the presently-developed MMAE model. Also, contrary to surrogate models, we carry out classical finite element computations in the subdomain. This approach provides much more information on the mechanical response induced by the crack, that may in turn be interpreted.

The reconstructed 2D image will be used to define an error indicator. We then determine whether a linear relationship exists between the 2D image reconstruction and the error committed on 3D displacement field reconstruction.

## 2. Dataset and mechanical problem

In this work a tensile test is simulated on a specimen containing a crack inside the bulk material. The size of the crack compared to that of the specimen is not negligible and may have an impact larger than 20% on the limit load. The position of the crack varies slightly in the middle plane of the specimen but the shapes and sizes of the cracks vary greatly.

The defect dataset that is used in this study are random 2D planar cracks. They are generated by taking slices of 3D defects obtained from tomography [14, 2]. The resulting defects are therefore 2D images representing non-parametric cracks. Hence it is important to keep in

mind that this dataset is purely artificial and is not based on actual images of cracks. A large variety of cracks is obtained with various shapes and, for some of them, the 2D image containing the defect contains more than one crack. Since every crack is created with a 2D image, they are all planar cracks. A histogram measuring how close the defects are to a convex shape is represented in Fig. (1). The convexity criterion is the ratio between the perimeter of the crack, seen as a shape in a plane, and that of the convex envelope, included in the same plane.

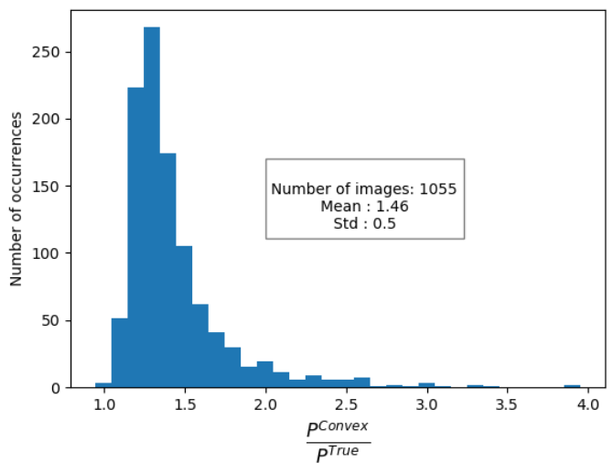


Figure 1: Histogram of the ratio between the perimeter of the convex envelope surface ($P^{convex}$) and that of the shape ($P^{true}$).

As shown in Fig. (1), a large percentage of the cracks are strongly non-convex. About 25% have a convexity ratio larger than 1.5. These cracks are inserted in a 3D specimen shown in Fig. (2a). The information contained at the ends of the full specimen is poor and the mesh is coarse therefore partial differential equations and their finite element approximation are evaluated on the domain delimited by the red box shown on Fig. (2.a). This box is a parallelepiped of dimension $200 \times 100 \times 34\ mm^3$. The mesh contains about 170, 000 degrees of freedom (but varies with the crack shape). The elements used are reduced linear tetrahedrons. The ratio between the size of the elements on the ends and near the crack is around 40. The Hausdorff parameter [15] used to control the remeshing is equal to 0.3. Fig. (2b) and Fig. (2c) show the meshed zone of interest of the specimen and a cut view to see the size of the mesh around the crack.

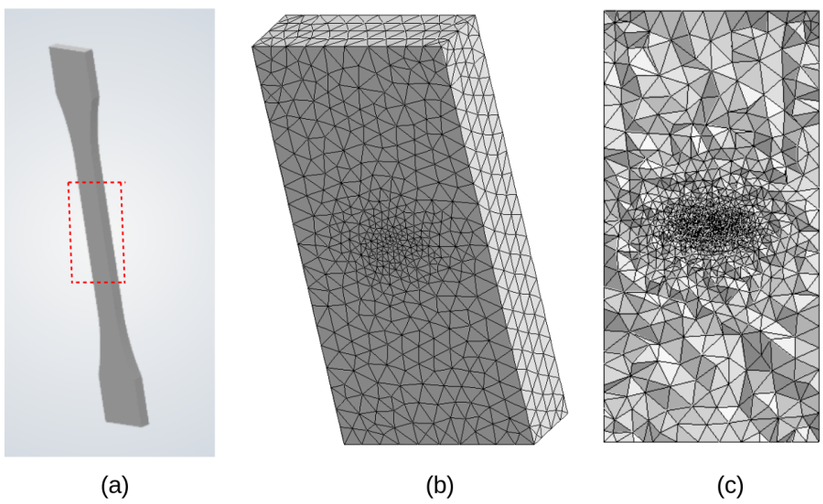


Figure 2: (a) Traction specimen example, (b) meshed zone of interest, (c) cut view of the meshed zone of interest.

In the remainder of this study, the cracks are in the middle plane but the crack is not necessarily centered in the box. Fig. (3) shows three images of cracks and below them the insertion of the crack in the 3D structure for defects 4, 21 and 22 (note that only the free surfaces are shown). For common crack shapes such as a penny shape, the limit load can be analytically evaluated in such simple structures. But for non-parametric random cracks or for structures containing multiple cracks that interact with each other, analytical results cannot be obtained in general. Finite element simulation is an option to compute those quantities though it usually leads to huge computation time. Despite the fact that the defect is large enough to have an important effect on the structure, it needs to be meshed finely since its size is much smaller than the whole structure. Hence elements around the cracks are much smaller than elements on the border of the domain $\Omega$ as shown in Fig. (3).

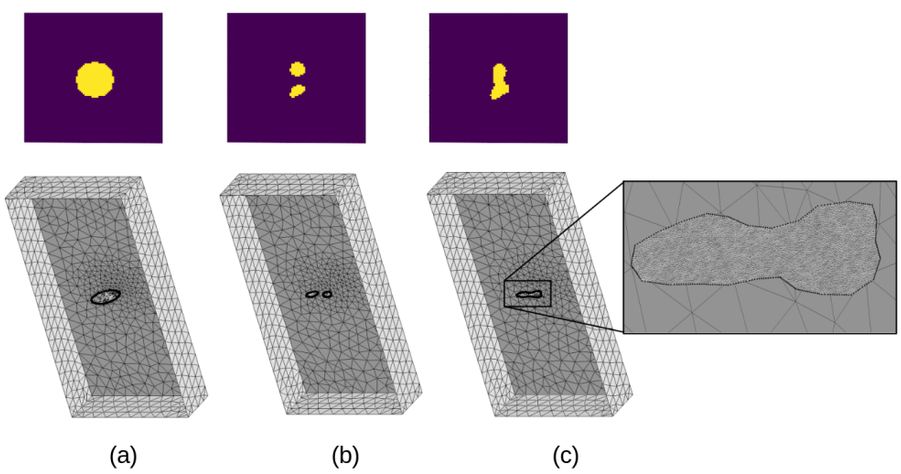


Figure 3: 2D cracks and insertion in 3D specimen for (a) defect 4,(b) defect 21 and (c) defect 22.

Moreover problems such as volumetric locking and non convergence might appear due to the localization at the crack front [16, 17]. In this study a nonlinear problem that involves finite strains and plasticity is considered. The Zset software [18, 19, 20, 21] is used. The primal variable of finite element models in mechanics is the displacement field. In the finite element (FE) model [22], the shape functions of the FE basis are denoted by $(\phi_j)_{j=1}^{n}$ with $n$ the number of discretization nodes. It is convenient to introduce the functions $\boldsymbol{\phi}_i = \phi_j \mathbf{e}_k$ where $i = (j-1) \times d + k$, $i = 1, ..., \mathcal{N}$, $j = 1, ..., n$, $k = 1, ..., d$, $d$ is the dimension of the problem and $\mathbf{e}_k$ refer to the canonical vectors of a Cartesian coordinates system. The approximation of the displacement with the shape functions $(\boldsymbol{\phi}_i)_{i=1}^{\mathcal{N}}$ reads:

$$\boldsymbol{v}(\boldsymbol{x}) = \boldsymbol{v}_0(\boldsymbol{x}) + \sum_{i=1}^{\mathcal{N}} \boldsymbol{\phi}_i(\boldsymbol{x}) u_i, \qquad \boldsymbol{x} \in \Omega, \tag{1}$$

where $\mathcal{N} = n \times d$ is the number of degrees of freedom (DOF) of the structure, $\boldsymbol{v}_0$ is a given displacement field that fulfills Dirichlet boundary conditions, $\boldsymbol{v}$ is the approximate finite element solution and $\mathbf{u} = (u_i)_{i=1}^{\mathcal{N}}$ the vector of the related degrees of freedom. For this work a large strain formulation which uses a logarithmic strain measurement is used [23, 24]. The mechanical equations for the prediction of the displacement field then read:

$$\begin{aligned}
&\text{Strain gradient decomposition:} && \underset{\sim}{F} = \underset{\sim}{I} + \underset{\sim}{\nabla}\mathbf{u} && \text{(2a)}\\
&\text{Logarithmic strain:} && \underset{\sim}{E} = \frac{1}{2}\log(\underset{\sim}{F}^T.\underset{\sim}{F}) && \text{(2b)}\\
&\text{Elastic/plastic partition is supposed:} && \underset{\sim}{E} = \underset{\sim}{E}^e + \underset{\sim}{E}^p && \text{(2c)}\\
&\text{Constitutive law in logarithmic space:} && \underset{\sim}{T} = \underset{\approx}{C} : \underset{\sim}{E}^e && \text{(2d)}\\
&\text{Second Piola-kirchhoff stress:} && \underset{\sim}{S} = \underset{\approx}{P} : \underset{\sim}{T} && \text{(2e)}\\
&\text{Second invariant of the stress tensor:} && J_2(\underset{\sim}{S}) = \sqrt{\frac{3}{2}\,\mathrm{dev}(\underset{\sim}{S}) : \mathrm{dev}(\underset{\sim}{S})} && \text{(2f)}\\
&\text{Yield stress:} && R_0 && \text{(2g)}\\
&\text{Yield function:} && f(\underset{\sim}{S}, R_0) = J_2(\underset{\sim}{S}) - R_0 && \text{(2h)}\\
&\text{Relation with global Cauchy stress:} && \underset{\sim}{\sigma} = \det(\underset{\sim}{F})^{-1} \underset{\sim}{F} \cdot \underset{\sim}{S} \cdot \underset{\sim}{F}^T && \text{(2i)}
\end{aligned}$$

More details on the projector $\underset{\approx}{P}$ and the dual stress $\underset{\sim}{T}$ of the logarithmic strain $\underset{\sim}{E}$ are given in [23, 24]. The material considered here is similar to aluminium. The Young modulus used for this simulation is $E = 70,000$ MPa, the Poisson coefficient is $\nu = 0.3$ and the elasticity limit is $R_0 = 400$ MPa. Hardening is not accounted for in this study. This is the reason why it is desirable to assist a submodel construction by artificial intelligence, via the selection of approriate boundary conditions.

In order to save useful data around the crack, a parallelepipedic box is defined and is refered to as the encoding mesh. With the goal of designing a common ambient space for mechanical data, the solution of the full specimen is transferred on it. Since the encoding mesh is much smaller and located at the same place as the crack, only the field around the crack is transferred on it. The encoding mesh, containing $64 \times 64 \times 64$ nodes, is defined using regular hexahedral elements and therefore is equivalent to a 3D image with each element representing a voxel. This allows using classical computer vision tools. Object detection techniques [25] can be used to obtain the cracks position. In the present work, all cracks are located in the same subdomain. Cracks are obtained from a database of 2D images and inserted in

the subdomain randomly, so that they are not necessarily centered in the subdomain. The zone of interest where the crack is located is accordingly always the same. To treat a more general problem where the crack position in the entire domain and its orientation were random, additional parameters defining the position and orientation of the subdomain would be required. Fig. (4) illustrates the process needed to obtain the encoded field that contains the information around the crack.

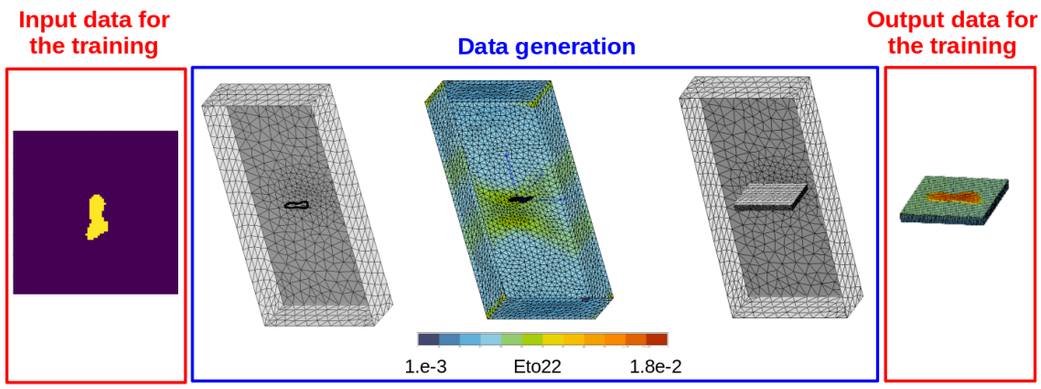


Figure 4: (a) 2D image representing the crack, (b) insertion of the 2D crack in the 3D mesh, (c) $\underset{\sim}{E}_{22}$ field, (d) position of the encoding mesh in the full structure and (e) the encoding mesh with the transferred information.

From left to right the figure 4 shows the 2D image representing the crack, the insertion of the 2D crack in the 3D mesh, the logarithmic strain along the vertical axis obtained with a finite element simulation (denoted $\underset{\sim}{E}_{22}$ as in eq.2), the position of the encoding mesh in the full structure and the encoding mesh containing the transferred information. Simulation on the full specimen are only made to generate the input arrays for the training of the MMAE. During the online phase the MMAE generates a displacement field on the encoding mesh thanks to an input image of a crack. This displacement field on the encoding mesh is then transfered on a subdomain extracted from the full mesh.
The mechanical equations on the displacement $\mathbf{u}(t)$ read:

$$\begin{aligned} \mathrm{div}[\underset{\sim}{\sigma}(\mathbf{u}(t))] &= \mathbf{0} \qquad \text{applied on } \Omega \\ \mathbf{u}(t) &= \mathbf{u}_0(t) \quad \text{applied on } \Gamma^{BC} \\ \underset{\sim}{\sigma}(\mathbf{u}(t)) \cdot \mathbf{u} &= \mathbf{0} \qquad \text{applied on } \Gamma \end{aligned} \tag{3}$$

where $\Omega$ represents the whole domain, $\Gamma^{BC}$ represents the surface where the Dirichlet boundary conditions are applied and $\Gamma$ represents the free surfaces where no boundary conditions are applied (including the free surface of the crack lips). The tensor $\sigma(\mathbf{u}(t))$ is obtained with the relation detailed in Eq. (2). In order to solve the partial differential equation described in Eq. 3, a quasi-static approach is used. The scheme shown on Fig. (4) is applied on the whole dataset of 2D images to generate 3D displacement fields expressed on the encoding mesh. The defect dataset contains 1,055 2D images. Finite element predictions of the displacement field have been performed for each defect. The mechanical dataset contains all the displacement fields associated to their respective 2D images. They are saved on the encoding mesh. The encoding mesh is represented as a array of dimension 5. The first three dimensions represent the spatial dimensions $(x, y, z)$. The fourth dimension refers to the considered field either $U_x$, $U_y$

or $U_z$. The fifth dimension, denoted $t$, is the time. In this study the time is assimilated to the incremental loading parameter and varies from 0 to 1. The displacement field is saved along the encoding mesh in a 5-dimensional array $T^{(j)}$ so that $T^{(j)}[x, y, z, i, k] = U_i^{(j)}(x, y, z, t_k)$ where $i \in \{x, y, z\}$ and $U_i^{(j)}(x, y, z, t_k)$ is the displacement in direction $i$ at point $(x, y, z)$ and time $t_k$ for defect $j$. The tight local volume (TLV) is a part of the full mesh. It is extracted around the crack where the needed information is located. The TLV model gives access to all standard mechanical variables by using finite element modelling. This approach enables transfer learning in the sense that all the modelling capabilities of the finite element method do not need to be retrained and constitutes a huge asset of the developed method. As such, the model does not need to be trained again when new quantities of interest or new element types are used.

## 3. Multimodal autoencoder and transfer learning

As explained in [26], feed forward neural network (FNN) is a classical architecture in machine learning.A deep FNN contains many layers of artificial neural networks. The data is given to an input layer and then pass through some hidden layers. The last layer is called the output layer and gives the prediction. The weights $w$ make a full the connection between the neurons from different layers. During the prediction phase, the data flows in one way from the input layer to the output layer. In the training phase, the global error defined by the mean-squared difference between the target value and the FNN output will be back-propagated through the hidden layers. This step is performed in order to update the weights, where the objective is to minimize the global error. An activation function is attached to each neuron. The output of each neuron is computed by multiplying the outputs from the previous layer with the corresponding weights. For the neuron $j$ in the layer $k$, the data of the previous layer $k-1$ is summed up and then altered by an activation function. The output of the neuron $j$ in layer $k$ is computed as:

$$o_j^k = f\left(\sum_{i=1}^{N_{k-1}} w_{ij} o_i^{k-1} + b_i^{k-1}\right), \tag{4}$$

where $N_{k-1}$ is the number of neurons in the previous layer $k-1$, $w_{ij}$ is the weight connecting neurons $i$ and $j$, $o_i^{k-1}$ is the output of the neuron $i$ in layer $k-1$. A common choice for the activation function is the rectified linear function ("ReLu"):

$$f(x) = \begin{cases} x, & \text{if } x \geq 0, \\ 0, & \text{otherwise.} \end{cases} \tag{5}$$

The specific architecture of the FNN, such as the number of layers and the number of neurons in each layer, has to be determined according to the complexity of the dataset. The global error, also called loss function or network performance, is defined according to the difference between the network prediction and the target data. The mean squared error can be used to measure the loss (but many other loss function can be used):

$$E(\mathbf{w}) = \frac{1}{N_o} \sum_{i=1}^{N_o} [o_i(\mathbf{w}) - t_i]^2, \tag{6}$$

where $N_o$ is the number of outputs, $o_i$ is the $i^{th}$ output, $\mathbf{w}$ is the vector that contains the weights of neural network, and $t_i$ is the $i^{th}$ target value. Training a feed forward neural network is an optimization problem, where the global error is treated as the objective function.

One way to minimize the global error is to use the gradient descent algorithm to update the weighs [27] with the following:

$$\mathbf{w}^{n+1} = \mathbf{w}^n - \mu \frac{\partial \mathbf{E}(\mathbf{w}^n)}{\partial \mathbf{w}^n}. \tag{7}$$

The term $\frac{\partial \mathbf{E}(\mathbf{w}^n)}{\partial \mathbf{w}^n}$ is evaluated with the back propagation [28]. In the training process, many iterations are required to update the weights until the stopping criteria is fulfilled, where one iteration is also known as one epoch. Since 2D images and 3D displacement fields are considered in this work use of convolutional neuron networks is made. Good results for 2D and 3D images have been obtained with this method [29]. Details on convolutional layers are given in [4].

Autoencoders enable to compress the input information in a much smaller latent space and reconstruct it afterwards. This allows one to define a small latent space in which all the information is condensed [30]. Many applications of this bottleneck effect exist: clustering the data, denoising data or else exploring the smaller space. An autoencoder employs an input layer and an output layer connected by one or more hidden layers. The output layer has the same number of nodes (neurons) as the input layer. Its purpose is to reconstruct its inputs (minimizing the difference between the input and the output) instead of predicting a target value Y given inputs X . Therefore, autoencoders are selfsupervised learning models. They do not require labeled inputs to enable learning [31]. The feature space $\mathcal{F}$ should have lower dimensionality than the input space $\mathcal{X}$. An autoencoder consists of two parts, the encoder and the decoder, which can be defined as transitions $\Phi$ and $\Psi$ such that:

$$\begin{aligned} \Phi &: \mathcal{X} \to \mathcal{F}, \\ \Psi &: \mathcal{F} \to \mathcal{X}, \\ \Phi, \Psi &= \underset{\Phi,\Psi}{\operatorname{argmin}} ||X - (\Psi \circ \Phi)X||^2, \\ \dim(\mathcal{F}) &\ll \dim(\mathcal{X}). \end{aligned} \tag{8}$$

Multimodal autoencoders (MMAE) category, which is a specific branch of autoencoders, are detailed in [3]. The main idea of MMAE is to take various inputs from different nature (such as 2D images and 3D images) and to compress them in the same latent space before rebuilding them. One of the main asset of MMAE it to remove some input channel during the online phase in order to reconstruct all of the channels [32] as the red border suggests on Fig. (5).

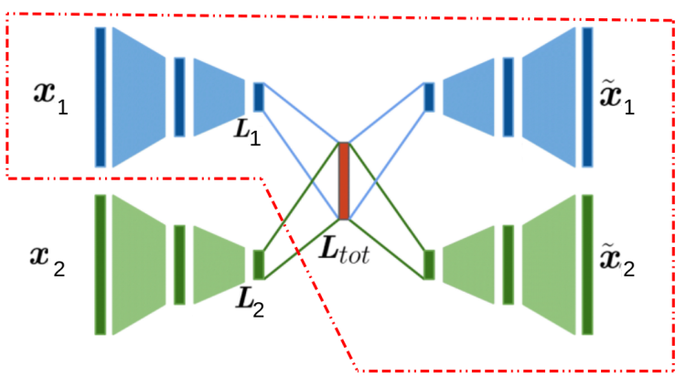


Figure 5: Multimodal autoencoder representation.

$x_i$ are the different input channels, $\widetilde{x}_i$ are the different output channels and $L_i$ is the size of the latent space. The aim of this article is to take advantage of this multi-modal aspect in order to train a mapping between morphological data and mechanical predictions as a surrogate model for fast mechanical prediction. A standard convolutional neuron network could be used to associate a 3D displacement field to a 2D image. But with a MMAE approach it is possible to interpret how features are represented in the latent space. Moreover an innovative point of the study is to use the reconstructed 2D image in order to create an error indicator depending on the training set to evaluate whether the 3D displacement field is accurate or not. The proposed MMAE has four modalities, in the sense that it has four encoders and four related decoders. This architecture is motivated by the dimension of the displacement field on the encoding mesh. Indeed this input contains the spatial information (3 dimensions), the temporal information and the field information ($U_x$,$U_y$ or $U_z$) which results in an array of dimension 5. In order to reshape the dimension of the array into the usual dimensions of data in computer vision, the three displacement fields are treated with three different modalities, using three dedicated encoders and decoders.

The outputs of these three mechanical encoders are connected to the three inputs of the mechanical decoders via a mechanical latent space by using dense layers, termed mechanical dense layers, behind and in front of the latent layer. The mechanical latent space is a three dimensional space. It has latent variables for each dimension of the displacement field and there is no connection between these dimensions in the mechanical dense layers in front of the 3D latent space and behind it. The dimension of the latent space is 600. There are 200 latent variables per component of the displacement field. Latent variables related to each dimension of the displacement field are stacked together to create a common mechanical latent space.

The morphological encoder and decoder are connected to the mechanical latent space by two additional dense layers, termed multimodal dense layers, behind and in front of the three dimensional latent space. The inputs of the morphological encoder, being the 2D image, is $80 \times 80$ whereas for the displacement field is of size $64 \times 64 \times 64 \times 5(\times 3)$. The $(\times 3)$ is between parenthesis to express that the three components of the displacement fields have separated modalities. This architecture is represented on Fig. (6). The 4 encoders and decoders are coupled together by the multimodal dense layers, named left fully connected and right fully connected in Fig. (6). This architecture is non conventional and constitutes a important point of this paper.

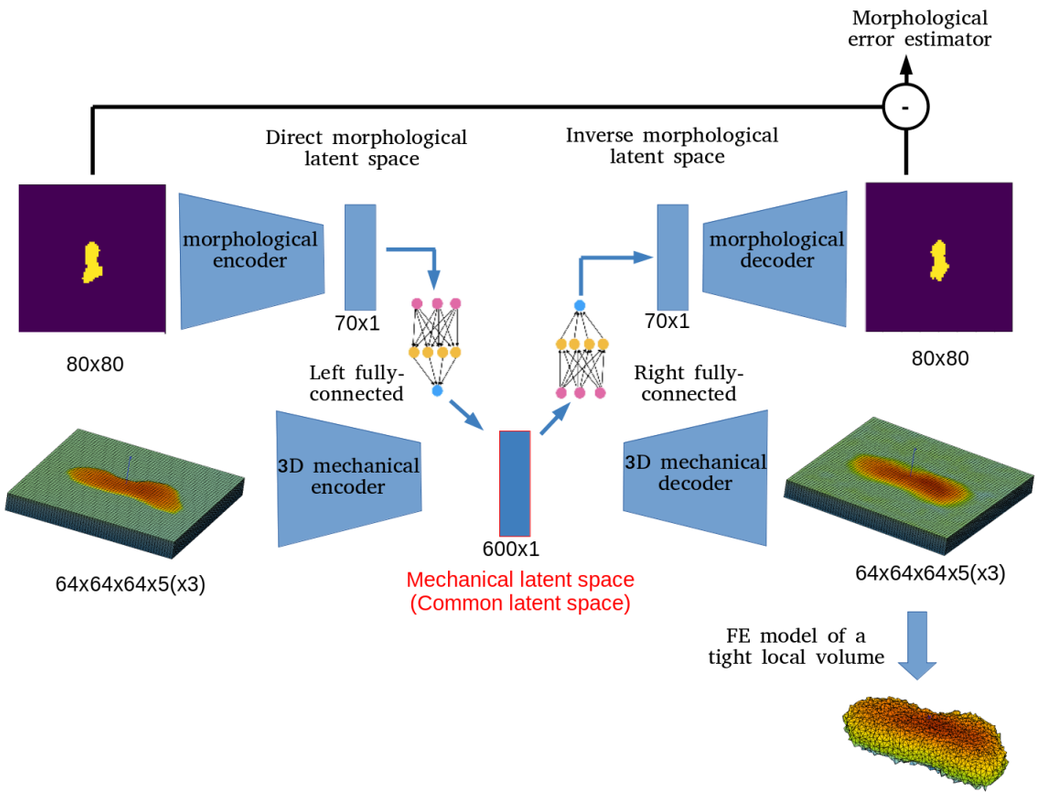


Figure 6: Modified MMAE approach and error indicator to generate displacement field on TLV.

During the training phase of the MMAE we have noticed that the 3D displacement channels are the hardest to fit. Hence a transfer learning is accordingly carried out in two steps, the first step being used to train separate autoencoder for each modality and the second step being used to train the weights of the muldimodal dense layers. In the second step, the weights of convolutional layers and those of the mechanical dense layers are kept as constant. Then we know the latent variables of the proposed MMAE at the end of the first step of the transfer learning strategy. We also know morphological latent variables. Hence the multimodal dense layers, left fully connected and right fully connected in Fig. (6), are trained separately. The left fully-connected layer is trained to map the morphological latent coordinates, expressed as a 70-components vector, to the mechanical latent coordinates, expressed as a 600-components vector. The right fully-connected layer is trained as an inverse mapping that maps the mechanical latent coordinates to the morphological latent coordinates.

Using MMAE, the morphological as well as mechanical latent coordinates can be obtained from an image of a crack, and the associated displacement field can be predicted. The latent variable in the mechanical latent space can be used to recover the input image from the right fully-connected network. The discrepancy between the input and reconstructed images may then be used to define an error indicator. Such error indicator is meaningful since the reconstructed image and the displacement field come from a common latent space. Also, use of a 2D crack is made to forecast a 3D displacement field on the encoding mesh. In parallel the TLV is extracted from the full mesh of the target defect. The 3D displacement field from the encoding mesh gives access to the Dirichlet boundary conditions applied on the TLV. A standard FE prediction is then made with the displacement field on the external surface applied as Dirichlet boundary conditions. Fig. (7) illustrates this methodology.

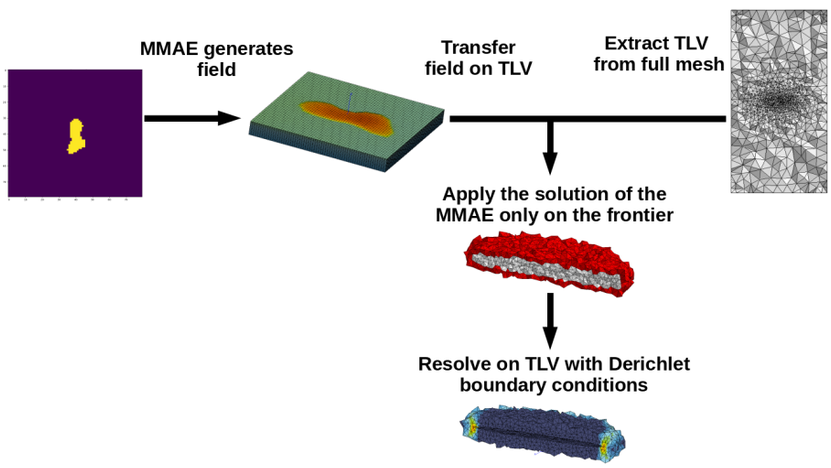


Figure 7: Online scheme

For nodal fields, the transfer operator is straightforward. First, each node of the new mesh, having $X_{new}$ as coordinates, is localized in the old mesh, then the shape functions $\phi_i^{old}$ of the old mesh are used to compute the value of the field $f$ on the new mesh:

$$f(X_{new}) = \sum_i \phi_i^{old}(X_{new}) \cdot f(X_i), \tag{9}$$

where $X_i$ is the coordinate of the vertex $i$ of the corresponding element. The error due to the transfer has been measured by transferring the displacement field of the encoding mesh as Dirichlet boundary conditions of the TLV without using the MMAE. The error results of the two transfers, the first one from the full mesh to the encoding mesh and the second one from the encoding mesh to the TLV. The error is evaluated on the cumulated plasticity (see Eq. 10). The error that is used is an extension of the normalized mean squared error to continuous functions. Compairing the error based on the displacement and these of the cumulated plastic strain on cases of the training set it appeared that the first error measurement is more conservative than the second.

$$\eta = \frac{\frac{1}{\int_{d\Omega}} \int (\Delta\varepsilon^{pcum})^2 d\Omega}{\frac{1}{\int_{d\Omega}} \int (\varepsilon_{FOM}^{pcum})^2 d\Omega} = \frac{\int_\Omega (\Delta\varepsilon^{pcum})^2 d\Omega}{\int_\Omega (\varepsilon_{FOM}^{pcum})^2 d\Omega}, \qquad \text{where } \Delta\varepsilon^{pcum} = \varepsilon_{FOM}^{pcum} - \varepsilon_{Model}^{pcum}, \tag{10}$$

and where $\Omega$ describes the TLV domain, the subscript "FOM" refers to the Full Order Model simulation and the subscript "Model" refers to the solution obtained with the MMAE approach detailed in this paper. After computing this error for all the defects of the dataset the mean error has been computed and is equal to 0.07% and the standard deviation is 0.07%, this shows that the transfer operations does not generate much error. Importantly, the TLV must be included in the encoding mesh otherwise the field transfer from the encoding mesh to the TLV cannot be done properly. The latter reads:

$$\Omega_{TVL} \subseteq \Omega_{EM} \tag{11}$$

where $\Omega_{EM}$ refers to the encoding mesh domain and $\Omega_{TLV}$ to the tight little volume domain. Fig. (8) illustrates this necessary condition.

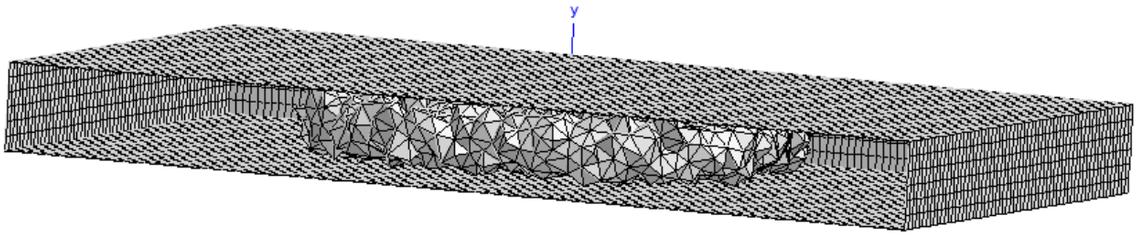


Figure 8: $\Omega_{TVL} \subseteq \Omega_{EM}$.

## 4. Results and interpretability

The displacement field shows varying orders of magnitude depending on time and displacement component. The MMAE is accordingly trained on the following rescaled field $\widetilde{T^{(j)}}$:

$$\begin{aligned} \widetilde{T^{(j)}}[x,y,z,i,k] &= \frac{T^{(j)}[x,y,z,i,k] - m_{ik}}{M_{ik} - m_{ik}}, \\ M_{ik} &= \max_{x,y,z,j} T^{(j)}[x,y,z,i,k], \\ m_{ik} &= \min_{x,y,z,j} T^{(j)}[x,y,z,i,k] \end{aligned} \tag{12}$$

for a given defect $j$. Note that since the images of defects are binary images, these do not need to be rescaled.

As explained in the previous section the four autoencoders have been trained separately (a single 2D AE and three 3D AE) and two dense neuron networks have been trained afterwards in order to map the morphological and mechanical latent spaces. Since the 3D displacement field data are 4 dimensional (time and space) the filter channel (associated to the three color red, green and blue) of the 3D convolution layers is used as another dimension enabling to treat 4D data. In our case the filter channel will contain the displacement field ($Ux$,$Uy$ or $Uz$). Classical CNN architectures are presented in [33] and the same notation is used to present the developed architecture. The 2D encoder is composed of two blocks of convolution and max pooling followed by an additional convolution. Then two dense layers lead to the latent space. For each layer the activation function is rectified linear (ReLu). Fig. (9) illustrates the architecture of the 2D and 3D encoder. The yellow R symbolises that the activation function is ReLu. The decoding part is exactly the same in the reverse way and the "max pooling" blocks are replaced by "up sampling" blocks.

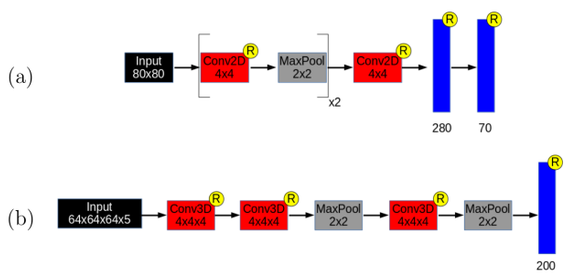


Figure 9: 2D (a) and 3D (b) encoder architectures.

In this work the ReLu activation function has been used. This activation function sometimes generates gradient losses during the training when not large enough dataset are used. We emphasize that the Exponential Linear Unit (ELU) activation function as an alternative. More details on the architectures such as the number of filters or the number of trainable parameters are given in Appendix A. The loss function used for each optimization is a L2 norm and the optimizer used is adam. Fig. (10) shows the loss in function of the epoch for the optimization process.

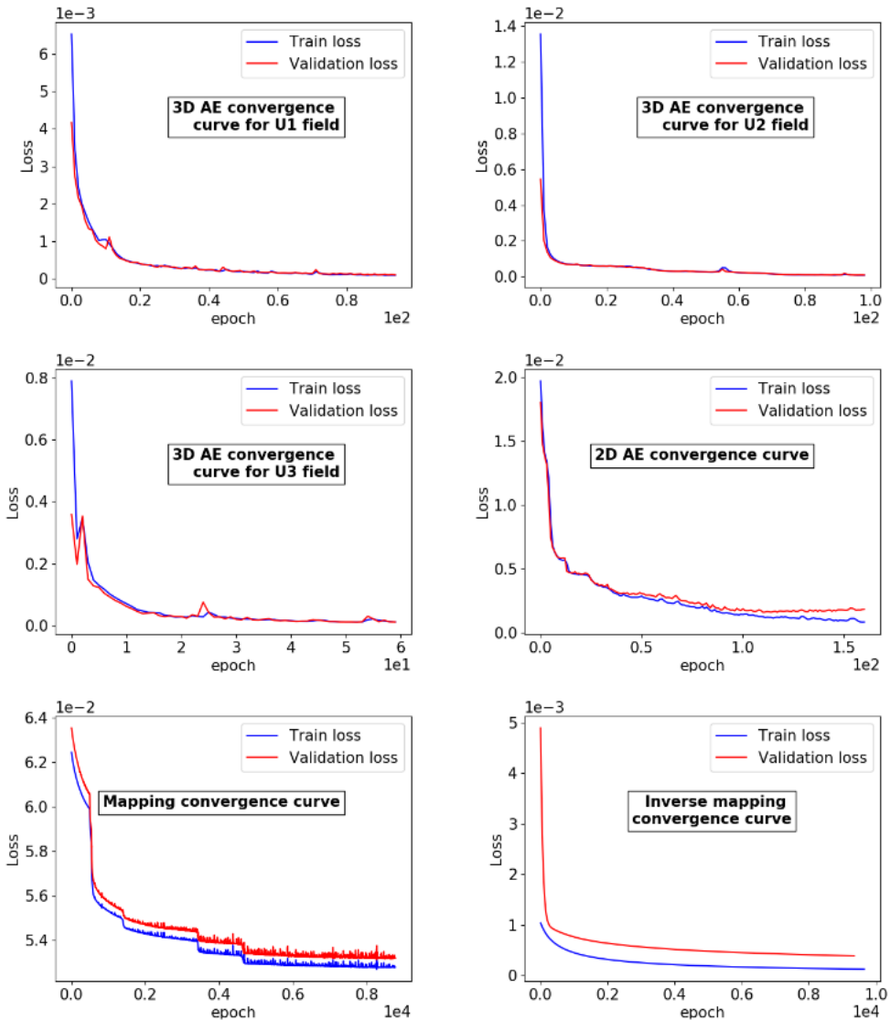


Figure 10: Loss curve for each optimization.

The position in $\Omega_{EM}$ where the error on the displacement field made by the MMAE in average can be evaluated with Eq. (13).The nodes where the error $\bar{\zeta}$ is superior to 1% are shown in red in Fig. (11). A circular crack with the mean diameter of the whole data set is also drawn, so that:

$$\zeta = \frac{|U_{FOM} - U_{MMAE}|}{U_{mean}}, \qquad \bar{\zeta} = \frac{\sum_{i=1}^{N_{defect}} \zeta_i}{N_{defect}} \tag{13}$$

where $N_{defect}$ is the number of defects,$U_{FOM}$ and $U_{MMAE}$ refer to the solution for the displacement field of the full order model and of the MMAE approach respectively. $U_{mean}$ is the mean displacement in the encoding mesh.

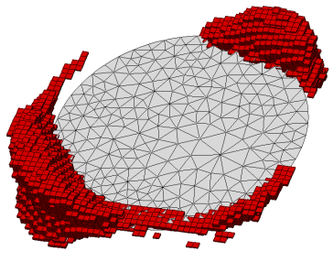

Figure 11: Element of the encoding mesh where $\bar{\zeta} > 1\%$ (red) with mean circular crack (grey)

The error is located on the crack front and more precisely on the two closest sides from the front and the back of the specimen. For each 2D crack images the corresponding reconstructed 2D crack image and a reconstructed 3D displacement field is generated. Fig. (12) shows the reconstructions for defects 122, 131 and 16 which are data from the training set.

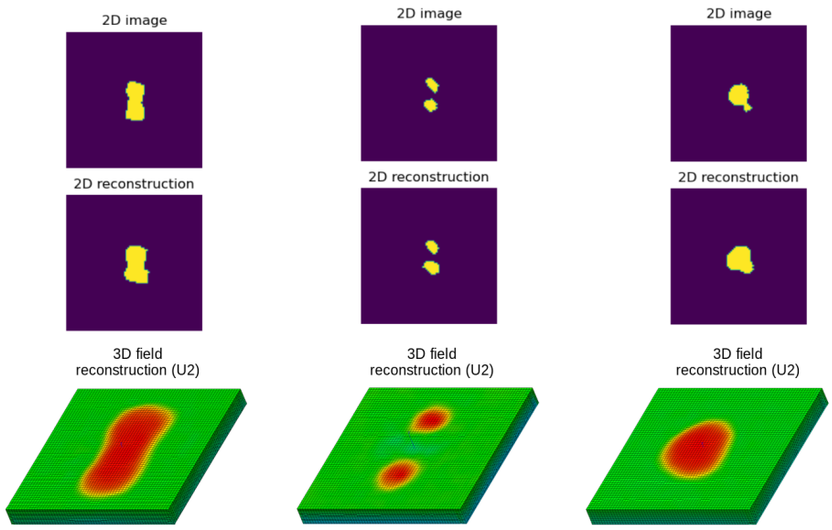


Figure 12: Initial crack images from training set, their reconstruction and the cross modal displacement field reconstruction (cracks 122, 131 and 16 from the training set).

One of the reason why MMAE are used in this work is to see whether a relation between the error made during the online phase and the 2D image reconstruction can be made. The information of the input image is encoded in the common latent space and so gives a global indication, for both morphological and mechanical data, that would not be obtained if solely the morphological AE was used. During the online phase the displacement field generated on the encoding mesh generated by the cross modal reconstruction is transferred on the external surface of the TLV. The error $\eta$ of the online phase is based on the cumulated plasticity defined by Eq. (10). The following error indicator $\widetilde{\eta}$ is the average difference between the

original image and its reconstruction:

$$\widetilde{\eta} = \frac{\sum_{i=1}^{N} |P(i) - \widetilde{P}(i)|}{\sum_{i=1}^{N} P(i)}, \qquad P(i), \widetilde{P}(i) \in \{0; 1\}, \tag{14}$$

where $P(i)$ and $\widetilde{P}(i)$ represent the value of the pixel $i$ for the original and reconstructed image respectively. The number of pixel of the image is $N = 84 \times 84$. In order to see whether a linear relation between those two errors exists, for each simulation $\widetilde{\eta}$ and $\eta$ are plotted on the same graph. Since there are few extreme values a probability density function is used to have a clear insight of the tendency. A linear relation is defined with the least mean square and a 40% error cone is drawn on Fig. (13).

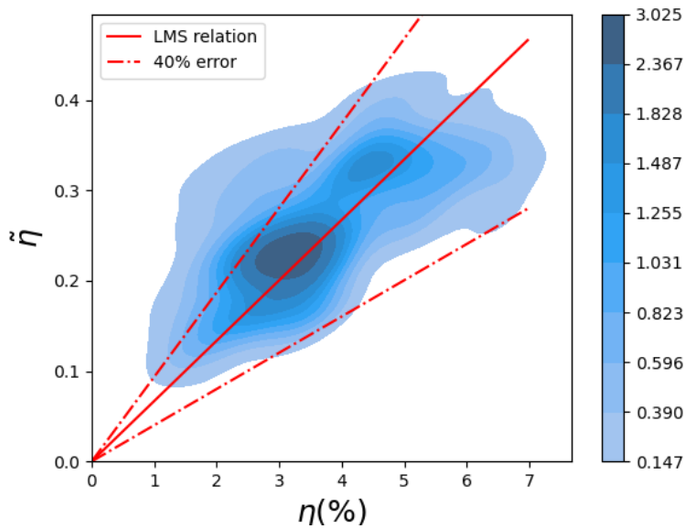


Figure 13: Error indicator evaluation map.

A tendency is observed but the precision of the indicator is not high, it would give a good hint about the online computation. With a fixed criterion (here 5%) on the actual error $\eta$ one can evaluate the True Positive (indicator low and true error low), True Negative (indicator high and true error high), False Positive (indicator low and true error high) and False Negative (indicator high and true error low) repartition. This repartition is shown in Fig. (14).

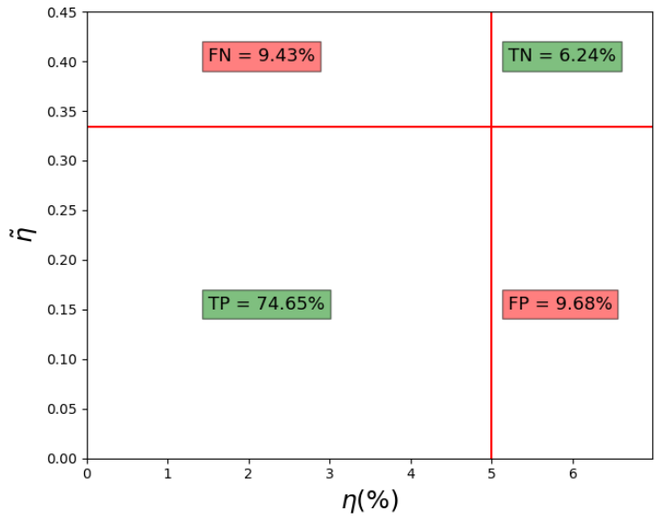


Figure 14: True Positive, True Negative, False Positive and False Negative repartition with a criterion of 5% of error.

If the estimated error is too high then a full finite element simulation should be made. Therefore in order to be the more conservative the false positive should be minimized. Moreover the linear relation can be adapted in order to be more conservative if needed. In order to see more precisely the error that can be encountered for defects, a 2D histogram is made for defect 1042. This defect belongs to the test dataset hence the model has not been trained on this defect. It shows the density of Gauss points according to their value of cumulated plasticity and von Mises stress for the full order model (FOM) and for the developed model. Since at the end of the simulation most of the points are fully plastic and the von Mises value is equal to the limit stress $R_0 = 400MPa$, the graphs are drawn at t=0.8. Remind that the error is evaluated on the TLV only. This is represented in Fig (15).

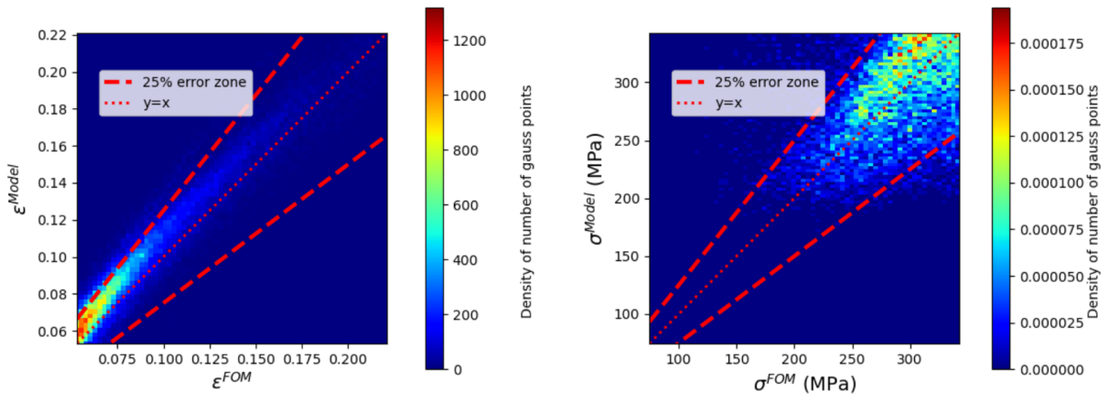


Figure 15: Error Graph on $\varepsilon^{pcum}$ and $\sigma^{Mises}$ t=0.8 for defect 1042 from test dataset.

Almost all the points are included in the 25% error zone, showing the good performance of the method for the defect 1042. The result maps of the cumulated plasticity for defect 1042 is shown Fig. (16).

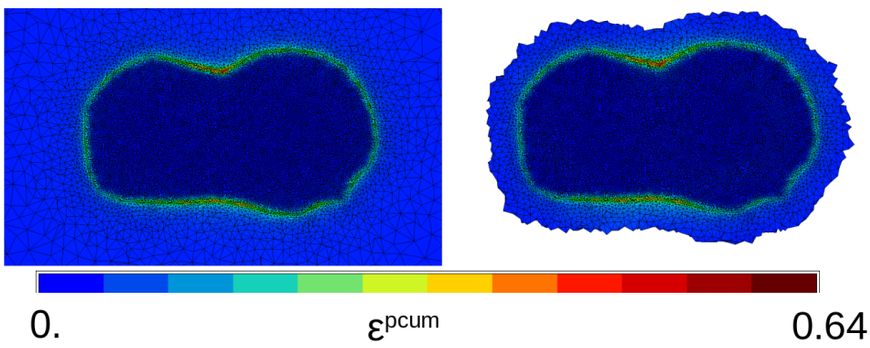


Figure 16: $\varepsilon^{pcum}$ with FOM (left) and with the model (right) on the TLV for defect 1042 from test dataset.

It is clearly shown that the global aspect of the field between the two methods is highly similar. In order to have a more global view of the capacities of the so developed model an histogram of the error based on the cumulated plasticity (see Eq. 10) is made. Since the TLV is included in the full mesh, the error is computed strictly on the TLV. The classical split has been applied to train the model so the three sets "train", "validation" and "test" are represented on this histogram Fig. (17a).

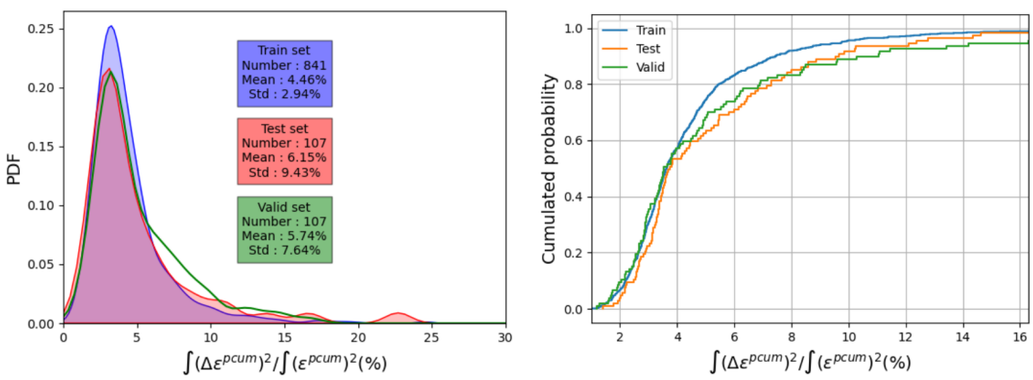


Figure 17: (a) Probability density function and (b) cumulated probability of the error for the training, validation and test sets

The cumulated probability graph in Fig. (17b) shows that 95% of the defects have an error below 9.8% for the training set, 12.4% for the validation set and 16.3% for the testing set. Good results are achieved with the developed methodology. For every set of data the average error is lower than 7% underlining the accuracy of the model. In order to put into relief the need to developed such a model a naive model has been created. Instead of generating a specific 3D displacement field for each 2D image, a mean displacement field is computed over the training set. All the training data have been taken and a mean field have been generated (see Fig. 19a). The latter is then used to apply the boundary condition on the TLV that are free from defect dependency. As it has been done before, an histogram of the error made on the cumulated plasticity is made for the test set and compared with the developed model. Those results are shown on Fig. (18).

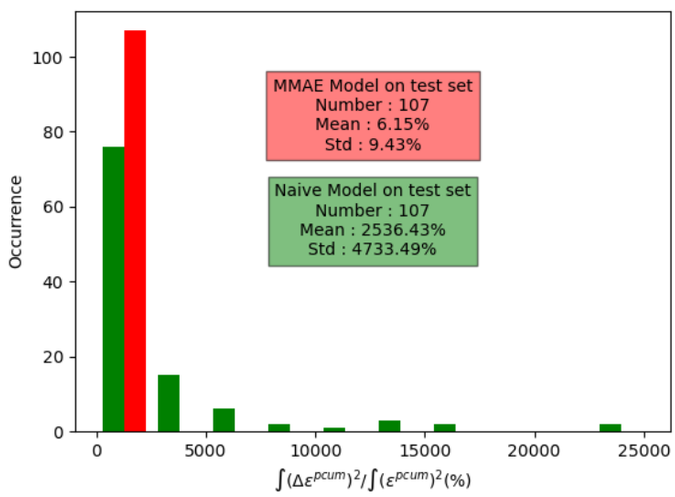


Figure 18: Histogram of the error for the test sets with the MMAE model and the naive model

Very high error are obtained with this method except for defects having a shape close to the average shape in the training set. Indeed for small defects large displacements are imposed on the external surface generating important strains and stresses. The difference between the FOM and the naive model for defect 989 is shown on Figs. (19b,19c).

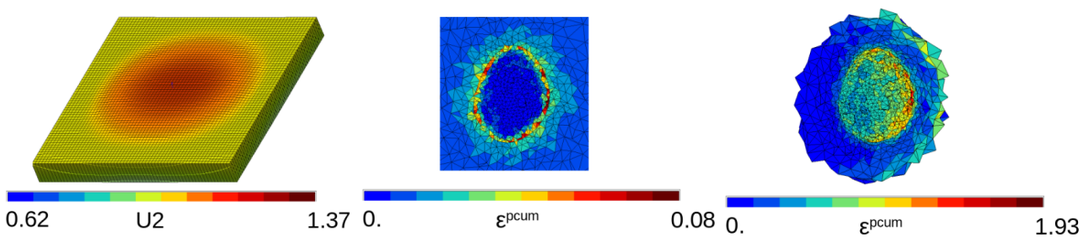


Figure 19: Encoding mesh with mean U2 field (a), $\varepsilon^{pcum}$ field with FOM (b) and $\varepsilon^{pcum}$ field with naive method (c) for defect 989

The fluctuation of the displacement field caught by the MMAE is therefore necessary to achieve good performance. To the contrary one can question why the use of the MMAE solution solely on the external surface is made and not on the whole domain. This would made great different for the computation time since only the integration of the constitutive law would be required. Therefore comparison is made on defect 1042 from the test set with boundary conditions on the whole domain and solely on the external surface is made. Solely the meshed domain where $\Delta\varepsilon^{pcum} > 5\%$ is conserved in both case in order to see the impact of the position of the boundary conditions. This is shown in Fig.( 20a), (20b).

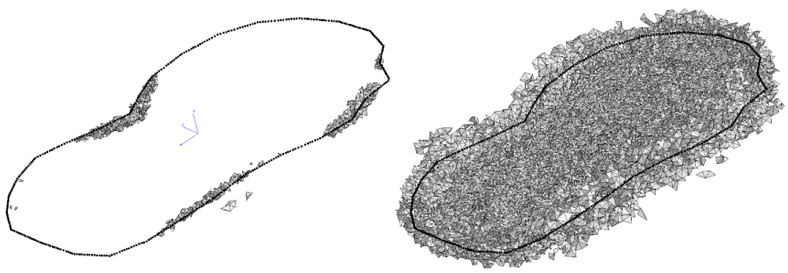

(a) (b)

Figure 20: Mesh of defect 1042 where $\Delta\varepsilon^{pcum} > 5\%$ when (a) the BC are applied on the external surface of the TLV and when (b) the BC are applied on the whole TLV.

The number of element where $\Delta\varepsilon^{pcum} > 5\%$ is clearly inferior when the boundary conditions are applied on the external surface. The fact that the boundary conditions are solely on the external surface enables to make a finite element correction of the solution find by the MMAE.

The use of MMAE allows one to represent each defect as a point encoded in the latent space. Fig. (21) represents all the defect in the latent space, since the latent space is of dimension 600 a multi dimensional scaling (MDS) is made to have a 2D representation of this space [34, 35].

MDS is an information visualization method which consists in finding a low-dimensional dataset $\mathbf{Z}_0$whose matrix of Euclidean distances $d(\mathbf{Z}_0)$ is an approximation of the input dissimilarity matrix $\delta$. To that end, a cost function called stress function is minimized with respect to $\mathbf{Z}$:

$$\mathbf{Z}_0 = \underset{\mathbf{Z}}{\operatorname{argmin}} \left( \sum_{i<j} (\delta_{ij} - d_{ij}(\mathbf{Z}))^2 \right) \tag{15}$$

From left to right the blue dots represent the defects 539, 938, 537 and 341 while the red dots represent their nearest neighbour respectively being the defects 4, 612, 105 and 368.

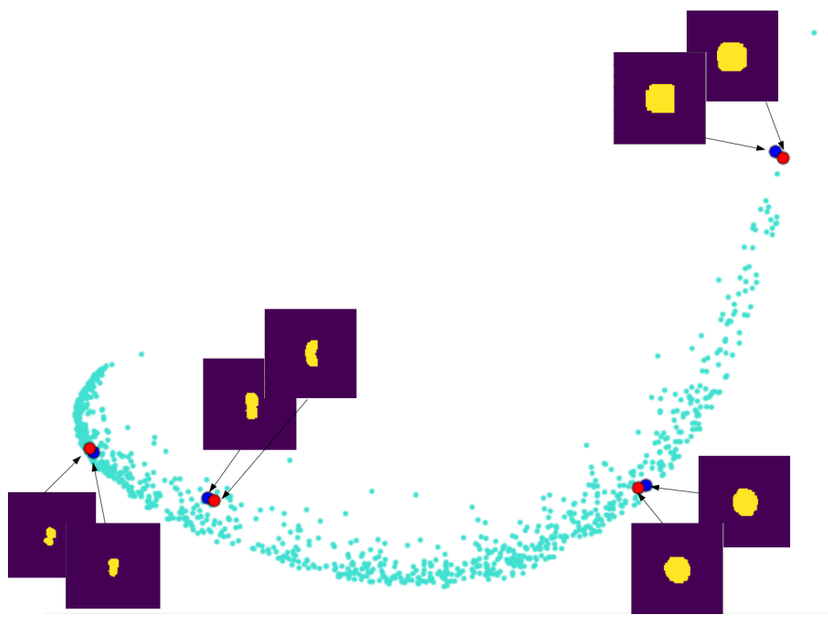

Figure 21: Low dimensional representation of the common latent space

We remark one may use the reduced basis of the nearest neighbour in the common latent space where a full order model is computed to solve the problem. This would be an alternative since the latent space is common to the image and the displacement field. As shown in [36], no bijection necessary exists between the mechanical and the morphological latent space. This warrants the use of a common latent space generated with the MMAE. The technique consisting in using a reduced basis recommended by a neurone network is called "ROM-net" [37]. This approach works well for defects like gaz pores and has also been used in [36]. Nevertheless this method offers non-optimal results when dealing with cracks. The singularity at the crack tip is poorly represented on a reduced basis selected in a dataset of reduced basis. As illustrated in Fig. (11), the error is located at the crack tip, which is the zone of interest. Use of a submodelling approach and an adequate subdomain enables to circumvent this problem.

## 5. High level engineering analysis to assess the safety of structures containing cracks

The use of fracture assessement diagram (FAD) is common in the industry to certify whether a structure containing cracks are still operational or not. The determination of the stress intensity factor (SIF) and the limit load is necessary to use them [38]. Two domains (safe and unsafe) can then be drawn on this diagram. Such mechanical quantities of interest are usual outputs of finite element software in engineering. An explanatory FAD is given in Fig. (22) which is taken from [39].

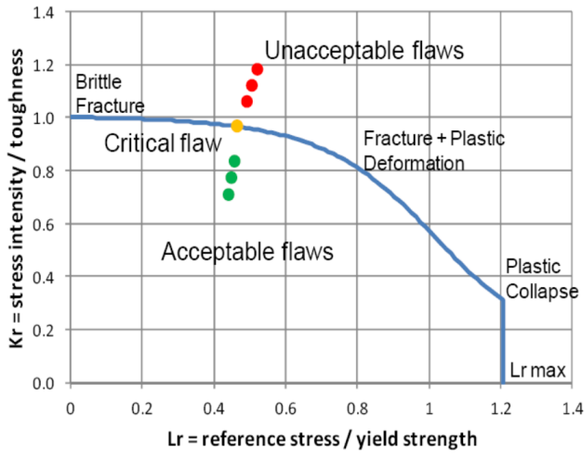


Figure 22: FAD example with the different regions

With surrogate models, only specific quantities of interest can be computed. With the presented work all quantities around the crack such as the stress intensity factor and the $J$ integral can be computed with classical finite element methods. On the contrary the limit load is evaluated with the reaction forces at the extremities of the specimen. Not enough information are present on the TLV to compute the limit load. The gappy proper orthogonal decomposition enable to recover the full field when a reduced base is available. In this context the use of MMAE happens to be a very relevant choice and constitutes a major point of this paper. Indeed reduced basis can be computed for the training phase and then, during the online phase, the reduced base of the $k$-nearest neighbours ($k$-NN) in the latent space can be used to recover the full field and hence compute the limit load. This methodology consisting in using a reduced base from another defect has already been used in the literature [37, 2].

Considering a reduced basis $\mathbf{V}$ and following on the Gappy POD [40], any vector $\mathbf{u}$ which belongs to the column space $colspan(\mathbf{V})$ of $\mathbf{V}$ may be recovered by using few entries $\mathbf{u}[\mathcal{F}]$ of $\mathbf{u}$, if $\mathbf{V}[\mathcal{F},:]$ is a full column rank matrix. Here the set of degree of freedom $\mathcal{F}$ corresponds to the ones of the TLV. Such recovery procedure takes the form:

$$\mathbf{u} \in colspan(\mathbf{V}), \qquad \mathbf{u} = \mathbf{V} \cdot \left(\mathbf{V}[\mathcal{F},:]^T \cdot \mathbf{V}[\mathcal{F},:]\right)^{-1} \cdot \mathbf{V}[\mathcal{F},:]^T \cdot \mathbf{u}[\mathcal{F}] \tag{16}$$

Fig. (23) shows the global workflow that allows one to recover the full field by taking advantage of the information contained in the latent space. Note that if more than one reduced basis is selected (i.e. $k > 1$) to recover the full field, techniques have been developed in [38, 41] to create a global basis based on many others.

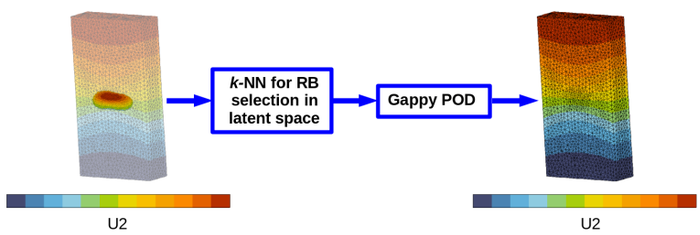


Figure 23: Full field recovery with use of the information contained in the latent space and gappy POD process

The same idea can be used for the stress field $\boldsymbol{\sigma}$ using the reduced basis of the stresses $\mathbf{V}^{\sigma}$. Once $\boldsymbol{\sigma}$ is recovered it is possible to integrate this field on the top surface to obtain the force at every time step and so the limit load. It is then possible to evaluate the limit load for every defect by taking the reduced basis of its the nearest neighbour in the latent space. To evaluate the $J$ integral the information present in the TLV are sufficient. Two methods to evaluated the $J$ integral are used. One for which the $J$ integral is computed as the mean on the curvilinear abscissa and one more conservative method where $J$ is equal to the maximum value along the crack front. Both of these quantities are detailed in Eq. (17).

$$J_{max} = \max_{s} J(s), \quad \bar{J} = \frac{\oint\limits_{front} J(s)ds}{\oint\limits_{front} ds}. \tag{17}$$

Hence graphs to evalutate the error between the full order model (FOM) and the developped model are computed over the validation and testing set. Fig. (24) shows that good results are obtained, most of the points are contained in the 20% error zone. If a closer look at defect 1042 (belonging to the test set) is taken, its nearest neighbour in the latent space is the defect 53 (belonging to the training set). Fig. (25) shows the force displacement curve for defect 1042 with the described method and with a full order model (FOM).

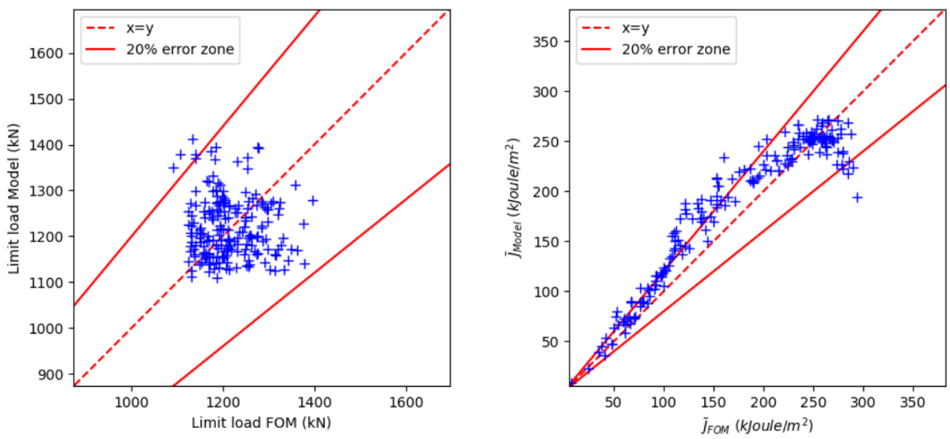


Figure 24: Limit load value with model and FOM (left) and $\bar{J}$ with model and FOM (right)

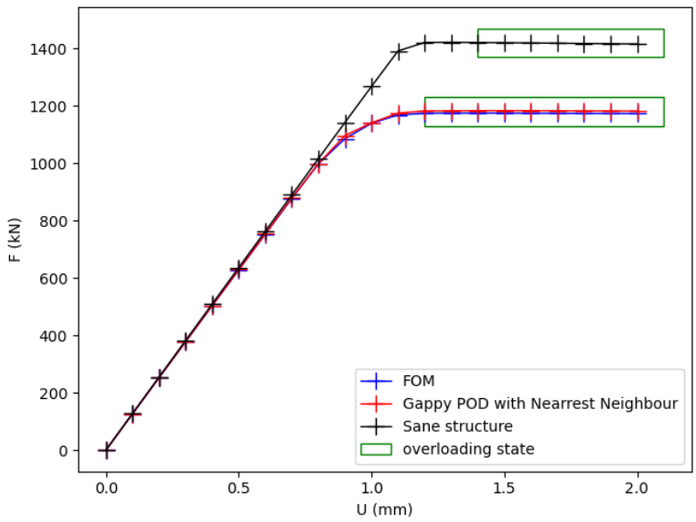


Figure 25: Traction curve for defect 1042

The traction curve is also obtained with the developed methodology is very similar to the curve of the FOM. Similarly it is possible to compute the $J$ integral along the curvilinear abscissa for defect 1042 at specific time step on Fig. (26). The mean error for each figure reads:

$$\mu = \frac{1}{N_{nodes}} \sum_{i \leq N_{\text{nodes}}} \frac{|J_i^{FOM} - J_i^{Model}|}{|J_i^{FOM}|}, \tag{18}$$

where $N_{nodes}$ refers to the number of nodes at the crack front and $J_i^{FOM}$ and $J_i^{Model}$ refer to the value of the $J$ integral at the node $i$.

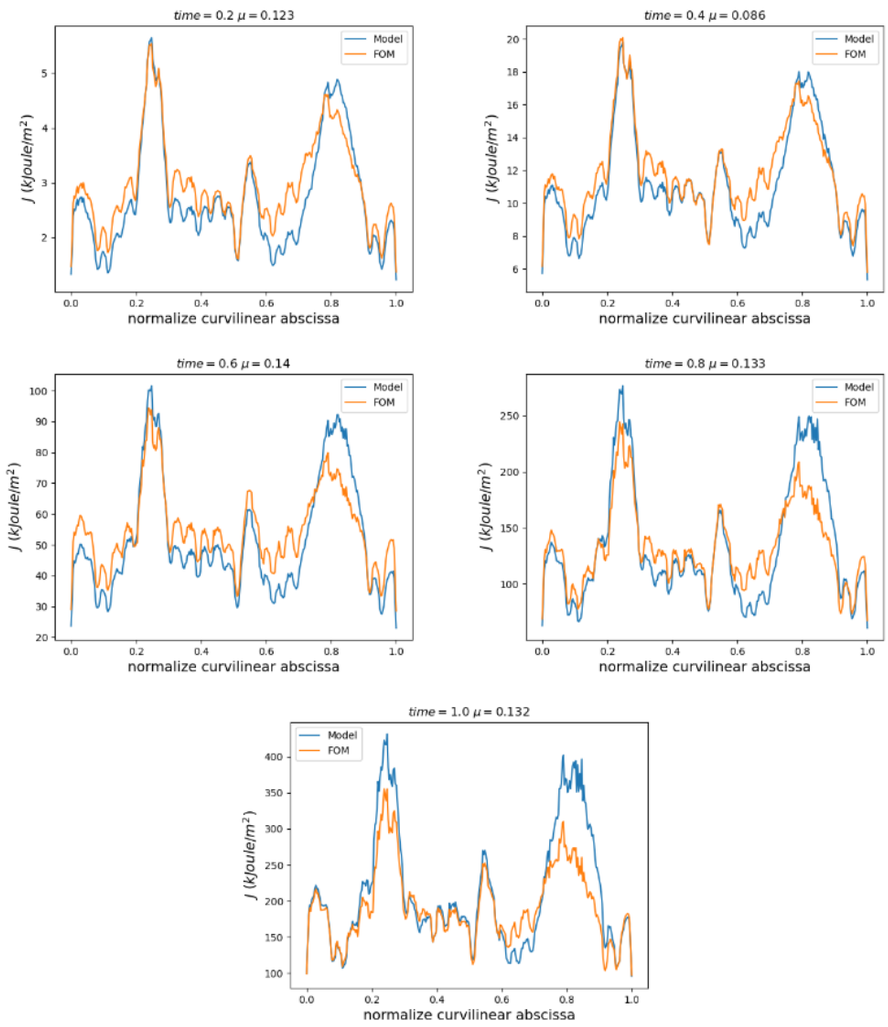


Figure 26: $J$-integral along the curvilinear abscissa for defect 1042 at each time step

Good results are achieved for the computation of the $J$ integral as well as for the limit load, underlining the performance of the so developed model. When the limit load is reached (green zone in 25) at t = 0.6 the error on the J-integral curves starts to increase (see Fig. 26). This is due to volumetric locking which is a common problem when cracked structures are considered. This type of problem is not related to the developed method. It is intrinsic to the finite element formulation and is an active field of research [16, 17]. Nevertheless to draw accurate FAD diagram the solution up to the limit load is sufficient. Both quantities $J$ integral and limit load can be computed hence the loading path for a specific defect on FAD diagrams can be drawn. FAD diagrams are usually drawn with the SIF rather than with the $J$ integral, the relation between these quantities is given in eq. 19.

$$K = \sqrt{J.E'} \qquad \text{with: } E' = \frac{E}{1-\nu^2} \tag{19}$$

On FAD the loading and the SIF are respectively normalized by the limit load and the material SIF ($Kmat$). The value of the material SIF is similar to the value of an aluminium material:

$K_{mat} = 35$ kJoule/m$^2$. Fig. (27) shows the loading path for defect 1042 with the model and with the reference FOM. The loading path is restricted to the domain up to the overloading state as the structure necessarily belongs to the unacceptable flaws domain afterwards (see Fig. 22). Recall that the reduced base of defect 53 has been used to compute the force since it is the nearest neighbour of defect 1042 in the latent space. For each of the plotted path, the value of the stress intensity factor K is equal to the maximum value around the crack front. Both defects 1042 and 53 are represented on Fig. (27).

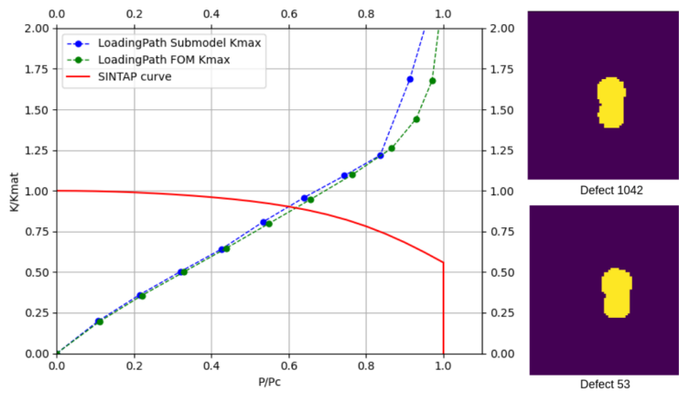


Figure 27: FAD with Model and FOM for defect 1042 (left) and the image of defect 1042 and 53, its nearest neighbour (right).

The loading path is similar to the reference one. Barely no error is made on the limit load compared to the evaluation of SIF. This problem is partially due to volumetric locking and bad pressure field computation around the front crack [17, 42]. speed-ups which are obtained for all the defects are around 3 in average and up to 10 for the best. The value of the speed-ups for each defect are represented on the histogram Fig. (28a).

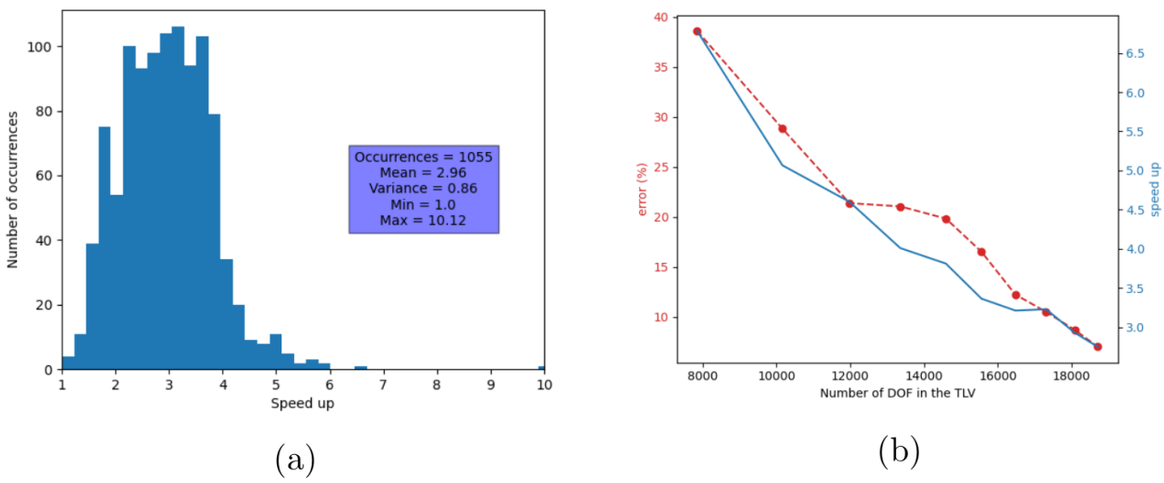


(a) (b)

Figure 28: speed-up histogram (a) and variation of the speed-up with the size of the problem for defect 1042 (b) speed-up and error evolution curve in function of the number of DOF.

The speed-ups can be improved by reducing the TLV but this will increase the error hence a compromise between speed and accuracy has to be made as it is shown on Fig. (28b).

The strength of this method is that once the MMAE has learned the link between the displacement field and the 2D images, any type of element can be used for the TLV. Moreover the mesh of the later can also be refined if needed. These modifications can enhance the speed-up. A smaller TLV for defect 1054 has been defined which consists in a torus around the front crack (see Fig. 29).

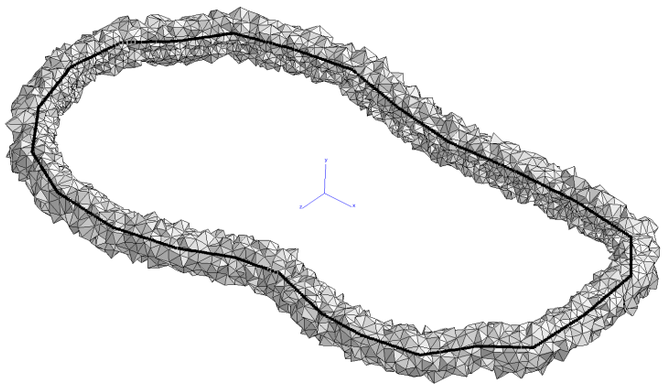

Figure 29: Smaller TLV for defect 1054

Other element type have been used with pressure control. They are more adapted for cracked structures simulations than the linear tetrahedron with reduced integration. This type of elements has additional degrees of freedom and need to be used with a quadratic formulation of the element [43, 44]. Therefore the computation times are much larger than the ones previously done. This is the reason why the training phase has not been done with these elements. The same MMAE model that has been trained in the previous section is used. The cumulated plasticity field obtained for defect 1042 with the MMAE approach and with the FOM are shown in Fig. (30a) while Fig. (30b) shows the evolution of the error $\eta$ and the speed-up in function of the number of degrees of freedom also for defect 1042.

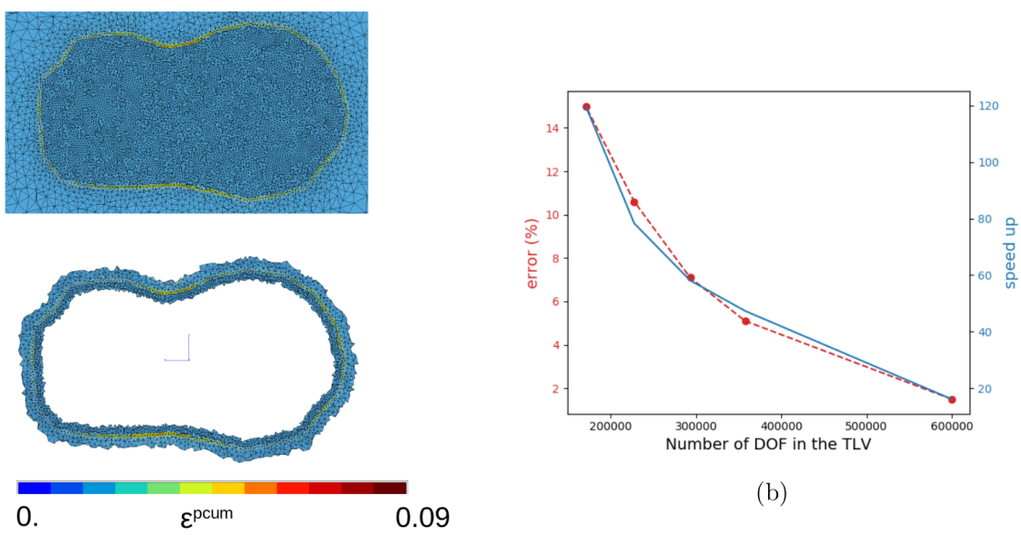


(a) (b)

Figure 30: (a) $\varepsilon^{pcum}$ with FOM (up) and with the model (down) on the reduced TLV for defect 1042 and (b) speed-up and error evolution curve in function of the number of DOF.

Much larger speed-ups are obtained with this configuration: up to 120 times faster (see Fig. 30). This type of approach enable to take entirely profit from the submodelling approach of the developed methodology. Nevertheless with such TLV the computation of the cumulated plasticity works well but for the $J$ integral it leads to high level of error when not enough elements (radius of the thorus inferior to $4.5mm$) around the front crack are present.

## 6. Conclusion

The mechanical effect of cracks in 3D volumes is known to be a function of crack morphology. We show how a MMAE can be trained to learn this implicit function from experimental data and simulation data. An automatic mechanistic simulation chain is required to get the simulation data prior training the MMAE. A high level engineering analysis of the prediction is enabled by using a mechanical submodel, termed tight local volume, feed by the MMAE predictions. The encoding mesh, that supports simulation data, is a continuous mesh. It does not allow to represent the discontinuity induced by cracks. Nevertheless, this encoding mesh is sufficient to develop an artificial intelligence for boundary conditions on a tight local volume. Good results have been achieved with the developed method. Low errors on the whole TLV are obtained (around 5%). The need of such a method has been demonstrated by comparing it with a naive model. All the standard outputs of a classical finite element computation are available and enables one to draw FAD if needed. speed-ups between 3 and 120 are obtained. Better speed-ups have been obtained by reducing the TLV size to the detriment of the accuracy. Indeed when large speed-ups are obtained the $J$ integral is very inaccurate due to the lack of element around the crack front. Moreover with this method, speed-ups depends on the mesh hence with more complex geometries it would be possible to increase the speed-up. Nevertheless the model suffers from a major limitation at the moment. The position of the crack should, in full generality, be in the encoding mesh. Not all configurations can accordingly be handled. Adding two new parameters for the position and orientation of the crack could be an option. The encoding mesh would then be implanted according to these

parameters. The main asset of this method is that all the possible outputs of a standard finite element computation are also available with the so developed model hence it has been possible to launch simulation with new elements though the MMAE model had been trained with different elements. On the contrary a surrogate model would have larger speed-up but would be trained to predict only specific outputs and would need to be retrained each time other output would be needed.

*Availability of data and materials.* The data for the present work has presently not been made available.

*Competing interests.* The authors declare no competing interests.

## Appendix A. Detail of the 2D and 3D autoencoders

Details of the 2D and 3D autoencoders, as provided by the TensorFlow summary, are given in Fig. (A.31).

```
################# Encoder #################
Model: "model"
_________________________________________________________________
Layer (type)                 Output Shape              Param #
=================================================================
input_1 (InputLayer)         [(None, 80, 80, 1)]       0
_________________________________________________________________
conv2d (Conv2D)              (None, 80, 80, 16)        272
_________________________________________________________________
max_pooling2d (MaxPooling2D) (None, 40, 40, 16)        0
_________________________________________________________________
conv2d_1 (Conv2D)            (None, 40, 40, 32)        8224
_________________________________________________________________
max_pooling2d_1 (MaxPooling2 (None, 20, 20, 32)        0
_________________________________________________________________
conv2d_2 (Conv2D)            (None, 20, 20, 64)        32832
_________________________________________________________________
flatten (Flatten)            (None, 25600)             0
_________________________________________________________________
dense (Dense)                (None, 280)               7168280
_________________________________________________________________
dense_2 (Dense)              (None, 70)                19670
=================================================================
Total params: 7,229,278
Trainable params: 7,229,278
Non-trainable params: 0
_________________________________________________________________
################# Decoder #################
Model: "model_1"
_________________________________________________________________
Layer (type)                 Output Shape              Param #
=================================================================
input_2 (InputLayer)         [(None, 70)]              0
_________________________________________________________________
dense_3 (Dense)              (None, 70)                4970
_________________________________________________________________
dense_4 (Dense)              (None, 280)               19880
_________________________________________________________________
dense_5 (Dense)              (None, 25600)             7193600
_________________________________________________________________
reshape (Reshape)            (None, 20, 20, 64)        0
_________________________________________________________________
conv2d_3 (Conv2D)            (None, 20, 20, 64)        65600
_________________________________________________________________
up_sampling2d (UpSampling2D) (None, 40, 40, 64)        0
_________________________________________________________________
conv2d_4 (Conv2D)            (None, 40, 40, 32)        32800
_________________________________________________________________
up_sampling2d_1 (UpSampling2 (None, 80, 80, 32)        0
_________________________________________________________________
conv2d_5 (Conv2D)            (None, 80, 80, 16)        8208
_________________________________________________________________
conv2d_6 (Conv2D)            (None, 80, 80, 1)         257
=================================================================
Total params: 7,325,315
Trainable params: 7,325,315
Non-trainable params: 0
```

(a)

```
################# Encoder #################
Model: "model"
_________________________________________________________________
Layer (type)                 Output Shape              Param #
=================================================================
input_1 (InputLayer)         [(None, 64, 64, 64, 5)]   0
_________________________________________________________________
conv3d (Conv3D)              (None, 64, 64, 64, 8)     2568
_________________________________________________________________
conv3d_1 (Conv3D)            (None, 64, 64, 64, 16)    8208
_________________________________________________________________
max_pooling3d (MaxPooling3D) (None, 32, 32, 32, 16)    0
_________________________________________________________________
conv3d_2 (Conv3D)            (None, 32, 32, 32, 16)    16400
_________________________________________________________________
max_pooling3d_1 (MaxPooling3 (None, 16, 16, 16, 16)    0
_________________________________________________________________
flatten (Flatten)            (None, 65536)             0
_________________________________________________________________
dense (Dense)                (None, 200)               13107400
=================================================================
Total params: 13,134,576
Trainable params: 13,134,576
Non-trainable params: 0
_________________________________________________________________
################# Decoder #################
Model: "model_1"
_________________________________________________________________
Layer (type)                 Output Shape              Param #
=================================================================
input_2 (InputLayer)         [(None, 200)]             0
_________________________________________________________________
dense_1 (Dense)              (None, 200)               40200
_________________________________________________________________
dense_2 (Dense)              (None, 65536)             13172736
_________________________________________________________________
reshape (Reshape)            (None, 16, 16, 16, 16)    0
_________________________________________________________________
conv3d_transpose (Conv3DTran (None, 16, 16, 16, 16)    16400
_________________________________________________________________
up_sampling3d (UpSampling3D) (None, 32, 32, 32, 16)    0
_________________________________________________________________
conv3d_transpose_1 (Conv3DTr (None, 32, 32, 32, 16)    16400
_________________________________________________________________
up_sampling3d_1 (UpSampling3 (None, 64, 64, 64, 16)    0
_________________________________________________________________
conv3d_transpose_2 (Conv3DTr (None, 64, 64, 64, 8)     8200
_________________________________________________________________
conv3d_transpose_3 (Conv3DTr (None, 64, 64, 64, 5)     2565
=================================================================
Total params: 13,256,501
Trainable params: 13,256,501
Non-trainable params: 0
```

(b)

```
############# Fully connected left neurone network #############
_________________________________________________________________
Layer (type)                 Output Shape              Param #
=================================================================
input_1 (InputLayer)         [(None, 70)]              0
_________________________________________________________________
dense_2 (Dense)              (None, 70)                4970
_________________________________________________________________
dense_3 (Dense)              (None, 600)               42600
=================================================================
Total params: 47,570
Trainable params: 47,570
Non-trainable params: 0
_________________________________________________________________


############# Fully connected right neurone network #############
_________________________________________________________________
Layer (type)                 Output Shape              Param #
=================================================================
input_1 (InputLayer)         [(None, 600)]             0
_________________________________________________________________
dense (Dense)                (None, 600)               360600
_________________________________________________________________
dense_1 (Dense)              (None, 70)                42070
=================================================================
Total params: 402670
Trainable params: 402670
Non-trainable params: 0
```

(c)

Figure A.31: Summary of the 2D autoencoder (a), the 3D autoencoder for any field U1, U2 or U3 (b) and the fully-connected left and right neurone network (c).

## References


[1] L. Lacourt, D. Ryckelynck, S. Forest, V. Rancourt, and S. Flouriot, "Hyper-reduced direct numerical simulation of voids in welded joints via image-based modeling," *International Journal for Numerical Methods in Engineering*, Feb. 2020.

[2] D. Ryckelynck, T. Goessel, and F. Nguyen, "Mechanical dissimilarity of defects in welded joints via grassmann manifold and machine learning." working paper or preprint, July 2020.

[3] G. Bhatt, P. Jha, and B. Raman, "Representation learning using step-based deep multi-modal autoencoders," *Pattern Recognition*, vol. 95, pp. 12–23, 2019.

[4] K. Lee and K. T. Carlberg, "Model reduction of dynamical systems on nonlinear manifolds using deep convolutional autoencoders," *Journal of Computational Physics*, vol. 404, p. 108973, 2020.

[5] P. Le Delliou, A. Dahl, C. Sonnefraud, and W. Vincent, "Experimental Results and Numerical Analyses of Tests Conducted on Large Alloy 600 Centre Cracked Tensile Specimens," vol. Volume 3B: Design and Analysis, 07 2018.

[6] U. Zerbst and Al, "Chapter 5 - the model parameters," pp. 89 – 135, 2007.

[7] J. Berg and K. Nyström, "A unified deep artificial neural network approach to partial differential equations in complex geometries," *Neurocomputing*, vol. 317, p. 28–41, Nov 2018.

[8] M. Layouni and al, "Detection and sizing of metal loss defects in oil and gas pipelines using pattern-adapted wavelets and machine learning," *Applied Soft Computing*, 2017.

[9] M. San Biagio, C. Beltran-Gonzalez, S. Giunta, A. Del Bue, and V. Murino, "Automatic inspection of aeronautic components," *Machine Vision and Applications*, vol. 28, pp. 1–15, 05 2017.

[10] C. Escobar and R. Morales Menendez, "Machine learning techniques for quality control in high conformance manufacturing environment," *Advances in Mechanical Engineering*, vol. 10, p. 168781401875551, 02 2018.

[11] C. Sobie, C. Freitas, and M. Nicolai, "Simulation driven machine learning: Bearing fault classification," *Mechanical Systems and Signal Processing*, vol. 99, pp. 403–419, 01 2018.

[12] Z. Ji, Y. Zhao, Y. Pang, and X. Li, "Cross-modal guidance based auto-encoder for multi-video summarization," *Pattern Recognition Letters*, vol. 135, pp. 131–137, 2020.

[13] Y. Zhang, Y. Qiu, Y. Cui, S. Liu, and W. Zhang, "Predicting drug-drug interactions using multi-modal deep auto-encoders based network embedding and positive-unlabeled learning," *Methods*, vol. 179, pp. 37–46, 2020. Interpretable machine learning in bioinformatics.

[14] L. Lacourt, *Étude numérique de la nocivité des défauts dans les soudures*. PhD thesis, Mines ParisTech - Université PSL, 2019.

[15] M. Bartoň, I. Hanniel, G. Elber, and M.-S. Kim, "Precise hausdorff distance computation between polygonal meshes," *Computer Aided Geometric Design*, vol. 27, no. 8, pp. 580–591, 2010. Advances in Applied Geometry.

[16] J. Besson, C. Berdin, S. Bugat, R. Desmorat, F. Feyel, S. Forest, E. Lorentz, E. Maire, T. Pardoen, A. Pineau, and B. Tanguy, *Local approach to fracture*. 01 2004.

[17] V. Davaze, N. Vallino, B. Langrand, J. Besson, and S. Feld-Payet, "A non-local damage approach compatible with dynamic explicit simulations and parallel computing," *International Journal of Solids and Structures*, 2021.

[18] J. Besson and R. Foerch, "Large scale object–oriented finite element code design," *Comp. Meth. Appl. Mech. Engng*, vol. 142, pp. 165–187, 1997.

[19] R. Foerch, J. Besson, G. Cailletaud, and P. Pilvin, "Polymorphic constitutive equations in finite element codes," *Comp. Meth. Appl. Mech. Engng*, vol. 141, pp. 355–372, 1997.

[20] J. Besson and R. Foerch, "Application of object–oriented programming techniques to the finite element method. Part I— General concepts," *Revue Européenne des éléments finis*, vol. 7, no. 5, pp. 535–566, 1998.

[21] J. Besson, R. Le Riche, R. Foerch, and G. Cailletaud, "Application of object–oriented programming techniques to the finite element method. Part II— Application to material behaviors," *Revue Européenne des éléments finis*, vol. 7, no. 5, pp. 567–588, 1998.

[22] P. G. Ciarlet, "The finite element method for elliptic problems," 1978.

[23] S. Fayolle, "Modèles de grandes déformations gdef log et gdef hypo elas." Open source on www.codeaster.org, 2015.

[24] C. Miehe, N. Apel, and M. Lambrecht, "Anisotropic additive plasticity in the logarithmic strain space: modular kinematic formulation and implementation based on incremental minimization principles for standard materials," *Computer Methods in Applied Mechanics and Engineering*, vol. 191, no. 47, pp. 5383–5425, 2002.

[25] J. Chai, H. Zeng, A. Li, and E. W. Ngai, "Deep learning in computer vision: A critical review of emerging techniques and application scenarios," *Machine Learning with Applications*, vol. 6, p. 100134, 2021.

[26] D. Huang, J. N. Fuhg, C. Weißenfels, and P. Wriggers, "A machine learning based plasticity model using proper orthogonal decomposition," *Computer Methods in Applied Mechanics and Engineering*, vol. 365, p. 113008, 2020.

[27] P. Cheridito, A. Jentzen, and F. Rossmannek, "Non-convergence of stochastic gradient descent in the training of deep neural networks," *Journal of Complexity*, vol. 64, p. 101540, 2021.

[28] Y. Guo, J. Chen, Q. Du, A. Van Den Hengel, Q. Shi, and M. Tan, "Multi-way backpropagation for training compact deep neural networks," *Neural Networks*, vol. 126, pp. 250–261, 2020.

[29] Y. Le Cun, B. Boser, J. S. Denker, D. Henderson, R. E. Howard, W. Hubbard, and L. D. Jackel, "Handwritten digit recognition with a back-propagation network," p. 396–404, 1989.

[30] G. E. Hinton and R. R. Salakhutdinov, "Reducing the dimensionality of data with neural networks," *Science*, vol. 313, no. 5786, pp. 504–507, 2006.

[31] E. Gomede, R. M. de Barros, and L. de Souza Mendes, "Deep auto encoders to adaptive e-learning recommender system," *Computers and Education: Artificial Intelligence*, vol. 2, p. 100009, 2021.

[32] Y. Wu, S. Wang, and Q. Huang, "Multi-modal semantic autoencoder for cross-modal retrieval," *Neurocomputing*, vol. 331, pp. 165–175, 2019.

[33] K. Raimi, "towards data science, illustrated: 10 cnn architectures," 2019.

[34] J. T. Machado and Y. Luchko, "Multidimensional scaling and visualization of patterns in distribution of nontrivial zeros of the zeta-function," *Communications in Nonlinear Science and Numerical Simulation*, p. 105924, 2021.

[35] I. Borg and P. J. F. Groenen, *Modern Multidimensional Scaling Theory and Applications*. New York: Springer, 2005.

[36] H. Launay, F. Willot, D. Ryckelynck, and J. Besson, "Mechanical assessment of defects in welded joints: morphological classification and data augmentation," *Journal of Mathematics in Industry 11*, 2021.

[37] T. Daniel, F. Casenave, N. Akkari, and D. Ryckelynck, "Model order reduction assisted by deep neural networks (rom-net)," *Submitted to Advanced Modeling and Simulation in Engineering Sciences*, 2020.

[38] H. Launay, J. Besson, D. Ryckelynck, and F. Willot, "Hyper-reduced arc-length algorithm for stability analysis in elastoplasticity," *International Journal of Solids and Structures*, vol. 208-209, pp. 167 – 180, 2021.

[39] R. K. Sharma, A. Ghosh, D. Bhachawat, S. Ingole, A. Balasubramanian, and U. Muktibodh, "Assessment of structural integrity of pressure tubes during cold pressurization," *Procedia Engineering*, vol. 86, pp. 359–366, 2014. Structural Integrity.

[40] R. Everson and L. Sirovich, "Karhunen-Loève procedure for gappy data," *J. Opt. Soc. Am. A*, vol. 12, pp. 1657–1664, 1995.

[41] D. Ryckelynck, K. Lampoh, and S. Quilicy, "Hyper-reduced predictions for lifetime assessment of elasto-plastic structures," *Meccanica*, vol. 51, pp. 309–317, Feb 2016.

[42] G. Hütter, T. Linse, U. Mühlich, and M. Kuna, "Simulation of ductile crack initiation and propagation by means of a non-local gurson-model," *International Journal of Solids and Structures*, vol. 50, no. 5, pp. 662–671, 2013.

[43] R. Taylor, "A mixed-enhanced formulation for tetrahedral finite elements," vol. 47, pp. 205–227, 2000.

[44] D. Al Akhrass, J. Bruchon, S. Drapier, and S. Fayolle, "Integrating a logarithmic-strain based hyperelastic formulation into a three-field mixed finite element formulation to deal with incompressibility in finite-strain elastoplasticity," *Finite Elements in Analysis and Design*, vol. 86, pp. 61–70, 2014.

# Chapter 6

# Conclusions and perspectives

**Contents**



**Résumé en français**


L'objectif principal de ce travail était de développer des méthodes basées sur l'apprentissage automatique et la réduction dimensionnelle afin d'accélérer les prédictions pour l'évaluation des structures et la création de jumeaux numériques à l'aide d'images. D'un point de vue industriel, l'objectif est de minimiser le nombre de composants rejetés qui auraient été fonctionnels. L'utilisation de graphiques et d'abaques est souvent trop conservative tandis que l'utilisation de simulations par éléments finis conduit souvent à des prédictions qui prennent beaucoup de temps. C'est pourquoi des méthodes telles que celles développées dans ce manuscrit sont proposées, permettant une évaluation rapide et précise des quantités d'intérêt. Trois études principales ont été menées dans cette thèse :
→ L'hyper-réduction d'un algorithme de longueur d'arc pour l'évaluation de la pression limite.
→ La détermination de la criticité des pores dans des joints soudés par la modélisation basée sur l'image et la résolution de problèmes de classification des défauts.
→ Le developpement de methodes d'apprentissage profond pour l'évaluation de la criticité de fissures non paramétriques dans les structures en utilisant un sous-modèle mécanique.
Les limites de chacune de ces méthodes sont abordées. Un prolongement de ce travail consisterait à créer une chaîne de calculs avec chacune de ces briques afin de tirer profit des avantages de chacune d'entre elles.


## 6.1 Summary of the approach and important results

The main objective of this work was to develop methods to make the safety assessment of structures. This safety assessment is often made with charts, which lead to over conservative dimensioning, or with numerical methods, which lead to time consuming computations. To overcome these two drawbacks (too conservative and time consuming), methods based on machine learning and dimensionality reduction have been proposed to accelerate predictions in order to evaluate structures and create accurate image-based digital twins. From an industrial point of view, the objective is to minimize the number of rejected components which would have been functional. The use of charts is often too conservative while the use of finite element simulations often leads to predictions which are highly time consuming. This is why methods such as those developed in this manuscript are proposed, allowing a rapid and precise evaluation of the quantities of interest. Three main studies were carried out in this work:
→ Hyper-reduction of finite element models for the evaluation of the limiting pressure, as an extension of dimensionality reduction to model order reduction including an arc-length algorithm.
→ Determination of the criticality of voids in welded joints via image-based modeling and solution of a defect classification problems.
→ Deep learning for the evaluation of nonparametric cracks in structures, using a mechanical submodel, comparable to the resolution of a regression problem between a defect image and boundary conditions for the submodel.

### 6.1.1 Hyper-reduction for limit pressure evaluation

The precise evaluation of the limit load in the pipes remains complex because of the plastic instability which appears and leads to a buckling phenomenon. When buckling occurs, a classical Newton algorithm diverges and it is therefore necessary to use specific algorithms such as

the arc-length algorithm. A new hyper-reduced version of this algorithm has been developed and implemented in the commercial Zset software. The method thus developed uses a greedy algorithm coupled with an error estimator in order to calculate an optimal reduced base thanks to those already present in a database. Figure 6.1 illustrates the overall methodology that has been detailed in the manuscript.

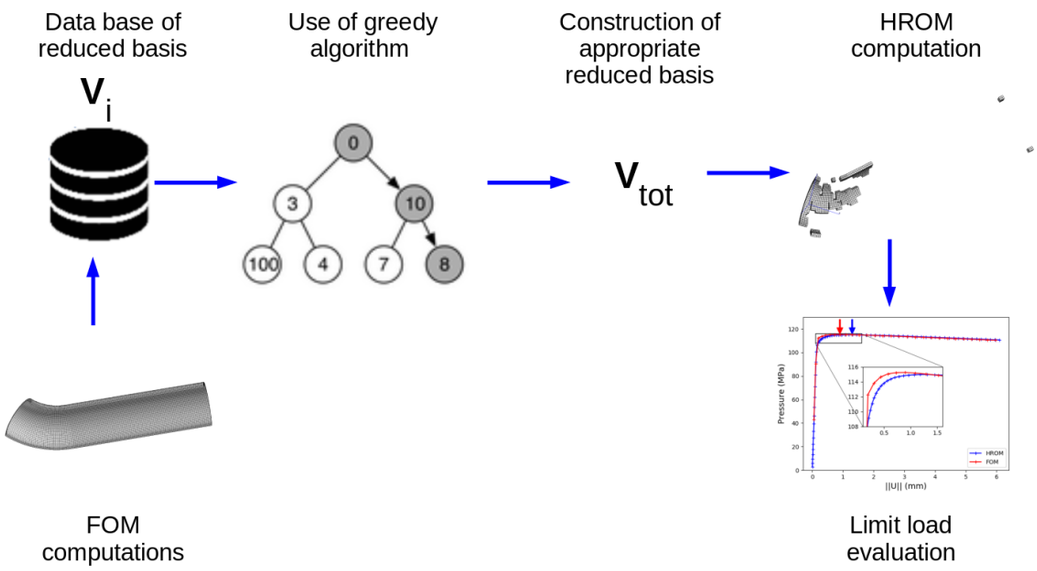


Figure 6.1: Diagram of the HR Riks algorithm.

The considered cases were defined with different parameters such as the radius of curvature, the outside radius, the thickness and the angle of the bent pipe. The parametric space was sampled with the HROM arc-length approach and the error estimator was used to define a confidence zone. Significant speed-ups have been obtained : up to 15 times faster predictions. This extension of the hyper-reduction method does not suffer from any limitation different from those of the classical hyper reduction method. It is based on a linear approach to dimensionality reduction. The latent space is assumed to be globally linear, over its validity domain.
One of the main perspective is to apply this new hyper reduced scheme to structures containing cracks. The presence of cracks leads to high local variations of the displacement field. This make it difficult to create an appropriate reduced basis for the online phase.

### 6.1.2 Determination of the criticality of voids in image-based digital twins of welded joints

Calculation of the maximum von Mises stress near defects as well as stress / strain loops are common inputs to assess the fatigue lifetime of structures. A decoupled approach is used to calculate these quantities. The mechanical quantities of the sane structure and of the isolated defect are calculated separately and then assembled in a common scale model to make a hyper-reduced prediction on the structure containing the defect. As many defect morphologies have been observed, a machine learning approach based on clustering and neural network was created. Instead of calculating the interesting mechanical quantities of the defect considered, this information is retrieved from a database using a classifier. This database was created using a clustering approach. The whole process is depicted in Fig 6.2.

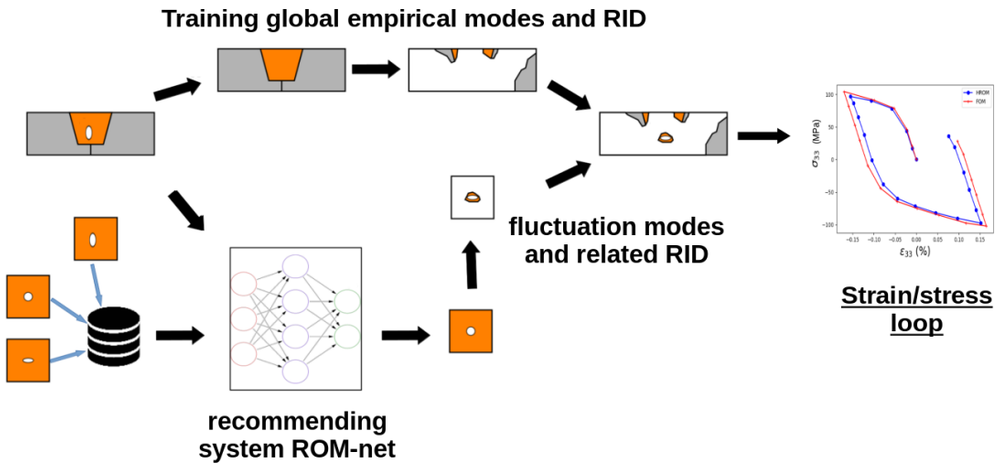


Figure 6.2: Two scales HROM with ROM-net recommender.

The complete workflow has been launched for all the compete dataset of 3D images of pores obtained by X-ray tomography. The strain/stress loops which have been drawn are close to those obtained with the classical finite element approach and large speed-ups have been achieved, up to 50 times faster predictions. Increasing the number of defect categories should improve mechanical results. Likewise, the way in which the boundary conditions are applied on the isolated defect can be criticized. In the developed methodology, the three tractions and the three shears were applied to the Representative Elementary Volume (REV). Instead, the strain measured at the location of the void on the sound structure could be applied to the REV to better mimic the stress that the defect actually experiences in the structure, in case of non-linear plastic strains. Another limitation of the method is that the defect must be inside the bulk. In order to be able to treat any defect, it would be necessary to extend the method for defects near or on the surface of the structure.
In this work, a single fatigue cycle has been applied. It would be interesting to apply a high number of cycles in order to obtained the stabilized strain/stress loops.
A different application than this of voids in welded joints would be to assess discs in gas turbine engines. This discs can contain particles that play the role of stress concentrators just like voids in welded joints. The crack initiation due to the presence of particles in turbine discs has been studied in [Alexandre et al., 2004, Abdesselam et al., 2018], this would be a perfect study case for the developed methodology.

### 6.1.3 Deep learning for the evaluation of nonparametric cracks in structures

The calculation of cracked structure is complex and very costly in calculation. This is partly due to the singularity present at the end of the crack. Many models have been developed to overcome this difficulty, but the resulting computation time is very important. A new methodology based on deep Multi Modal Auto Encoder (MMAE) has been presented in this work. The main idea is to have a 2D image of the crack as input and to use the intermodal reconstruction to predict the displacement field on a small mechanical submodel. The 2D image reconstruction is used as an error indicator. This methodology is described in Fig.6.3.

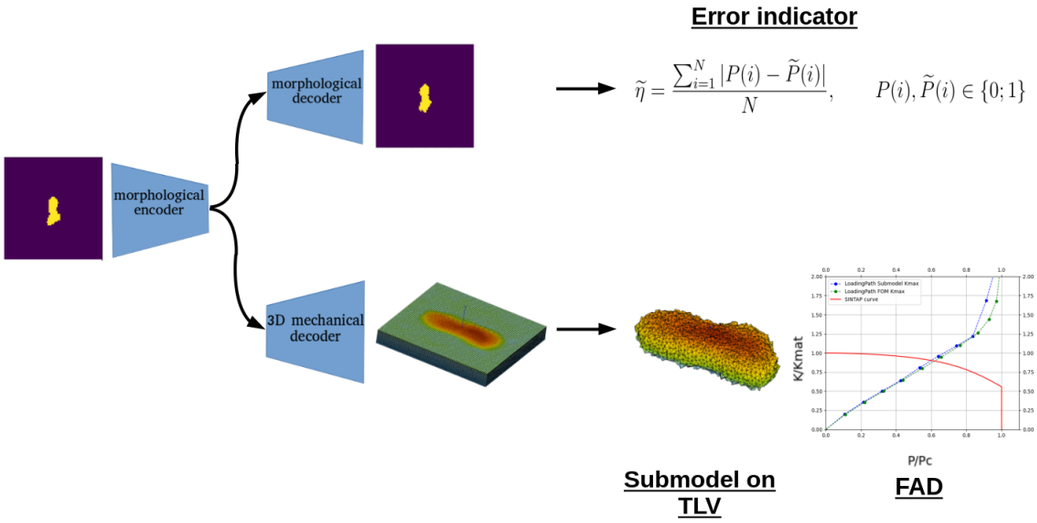


Figure 6.3: ChainMMAE.

In addition, the common latent space is used to recover the full field over the entire sample and not just the subfield. To do this, a nearest neighbor algorithm coupled with a POD gappy process is used. Accurate results have been obtained with an error of about 6% and significant speed-ups have been achieved, up to 120 times faster. Nevertheless the model suffers from a major limitation at the moment. The position of the crack must be in the encoding mesh so not all configurations can be handled. One option to get rid of this limitation would be to create an encoding mesh of the same size as the full sample, but such an approach would lead to extremely large encoding meshes and storage volumes. In case such storage resources are available, a new parameter should be introduced such as the position and orientation of the 2D images for its insertion in the mesh. These parameters should also be used for the training phase of the model. Moreover in this work the position of the cracks was necessary in the bulk. Extending the so developed workflow for surface cracks is a work in progress.
The simulations were made on a portion of the specimen, applying the method to the real structure is also an outlook.
From an industrial point of view, cracks are usually represented with parametrised shapes, it is important to underline that the so developed methodology can easily deal with a parametrised dataset of crack images.

## 6.2 Perspectives

In the work that has been done, the structures that contained these defects were rather simple (pipes, welded joints, tensile specimen...). It would be interesting to try all the workflows created on more complex structures. Another perspective would be to implement the workflows used for structures containing voids and the one for structures containing cracks in a dedicated software such as Z7. For the moment the raw codes are available on the github repositories of the laboratory. The work that has been done in this thesis has been divided into three main parts:
→ Hyper reduction of the arc length algorithm.
→ Reduced base machine learning classification for hyper reduced computations.
→ Deep multimodal automatic encoder to evaluate the criticality of cracks.
At first sight, these parts seem quite independent but one can imagine a larger workflow linking them together. Consider an R&D department studying a pipe network in which many cracks eventually appear. In order to calculate the burst pressure of the defective pipes, $N$ finite element simulations are run on $N$ different crack shapes that have been observed. In order to speedup the calculation for the next $N'$ simulations, a hyper-reduced approach using a hyper-reduced arc length algorithm is used, as described in the third chapter. But to run a hyper-reduced arc length simulation for a structure with a crack that has never been observed, an appropriate reduced basis, which already exists, must be selected. To do this, the methodology developed in the fourth chapter can be used. Once the $N + N'$ simulations are completed, they can be stored in a database and used to train an MMAE model as described in the fifth chapter. The remaining $N''$ simulations to be done can then be run with the MMAE approach. Fig. 6.4 illustrates this more complex workflow.

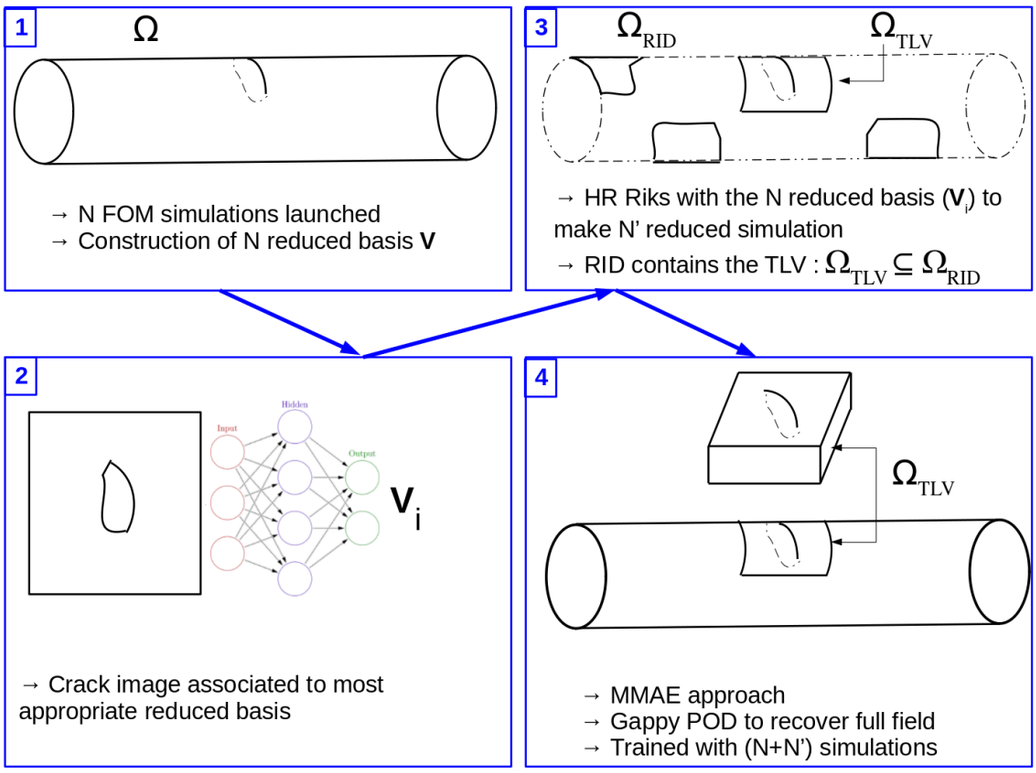


Figure 6.4: Full chain using the three main workflows which have been developed in this thesis.

Such a chain would give speedups to create the $N'$ simulations of the data set. The speedups are, for the HR Riks algorithm, about 15 times faster while speed ups uo to 120 times faster can be achieved for the last part of this workflow when the MMAE is used. The overall acceleration of these three chains would be :

$$\text{Speed up} = \frac{N + (15 \times N') + (120 \times N'')}{N + N' + N''} \tag{6.1}$$

Although this chain was not developed in this thesis work, it is important to see how they could all be deployed together in an industrial environment.

A major perspective for all the methods which have been developed in this work is to create an upper bound of the error. Three error indicators have been proposed in this work. The first one (chapter 3) is based on the reconstruction of the stress field with the Gappy POD procedure. A good correlation (less than 20% of error) has been obtained and this estimator has then been used as a selection criteria for a greedy algorithm.
The second one (chapter 4) was defined as a linear relation between the true error and the distance of the considered defect to its associated medoid.
Finally the third error indicator (chapter 5) was based on the reconstruction error of the 2D input image representing a crack. A linear relation between the true error and the error made on the reconstruction of the input image has been made.
The performance of the error indicators can be criticised mostly for the second one and third one. The main drawback of the so developed indicators is that none of them constitutes an upper bound of the error. In an industrial context such criteria is a must in order to avoid the falsely operational component.

# Bibliography


[MAD, 2002] (2002). Chapter 1 - fatigue design rules for welded steel joints. In MADDOX, S. J., editor, *Fatigue Strength of Welded Structures (Second Edition)*, Woodhead Publishing Series in Welding and Other Joining Technologies, pages 79–105. Woodhead Publishing, second edition edition.

[Abdesselam et al., 2018] Abdesselam, H., Crépin, J., Pineau, A., Rouffié, A.-L., Gaborit, P., Menut-Tournadre, L., and Morgeneyer, T. F. (2018). On the crystallographic, stage I-like, character of fine granular area formation in internal fish-eye fatigue cracks. *International Journal of Fatigue*, 106:132–142.

[Alexandre et al., 2004] Alexandre, F., Deyber, S., and Pineau, A. (2004). Modelling the optimum grain size on the low cycle fatigue life of a ni based superalloy in the presence of two possible crack initiation sites. *Scripta Materialia*, 50(1):25–30.

[Almroth et al., 1978] Almroth, B. O., Stern, P., and Brogan, F. A. (1978). Automatic choice of global shape functions in structural analysis. *AIAA Journal*, 16(5):525–528.

[Ammar et al., 2006] Ammar, A., Mokdad, B., Chinesta, F., and Keunings, R. (2006). A new family of solvers for some classes of multidimensional partial differential equations encountered in kinetic theory modeling of complex fluids. *Journal of Non-Newtonian Fluid Mechanics*, 139(3):153–176.

[Amsallem and Haasdonk, 2016] Amsallem, D. and Haasdonk, B. (2016). Pebl-rom: Projection-error based local reduced-order models. *Advanced Modeling and Simulation in Engineering Sciences*, 3.

[Amsallem et al., 2012] Amsallem, D., Zahr, M. J., and Farhat, C. (2012). Nonlinear model order reduction based on local reduced-order bases. *International Journal for Numerical Methods in Engineering*, 92(10):891–916.

[Amsallem et al., 2015] Amsallem, D., Zahr, M. J., and Washabaugh, K. (2015). Fast local reduced basis updates for the efficient reduction of nonlinear systems with hyper-reduction. *Advances in Computational Mathematics*, 41:1187–1230.

[Bae et al., 2021] Bae, H., Jang, K., and An, Y.-K. (2021). Deep super resolution crack network (srcnet) for improving computer vision–based automated crack detectability in in situ bridges. *Structural Health Monitoring*, 20(4):1428–1442.

[Barrault and Al., 2004] Barrault, M. and Al. (2004). An empirical interpolation method: application to efficient reduced-basis discretization of partial differential equations. *Comptes Rendus Math ;339(9):667-672.*

[Barsoum, 1977] Barsoum, R. S. (1977). Triangular quarter-point elements as elastic and perfectly-plastic crack tip elements. *International Journal for Numerical Methods in Engineering*, 11(1):85–98.

[Bhonsle et al., 2009] Bhonsle, S., Klinzmann, A., Park, F., and Esser, E. (2009). Centroid Distance Function and the Fourier Descriptor with Applications to Cancer Cell Clustering.

[Boucard and Ladeveze, 1999] Boucard, P.-A. and Ladeveze, P. (1999). A multiple solution method for non-linear structural mechanics. *Mechanical Engineering*, 50.

[Brand, 2002] Brand, M. (2002). Incremental singular value decomposition of uncertain data with missing values. In Heyden, A., Sparr, G., Nielsen, M., and Johansen, P., editors, *Computer Vision — ECCV 2002*, pages 707–720, Berlin, Heidelberg. Springer Berlin Heidelberg.

[Brisard and Dormieux, 2010] Brisard, S. and Dormieux, L. (2010). FFT-based methods for the mechanics of composites: A general variational framework. *Computational Materials Science*, 49(3):663–671.

[Cha et al., 2017] Cha, Y.-J., Choi, W., and Büyüköztürk, O. (2017). Deep learning-based crack damage detection using convolutional neural networks. *Computer-Aided Civil and Infrastructure Engineering*, 32(5):361–378.

[Chaturantabut and Sorensen, 2009] Chaturantabut, S. and Sorensen, D. (2009). Discrete empirical interpolation for nonlinear model reduction. *Discrete Empirical Interpolation for nonlinear model reduction.*

[Chen and Jahanshahi, 2018] Chen, F.-C. and Jahanshahi, M. (2018). Nb-cnn: Deep learning-based crack detection using convolutional neural network and naïve bayes data fusion. *IEEE Transactions on Industrial Electronics*, 65(5):4392–4400. cited By 360.

[Chinesta et al., 2010] Chinesta, F., Ammar, A., and Cueto, E. (2010). Recent advances and new challenges in the use of the proper generalized decomposition for solving multidimensional models. *Archives of Computational Methods in Engineering*, 17:327–350.

[Chinesta and Ladeveze, 2014] Chinesta, F. and Ladeveze, P. (2014). *Separated Representations and PGD-Based Model Reduction: Fundamentals and Applications.*

[Daniel et al., 2020] Daniel, T., Casenave, F., Akkari, N., and Ryckelynck, D. (2020). Model order reduction assisted by deep neural networks (rom-net). *Submitted to Advanced Modeling and Simulation in Engineering Sciences.*

[Daniel et al., 2021a] Daniel, T., Casenave, F., Akkari, N., Ryckelynck, D., and Rey, C. (2021a). Uncertainty quantification for industrial design using dictionaries of reduced order models.

[Daniel et al., 2021b] Daniel, T., Ketata, A., Casenave, F., and Ryckelynck, D. (2021b). Physics-informed cluster analysis and a priori efficiency criterion for the construction of local reduced-order bases. *ArXiv*, abs/2103.13683.

[De Lathauwer et al., 2000] De Lathauwer, L., De Moor, B., and Vandewalle, J. (2000). A multilinear singular value decomposition. *SIAM Journal on Matrix Analysis and Applications*, 21(4):1253–1278.

[Dihlmann et al., 2011] Dihlmann, M., Drohmann, M., and Haasdonk, B. (2011). Model reduction of parametrized evolution problems using the reduced basis method with adaptive time partitioning.

[Duan and Shen, 2006] Duan, Z.-X. and Shen, S.-M. (2006). Analysis and experiments on the plastic limit pressure of elbows. *International Journal of Pressure Vessels and Piping*, 83(10):707–713.

[E. H. and D. S., 2012] E. H., G. and D. S., S. (2012). The digital twin paradigm forfuture nasa and u.s. air force vehicles.

[Eckart and Young, 1936] Eckart, C. and Young, G. (1936). The approximation of one matrix by another of lower rank. *Psychometrika*, 1:211–218.

[Everson and Sirovich, 1995] Everson, R. and Sirovich, L. (1995). Karhunen-Loève procedure for gappy data. *J. Opt. Soc. Am. A*, 12:1657–1664.

[Fan et al., 2003] Fan, J., McDowell, D., Horstemeyer, M. F., and Gall, K. (2003). Cyclic plasticity at pores and inclusions in cast al-si alloys. *Engineering Fracture Mechanics*, 70:1281–1302.

[Fauque, 2018] Fauque, J. (2018). *Modèle d'ordre réduit en mécanique du contact. Application à la simulation du comportement des combustibles nucléaires.* PhD thesis, Mines ParisTech - Université PSL.

[Fauque et al., 2018] Fauque, J., Ramiere, I., and Ryckelynck, D. (2018). Hybrid hyper-reduced modeling for contact mechanics problems. *International Journal for Numerical Methods in Engineering*, 115(1):117–139.

[Fomin and Kashaev, 2017] Fomin, F. and Kashaev, N. (2017). Influence of porosity on the high cycle fatigue behaviour of laser beam welded ti-6al-4v butt joints. *Procedia Structural Integrity*, 7:415–422.

[Fritzen et al., 2016] Fritzen, F., Haasdonk, B., Ryckelynck, D., and Schöps, S. (2016). An algorithmic comparison of the hyper reduction and the discrete empirical interpolation method for a nonlinear thermal problem. *Mathematical and Computational Applications*, 23.

[Fu et al., 2021] Fu, R., Xiao, D., Navon, I. M., and Wang, C. (2021). A data driven reduced order model of fluid flow by auto encoder and self-attention deep learning methods.

[Geneva and Zabaras, 2020] Geneva, N. and Zabaras, N. (2020). Modeling the dynamics of pde systems with physics constrained deep auto regressive networks. *Journal of Computational Physics*, 403:109056.

[Ghnatios et al., 2019] Ghnatios, C., Asmar, G., Chakar, E., and Mosleh, C. B. (2019). A reduced-order model manifold technique for automated structural defects judging using the pgd with analytical validation. *Comptes Rendus Mécanique*, 347(2):101–113.

[Golub and Van Loan, 1983] Golub, G. H. and Van Loan, C. F. (1983). *Matrix Computations*. The Johns Hopkins University Press, third edition.

[Goodall, 1978] Goodall, I. (1978). *Lower Bound Limit Analysis of Curved Tubes Loaded by Combined Internal Pressure and In-Plane Bending Movement*. CEGB.

[Grimberg et al., 2020] Grimberg, S., Farhat, C., Tezaur, R., and Bou-Mosleh, C. (2020). Mesh sampling and weighting for the hyperreduction of nonlinear petrov-galerkin reduced-order models with local reduced-order bases. *arXiv: Numerical Analysis*.

[Haasdonk et al., 2011] Haasdonk, B., Dihlmann, M., and Ohlberger, M. (2011). A training set and multiple bases generation approach for parametrized model reduction based on adaptive grids in parameter space. *Mathematical and Computer Modelling of Dynamical Systems*, 17:423–442.

[Hackbusch and Kühn, 2009] Hackbusch, W. and Kühn, S. (2009). A new scheme for the tensor representation. *Journal of Fourier Analysis and Applications*, 15:706–722.

[Henshell and Shaw, 1975] Henshell, R. D. and Shaw, K. G. (1975). Crack tip finite elements are unnecessary. *International Journal for Numerical Methods in Engineering*, 9(3):495–507.

[Hinton and Salakhutdinov, 2006] Hinton, G. E. and Salakhutdinov, R. R. (2006). Reducing the dimensionality of data with neural networks. *Science*, 313(5786):504–507.

[Hougardy, 2010] Hougardy, S. (2010). The floyd–warshall algorithm on graphs with negative cycles. *Information Processing Letters*, 110(8):279–281.

[I. Borg, 2005] I. Borg, P. J. F. G. (2005). *Modern Multidimensional Scaling*. Springer-Verlag New York.

[Irwin, 1957] Irwin, G. R. (1957). Analysis of stresses and strains near the end of a crack traversing a plate. *Journal of Applied Mechanics*, 24(3):361–364.

[Jang et al., 2019] Jang, K., Kim, N., and An, Y.-K. (2019). Deep learning–based autonomous concrete crack evaluation through hybrid image scanning. *Structural Health Monitoring*, 18(5-6):1722–1737.

[Jogdand and Murthy, 2010] Jogdand, P. and Murthy, K. (2010). A finite element based interior collocation method for the computation of stress intensity factors and t-stresses. *Engineering Fracture Mechanics*, 77(7):1116–1127.

[Karhunen, 1946] Karhunen, K. (1946). Zur spektraltheorie stochastischer prozesse. *Ann. Acad. Sci. Finnicae, Ser. A*, 1:34.

[Khalaj Khalajestani et al., 2015] Khalaj Khalajestani, M., Bahaari, M. R., Salehi, A., and Shahbazi, S. (2015). Predicting the limit pressure capacity of pipe elbows containing single defects. *Applied Ocean Research*, 53:15–22.

[Kim et al., 2013] Kim, J. W., Yoon, M. S., and Park, C. Y. (2013). The effect of load-controlled bending load on the failure pressure of wall-thinned pipe elbows. *Nuclear Engineering and Design*, 265:174–183.

[Kruskal, 1964] Kruskal, J. (1964). Multidimensional scaling by optimizing goodness of fit to a nonmetric hypothesis. *Psychometrika*, 29(1):1–27.

[Lacourt, 2019] Lacourt, L. (2019). *Étude numérique de la nocivité des défauts dans les soudures*. PhD thesis, Mines ParisTech - Université PSL.

[Lacourt et al., 2020] Lacourt, L., Ryckelynck, D., Forest, S., Rancourt, V., and Flouriot, S. (2020). Hyper-reduced direct numerical simulation of voids in welded joints via image-based modeling. *International Journal for Numerical Methods in Engineering*.

[Ladevèze et al., 2018] Ladevèze, P., Paillet, C., and Néron, D. (2018). *Extended-PGD Model Reduction for Nonlinear Solid Mechanics Problems Involving Many Parameters*, pages 201–220. Springer International Publishing, Cham.

[Ladevèze et al., 2010] Ladevèze, P., Passieux, J.-C., and Néron, D. (2010). The latin multiscale computational method and the proper generalized decomposition. *Computer Methods in Applied Mechanics and Engineering*, 199(21):1287–1296. Multiscale Models and Mathematical Aspects in Solid and Fluid Mechanics.

[Lam and Zhou, 2016] Lam, C. and Zhou, W. (2016). Statistical analyses of incidents on onshore gas transmission pipelines based on phmsa database. *International Journal of Pressure Vessels and Piping*, 145(C):29–40.

[Launay et al., 2021] Launay, H., Besson, J., Ryckelynck, D., and Willot, F. (2021). Hyper-reduced arc-length algorithm for stability analysis in elastoplasticity. *International Journal of Solids and Structures*, 208-209:167 – 180.

[LeCun et al., 2015] LeCun, Y., Bengio, Y., and Hinton, G. (2015). Deep learning. *Nature*, 521(7553):436–444.

[Lecun et al., 1998] Lecun, Y., Bottou, L., Bengio, Y., and Haffner, P. (1998). Gradient-based learning applied to document recognition. *Proceedings of the IEEE*, 86(11):2278–2324.

[Lee et al., 2015] Lee, G. H., Pouraria, H., Seo, J. K., and Paik, J. K. (2015). Burst strength behaviour of an aging subsea gas pipeline elbow in different external and internal corrosion-damaged positions. *International Journal of Naval Architecture and Ocean Engineering*, 7(3):435–451.

[Lee and Carlberg, 2020] Lee, K. and Carlberg, K. T. (2020). Model reduction of dynamical systems on nonlinear manifolds using deep convolutional autoencoders. *Journal of Computational Physics*, 404:108973.

[Li et al., 2001] Li, Z., Yinpei, W., Jin, C., and Cengdian, L. (2001). Evaluation of local thinned pressurized elbows. *International Journal of Pressure Vessels and Piping*, 78(10):697–703.

[Liu et al., 2020] Liu, X., Athanasiou, C. E., Padture, N. P., Sheldon, B. W., and Gao, H. (2020). A machine learning approach to fracture mechanics problems. *Acta Materialia*, 190:105–112.

[Loève, 1955] Loève, M. (1955). *Probability Theory*. University series in higher mathematics. Springer-Verlag.

[Long et al., 2021] Long, X., Zhao, S., Jiang, C., Li, W., and Liu, C. (2021). Deep learning-based planar crack damage evaluation using convolutional neural networks. *Engineering Fracture Mechanics*, 246:107604.

[Lumley, 1967] Lumley, J. L. (1967). The structure of inhomogeneous turbulent flows. *Atmospheric Turbulence and Radio Wave Propagation*.

[Machado and Luchko, 2021] Machado, J. T. and Luchko, Y. (2021). Multidimensional scaling and visualization of patterns in distribution of nontrivial zeros of the zeta-function. *Communications in Nonlinear Science and Numerical Simulation*, page 105924.

[Maday and Rønquist, 2002] Maday, Y. and Rønquist, E. M. (2002). A reduced-basis element method. *Comptes Rendus Mathematique*, 335(2):195–200.

[Mahoney, 2011] Mahoney, M. W. (2011). Randomized algorithms for matrices and data. *CoRR*, abs/1104.5557.

[Martínez et al., 2021] Martínez, E. R., Chakraborty, S., and Tesfamariam, S. (2021). Machine learning assisted stochastic-xfem for stochastic crack propagation and reliability analysis. *Theoretical and Applied Fracture Mechanics*, 112:102882.

[Michel et al., 2001] Michel, J. C., Moulinec, H., and Suquet, P. (2001). A computational scheme for linear and non-linear composites with arbitrary phase contrast. *International Journal for Numerical Methods in Engineering*, 52(1-2):139–160.

[Miller, 1988] Miller, A. (1988). Review of limit loads of structures containing defects. *International Journal of Pressure Vessels and Piping*, 32(1):197–327.

[Mojgani and Balajewicz, 2020] Mojgani, R. and Balajewicz, M. (2020). Physics-aware registration based autoencoder for convection dominated pdes.

[Murakami, 2002] Murakami, Y. (2002). Chapter 6 - effects of nonmetallic inclusions on fatigue strength. In Murakami, Y., editor, *Metal Fatigue*, pages 75–127. Elsevier Science Ltd, Oxford.

[Nagy, 1979] Nagy, D. A. (1979). Modal representation of geometrically nonlinear behavior by the finite element method. *Computers and Structures*, 10(4):683–688.

[Nasiri and Khosravani, 2021] Nasiri, S. and Khosravani, M. R. (2021). Machine learning in predicting mechanical behavior of additively manufactured parts. *Journal of Materials Research and Technology*, 14:1137–1153.

[Nguyen et al., 2018] Nguyen, F., Barhli, S. M., Munoz, D. P., and Ryckelynck, D. (2018). Computer vision with error estimation for reduced order modeling of macroscopic mechanical tests. *Complexity*.

[Noor and Peters, 1980] Noor, A. K. and Peters, J. M. (1980). Reduced basis technique for nonlinear analysis of structures. *AIAA Journal*, 18(4):455–462.

[Pearson, 1901] Pearson, K. (1901). LIII. On lines and planes of closest fit to systems of points in space.

[Pedregosa et al., 2011] Pedregosa, F., Varoquaux, G., Gramfort, A., Michel, V., Thirion, B., Grisel, O., Blondel, M., Prettenhofer, P., Weiss, R., Dubourg, V., Vanderplas, J., Passos, A., Cournapeau, D., Brucher, M., Perrot, M., and Duchesnay, E. (2011). Scikit-learn: Machine learning in Python. *Journal of Machine Learning Research*, 12:2825–2830.

[Peherstorfer et al., 2014] Peherstorfer, B., Butnaru, D., Willcox, K., and Bungartz, H.-J. (2014). Localized discrete empirical interpolation method. *SIAM Journal on Scientific Computing*, 36(1):A168–A192.

[Phan and Dhar, 2021] Phan, H. C. and Dhar, A. S. (2021). Predicting pipeline burst pressures with machine learning models. *International Journal of Pressure Vessels and Piping*, 191:104384.

[Pidaparti et al., 2010] Pidaparti, R. M., Aghazadeh, B. S., Whitfield, A., Rao, A., and Mercier, G. P. (2010). Classification of corrosion defects in nial bronze through image analysis. *Corrosion Science*, 52(11):3661–3666.

[Prud'homme et al., 2002] Prud'homme, C., Rovas, D., Veroy, K., Machiels, L., Maday, Y., Patera, A., and Turinici, G. (2002). Reliable real-time solution of parametrized partial differential equations: Reduced-basis output bound methods. *Journal of Fluids Engineering*, 124:70.

[Qian et al., 2016] Qian, L., Cui, X., Liu, S., Chen, M., Ma, P., Xie, H., Zhang, F., and Meng, J. (2016). Image-based numerical simulation of the local cyclic deformation behavior around cast pore in steel. *Materials Science and Engineering: A*, 678:347–354.

[Redeker and Haasdonk, 2014] Redeker, M. and Haasdonk, B. (2014). A pod-eim reduced two-scale model for crystal growth. *Advances in Computational Mathematics*, 41.

[Rewienski and White, 2003] Rewienski, M. and White, J. (2003). A trajectory piecewise-linear approach to model order reduction and fast simulation of nonlinear circuits and micromachined devices. *Computer-Aided Design of Integrated Circuits and Systems, IEEE Transactions on*, 22:155 – 170.

[Rice, 1968] Rice, J. R. (1968). A Path Independent Integral and the Approximate Analysis of Strain Concentration by Notches and Cracks. *Journal of Applied Mechanics*, 35(2):379–386.

[Roweis and Saul, 2000] Roweis, S. T. and Saul, L. K. (2000). Nonlinear dimensionality reduction by locally linear embedding. *Science*, 290(5500):2323–2326.

[Ryckelynck et al., 2006] Ryckelynck, D., Chinesta, F., Cueto, E., and Ammar, A. (2006). On the "a priori" model reduction: Overview and recent developments. *Archives of Computational Methods in Engineering*, 13:91–128.

[Ryckelynck et al., 2016] Ryckelynck, D., Lampoh, K., and Quilicy, S. (2016). Hyper-reduced predictions for lifetime assessment of elasto-plastic structures. *Meccanica*, 51(2):309–317.

[Schölkopf et al., 1998] Schölkopf, B., Smola, A., and Müller, K.-R. (1998). Nonlinear component analysis as a kernel eigenvalue problem. *Neural Computation*, 10(5):1299–1319.

[Shih et al., 1986] Shih, C., Moran, B., and Nakamura, T. (1986). Energy release rate along a three-dimensional crack front in a thermally stressed body. *International Journal of Fracture*, 30:79–102.

[Sirovich, 1987] Sirovich, L. (1987). Turbulence and the dynamics of coherent structures part iii: Dynamics and scaling. *Quarterly of Applied Mathematics*, 45(3):583–590.

[Sniedovich, 2010] Sniedovich, M. (2010). *Dynamic programming: foundations and principles*. CRC press.

[Stewart, 1993] Stewart, G. W. (1993). On the early history of the singular value decomposition. *SIAM Review*, 35(4):551–566.

[Tada et al., 2000] Tada, H., Paris, P. C., and Irwin, G. R. (2000). *The Stress Analysis of Cracks Handbook, Third Edition*. ASME Press.

[Tenenbaum et al., 2000] Tenenbaum, J. B., Silva, V. d., and Langford, J. C. (2000). A global geometric framework for nonlinear dimensionality reduction. *Science*, 290(5500):2319–2323.

[Vinogradov and Milton, 2008] Vinogradov, V. and Milton, G. (2008). An accelerated fft algorithm for thermoelastic and non linear composites. *International Journal for Numerical Methods in Engineering*, 76:1678 – 1695.

[Wang et al., 2018] Wang, X., Phlipot, G., Perez, R., and Mignolet, M. (2018). Locally enhanced reduced order modeling for the nonlinear geometric response of structures with defects. *International Journal of Non-Linear Mechanics*, 101:1–7.

[Washabaugh et al., 2012] Washabaugh, K., Amsallem, D., Zahr, M., and Farhat, C. (2012). Nonlinear model reduction for cfd problems using local reduced order bases.

[Weinberger et al., 2004] Weinberger, K. Q., Sha, F., and Saul, L. K. (2004). Learning a kernel matrix for nonlinear dimensionality reduction. In *Proceedings of the Twenty-First International Conference on Machine Learning*, ICML '04, page 106, New York, NY, USA. Association for Computing Machinery.

[Wen et al., 2021] Wen, J., Zou, Q., and Wei, Y. (2021). Physics-driven machine learning model on temperature and time-dependent deformation in lithium metal and its finite element implementation. *Journal of the Mechanics and Physics of Solids*, 153:104481.

[Wieland, 2015] Wieland, B. (2015). Implicit partitioning methods for unknown parameter sets. *Advances in Computational Mathematics*, 41.

[Willot et al., 2013] Willot, F., Abdallah, B., and Pellegrini, Y. (2013). Fourier based schemes with modified green operator for computing the electrical response of heterogeneous media with accurate local fields. *International Journal for Numerical Methods in Engineering*, 98:518–533.

[Yadav et al., 2007] Yadav, R. B., Nishchal, N. K., Gupta, A. K., and Rastogi, V. K. (2007). Retrieval and classification of shape-based objects using fourier, generic fourier, and wavelet-fourier descriptors technique: A comparative study. *Optics and Lasers in Engineering*, 45(6):695–708.

[Yang et al., 2016] Yang, B., Xiang, M., and Zhang, Y. (2016). Multi-manifold discriminant isomap for visualization and classification. *Pattern Recognition*, 55:215–230.

[Yang et al., 2008] Yang, M., Kpalma, K., and Ronsin, J. (2008). A Survey of Shape Feature Extraction Techniques. In Yin, P.-Y., editor, *Pattern Recognition*, pages 43–90. IN-TECH. 38 pages.

[Yang and Su, 2009] Yang, M.-D. and Su, T.-C. (2009). Segmenting ideal morphologies of sewer pipe defects on cctv images for automated diagnosis. *Expert Systems with Applications*, 36(2, Part 2):3562–3573.

[Zhan et al., 2021] Zhan, Z., Hu, W., and Meng, Q. (2021). Data-driven fatigue life prediction in additive manufactured titanium alloy: A damage mechanics based machine learning framework. *Engineering Fracture Mechanics*, 252:107850.

[Zhang and Lu, 2002] Zhang, D. and Lu, G. (2002). Enhanced generic fourier descriptors for object-based image retrieval. volume 4, pages IV–3668.

[Zhang et al., 2015] Zhang, S. H., Chen, X., Wang, X., and Hou, J. (2015). Modeling of burst pressure for internal pressurized pipe elbow considering the effect of yield to tensile strength ratio. *Meccanica*, 50.

[Ñanculef et al., 2020] Ñanculef, R., Radeva, P., and Balocco, S. (2020). Chapter 9 - training convolutional nets to detect calcified plaque in ivus sequences. In Balocco, S., editor, *Intravascular Ultrasound*, pages 141–158. Elsevier.

## RÉSUMÉ

La tenue mécanique des structures est directement liée à la présence de défauts. Ces derniers jouent le rôle de concentrateur de contrainte, ce qui réduit considérablement la charge limite que les composants peuvent supporter ou encore leur durée de vie en fatigue. Néanmoins, d'un point de vue économique, il n'est pas envisageable de rebuter toute pièce défectueuse. Des critères permettant de statuer sur leur criticité ont donc été mis en place. Cependant ces derniers sont très conservatifs, par conséquent certains composants fonctionnels se trouvent mis au rebut. Pour pallier cette difficulté, des méthodes d'évaluation plus précises fondées sur le calcul numérique, telles que la méthode des éléments finis, sont utlisées. Toutefois ces dernières sont coûteuses en temps et en puissance de calcul. L'essor des techniques de science des données permet de tirer profit des informations collectées afin d'accélérer les simulations numériques. Ce travail de thèse vise à développer des méthodes de réduction de modèle par apprentissage automatique pour l'analyse de la nocivité de défauts en mécanique des matériaux. Par ailleurs, les méthodes d'apprentissage automatique permettent d'éviter le paramétrage des objets à modéliser. C'est une propriété particulièrement intéressante pour l'analyse des défauts, qui sont ici représentés à l'aide d'images (2D ou 3D) et associés à un champ mécanique calculé par la méthode des éléments finis ou FFT. Dans ce travail, des défauts locaux dans des matériaux métalliques ductiles sont considérés. L'objectif est de constituer des modèles numériques débouchant sur une décision rapide quant à la nocivité d'un défaut local à l'aide d'outils basés sur l'apprentissage automatique. Les approches proposées dans ce mémoire s'appuient en particulier sur des techniques de classification automatique des formes, reposant sur des distances morphologiques et mécaniques, et sur la représentation géométrique et mécanique des formes dans l'espace latent d'autoencodeurs multimodaux. Des méthodes d'estimation d'erreur sont également abordées afin d'évaluer la véracité des résultats trouvés.



## MOTS CLÉS

Mécanique numérique, méthodes FFT, méthodes d'hyper-réduction, apprentissage automatique, intelligence artificielle.



## ABSTRACT

The mechanical behaviour of structures is directly related to the presence of defects or not. They act as stress concentrators which considerably reduce the limit load that the components can support or their fatigue lifetime. However, from an economic point of view, it is not feasible to reject every component containing a defect. Criteria have therefore been developed to assess their criticality. However, they are very conservative, as a consequence some functional components are rejected. To avoid this difficulty, more accurate evaluation methods based on numerical calculation, such as the finite element method, are used. However, these numerical techniques are costly in terms of computation time and power. The explosive growth of data science allows the use of previously collected data to speed up numerical simulations. The aim of this thesis is to develop methods for model order reduction by machine learning for the analysis of the harmfulness of defects in mechanics of materials. The simulation-driven machine learning approach is very attractive when models are available. Moreover, machine learning methods are appropriate to avoid the parametrization of the objects to be modelled. This is a particularly interesting property for defect analysis. In this work, defects are represented using images (2D or 3D) as well as their associated mechanical response, predicted by a Fourier-based or finite element method. In this thesis we will focus on local defects in ductile metallic materials. The objective of the thesis is to build numerical models that allow a quick decision on the harmfulness of a local defect using a machine learning-based tool. Our approaches involve, in particular, automatic classification of shapes using both morphological and mechanically relevant distances as well as the representation of geometrical and mechanical shapes on the latent spaces of multimodal autoencoders. Error estimation methods are also discussed in order to evaluate the veracity of the results found.



## KEYWORDS

Numerical mechanics, FFT methods, hyper-reduction methods, machine learning, artificial intelligence.